Microstrip and Printed Antenna Design 2nd Edition

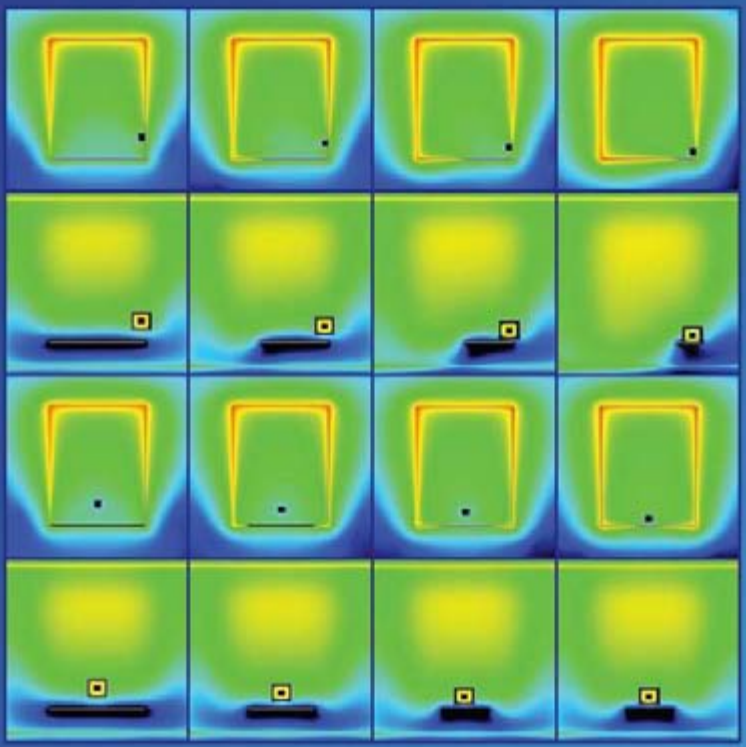

Randy Bancroft

Microstrip and Printed Antenna Design

Second Edition

Microstrip and Printed Antenna Design

Second Edition

Randy Bancroft

SciTech Publishing, Inc.
Raleigh, NC
www.scitechpub.com

© 2009 by SciTech Publishing Inc.
All rights reserved. No part of this book may be reproduced or used in any form whatsoever without written permission except in the case of brief quotations embodied in critical articles and reviews. For information, contact SciTech Publishing, Inc.

Printed in the U.S.A.
10 9 8 7 6 5 4 3 2 1

ISBN13: 9781891121739

SciTech President: Dudley R. Kay
Production Director: Susan Manning
Production Coordinator: Robert Lawless
Cover Design: Kathy Gagne

This book is available at special quantity discounts to use as premiums and sales promotions, or for use in corporate training programs. For more information and quotes, please contact:

Director of Special Sales
SciTech Publishing, Inc.
911 Paverstone Dr.—Ste. B
Raleigh, NC 27613

Phone: (919)847-2434
E-mail: sales@scitechpub.com
http://www.scitechpub.com

Library of Congress Cataloging-in-Publication Data

Bancroft, Randy.
Microstrip and printed antenna design / Randy Bancroft.—2nd ed.
p. cm.
ISBN 978-1-891121-73-9 (hbk. : alk. paper)
1. Microstrip antennas. I. Title.
TK7871.67.M5B35 2008
621.382′4—dc22

2008022523

To the memory of
Leslie “Skeez” Hartsock

Contents

Preface to Second Edition xi
Acknowledgment xiii
Chapter 1 Microstrip Antennas 1
1.1 The Origin of Microstrip Radiators 1
1.2 Microstrip Antenna Analysis Methods 4
1.3 Microstrip Antenna Advantages and Disadvantages 5
1.4 Microstrip Antenna Applications 6
References 7

Chapter 2 Rectangular Microstrip Antennas 10
2.1 The Transmission Line Model 10
2.2 The Cavity Model 19
2.2.1 The TM_{10} and TM_{01} Mode 24
2.3 Radiation Pattern and Directivity of a Linear Rectangular Microstrip Patch Antenna 28
2.4 Quarter-Wave Rectangular Microstrip Antenna 34
2.5 $\frac{\lambda}{4} \times \frac{\lambda}{4}$ Rectangular Microstrip Antenna 36
2.6 Circular Polarized Rectangular Microstrip Antenna Design 38
2.6.1 Single-Feed Circularly Polarized Rectangular Microstrip Antenna Design 38
2.6.2 Dual-Feed Circularly Polarized Rectangular Microstrip Antenna Design 49
2.6.3 Quadrature (90^o) Hybrid 50
2.7 Impedance and Axial Ratio Bandwidth 52
2.8 Efficiency 54
2.9 Design of a Linearly Polarized Microstrip Antenna with Dielectric Cover 56

2.10 Design Guidelines for a Linearly Polarized Rectangular Microstrip Antenna 60
2.11 Design Guidelines for a Circularly Polarized Rectangular Microstrip Antenna 64
2.12 Electromagnetically Coupled Rectangular Microstrip Antenna 65
2.13 Ultrawide Rectangular Microstrip Antenna 67
References 70

Chapter 3 Circular Microstrip Antennas 76
3.1 Circular Microstrip Antenna Properties 76
3.2 Directivity 80
3.3 Input Resistance and Impedance Bandwidth 81
3.3.1 Gain, Radiation Pattern, and Efficiency 82
3.4 Circular Microstrip Antenna Radiation Modes 83
3.4.1 The TM_{11} Bipolar Mode 83
3.4.2 The TM_{11} Bipolar Mode Circular Polarized Antenna Design 84
3.4.3 The TM_{21} Quadrapolar Mode 88
3.4.4 The TM_{02} Unipolar Mode 91
3.5 Microstrip Antenna Cross Polarization 92
3.6 Annular Microstrip Antenna 97
References 100

Chapter 4 Broadband Microstrip Antennas 102
4.1 Broadband Microstrip Antennas 102
4.2 Microstrip Antenna Broadbanding 103
4.2.1 Microstrip Antenna Matching with Capacitive Slot 105
4.2.2 Microstrip Antenna Broadband Matching with Bandpass Filter 106
4.2.3 Microstrip Antenna Broadband Matching Using Lumped Elements 111
4.2.4 Lumped Elements to Transmission Line Section Conversion 113

4.2.5 Real Frequency Technique Broadband Matching 119
4.2.6 Matching Network Optimization Using Genetic Algorithms 119
4.3 Patch Shape for Optimized Bandwidth 120
4.3.1 Patch Shape Bandwidth Optimization Using Genetic Algorithms 121
References 123

Chapter 5 Dual-Band Microstrip Antennas 126
5.0 Dual-Band Microstrip Antennas 126
5.1 Single-Resonator Rectangular Microstrip Dual-Band Antenna 126
5.2 Multiple Resonator Dual-Band Antennas 131
5.2.1 Coupled Microstrip Dipoles 131
5.2.2 Stacked Rectangular Microstrip Antennas 131
5.3 Dual-Band Microstrip Antenna Design Using a Diplexer 134
5.3.1 Example Dual-Band Microstrip Antenna Design Using a Diplexer 137
5.4 Multiband Microstrip Design Using Patch Shaping and a Genetic Algorithm 140
References 141

Chapter 6 Microstrip Arrays 142
6.0 Microstrip Arrays 142
6.1 Planar Array Theory 142
6.2 Rectangular Microstrip Antenna Array Modeled Using Slots 146
6.3 Aperture Excitation Distribution 148
6.4 Microstrip Array Feeding Methods 154
6.4.1 Corporate Fed Array 154
6.4.2 Series Fed Array 157
6.5 Phase and Amplitude Error 163
6.6 Mutual Coupling 165
6.6.1 Mutual Coupling Between Square Microstrip Antennas 170
References 176

Chapter 7 Printed Antennas 178
7.0 Printed Antennas 178
7.1 Omnidirectional Microstrip Antenna 178
7.1.1 Low Sidelobe Omnidirectional Microstrip Antenna 186
7.1.2 Element Shaping of Omnidirectional Microstrip Antenna 188
7.1.3 Single-Short Omnidirectional Microstrip Antenna 191
7.2 Stripline Fed Tapered Slot Antenna 192
7.2.1 Stripline Fed Vivaldi Antenna 197
7.3 Meanderline Antenna 199
7.3.1 Electrically Small Antennas 199
7.3.2 Meanderline Antenna Design 203
7.3.2.1 Meanderline Antenna Impedance Bandwidth 203
7.3.2.2 Meanderline Antenna Radiation Patterns 207
7.4 Half-Patch with Reduced Short Circuit Plane 211
7.4.1 Dual-Band PIFA 217
7.5 Rectangular Microstrip Fed Slot Antenna 219
7.5.1 Slot Antenna “Fictitious Resonance” 222
7.6 Microstrip Fed Log Periodic Balun Printed Dipole 225
7.7 Microstrip Fed Tapered Balun Printed Dipole 228
References 232

Appendix A: Microstrip Antenna Substrates 235
Appendix B: Numerical Methods 243
Appendix C: Microstrip Transmission Line Design and Discontinuities 249
Appendix D: Antenna Topics 257
Appendix E: Impedance Matching Techniques 268

Index 284

Preface to Second Edition

As with the first edition of this book, it is written for designers of planar microstrip antennas who develop antennas for wireless applications, and should also be useful to those who design antennas for the aerospace industry. Many of the subjects chosen for examination reflect those found to be useful by the author during his career. The text includes the most useful recent work available from researchers in the microstrip and printed antenna field. This book is intended to be used as a succinct, accessible handbook which provides useful, practical, simple, and manufacturable antenna designs but also offers references which allow the reader to investigate more complex designs.

The second edition has numerous additions to the earlier text which I hope will make the concepts presented clearer. New cavity model analysis equations of circular polarization bandwidth, axial ratio bandwidth and power fraction bandwidth have been included. The section on omnidirectional microstrip antennas is expanded with further design options and analysis. This also true of the section on Planar Inverted F (PIFA) antennas. The discovery and description of the "fictious resonance" mode of a microstrip slot antenna has been added to that section. Appendix A on microstrip antenna substrates has been expanded to provide more detail on the types of substrate and their composition. This is often neglected in other texts. An appendix on elementary impedance matching techniques has been added as these methods have proven useful in my industrial work.

Numerous books have been published about microstrip antenna design which have an intimidating variety of designs. This volume attempts to distill these designs down to those which have considerable utility and simplicity. It also attempts to present useful new research results and designs generally not emphasized in other volumes.

In the last ten years, computer methods of electromagnetic analysis such as the Finite Difference Time Domain (FDTD) method, Finite Element Method (FEM) and Method of Moments (MoM) have become accessible to most antenna designers. This book introduces elementary analysis methods which may be used to estimate design dimensions. These methods should be implementable with relative ease. Full wave methods may then be used to refine the initial designs.

When mathematics beyond algebra is presented, such as integrations and infinite sums, appendices are provided which explain how to undertake their numerical computation. Results from advanced methods such as FDTD, FEM or MoM are presented with input dimensions and parameters which were used to generate them. This is so the reader can reproduce and alter them to aid their understanding. These results are used to provide insight into a design. The author's preferred method of analysis is the Finite Difference Time Domain method which is generously represented in this volume. In the second edition Ansoft HFSS has provided a larger share of the analysis.

I would like to thank Paul Cherry for his generous assistance and discussions which allowed me to implement FDTD analysis code and his thermal viewing software whose images grace these pages.

Acknowledgments

SciTech Publishing arranged for a number of extremely helpful peer reviews during the development of the book. As is the usual practice, these reviewers and their comments were sent anonymously to me until everything in the book was completed. With SciTech's assistance I now can gratefully acknowledge and heartily thank the men and woman, the academics and practicing engineers, who helped me achieve the balance, consistency, and clarity in my prose that might not otherwise have been possible. Excellent work.

Dr. Reyhan Baktur
Dept. of Electrical and Computer Engineering
Utah State University
Logan, UT

Gabe Edde
Research Engineer
Thomson Inc.
Indianapolis, Indiana

Howard Freidenberg
Sr. RF Engineer
Moseley Associates, Inc.
Santa Barbara, California

James Gitre
RF Design Engineer
Motorola—Future Wireless Modem Technology
Group
Austin, Texas

Dr. Peter Petkov
Dept. of Radiotechnics
Technical University of Sofia
Bulagria

Nate Stutzke
RF Design Engineer
Ball Aerospace & Technologies Corp.
Broomfield, Colorado

Michael Zinanti
Senior Design Engineer
Ball Aerospace & Technologies Corp.
Broomfield, Colorado

I would like to thank the SciTech Publishing team. This is my third book, and I can honestly say this was by far the most professional team effort by a publisher. From Dudley Kay, President and Editorial Director, I received encouragement to undertake the revision and not be satisfied with the first submission. He lined up the enthusiastic and helpful reviewers. Under the guidance of Director of Operations Susan Manning, Production Assistant Robert Lawless oversaw the entire book production process and worked with me personally on the cover design and redrawing of art. Of course, any errors of omission or commission are mine alone, and I welcome your feedback for corrections and improvements.

Chapter 1

Microstrip Antennas

1.1 The Origin of Microstrip Radiators

The use of coaxial cable and parallel two wire (or "twin lead") as a transmission line can be traced to at least the 19th century. The realization of radio frequency (RF) and microwave components using these transmission lines required considerable mechanical effort in their construction. The advent of printed circuit board techniques in the mid-20th century led to the realization that printed circuit versions of these transmission lines could be developed which would allow for much simpler mass production of microwave components. The printed circuit analog of a coaxial cable became known as stripline. With a groundplane image providing a virtual second conductor, the printed circuit analog of two wire ("parallel plate") transmission line became known as microstrip. For those not familiar with the details of this transmission line, they can be found in Appendix B at the end of this book.

Microstrip geometries which radiate electromagnetic waves were originally contemplated in the 1950s. The realization of radiators that are compatible with microstrip transmission line is nearly contemporary, with its introduction in 1952 by Grieg and Englemann.[1] The earliest known realization of a microstrip-like antenna integrated with microstrip transmission line was developed in 1953 by Deschamps[2,3] (Figure 1-1). By 1955, Gutton and Baissinot patented a microstrip antenna design.[4]

Early microstrip lines and radiators were specialized devices developed in laboratories. No commercially available printed circuit boards with controlled dielectric constants were developed during this period. The investigation of microstrip resonators that were also efficient radiators languished. The theoretical basis of microstrip transmission lines continued to be the object of academic inquiry.[5] Stripline received more interest as a planar transmission

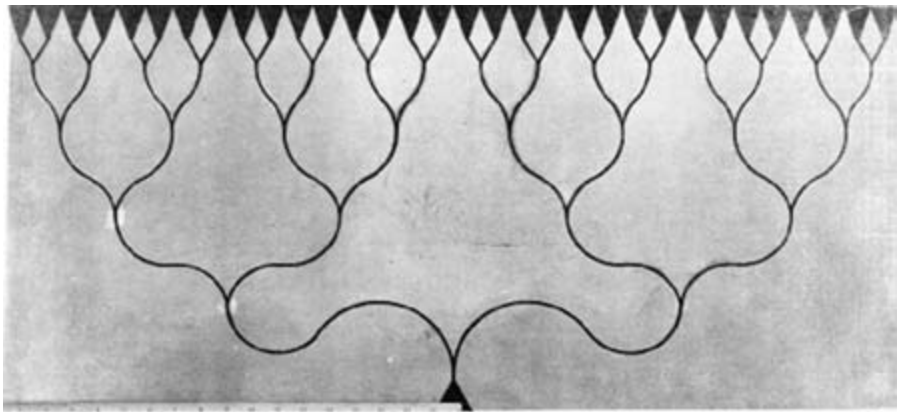

Figure 1-1 Original conformal array designed by Deshamps [2] in 1953 fed with microstrip transmission line.

line at the time because it supports a transverse electromagnetic (TEM) wave and allowed for easier analysis, design, and development of planar microwave structures. Stripline was also seen as an adaptation of coaxial cable and microstrip as an adaptation of two wire transmission line. R. M. Barrett opined in 1955 that the "merits of these two systems [stripline and microstrip] are essentially the merits of their respective antecedents [coaxial cable and two wire]."[6] These viewpoints may have been some of the reasons microstrip did not achieve immediate popularity in the 1950s. The development of microstrip transmission line analysis and design methods continued in the mid to late 1960s with work by Wheeler[7] and Purcel et al.[8,9]

In 1969 Denlinger noted rectangular and circular microstrip resonators could efficiently radiate.[10] Previous researchers had realized that in some cases, 50% of the power in a microstrip resonator would escape as radiation. Denlinger described the radiation mechanism of a rectangular microstrip resonator as arising from the discontinuities at each end of a truncated microstrip transmission line. The two discontinuities are separated by a multiple of a half wavelength and could be treated separately and combined to describe the complete radiator. It was noted that the percentage of radiated power to the

total input power increased as the substrate thickness of the microstrip radiator increased. These correct observations are discussed in greater detail in Chapter 2. Denlinger's results only explored increasing the substrate thickness until approximately 70% of the input power was radiated into space. Denlinger also investigated radiation from a resonant circular microstrip disc. He observed that at least 75% of the power was radiated by one circular resonator under study. In late 1969, Watkins described the fields and currents of the resonant modes of circular microstrip structures.[11]

The microstrip antenna concept finally began to receive closer examination in the early 1970s when aerospace applications, such as spacecraft and missiles, produced the impetus for researchers to investigate the utility of conformal antenna designs. In 1972 Howell articulated the basic rectangular microstrip radiator fed with microstrip transmission line at a radiating edge.[12] The microstrip resonator with considerable radiation loss was now described as a microstrip antenna. A number of antenna designers received the design with considerable caution. It was difficult to believe a resonator of this type could radiate with greater than 90% efficiency. The narrow bandwidth of the antenna seemed to severely limit the number of possible applications for which the antenna could prove useful. By the late 1970s, many of these objections had not proven to derail the use of microstrip antennas in numerous aerospace applications. By 1981, microstrip antennas had become so ubiquitous and studied that they were the subject of a special issue of the *IEEE Transactions on Antennas and Propagation*.[13]

Today a farrago of designs have been developed, which can be bewildering to designers who are new to the subject. This book attempts to explain basic concepts and present useful designs. It will also direct the reader who wishes to research other microstrip antenna designs, which are not presented in this work, to pertinent literature.

The geometry which is defined as a microstrip antenna is presented in Figure 1-2. A conductive patch exists along the plane of the upper surface of a dielectric slab. This area of conductor, which forms the radiating element, is generally rectangular or circular, but may be of any shape. The dielectric substrate has groundplane on its bottom surface.

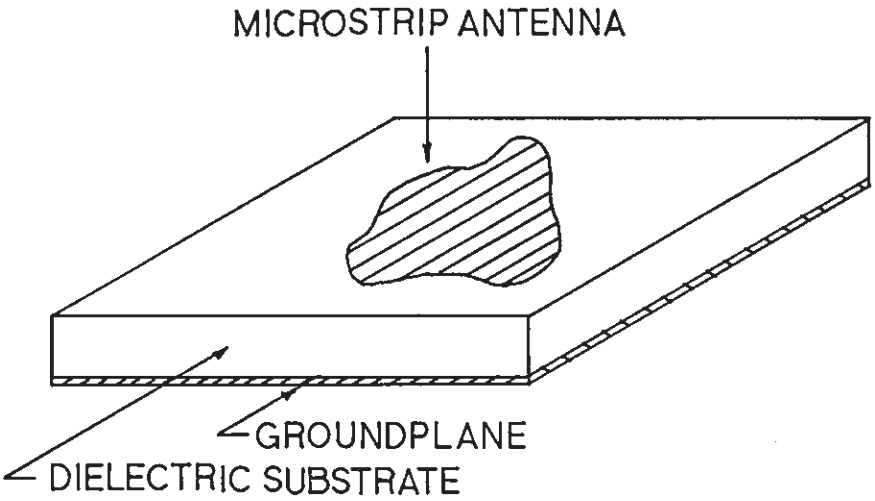

Figure 1-2 Geometry of a microstrip antenna.

1.2 Microstrip Antenna Analysis Methods

It was known that the resonant length of a rectangular microstrip antenna is approximately one-half wavelength with the effective dielectric constant of the substrate taken into account. Following the introduction of the microstrip antenna, analysis methods were desired to determine the approximate resonant resistance of a basic rectangular microstrip radiator. The earliest useful model introduced to provide approximate values of resistance at the edge of a microstrip antenna is known as the transmission line model, introduced by Munson.[14] The transmission line model provides insight into the simplest microstrip antenna design, but is not complete enough to be useful when more than one resonant mode is present. In the late 1970s Lo et al. developed a model of the rectangular microstrip antenna as a lossy resonant cavity.[15] Microstrip antennas, despite their simple geometry, proved to be very challenging to analyze using exact methods. In the 1980s, the method of moments (MoM) became the first numerical analysis method that was computationally efficient enough so that contemporary computers

could provide enough memory and CPU speed to practically analyze microstrip antennas.[16–19]

Improvements in computational power and memory size of personal computers during the 1990s made numerical methods such as the finite difference time domain (FDTD) method and finite element method (FEM), which require much more memory than MoM solutions, workable for everyday use by designers. This book will generally use FDTD as a full-wave analysis method as well as Ansoft HFSS.[20,21]

1.3 Microstrip Antenna Advantages and Disadvantages

The main advantages of microstrip antennas are:

- Low-cost fabrication.
- Can easily conform to a curved surface of a vehicle or product.
- Resistant to shock and vibration (most failures are at the feed probe solder joint).
- Many designs readily produce linear or circular polarization.
- Considerable range of gain and pattern options (2.5 to 10.0 dBi).
- Other microwave devices realizable in microstrip may be integrated with a microstrip antenna with no extra fabrication steps (e.g., branchline hybrid to produce circular polarization or corporate feed network for an array of microstrip antennas).
- Antenna thickness (profile) is small.

The main disadvantages of microstrip antennas are

- Narrow bandwidth (5% to 10% [2:1 voltage standing wave ratio (VSWR)] is typical without special techniques).
- Dielectric and conductor losses can be large for thin patches, resulting in poor antenna efficiency.
- Sensitivity to environmental factors such as temperature and humidity.

1.4 Microstrip Antenna Applications

A large number of commercial needs are met by the use of microstrip and printed antennas, these include the ubiquitous Global Positioning System (GPS), Zigbee, Bluetooth, WiMax, WiFi applications, 802.11a,b,g, and others. The most popular microstrip antenna is certainly the rectangular patch (Chapter 2). GPS applications, such as asset tracking of vehicles as well as marine uses, have created a large demand for antennas. The majority of these are rectangular patches that have been modified to produce right-hand circular polarization (RHCP) and operate at 1.575 GHz. Numerous vendors offer patches designed using ceramics with a high dielectric constant (ε_r = 6, 20, 36) to reduce the rectangular microstrip antenna to as small a footprint as possible for a given application. The patches are provided ready for circuit board integration with low noise amplifiers. Rectangular patch antennas are also used for Bluetooth automotive applications (2.4 GHz) with RHCP.

In recent years Satellite Digital Audio Radio Services (SDARS) have become a viable alternative to AM and FM commercial broadcasts in automobiles. The system has strict radiation pattern requirements which have been met with a combination of a printed monopole and a TM_{21} mode annular microstrip antenna that has been altered with notches to produce left-hand circular polarization at 2.338 GHz.[22] The annular microstrip antenna is addressed in Chapter 3.

Wireless local area networks (WLAN) provide short-range, high-speed data connections between mobile devices (such as a laptop computer) and wireless access points. The range for wireless data links is typically around 100 to 300 feet indoors and 2000 feet outdoors. Wireless data links use the IEEE Standards 802.11a,b,g. The majority of WLANs use the unlicensed 2.4 GHz band (802.11b and 802.11g). The 802.11a standard uses the 5 GHz unlicensed frequency band. Multiband printed antennas that are integrated into ceiling tiles use a microstrip diplexer (Chapter 5) to combine the signal from Global System for Mobile communication (GSM) cell phones (860 MHz band), personal communications services (PCS) cell phones (1.92 GHz band), and 802.11a WLAN service (2.4 GHz band) provided by two integrated microstrip dipoles.[23]

Wireless local area network systems sometimes require links between buildings that have wireless access points. This is sometimes accomplished using microstrip phased arrays at 5 GHz (Chapter 6).

In other applications, such as warehouse inventory control, a printed antenna with an omnidirectional pattern is desired (Chapter 7). Omnidirectional microstrip antennas are also of utility for many WiMax applications (2.3, 2.5, 3.5, and 5.8 GHz are some of the frequencies currently of interest for WiMax applications) and for access points. Microstrip fed printed slot antennas have proven useful to provide vertical polarization and integrate well into laptop computers (Chapter 7) for WLAN.

The advantages of using antennas in communication systems will continue to generate new applications which require their use. Antennas have the advantage of mobility without any required physical connection. They are the device which enables all the "wireless" systems that have become so ubiquitous in our society. The use of transmission line, such as coaxial cable or waveguide, may have an advantage in transmission loss for short lengths, but as distance increases, the transmission loss between antennas becomes less than any transmission line, and in some applications can outperform cables for shorter distances.[24] The material costs for wired infrastructure also encourages the use of antennas in many modern communication systems.

References

[1] Grieg, D. D., and Englemann, H. F., "Microstrip—a new transmission technique for the kilomegacycle range," *Proceedings of the IRE*, 1952, Vol. 40, No. 10, pp. 1644–1650.

[2] Deschamps, G. A., "Microstrip Microwave Antennas," Third Symposium on the USAF Antenna Research and Development Program, University of Illinois, Monticello, Illinois, October 18–22, 1953.

[3] Bernhard, J. T., Mayes, P. E., Schaubert, D., and Mailoux, R. J., "A commemoration of Deschamps' and Sichak's 'Microstrip Microwave Antennas': 50 years of development, divergence, and new directions," *Proceedings of the 2003 Antenna Applications Symposium*, Monticello, Illinois, September 2003, pp. 189–230.

[4] Gutton, H., and Baissinot, G., "Flat aerial for ultra high frequencies," French Patent no. 703113, 1955.

[5] Wu, T. T., "Theory of the microstrip," *Journal of Applied Physics*, March 1957, Vol. 28, No. 3, pp. 299–302.

[6] Barrett, R. M., "Microwave printed circuits—a historical survey," *IEEE Transactions on Microwave Theory and Techniques*, Vol. 3, No. 2, pp. 1–9.

[7] Wheeler, H. A., "Transmission line properties of parallel strips separated by a dielectric sheet," *IEEE Transactions on Microwave Theory of Techniques*, March 1965, Vol. MTT-13, pp. 172–185.

[8] Purcel, R. A., Massé, D. J., and Hartwig, C. P., "Losses in microstrip," *IEEE Transactions on Microwave Theory and Techniques* , June 1968, Vol. 16, No. 6, pp. 342–350.

[9] Purcel, R. A., Massé, D. J., and Hartwig, C. P., "Errata: 'Losses in microstrip,'" *IEEE Transactions on Microwave Theory and Techniques*, December 1968, Vol. 16, No. 12, p. 1064.

[10] Denlinger, E. J., "Radiation from microstrip radiators," *IEEE Transactions on Microwave Theory of Techniques*, April 1969, Vol. 17, No. 4, pp. 235–236.

[11] Watkins, J., "Circular resonant structures in microstrip," *Electronics Letters*, Vol. 5, No. 21, October 16, 1969, pp. 524–525.

[12] Howell, J. Q., "Microstrip antennas," IEEE International Symposium on Antennas and Propagation, Williamsburg Virginia, 1972, pp. 177–180.

[13] *IEEE Transactions on Antennas and Propagation*, January 1981.

[14] Munson, R. E., "Conformal microstrip antennas and microstrip phased arrays," *IEEE Transactions on Antennas and Propagation*, January 1974, Vol. 22, No. 1, pp. 235–236.

[15] Lo, Y. T., Solomon, D., and Richards, W. F., "Theory and experiment on microstrip antennas," *IEEE Transactions on Antennas and Propagations*, 1979, AP-27, pp. 137–149.

[16] Hildebrand, L. T., and McNamara, D. A., "A guide to implementational aspects of the spatial-domain integral equation analysis of microstrip antennas," *Applied Computational Electromagnetics Journal*, March 1995, Vol. 10, No. 1, ISSN 1054-4887, pp. 40–51.

[17] Mosig, J. R., and Gardiol, F. E., "Analytical and numerical techniques in the Green's function treatment of microstrip antennas and scatterers," *IEE Proceedings*, March 1983, Vol. 130, Pt. H., No. 2, pp. 175–182.

[18] Mosig, J. R., and Gardiol, F. E., "General integral equation formulation for microstrip antennas and scatterers," *IEE Proceedings*, December 1985, Vol. 132, Pt. H, No. 7, pp. 424–432.

[19] Mosig, J. R., "Arbitrarily shaped microstrip structures and their analysis with a mixed potential integral equation," *IEEE Transactions on Microwave Theory and Techniques*, February 1988, Vol. 36, No. 2. pp. 314–323.

[20] Tavlov, A., and Hagness, S. C., *Computational Electrodynamics: The Finite-Difference Time-Domain Method*, 2nd ed., London: Artech House, 2000.

[21] Tavlov, A., ed., *Advances in Computational Electrodynamics: The Finite Difference Time-Domain Method*, London: Artech House, 1998.

[22] Licul, S., Petros, A., and Zafar, I., "Reviewing SDARS antenna requirements," *Microwaves & RF*, September 2003, ED Online ID #5892.

[23] Bateman, B. R., Bancroft, R. C., and Munson, R. E., "Multiband flat panel antenna providing automatic routing between a plurality of antenna elements and an input/output port," U.S. Patent No. 6,307,525.

[24] Milligan, T., *Modern Antenna Design*, New York: McGraw Hill, 1985, pp. 8–9.

Chapter 2

Rectangular Microstrip Antennas

2.1 The Transmission Line Model

The rectangular patch antenna is very probably the most popular microstrip antenna design implemented by designers. Figure 2-1 shows the geometry of this antenna type. A rectangular metal patch of width $W = a$ and length $L = b$ is separated by a dielectric material from a groundplane by a distance h. The two ends of the antenna (located at 0 and b) can be viewed as radiating due to fringing fields along each edge of width W (= a). The two radiating edges are separated by a distance L (= b). The two edges along the sides of length L are often referred to as nonradiating edges.

Numerous full-wave analysis methods have been devised for the rectangular microstrip antenna.[1–4] Often these advanced methods require a considerable investment of time and effort to implement and are thus not convenient for computer-aided design (CAD) implementation.

The two analysis methods for rectangular microstrip antennas which are most popular for CAD implementation are the transmission line model and the cavity model. In this section I will address the least complex version of the transmission line model. The popularity of the transmission line model may be gauged by the number of extensions to this model which have been developed.[5–7]

The transmission line model provides a very lucid conceptual picture of the simplest implementation of a rectangular microstrip antenna. In this model, the rectangular microstrip antenna consists of a microstrip transmission line with a pair of loads at either end.[8,9] As presented in Figure 2-2(a), the resistive loads at each end of the transmission line represent loss due to radiation. At resonance, the imaginary components of the input impedance seen at

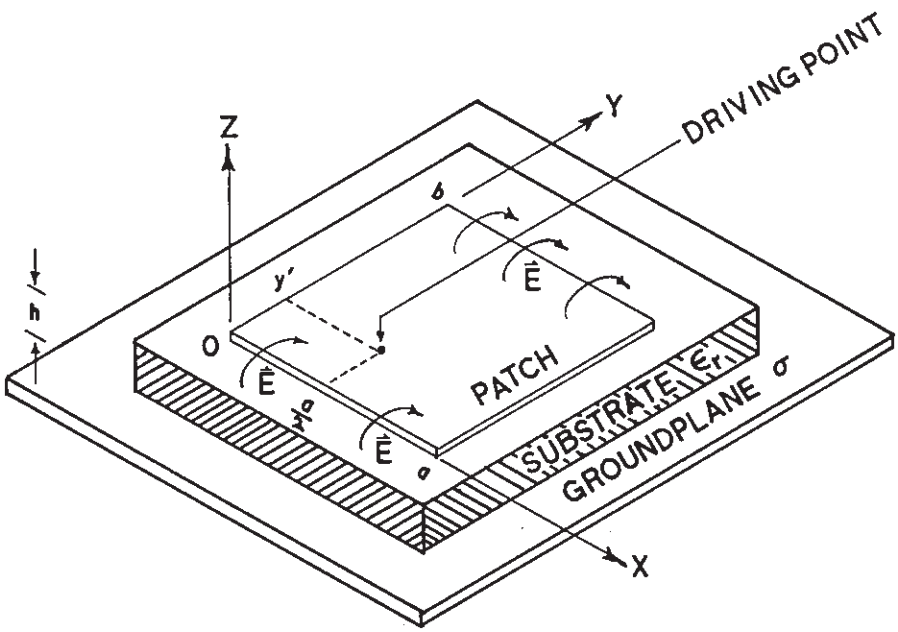

Figure 2-1 Rectangular microstrip patch geometry used to describe the transmission line model. The patch antenna is fed along the centerline of the antenna's dimension along $\hat{x}$ (i.e., $x = a/2$). The feed point is located at $\acute{y}$, which is chosen to match the antenna with a desired impedance. The radiation originates from the fringing electric field at either end of the antenna. These edges are called radiating edges, the other two sides (parallel to the $\hat{y}$ axis) are nonradiating edges.

the driving point cancel, and therefore the driving point impedance becomes exclusively real.

The driving point or feed point of an antenna is the location on an antenna where a transmission line is attached to provide the antenna with a source of microwave power. The impedance measured at the point where the antenna is connected to the transmission line is called the driving point impedance or input impedance. The driving point impedance (Z_{drv}) at any point along the center line of a rectangular microstrip antenna can be computed using the transmission line model. The transmission line model is most easily represented mathematically using the transmission line equation written in terms of admittances, as presented in equation (2.1):

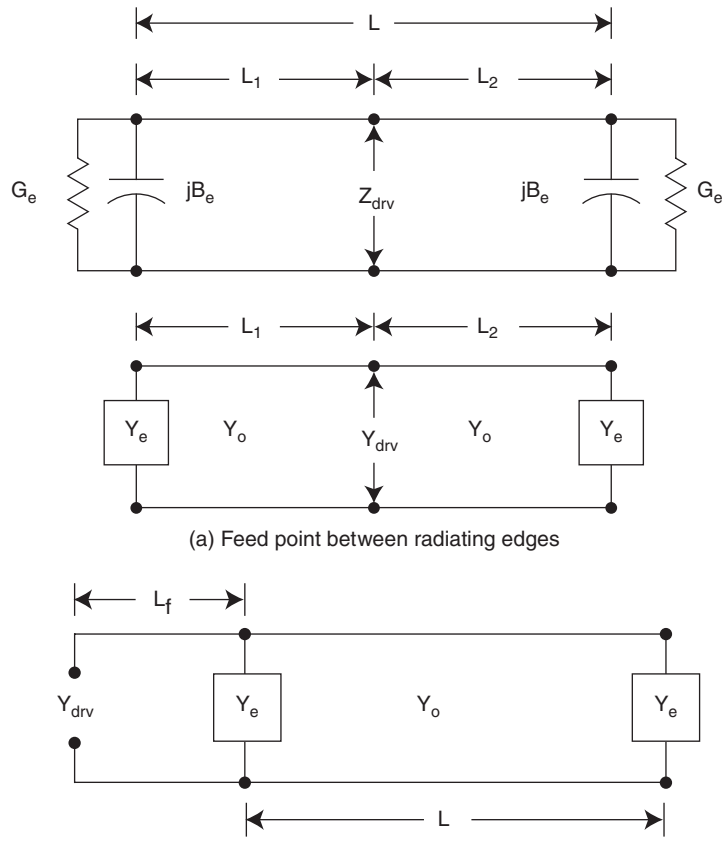

Figure 2-2 (a) The transmission line model of a rectangular microstrip antenna is a transmission line separating two loads. A driving point is chosen along the antenna length L which can be represented as a sum of L_1 and L_2. The two transmission line sections contribute to the driving point impedance. The antenna is readily analyzed using a pair of edge admittances (Y_e) separated by two sections of transmission line of characteristic admittance (Y_0). (b) The microstrip antenna may be fed at one of its radiating edges using a transmission line. In this case, the transmission line model is augmented with a feed line of characteristic admittance Y_f of length L_f connected to a radiating edge. The driving point admittance Y_{drv} is then computed at the end of this feed line.

$$Y_{in} = Y_0 \frac{Y_L + jY_0 \tan(\beta L)}{Y_0 + jY_L \tan(\beta L)} \tag{2.1}$$

Y_{in} is the input admittance at the end of a transmission line of length L (= b), which has a characteristic admittance of Y_0, and a phase constant of β terminated with a complex load admittance, Y_L. In other words, the microstrip antenna is modeled as a microstrip transmission line of width W (= a), which determines the characteristic admittance, and is of physical length L (= b) and loaded at both ends by an edge admittance Y_e which models the radiation loss. This is shown in Figure 2-2(a).

Using equation (2.1), the driving point admittance $Y_{drv} = 1/Z_{drv}$ at a driving point between the two radiating edges is expressed as:

$$Y_{drv} = Y_0 \left[\frac{Y_e + jY_0 \tan(\beta L_1)}{Y_0 + jY_e \tan(\beta L_1)} + \frac{Y_e + jY_0 \tan(\beta L_2)}{Y_0 + jY_e \tan(\beta L_2)} \right] \tag{2.2}$$

Y_e is the complex admittance at each radiating edge, which consists of an edge conductance G_e and edge susceptance B_e as related in equation (2.3). The two loads are separated by a microstrip transmission line of characteristic admittance Y_0:

$$Y_e = G_e + jB_e \tag{2.3}$$

Approximate values of G_e and B_e may be computed using equation (2.4) and equation (2.5).[10]

$$G_e = 0.00836 \frac{W}{\lambda_0} \tag{2.4}$$

$$B_e = 0.01668 \frac{\Delta l}{h} \frac{W}{\lambda_0} \varepsilon_e \tag{2.5}$$

The effective dielectric constant ($W/h \geq 1$) is given as

$$\varepsilon_e = \frac{\varepsilon_r + 1}{2} + \frac{\varepsilon_r - 1}{2} \left(1 + 12 \frac{h}{W} \right)^{-1/2} \tag{2.6}$$

The fringing field extension normalized to the substrate thickness h is

$$\frac{\Delta l}{h} = 0.412\frac{(\varepsilon_e + 0.3)(W/h + 0.264)}{(\varepsilon_e - 0.258)(W/h + 0.8)} \tag{2.7}$$

The value Δl is the line extension due to the electric field fringing at the edge of the patch antenna. The physical size of a resonant microstrip patch antenna would be $\lambda_{\varepsilon_e}/2$ were it not for the effect of fringing at the end of the rectangular microstrip antenna.[1] Equation (2.7) can be used to correct for this effect and compute the physical length of a rectangular microstrip antenna which will resonate at a desired design frequency f_r.

Figure 2-3 presents four common methods used to directly feed a microstrip antenna. The first method is often called a coaxial probe feed (Figure 2-3(a)). The outer shield of a coaxial transmission line is connected to the groundplane of the microstrip antenna. Metal is removed from the groundplane which is generally the same radius as the inside of the coaxial shield. The coaxial center conductor then passes through the dielectric substrate of the patch antenna and connects to the patch. Feeding the antenna in the center (i.e., at $a/2$) suppresses the excitation of a mode along the width of the antenna. This feed symmetry enforces the purest linear polarization along the length of the patch which can be achieved with a single direct feed.

The second feed method, shown in Figure 2-3(b), drives the antenna with a microstrip transmission line along a nonradiating edge. This feed method is modeled in an identical manner to the coaxial probe feed when using the transmission line model; in practice, it can often excite a mode along the width of the patch when $a \approx b$ and cause the antenna to radiate with an elliptical polarization. The advantage of this feed method is that it allows one to use a 50 Ω microstrip transmission line connected directly to a 50 Ω driving point impedance which eliminates the need for impedance matching.

The third feed method, shown in Figure 2-3(c), is to drive the antenna at one of its radiating edges with a microstrip transmission line. This disturbs the field distribution along one radiating edge, which causes slight changes in the

[1] This fringing is similar to the fringing at the end of a dipole antenna. The extra electrical length causes a dipole antenna to resonate at a length which is closer to 0.48λ rather than the 0.50λ expected if no end capacitance were present.

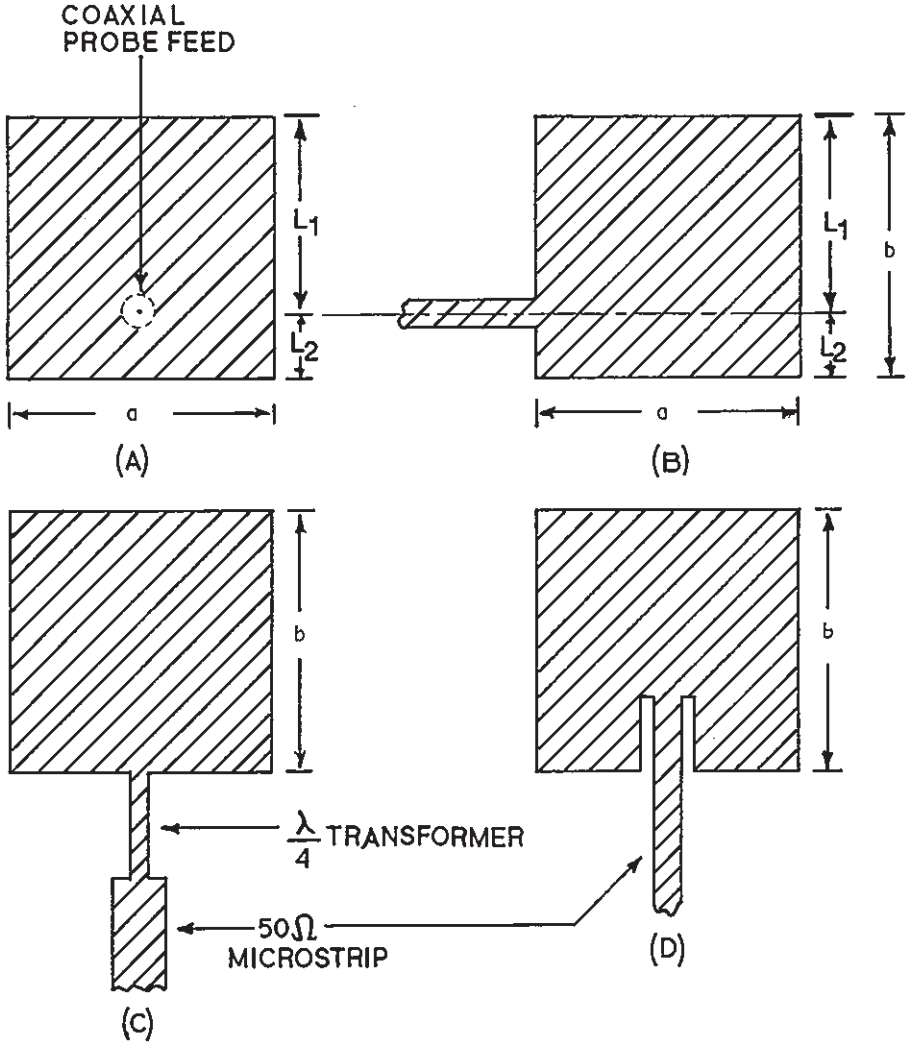

Figure 2-3 Common methods used to feed a rectangular microstrip antenna. (a) Coaxial feed probe. (b) Microstrip transmission line feed along a nonradiating edge. (c) Microstrip transmission feed along a radiating edge. (d) Microstrip feed line into a cutout in a radiating edge which is inset to a 50 Ω driving point.

radiation pattern. The impedance of a typical resonant rectangular ($a < 2b$) microstrip antenna at a radiating edge is around 200 Ω. This edge resistance R_{in} is $1/(2G_e)$ at resonance. In general, one must provide an impedance transformation to 50 Ω for this feed method. This is often accomplished using a quarter-wave impedance transformer between the radiating edge impedance and a 50 Ω microstrip feed line. A quarter-wave transformer has a larger bandwidth than the antenna element and therefore does not limit it. It is possible to widen a rectangular microstrip antenna ($a > b$) so the edge resistance at resonance is 50 Ω. In this special case, no impedance transformer is required to feed the antenna with a 50 Ω microstrip transmission line at a radiating edge.

A fourth feed method, illustrated in Figure 2-3(d), is to cut a narrow notch out of a radiating edge far enough into the patch to locate a 50 Ω driving point impedance. The removal of the notch perturbs the patch fields. A study by Basilio et al. indicates that a probe fed patch antenna has a driving point resistance that follows an $R_{in}\cos^2(\pi L_2/L)$, while a patch with an inset feed is measured to follow an $R_{in}\cos^4(\pi L_2/L)$ function, where $0 < L_2 < L/2$.[11] One can increase the patch width, which increases the edge conductance, until at resonance the edge impedance is 50 Ω. The inset distance into the patch goes to zero, which allows one to directly feed a patch for this special case using a 50 Ω microstrip line at a radiating edge. The patch width is large enough in this case to increase the antenna gain considerably.

Equation (2.8) may be used to compute the resonant length (L) of a rectangular microstrip antenna:

$$L = \frac{c}{2f_r\sqrt{\varepsilon_e}} - 2\Delta l = \frac{\lambda_{\varepsilon_e}}{2} - 2\Delta l \tag{2.8}$$

$$\lambda_{\varepsilon_e} = \frac{\lambda_0}{\sqrt{\varepsilon_e}} \tag{2.9}$$

Equation (2.2) provides a predicted input impedance at the desired design frequency f_r. Numerical methods for obtaining the roots of an equation such

as the Bisection Method (Appendix B) may be used with equation (2.2) to determine the value of L_1 and L_2, which correspond to a desired input resistance value. The initial guesses are along b at $b_1 = 0$ ($R_{in} = 1/2G_e$) and $b_2 = b/2$ ($R_{in} \approx 0$).

The predicted position of a desired driving point impedance to feed the antenna is generally close to measurement as long as the substrate height is not larger than about $0.1\lambda_0$. A good rule of thumb for an initial guess to the location of a 50 Ω feed point when determining the position in an empirical manner is 1/3 of the distance from the center of the antenna to a radiating edge, inward from a radiating edge.

Early investigation of the rectangular microstrip antenna, viewed as a linear transmission line resonator, was undertaken by Derneryd.[12] The input impedance characteristics of the transmission line model were altered by Derneryd in a manner which allows for the influence of mutual conductance between the radiating edges of the patch antenna. This model further allows for the inclusion of higher order linear transmission line modes.

In 1968, an experimental method to investigate the electric fields near surrounding objects was developed which used a liquid crystal sheet backed with a resistive thin film material.[13,14] Derneryd used a liquid crystal field detector of this type to map the electric field of a narrow microstrip antenna. Derneryd's results are reproduced in Figure 2-4, along with thermal (electric field magnitude) plots produced using the finite difference time domain (FDTD) method. The FDTD patch analysis used $a = 10.0$ mm, $b = 30.5$ mm, $\varepsilon_r = 2.55$, $h = 1.5875$ mm (0.0625 inches), and $\tan \delta = 0.001$. The feed point location is 5.58 mm from the center of the patch antenna along the centerline. The groundplane is 20 mm × 42 mm.

Figure 2-4(a) is the antenna without an electric field present. Figure 2-4(b) is Derneryd's element analyzed with a thermal liquid crystal display (LCD) which shows the first (lowest order) mode of this antenna. The frequency for this first mode is reported to be 3.10 GHz. A sinusoidal source at 3.10 GHz with FDTD was used to model this antenna. The FDTD plot is of the total magnitude of the electric field in the plane of the antenna. The FDTD simulation thermal plot is very similar to the shape of the measured LCD thermal pattern. We see two radiating edges at either end of the antenna in the lowest mode, with two nonradiating edges on the sides.

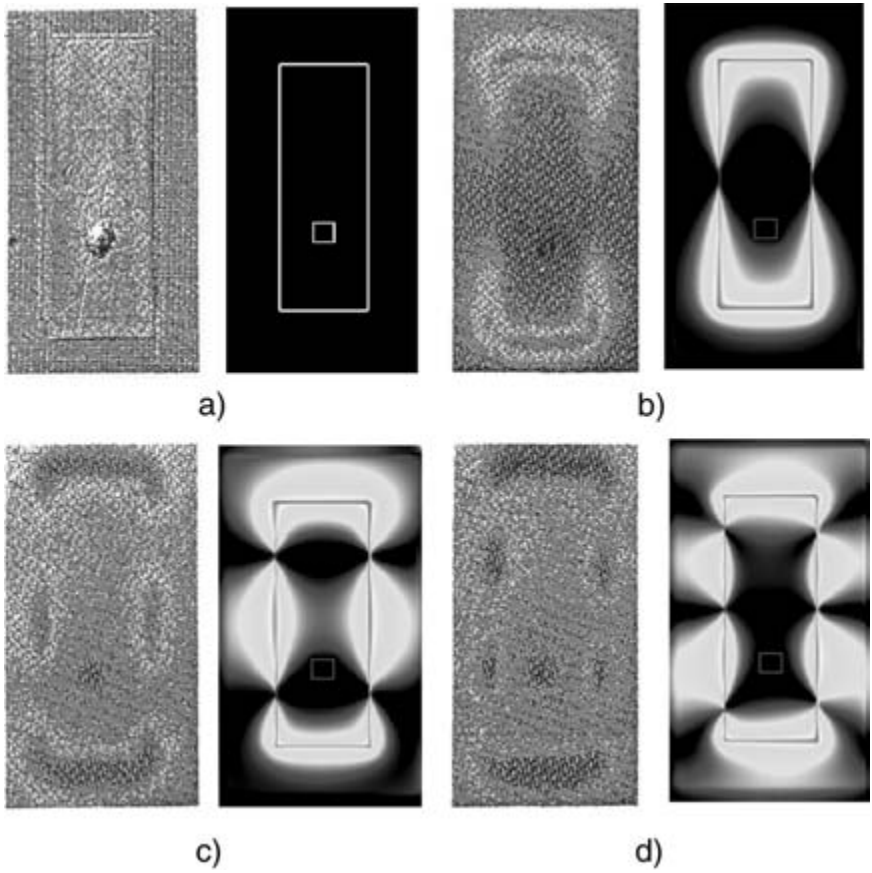

Figure 2-4 Electric field distribution surrounding a narrow patch antenna as computed using FDTD analysis and measured using a liquid crystal sheet: (a) patch without fields, (b) 3.10 GHz, (c) 6.15 GHz, and (d) 9.15 GHz. After Derneryd [12].

Figure 2-4(c) has Derneryd's measured LCD results with the antenna driven at 6.15 GHz. The LCD visualization shows the next higher order mode one would expect from transmission line theory. The electric field seen at either side of the center of the patch antenna along the nonradiating edges still contribute little to the antenna's radiation. In the far field, the radiation contribu-

tions from each side of the nonradiating edges cancel.* The FDTD thermal plot result in Figure 2-4(c) is once again very similar in appearance to Derneryd's LCD thermal measurement at 6.15 GHz.

The next mode is reported by Derneryd to exist at 9.15 GHz. The measured LCD result in Figure 2-4(d) and the theoretical FDTD thermal plot once again have good correlation. As before, the radiation from the nonradiating edges will cancel in the far field.

The LCD method of measuring the near fields of microstrip antennas is still used, but other photographic and probe measurement methods have been developed as an aid to the visualization of the fields around microstrip antennas.[15–18]

2.2 The Cavity Model

The transmission line model is conceptually simple, but has a number of drawbacks. The transmission line model is often inaccurate when used to predict the impedance bandwidth of a rectangular microstrip antenna for thin substrates. The transmission line model also does not take into consideration the possible excitation of modes which are not along the linear transmission line. The transmission line model assumes the currents flow in only one direction along the transmission line. In reality, currents transverse to these assumed currents can exist in a rectangular microstrip antenna. The development of the cavity model addressed these difficulties.

The cavity model, originated in the late 1970s by Lo et al., views the rectangular microstrip antenna as an electromagnetic cavity with electric walls at the groundplane and the patch, and magnetic walls at each edge.[19,20] The fields under the patch are the superposition of the resonant modes of this two-

* The far field of an antenna is at a distance from the antenna where a transmitted (spherical) electromagnetic wave may be considered to be planar at the receive antenna. This distance R is generally accepted for most practical purposes to be $R \geq \frac{2d^2}{\lambda}$. The value d is the largest linear dimension of transmit or receive antenna and λ is the free-space wavelength. The near field is a distance very close to an antenna where the reactive (nonradiating) fields are very large.

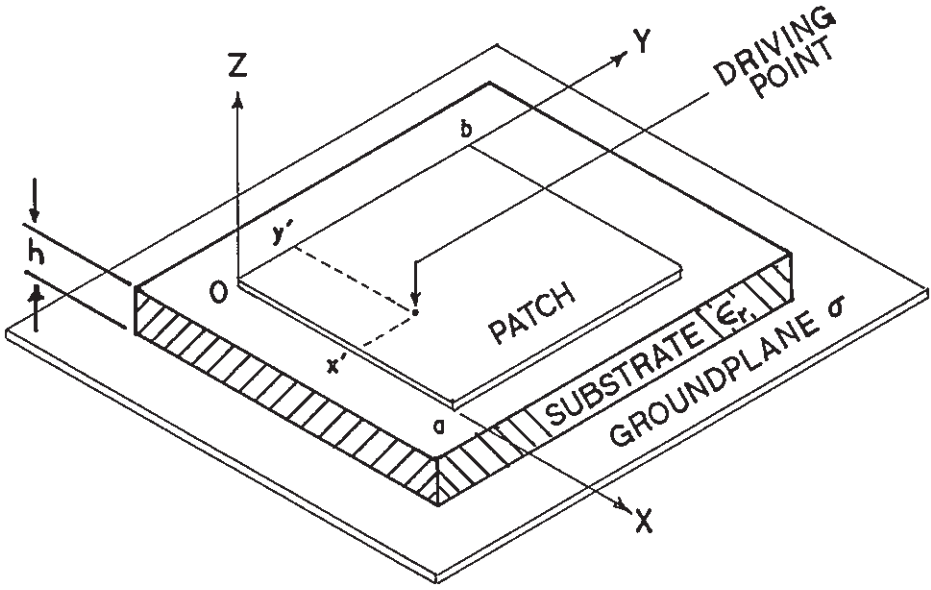

Figure 2-5 Rectangular microstrip patch geometry used for cavity model analysis.

dimensional radiator. (The cavity model is the dual of a very short piece of rectangular waveguide which is terminated on either end with magnetic walls.) Equation (2.10) expresses the ($\vec{E}_z$) electric field under the patch at a location (x,y) in terms of these modes. This model has undergone a considerable number of refinements since its introduction.[21,22] The fields in the lossy cavity are assumed to be the same as those that will exist in a short cavity of this type. It is assumed that in this configuration, where ($h \ll \lambda_0$), only a vertical electric field will exist ($\vec{E}_z$) which is assumed to be constant along $\hat{z}$, and only horizontal magnetic field components ($\vec{H}_x$ and $\vec{H}_y$) exist. The magnetic field is transverse to the $\hat{z}$ axis (Figure 2-5) and the modes are described as TM_{mn} modes (m and n are integers). The electric current on the rectangular patch antenna is further assumed to equal zero normal to each edge. Because the electric field is assumed to be constant along the $\hat{z}$ direction, one can multiply equation (2.10) by h to obtain the voltage from the patch to the groundplane. The driving point current can be mathematically manipulated to produce the ratio of voltage to current on the left side of equation (2.10). This creates an

expression which can be used to compute the driving point impedance [equation (2.15)] at an arbitrary point ($\acute{x}$,$\acute{y}$), as illustrated in Figure 2-5.

$$E_z = \sum_{m=0}^{\infty}\sum_{n=0}^{\infty} A_{mn}\Phi_{mn}(x,y) \tag{2.10}$$

$$A_{mn} = j\omega\mu\frac{<J_z, \Phi_{mn}>}{<\Phi_{mn}, \Phi_{mn}>}\left(\frac{1}{k_c^2 - k_{mn}^2}\right) \tag{2.11}$$

$$\Phi_{mn}(x,y) = \cos\left(\frac{m\pi x}{a_{eff}}\right)\cos\left(\frac{n\pi y}{b_{eff}}\right) \tag{2.12}$$

The cavity walls are slightly larger electrically than they are physically due to the fringing field at the edges, therefore we extend the patch boundary outward and the new dimensions become $a_{eff} = a + 2\Delta$ and $b_{eff} = b + 2\Delta$, which are used in the mode expansion. The effect of radiation and other losses is represented by lumping them into an effective dielectric loss tangent [equation (2.19)].

$$k_c^2 = \varepsilon_r(1 - j\delta_{eff})k_0^2 \tag{2.13}$$

$$k_{mn}^2 = \left(\frac{m\pi}{a_{eff}}\right) + \left(\frac{n\pi}{b_{eff}}\right) \tag{2.14}$$

The driving point impedance at ($\acute{x}$,$\acute{y}$) may be calculated using

$$Z_{drv} = \sum_{m=0}^{\infty}\sum_{n=0}^{\infty}\frac{j\omega\alpha_{mn}}{\omega_{mn}^2 - (1 - j\delta_{eff})\omega^2} \tag{2.15}$$

$$\omega_{mn} = \frac{c_0 k_{mn}}{\sqrt{\varepsilon_r}} \tag{2.16}$$

$$\alpha_{mn} = \frac{h\delta_m\delta_n}{a_{eff}b_{eff}\varepsilon_0\varepsilon_r}\cos^2\left(\frac{m\pi\acute{x}}{a_{eff}}\right)\cos^2\left(\frac{n\pi\acute{y}}{b_{eff}}\right)\mathrm{sinc}^2\left(\frac{m\pi w_p}{2a_{eff}}\right) \tag{2.17}$$

w_p is the width of the feed probe.

$$\delta_i = \begin{cases} 1 & \text{if } i = 0 \\ 2 & \text{if } i \neq 0 \end{cases} \tag{2.18}$$

The effective loss tangent for the cavity is computed from the total Q of the cavity.

$$\delta_{eff} = \frac{1}{Q_T} = \frac{1}{Q_d} + \frac{1}{Q_c} + \frac{1}{Q_r} + \frac{1}{Q_{sw}} \tag{2.19}$$

The total quality factor of the cavity Q_T consists of four components: Q_d, the dielectric loss; Q_c, the conductor loss; Q_r, the radiation loss; and Q_{sw}, the surface wave loss.

$$Q_d = \frac{1}{\tan\delta} \tag{2.20}$$

$$Q_c = \frac{1}{2}\eta_0\mu_r\left(\frac{k_0 h}{R_s}\right) \tag{2.21}$$

$$R_s = \sqrt{\frac{w\mu_0}{2\sigma}} \tag{2.22}$$

$$Q_r = \frac{2wW_{es}}{P_r} \tag{2.23a}$$

where W_{es} is the energy stored:

$$W_{es} = \frac{\varepsilon_0\varepsilon_r abV_0^2}{8h} \tag{2.23b}$$

The power radiated into space is P_r.[23]

$$P_r = \frac{V_0^2 A\pi^4}{23040}\left[(1-B)\left(1-\frac{A}{15}+\frac{A^2}{420}\right)+\frac{B^2}{5}\left(2-\frac{A}{7}+\frac{A^2}{189}\right)\right] \tag{2.24}$$

$$A = \left(\frac{\pi a}{\lambda_0} \right)^2 \tag{2.25a}$$

$$B = \left(\frac{2b}{\lambda_0} \right)^2 \tag{2.25b}$$

V_0 is the input (driving point) voltage.

The Q of the surface wave loss (Q_{sw}) is related to the radiation quality factor (Q_r):[24]

$$Q_{sw} = Q_r \left(\frac{e_r^{hed}}{1 - e_r^{hed}} \right) \tag{2.26}$$

$$e_r^{hed} = \frac{P_r^{hed}}{P_r^{hed} + P_{sw}^{hed}} \tag{2.27}$$

$$P_r^{hed} = \frac{(k_0 h)^2 (80\pi^2 \mu_r^2 c_1)}{\lambda_0^2} \tag{2.28a}$$

$$c_1 = 1 - \frac{1}{n_1^2} + \frac{2}{5n_1^4} \tag{2.28b}$$

$$n_1 = \sqrt{\varepsilon_r \mu_r} \tag{2.29}$$

$$P_{sw}^{hed} = \frac{\eta_0 k_0^2}{8} \frac{\varepsilon_r (x_0^2 - 1)^{3/2}}{\varepsilon_r (1 + x_1) + k_0 h \sqrt{x_0^2 - 1} (1 + \varepsilon_r^2 x_1)} \tag{2.30}$$

$$x_1 = \frac{x_0^2 - 1}{\varepsilon_r - x_0^2} \tag{2.31}$$

$$x_0 = 1 + \frac{-\varepsilon_r^2 + \alpha_0 \alpha_1 + \varepsilon_r \sqrt{\varepsilon_r^2 - 2\alpha_0 \alpha_1 + \alpha_0^2}}{(\varepsilon_r^2 - \alpha_1^2)} \tag{2.32}$$

$$\alpha_0 = \sqrt{\varepsilon_r - 1} \tan(k_0 h \sqrt{\varepsilon_r - 1}) \tag{2.33}$$

$$\alpha_1 = -\left[\frac{\tan(k_0 h\sqrt{\varepsilon_r - 1}) + \dfrac{k_0 h\sqrt{\varepsilon_r - 1}}{\cos^2(k_0 h\sqrt{\varepsilon_r - 1})}}{\sqrt{\varepsilon_r - 1}} \right] \tag{2.34}$$

The cavity model is conceptually accessible and readily implemented, but its accuracy is limited by assumptions and approximations that are only valid for electrically thin substrates. The self-inductance of a coaxial probe used to feed the rectangular microstrip antenna is not included in this model. The cavity model is generally accurate in its impedance prediction and is within 3% of measured resonant frequency for a substrate thickness of $0.02\lambda_0$ or less. When it is thicker than this, anomalous results may occur.[25]

2.2.1 The TM_{10} and TM_{01} Mode

When a rectangular microstrip antenna has its dimension a wider than dimension b and is fed along the centerline of dimension b, only the TM_{10} mode may be driven. When it is fed along the centerline of dimension a, only the TM_{01} mode may be driven.

When the geometric condition $a > b$ is met, the TM_{10} mode is the lowest order mode and possesses the lowest resonant frequency of all the time harmonic modes. The TM_{01} mode is the next highest order mode and has the next lowest resonant frequency (Figure 2-6).

When $b > a$, the situation is reversed, TM_{01} becomes the mode with the lowest resonant frequency and TM_{10} has the next lowest resonant frequency. If $a = b$, the two modes TM_{10} and TM_{01} maintain their orthogonal nature, but have identical resonant frequencies.

The integer mode index m of TM_{mn} is related to half-cycle variations of the electric field under the rectangular patch along a. Mode index n is related to the number of half-cycle electric field variations along b. In the case of the TM_{10} mode, the electric field is constant across any slice through b (i.e., the $\hat{y}$ direction) and a single half-cycle variation exists in any cut along a (i.e., the $\hat{x}$ direction). Figure 2-4 shows a narrow patch driven in the TM_{01}, TM_{02}, and TM_{03} modes according to cavity model convention.

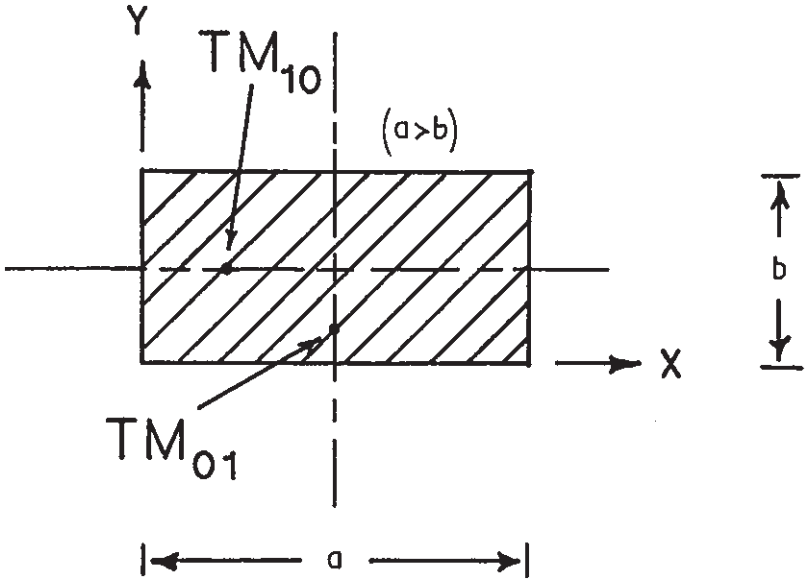

Figure 2-6 When $a > b$, the TM_{10} mode is the lowest order mode (lowest resonant frequency) for a rectangular microstrip antenna. The TM_{01} mode has the next highest resonant frequency.

One notes that the electric field is equal to zero at the center of a rectangular patch for both the TM_{10} and TM_{01} modes. This allows a designer the option of placing a shorting pin in the center of the rectangular patch without affecting the generation of either of the two lowest order modes. This shorting pin or via forces the groundplane and rectangular patch to maintain an equivalent direct current (DC) electrostatic potential. In many cases the buildup of static charge on the patch is undesirable from an electrostatic discharge (ESD) point of view, and a via may be placed in the center of the rectangular patch to address the problem.

Figure 2-7(a) shows the general network model used to represent a rectangular microstrip antenna. The TM_{00} mode is the static (DC) term of the series.[26] As described previously, the TM_{10} and/or TM_{01} are the two lowest order modes that are generally driven in most applications. When this is the case, the other higher order modes are below cut-off and manifest their presence as an infinite

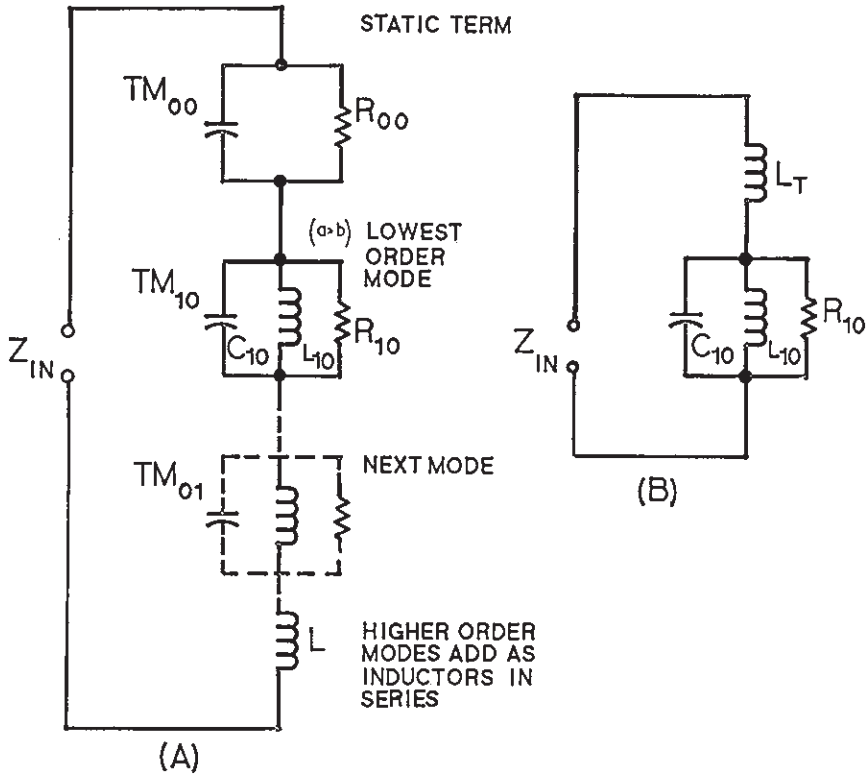

Figure 2-7 Network models used to represent a rectangular microstrip antenna. (a) General model. (b) Narrowband model which is valid for the TM_{10} mode.

Table 2-1 A 2.45 GHz linear microstrip antenna.

a	b	h	ε_r	$\tan\delta$	$\acute{x}$	$\acute{y}$
34.29 mm	30.658 mm	3.048 mm	3.38	0.0027	$a/2$	7.734 mm
Groundplane Dimensions = 63.5 mm × 63.5 mm						

number of small inductors which add in series with the driving point impedance. The convergent sum of these inductances may be lumped into a single series inductor which represents the contribution of the higher order modes to the driving point impedance. As the substrate thickness h of a microstrip

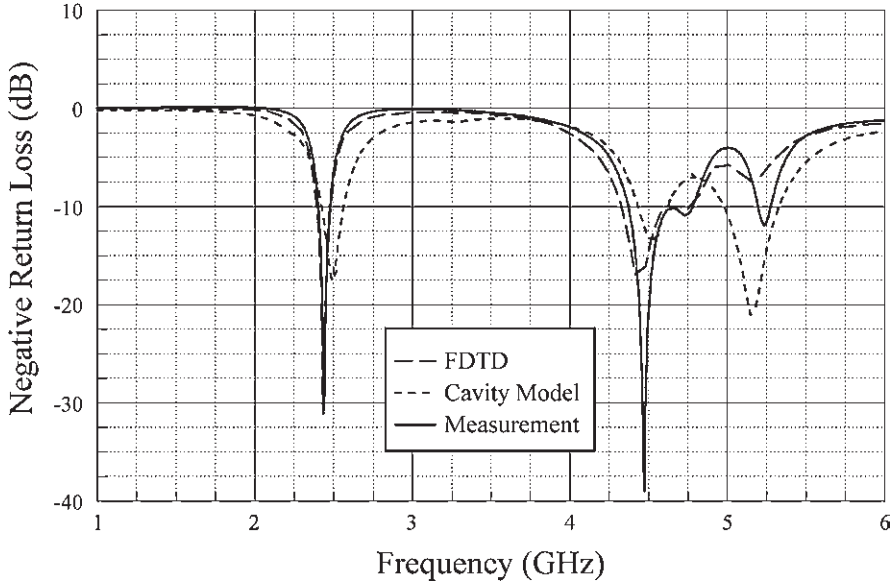

Figure 2-8 Comparison to measurement of predicted negative return loss of a rectangular microstrip patch (of parameters in Table 2-1) by the cavity model and FDTD analysis.

patch increases, the contribution of the equivalent series inductance of the higher order modes to the driving point impedance becomes larger and larger, which produces a larger and larger mismatch, until the patch antenna can no longer be matched by simply choosing an appropriate feed point location. The cavity model does not include the small amount of intrinsic self-inductance introduced by a coaxial feed probe.[27] Increasing the thickness of the substrate also increases the impedance bandwidth of the element. These two properties (impedance bandwidth and match) may need to be traded off in a design.

The cavity model is accurate enough to use for many engineering designs. Its advantage is that it is expressed with closed form equations, which allow efficient computation and ease of implementation. Its disadvantage is its accuracy when compared with more rigorous methods.

The cavity model equations presented previously were implemented for a rectangular patch antenna with $a = 34.29$ mm and a resonant length of $b = 30.658$ mm (TM_{01}). The feed point is 7.595 mm from the center of the patch,

Table 2-2 Resonance values.

Analysis Method	Resonant Frequency (GHz)
Cavity Model	2.492
Measurement	2.442
FDTD	2.434

$\acute{x} = a/2$ and $\acute{y} = 7.734$ mm. The dielectric thickness is $h = 3.048$ mm (0.120 inches) with $\varepsilon_r = 3.38$ and $\tan \delta = 0.0027$ (these values are in Table 2-1). The measured maximum return loss of a patch fabricated using these dimensions is 30.99 dB at 2.442 GHz. The FDTD method was also used to analyze this patch antenna. The impedance results for the cavity model, FDTD, and measurement are presented in Figure 2-8. The cavity model predicts a maximum return loss at 2.492 GHz, which is about a 2% error versus measurement. FDTD analysis predicts 2.434 GHz, which is a 0.33% error. These resonance values are presented in Table 2-2. The cavity model predicts a larger bandwidth for the first resonance than is actually measured, it is fairly good at predicting the next higher resonance, but then deviates significantly. The groundplane size of the fabricated antenna, also used in the FDTD analysis, is 63.5 mm × 63.5 mm with the dielectric flush to each groundplane edge.

2.3 Radiation Pattern and Directivity of a Linear Rectangular Microstrip Patch Antenna

The transmission line model, combined with the measured and computed thermal plots, suggests a model for the computation of radiation patterns of a rectangular microstrip patch antenna in the TM_{01} mode. The fringing fields at the edge of a microstrip antenna which radiate are centered about each edge of the antenna. This implies that the radiation pattern would be comparable to a pair of radiating slots centered about each radiating edge of the patch driven in phase. These slots can be viewed as equivalent to slots in a groundplane with a uniform electric field across them. This is illustrated in Figure 2-9(a). Figure 2-9(b) shows an FDTD thermal plot of the magnitude of the electric field

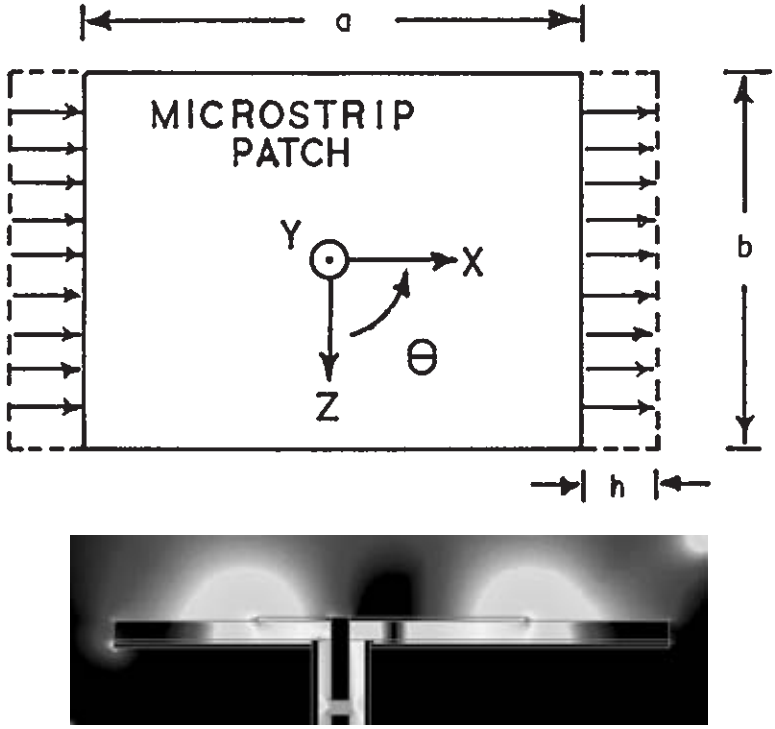

Figure 2-9 (a) Top view of a rectangular microstrip patch with a pair of equivalent slots located at a distance a apart. The electric fields across the slots radiate in phase. (b) Side view FDTD thermal plot of the electric field for the patch analyzed in Figure 2-8 fed with a square coaxial cable. This plot demonstrates the radiating electric fields are approximately constant at each radiating edge of the patch and extend for a distance that is nearly the thickness of the substrate. (Note the virtual short circuit at the center of the patch under the antenna is clearly visible.)

distribution of a microstrip antenna cut through the $\hat{x}$-$\hat{y}$ plane. We can see that the two radiating edges, and the fields which radiate, form a semicircle about each edge. The electric field extends outward from each edge along the dielectric substrate about the same amount as the dielectric thickness.

The radiating slots have a length b and are estimated to be of h (the substrate thickness) across. The two slots form an array. When the dielectric substrate is air, $\varepsilon_r \approx 1.0$, the resonant length a is nearly $\lambda_0/2$. When a pair of radiation sources

have this spacing in free space, the array produces a maximum directivity. As the dielectric constant increases, the resonant length of the patch along a decreases, which decreases the spacing between the radiating slots. The slots no longer optimally add broadside to the rectangular microstrip antenna, which decreases the directivity and hence increases the pattern beamwidth.

The electric field from a single slot with a voltage across the slot of V_0 is given as[28]

$$E_\phi = -j2V_0 b k_0 \frac{e^{-jk_0 r}}{4\pi r} F(\theta, \phi) \tag{2.35}$$

$$E_\theta = 0 \tag{2.36}$$

$$F(\theta, \phi) = \frac{\sin(k_0(h/2)\sin\theta\cos\phi)}{k_0(h/2)\sin\theta\cos\phi} \cdot \frac{\sin(k_0(b/2)\cos\theta)}{k_0(b/2)\cos\theta} \sin\theta \tag{2.37}$$

$$k_0 = \frac{2\pi}{\lambda_0} \tag{2.38}$$

For two slots spaced at a distance a apart, the E-plane radiation pattern is

$$F_E(\phi) = \frac{\sin(k_0(h/2)\cos\phi)}{k_0(h/2)\cos\phi} \cos(k_0 b/2\cos\phi) \tag{2.39}$$

The H-plane pattern is independent of the slot spacing a and is given by

$$F_H(\theta) = \frac{\sin(k_0 b\cos\theta)}{k_0 b\cos\theta} \sin\theta \tag{2.40}$$

The angle θ is measured from the $\hat{z}$ axis and ϕ is measured from the $\hat{x}$ axis.

The directivity of a microstrip antenna can be approximated by starting with the directivity of a single slot:[29]

$$D = \frac{4b^2\pi^2}{I_1 \lambda_0^2} \tag{2.41}$$

$$I_1 = \int_0^{\pi} \sin^2\left(\frac{k_0 b \cos\theta}{2}\right) \tan^2\theta \sin\theta d\theta \tag{2.42}$$

In the case of a microstrip antenna with a pair of radiating slots, the directivity D_s is

$$D_s = \frac{2D}{1 + g_{12}} \tag{2.43}$$

$$g_{12} = \frac{1}{120\pi^2} \int_0^{\pi} \frac{\sin^2\left(\frac{\pi b \cos\theta}{\lambda_0}\right) \tan^2\theta \sin\theta J_0\left(\frac{2\pi a}{\lambda_0} \sin\theta\right)}{G} d\theta \tag{2.44}$$

$J_0(x)$ is the zeroth-order Bessel function with argument x.

$$G = \frac{1}{R_r} \tag{2.45}$$

where R_r is the radiation resistance:

$$R_r = \frac{120\pi^2}{I_1} \tag{2.46}$$

The integrations in equation (2.42) and equation (2.44) may be accurately evaluated numerically with Gaussian quadrature (Appendix B). The directivity estimates and pattern functions do not take groundplane effects into account and are often lower than measured. These equations are very useful for estimating the directivity and radiation pattern of a rectangular microstrip antenna. It is always best to use a more powerful technique of analysis, such as FDTD or the finite element method (FEM), to refine the pattern prediction of a given design.

Figure 2-10 shows measured E- and H-plane patterns of the 2.45 GHz microstrip antenna of Table 2-1 plotted with results from the slot pair model and results using FDTD. The FDTD method results were obtained using a single-frequency square coaxial source and the patterns calculated using the

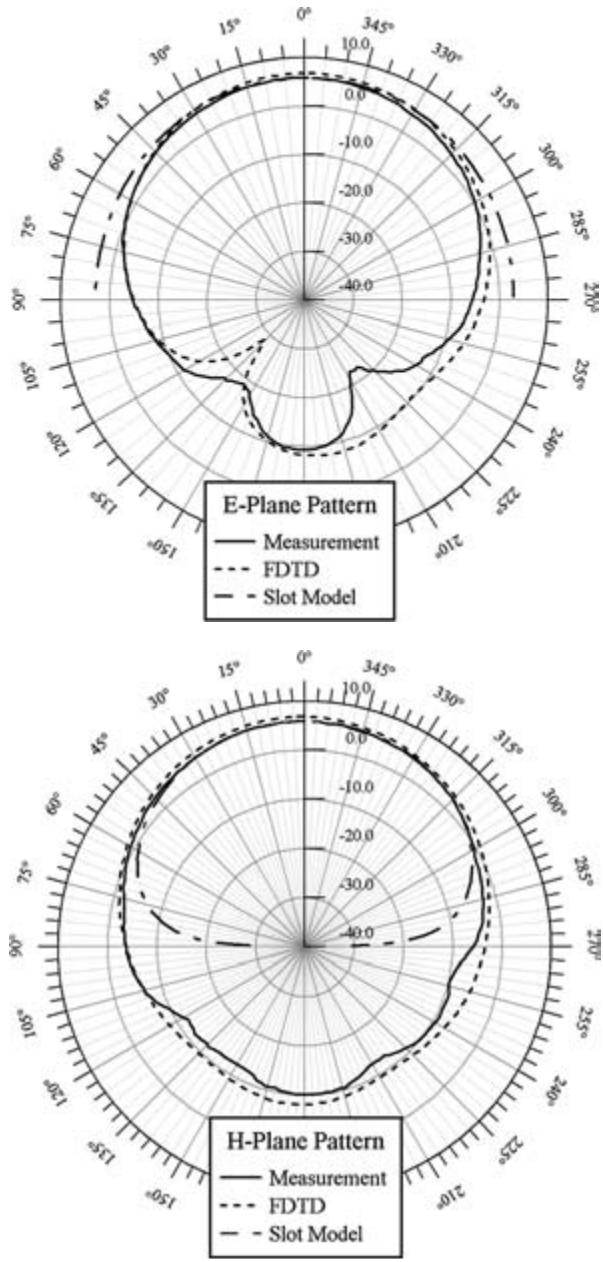

Figure 2-10 Comparison of the measured and predicted radiation pattern of the 2.45 GHz linear microstrip antenna of Table 2-1 using FDTD analysis and the slot model for the TM_{01} mode.

surface equivalence theorem.[30,31] One can see the measured and FDTD results are very similar for the upper hemisphere in both the E- and H-plane patterns. Equation (2.43) was used to compute the directivity for the slot model. The E-plane slot model pattern results are close for ±45°, but begin to deviate at low angles. The H-plane slot model is close up to about ±60°. The slot model does not take groundplane affects into account, but is clearly very accurate considering the simple model used.

The important parameter which determines the directivity of a microstrip antenna is the relative dielectric constant ε_r of the substrate. When the substrate is air ($\varepsilon_r \approx 1.0$), the two antenna edges are approximately half of a free space wavelength apart ($\lambda_0/2$). This spacing produces an array spacing for the slot model which produces maximum directivity. It is possible to achieve a directivity of almost 10 dB with an air loaded rectangular microstrip patch antenna. As the dielectric constant of the substrate is increased, the slots become closer in terms of free space wavelengths and no longer array to produce as high a directivity as in the free space case. As the substrate dielectric constant of a rectangular microstrip antenna increases, the directivity of a patch antenna decreases. Table 2-3 presents a comparison of the directivity predicted by the slot model and FDTD method for a square microstrip antenna. For low values of relative dielectric constant ($\varepsilon_r < 4.0$), the slot model is within approximately 1 dB. For $\varepsilon_r > 4.0$, the directivity of the slot model is still within about 1.5 dB. The slot model can be useful for estimating directivity.

Table 2-3 Directivity (dB) of a square linear microstrip antenna vs. ε_r (2.45 GHz, h = 3.048 mm, $\tan\delta = 0.0005$).

ε_r	Slot Model	FDTD
1.0	8.83	8.00
2.6	6.56	7.11
4.1	5.93	6.82
10.2	5.24	6.54
20.0	5.01	6.45

Square Groundplane Dimensions for FDTD = 63.5 mm × 63.5 mm
(Antenna Centered)

2.4 Quarter-Wave Rectangular Microstrip Antenna

Understanding the electric field distribution under a rectangular microstrip antenna allows us to develop useful variations of the original $\lambda/2$ rectangular microstrip antenna design. In the case where a microstrip antenna is fed to excite the TM_{01} mode exclusively, a virtual short-circuit plane exists in the center of the antenna parallel to the x axis centered between the two radiating edges. This virtual shorting plane can be replaced with a physical metal shorting plane to create a rectangular microstrip antenna that is half of its original length (approximately $\lambda_{eff}/4$), as illustrated in Figure 2-11. Only a single radiating edge remains with this design, which reduces the radiation pattern directivity compared with a half-wavelength patch. This rectangular microstrip antenna design is known as a quarter-wave microstrip patch or half-patch antenna. The use of a single shorting plane to create a quarter-wave patch antenna was first described by Sanford and Klein in 1978.[32] Later, Post and Stephenson[33]

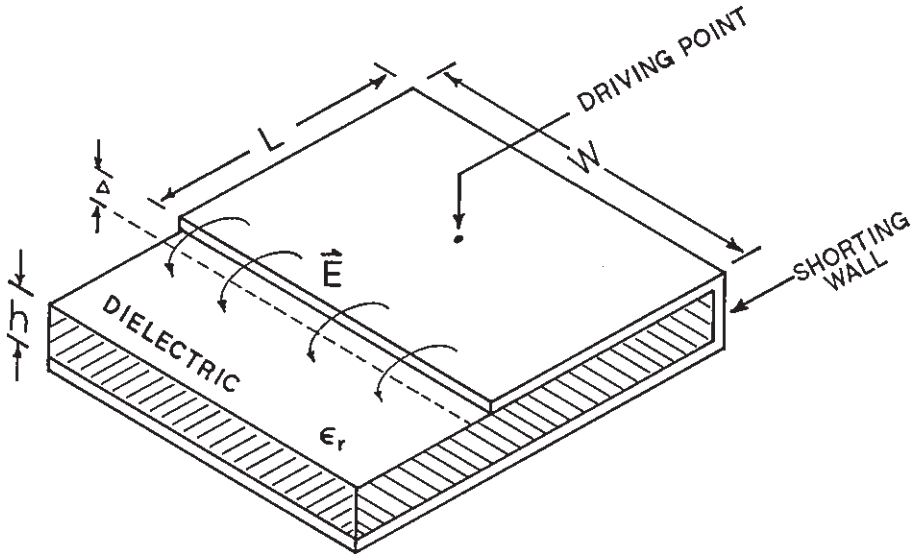

Figure 2-11 A quarter-wave microstrip antenna has a shorting wall which replaces the virtual short found in a half-wave microstrip antenna.

described a transmission line model to predict the driving point impedance of a λ/4 microstrip antenna.

The length of a quarter-wavelength patch antenna for a given operating frequency f_r is

$$L = \frac{c}{4 f_r \sqrt{\varepsilon_e}} - \Delta l \tag{2.47}$$

$$= \frac{\lambda_{\varepsilon_e}}{4} - \Delta l \tag{2.48}$$

$$Y_{drv} = Y_0 \frac{Y_e + jY_0 \tan(\beta L_2)}{Y_0 + jY_e \tan(\beta L_2)} - jY_0 \cot(\beta L_1) \tag{2.49}$$

The transmission line model of a quarter-wave microstrip antenna is presented in Figure 2-12. Equation (2.49) represents the driving point admittance at a point along L represented by $L = L_1 + L_2$. The final term in equation (2.49) is a pure susceptance at the driving point which is due to the shorted transmission line stub. The admittance at the driving point from the section of transmission line that translates the edge admittance Y_e along a transmission line of length L_2 resonates when its susceptance cancels the susceptance of the shorted stub. The 50 Ω input resistance location may be found from equation (2.49), with an appropriate root finding method such as the bisection method (Appendix B). The 50 Ω driving point impedance location is not exactly at the same position relative to the center short as the 50 Ω driving point location of a half-wavelength patch is to its virtual shorting plane. This is because, for the case of the half-wavelength patch, two radiators exist and have a mutual coupling term that disappears in the quarter-wavelength case. Equation (2.49) does not take this difference into account, but provides a good engineering starting point. This change in mutual coupling also affects the cavity Q, which in turn reduces the impedance bandwidth of a quarter-wavelength patch to approximately 80% of the impedance bandwidth of a half-wavelength patch.[34]

The short circuit of the quarter-wave patch antenna is critical. To maintain the central short, considerable current must exist within it. Deviation from a low impedance short circuit will result in a significant change in the resonant

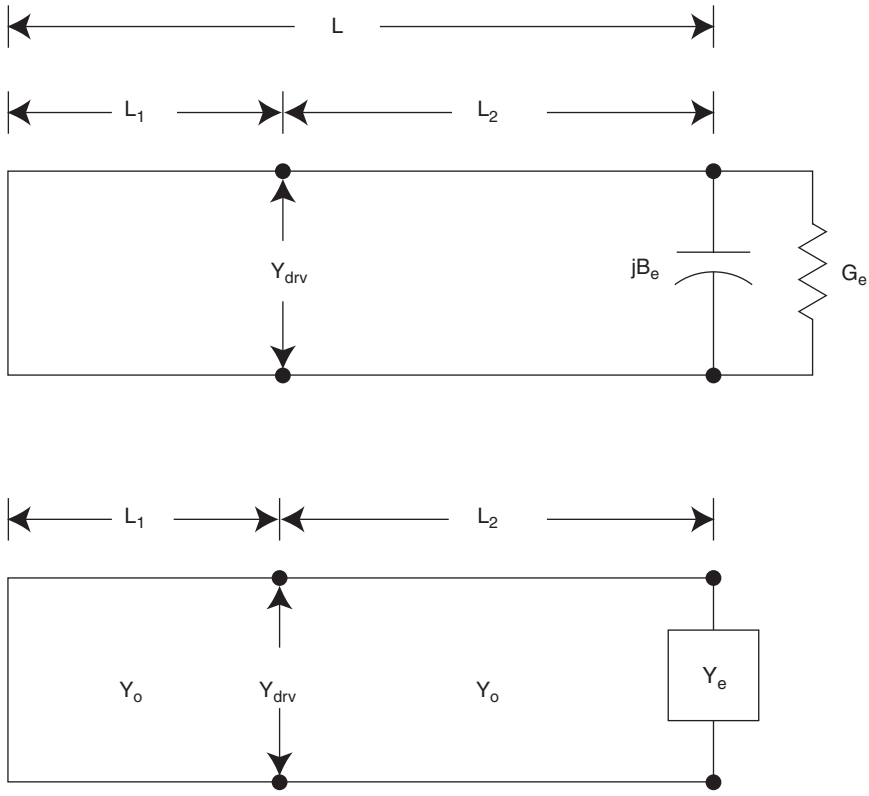

Figure 2-12 Transmission line model of a quarter-wave microstrip antenna.

frequency of the antenna and modify the radiation characteristics.[35] A design of this type often uses a single piece of metal with uniform width which is stamped into shape and utilizes air as a dielectric substrate.

2.5 $\lambda/4 \times \lambda/4$ Wavelength Rectangular Microstrip Antenna

When $a = b$, the TM_{01} and TM_{10} modes have the same resonant frequency (square microstrip patch). If the patch is fed along the diagonal, both modes can be excited with equal amplitude and in phase. This causes all four edges to become radiating edges. The two modes are orthogonal and therefore inde-

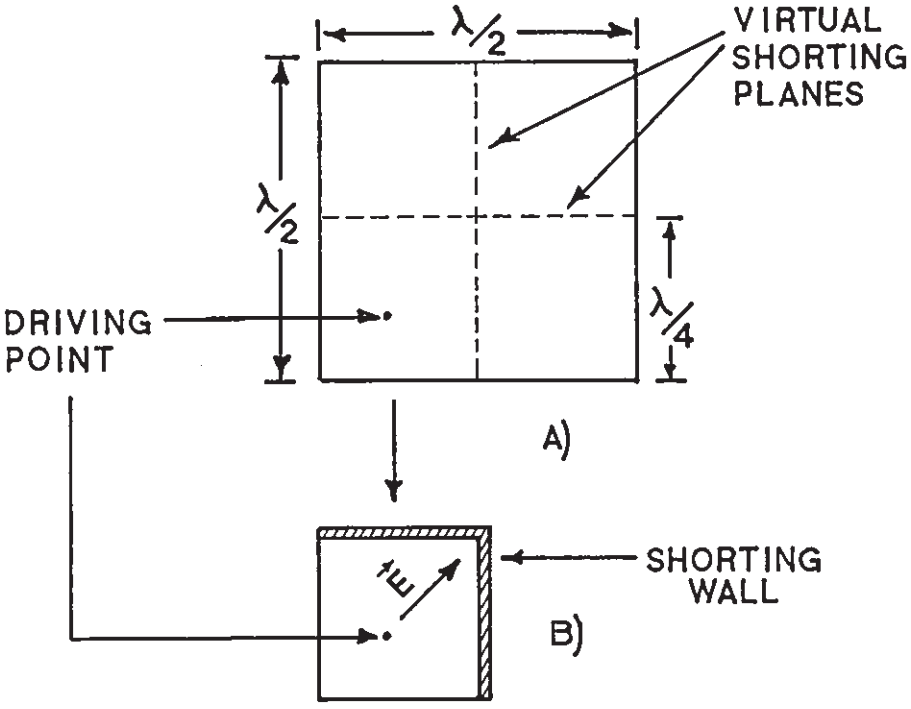

Figure 2-13 Development of a λ/4-by-λ/4 microstrip antenna from a square microstrip antenna. When a square microstrip antenna is driven along the diagonal, two virtual shorting planes appear. Replacing the virtual shorting planes with physical shorting planes allows one to remove a quarter section of the original antenna and drive it independently.

pendent. Because they are in phase, the resultant of the electric field radiation from the patch is slant linear along the diagonal of the patch.

When a square microstrip patch is operating with identical TM_{01} and TM_{10} modes, a pair of shorting planes exist centered between each of the pairs of radiating slots (Figure 2-13). We can replace the virtual shorting planes, which divide the patch into four sections, with physical shorting planes. We can remove one section (i.e., quadrant) and drive it separately due to the symmetry of the modes (Figure 2-14). This produces an antenna that has one-fourth the area of a square patch antenna.[36] This provides a design option for applications where volume is restricted.

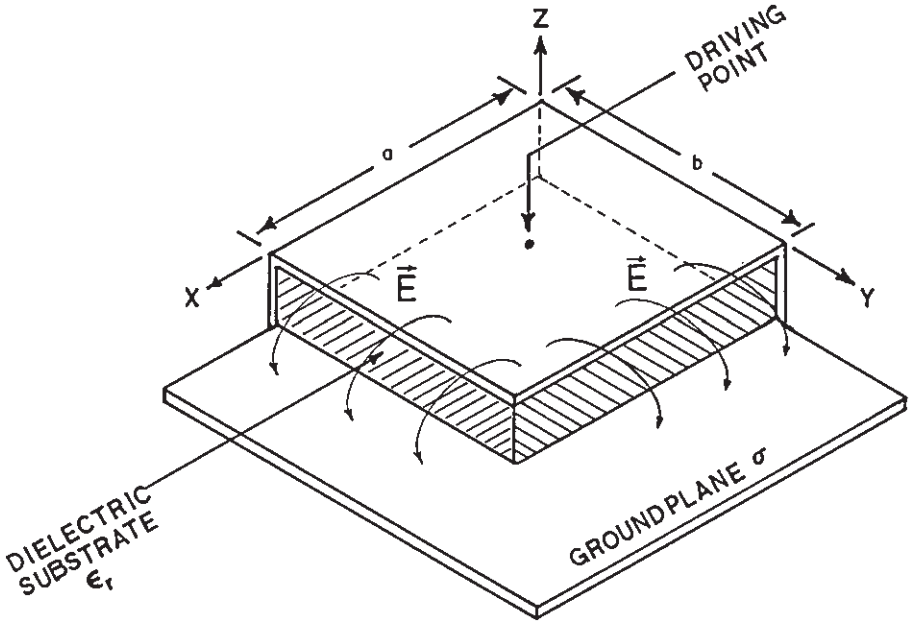

Figure 2-14 A λ/4-by-λ/4 microstrip antenna.

2.6 Circularly Polarized Rectangular Microstrip Antenna Design

2.6.1 Single-Feed Circularly Polarized Rectangular Microstrip Antenna Design

There are essentially two methods used to create rectangular circularly polarized microstrip antennas. The first is to feed the patch at a single point and perturb its boundary, or interior, so that two orthogonal modes exist at a single frequency which have identical magnitudes and differ in phase by 90°. The second is to directly feed each of two orthogonal modes with a microwave device that provides equal amplitudes and a 90° phase difference (e.g., 90° branchline hybrid). This section addresses the first type of design.

In Figure 2-15 we see four common methods used to create circularly polarized radiation from a rectangular microstrip antenna with a single driving point. The first method (I) is to choose an aspect ratio a/b such that the TM_{10} and

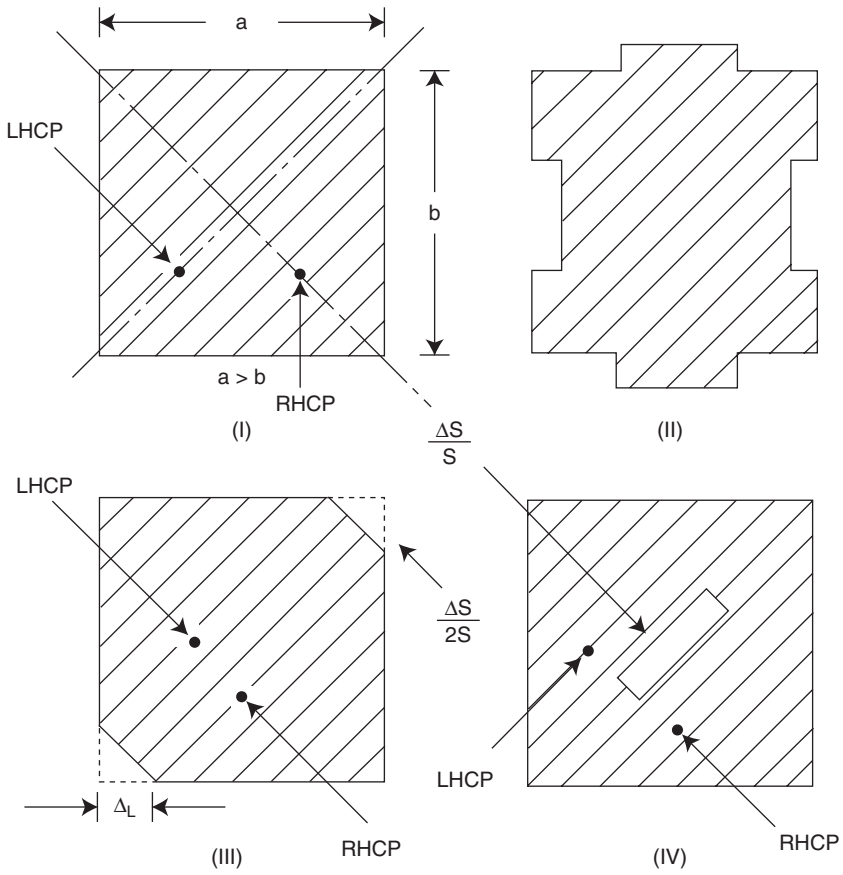

Figure 2-15 Four methods for generating circular polarization from a rectangular microstrip antenna using a single feed. (I) Using the aspect ratio of a patch to generate two orthogonal modes with equal amplitude and 90° out of phase. (II) Use of indentations and/or tabs. (III) Cutting off corners to create orthogonal modes. (IV) Introduction of a diagonal slot.

TM_{01} modes both exist at a single frequency where their magnitudes are identical and their phases differ by 90°. The two orthogonal modes radiate independently and sum in the far field to produce circular polarization.

The second method presented in Figure 2-15(II) is essentially the same as (I), but uses two rectangular tabs and two rectangular indentations to perturb

the modes to have a 90° phase difference. This situation is the most general geometry describing this type of circularly polarized patch. One could use a single tab, a single indent, a pair of tabs, or a pair of indents to perturb a rectangular microstrip antenna and produce circular polarization.

The third method illustrated in Figure 2-15(III) is to remove a pair of corners from the microstrip antenna. This creates a pair of diagonal modes (no longer TM_{10} and TM_{01} as the shape of the patch has been altered) that can be adjusted to have identical magnitudes and a 90° phase difference between these modes.

The fourth method in Figure 2-15(IV) is to place a slot diagonally across the patch. The slot does not disturb the currents flowing along it, but electrically lengthens the patch across it. The dimensions of the slot can be adjusted to produce circular polarization. It is important to keep the slot narrow so that radiation from the slot will be minimal. One only wishes to produce a phase shift between modes, not create a secondary slot radiator. Alternatively, one can place the slot across the patch and feed along the diagonal.[37]

Figure 2-16 illustrates how one designs a patch of type I. Figure 2-16(a) shows a perfectly square patch antenna probe fed in the lower left along the diagonal. This patch will excite the TM_{10} and TM_{01} modes with identical amplitudes and in phase. The two radiating edges which correspond to each of the two modes have a phase center that is located at the center of the patch. Therefore the phase center of the radiation from the TM_{10} and TM_{01} modes coincide and are located in the center of the patch. When $a = b$, the two modes will add in the far field to produce slant linear polarization along the diagonal. If the aspect ratio of the patch is changed so that $a > b$, the resonant frequency of each mode shifts. The TM_{10} mode shifts down in frequency and the TM_{01} mode shifts up compared with the original resonant frequency of the slant linear patch. Neither mode is exactly at resonance. This slightly nonresonant condition causes the edge impedance of each mode to possess a phase shift. When the phase angle of one edge impedance is +45° and the other is –45°, the total difference of phase between the modes is 90°. This impedance relationship clearly reveals itself when the impedance versus frequency of the patch is plotted on a Smith chart. The frequency of optimum circular polarization is the point on a Smith chart which is the vertex of a V-shaped kink.

Figure 2-17 presents the results of a cavity model analysis of a patch radiating left-hand circular polarization (LHCP) using a rectangular microstrip

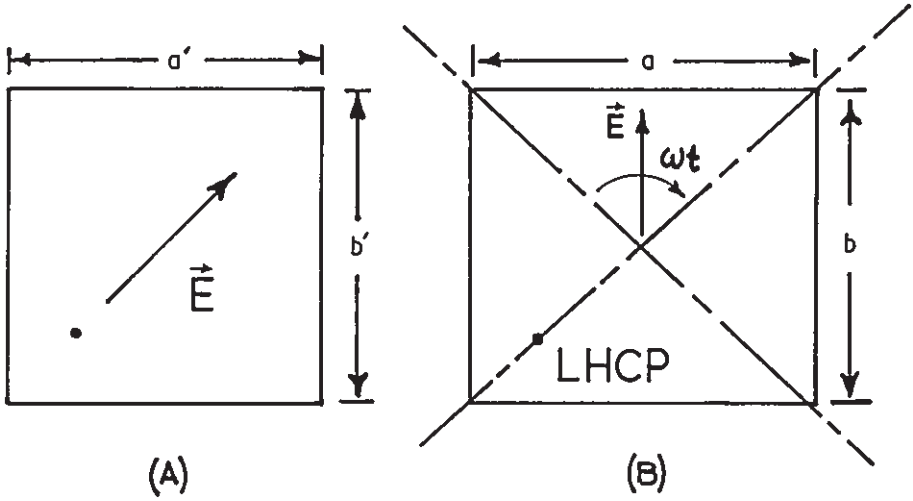

Figure 2-16 Development of a rectangular patch with circular polarization from a square patch. (a) Square patch fed along a diagonal produces TM_{10} and TM_{01} modes which are equal in magnitude and identical in phase. These two modes add together and produce linear polarization along the diagonal of the patch antenna. (b) The ratio of *a*/*b* may be adjusted to detune each mode slightly so that at a single frequency the amplitudes of each mode are equal, but their phase differs by 90°, producing a rotating electric field phasor.

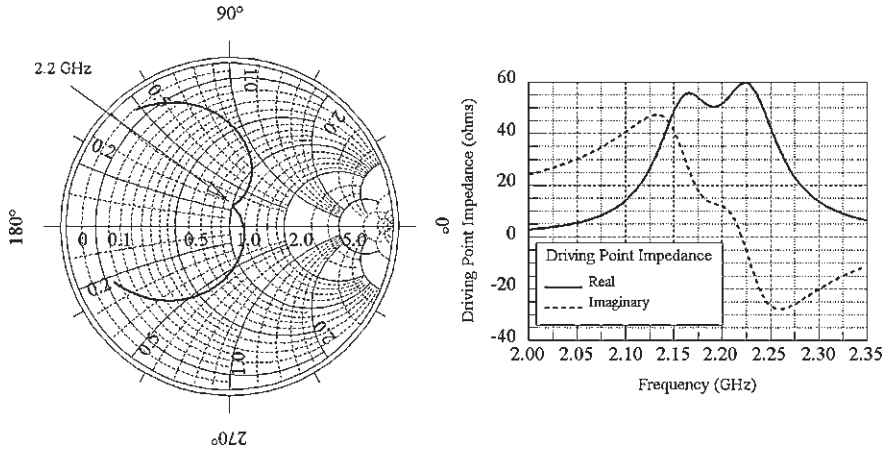

Figure 2-17 A Smith chart shows the impedance kink formed when the aspect ratio *a*/*b* has been adjusted to properly produce circular polarization. The rectangular plot shows the impedance as real and imaginary. The TM_{10} and TM_{01} mode resonant peaks which combine to produce circular polarization are clearly identifiable.

antenna with an appropriate a/b ratio. The antenna operates at 2.2 GHz, its substrate thickness is 1.5748 mm, with $\varepsilon_r = 2.5$, $\tan\delta = 0.0019$, $a = 40.945$ mm, and $b = 42.25$ mm. The patch is fed at $\acute{x} = 13.5$ mm, $\acute{y} = 14.5$ mm, and $W_p = 1.3$ mm. The approximate a/b ratio was arrived upon using trial and error with equation (2.54).

The design of a rectangular circularly polarized patch is difficult to realize due to the sensitivity of the patch to physical dimensions and dielectric constant. One method is to start with the case of the slant linear patch. The slant linear patch has $a = b$ and is therefore square and has its dimensions chosen to produce resonance at a desired design frequency. The ratio of a/b when the square patch aspect ratio has been adjusted to produce circular polarization has been derived using a perturbation technique:[38]

$$\frac{a}{b} = 1 + \frac{1}{Q_0} \tag{2.50}$$

The Q of the unperturbed slant linear patch (Q_0) is given by

$$\frac{1}{Q_0} = \frac{1}{Q_d} + \frac{1}{Q_c} + \frac{1}{Q_r} + \frac{1}{Q_{sw}} \tag{2.51}$$

The Q of a square rectangular microstrip antenna driven as a slant linear patch or as a linear patch are essentially identical. When a patch is square, the TM_{10} and TM_{01} modes are degenerate, the energy storage in the TM_{10} and TM_{01} modes are identical, as is the amount of energy loss in each for the slant linear case. If all the energy is stored in a single TM_{10} or TM_{01}, as occurs when the patch is driven in the linear case, the same total amount of energy will be lost as in the slant linear case. In both situations, the energy stored per cycle versus energy lost is the same, and therefore so is the Q.

If the slant linear patch has the dimension $\acute{a}$ (= $\acute{b}$), the new dimensions of the circularly polarized patch will be

$$a = \acute{a} + \Delta_L \tag{2.52a}$$

$$b = \acute{a} - \Delta_L \tag{2.52b}$$

Table 2-4 2.2 GHz LHCP microstrip antenna trial and error design.

a	b	h	ε_r	$\tan\delta$
40.945 mm	42.250 mm	1.5748 mm	2.5	0.0019

ẋ	ẏ	W_p
13.5 mm	14.5 mm	1.3 mm

Groundplane Dimensions = 63.5 mm × 63.5 mm

We can write

$$\Delta_L = \frac{\acute{a}}{2Q_0 + 1} \tag{2.53}$$

The use of equation (2.50) is illustrated by using the circularly polarized patch of Table 2-4, which has the proper impedance relationship to produce LHCP. The design values for that example were developed by adjusting the patch aspect ratio by trial and error until a circular polarization kink appeared. The center frequency of LHCP operation is 2.2 GHz.

We arrive at a slant linear patch design by taking the average of the values used to create the circularly polarized patch of Table 2-4: $(a + b)/2$ = (42.250 mm + 40.945 mm)/2 ≈ 41.6 mm. This average gives us a value of a slant linear patch on which we can apply equation (2.50) to compute an aspect ratio which should produce circular polarization. The new patch has a resonance at 2.2 GHz with a resistance of 88 Ω. The total Q (i.e., Q_0) from the cavity model is computed to be 29.3 at 2.2 GHz. Equation (2.53) allows us to compute the length change required to produce circular polarization:

$$\Delta_L = \frac{41.6 \text{ mm}}{(2 \cdot 29.3) + 1} = 0.698 \text{ mm}$$

We can now find the values of a and b:

$$a = 41.6 \text{ mm} + 0.698 \text{ mm} = 42.298 \text{ mm}$$

$$b = 41.6 \text{ mm} - 0.698 \text{ mm} = 40.902 \text{ mm}.$$

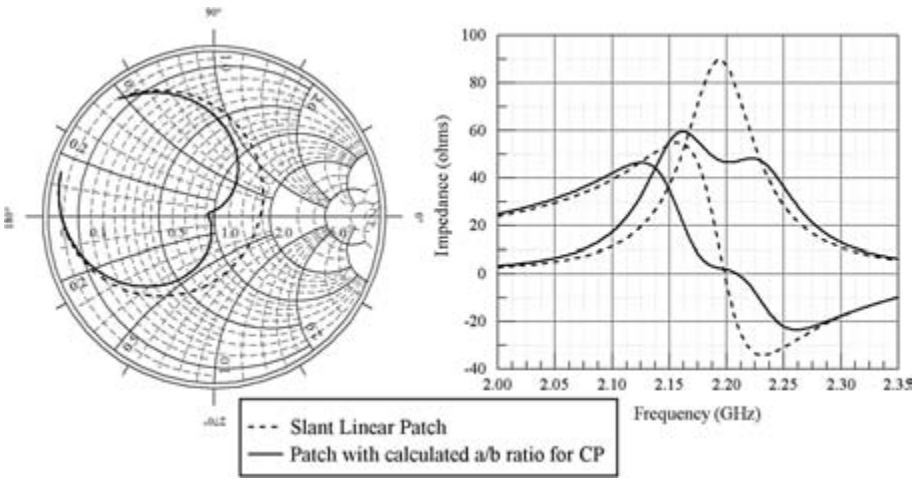

Figure 2-18 The rectangular patch antenna of Figure 2-17 has its dimensions averaged to create a slant linear patch which resonates at 2.2 GHz using cavity model analysis (dashed lines). Next, equation (2.52a) and equation (2.52b) are used to compute the values of a and b required to produce circular polarization at 2.2 GHz, which is then analyzed using the cavity model (solid lines).

The driving point impedance of the slant linear patch and the patch modified to have circular polarization using the a and b values computed with equation (2.52a) and equation (2.52b) are plotted in Figure 2-18. Again, the cavity model has been used to compute the driving point impedance. It can be seen that in this case the computation has the advantage that it produces a better match for the circularly polarized patch which has been modified to produce circular polarization than the trial and error method of the original patch. The input impedance at 2.2 GHz for the patch modified to produce circular polarization is $46.6 + j1.75\ \Omega$. This is about half the input resistance value of the slant linear patch. This calculation provides some insight into the sensitivity of the driving point impedance location of the design to physical parameters of the patch.

The cavity model can be used to compute the axial ratio of a circularly polarized rectangular patch.[39] The relationship between electric field and axial ratio is[40]

$$AR = \sqrt{\frac{1+|E_x/E_y|^2+T}{1+|E_x/E_y|^2-T}} \tag{2.54}$$

where AR is the axial ratio and

$$T = \sqrt{1+\left|\frac{E_x}{E_y}\right|^4+2\left|\frac{E_x}{E_y}\right|^2\cos(2\psi)} \tag{2.55}$$

where ψ is the phase of E_x/E_y.

The ratio of electric field components E_x and E_y from the cavity model may be approximated by

$$\frac{E_x}{E_y} \approx \frac{b(k_c^2-k_{01}^2)}{a(k_c^2-k_{10}^2)}\frac{\cos(\pi x/a)}{\cos(\pi y/b)}\operatorname{sinc}\left(\frac{\pi w_p}{2a}\right) \tag{2.56}$$

$$\frac{E_x}{E_y} = \begin{cases} j & \text{RHCP} \\ -j & \text{LHCP} \end{cases} \tag{2.57}$$

The input impedance calculated with the values in Table 2-4 using the cavity model is plotted with the axial ratio as a function of frequency and presented in Figure 2-19. We can see the minimum axial ratio occurs between the resonant peaks and where the imaginary value flattens out. Table 2-5 illustrates that often the driving point location which produces optimum axial ratio performance and driving point match is not exactly along the patch diagonal.

The sensitivity of this type of design is such that we need accurate values of Q to obtain the most accurate value of Δ_L possible. The cavity model often does not produce as accurate values for the Q of the slant linear patch as does the FDTD method or direct measurement. When the antenna is matched and driven in a single RLC-type impedance mode, the frequency of the maximum return loss, f_0, divided by the bandwidth between 3 dB values will provide a good approximation for the Q of a patch using measured or simulated data from a full-wave analysis method. Equation (2.53) works well with the cavity model, but experience indicates that

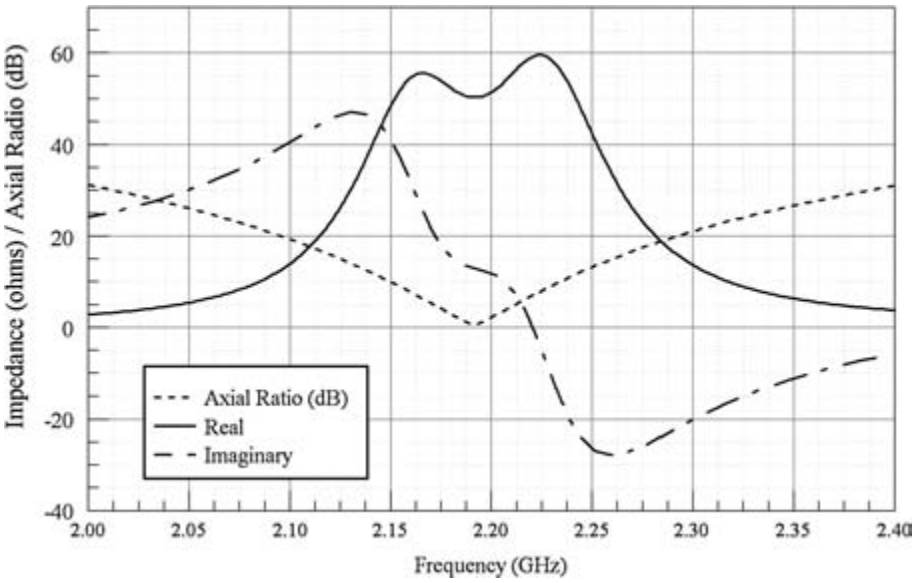

Figure 2-19 The rectangular CP patch antenna of Table 2-4 analyzed using the cavity model. The real and imaginary components of the driving point impedance are plotted with the computed axial ratio (in dB).

Table 2-5 2.2 GHz LHCP microstrip antenna (W_p = 1.3 mm).

a	b	h	ε_r	$\tan\delta$
42.298 mm	40.902 mm	1.5748 mm	2.50	0.0019

ẋ	ẏ
13.5 mm	14.5 mm

$$\Delta_L = \frac{\acute{a}}{3.395Q_0 + 1}$$

is more appropriate when using measured or computed (e.g., FDTD) S_{11} dB results of a slant linear patch to design a circularly polarized element.

Equation (2.53) also shows that as the antenna Q increases, Δ_L decreases. When a high dielectric constant is used as a substrate, the Q of the antenna becomes larger, which means the impedance bandwidth has become narrower. The high dielectric constant also decreases the size of the patch, which drives down the value of Δ_L, which tightens any manufacturing tolerances considerably.

A more complex iterative approach that uses the cavity model to compute single-feed circularly polarized rectangular patch designs is presented by Lumini et al.[41] Another design approach is to use a genetic algorithm optimization with the cavity model to develop a circularly polarized rectangular microstrip antenna design.[42] This method has the advantage that it optimizes for driving point match and axial ratio simultaneously. This eliminates first developing a slant linear patch and then using equation (2.52a) and equation (2.52b) to compute the dimensions to produce circular polarization. Experience with genetic algorithms indicates that it produces a design which is no better than the more straightforward method previously described.

Figure 2-15(II) uses indentation tabs to produce circular polarization. This type of design is undertaken experimentally.

Figure 2-15(III) has a pair of corners cut off to produce circular polarization. This creates a pair of diagonal modes (no longer TM_{10} and TM_{01}, as the shape of the patch has been altered) that can be adjusted to have identical magnitudes and a 90° phase difference between these modes. The antenna is fed along the centerline in this case so it will excite each of the diagonal modes with equal amplitude. In Figure 2-15 we see that if the upper right-hand corner and lower left-hand corner are reduced, we can view the situation as reducing the capacitance along that diagonal, making it more inductive. The opposite diagonal from lower right to upper left remains unchanged and has a larger capacitance by comparison. The amount of the area removed can be adjusted so the phase of the chopped corner diagonal is 45° and the phase of the unmodified diagonal is –45°. This situation creates right-hand circular polarization (RHCP). Leaving the feed point position unchanged and removing the opposite pair of corners reverses the phase, and thus the polarization sense.

We will define the total area removed to perturb the patch so it produces circular polarization as ΔS (Figure 2-15). The total area S of the unperturbed square patch prior to the corner removal to produce circular polarization is

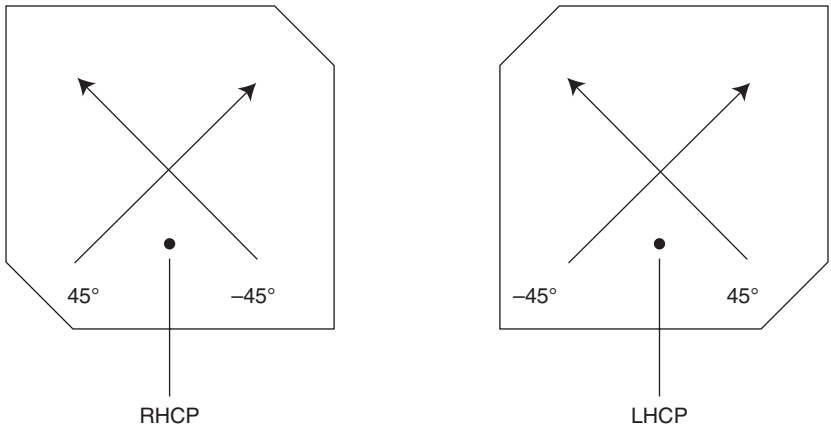

Figure 2-20 One may cut off a pair of opposing corners of a rectangular microstrip antenna to produce circular polarization. One can view cutting off a corner as reducing the capacitance of that diagonal mode. This will produce a more inductive impedance across the two chopped corners which will cause the electric field to have a phase of 45° compared with the –45° of the electric field with the capacitive impedance across the uncropped corners. Reversing the position of the corners reverses the polarization sense.

$S = a \cdot b = \acute{a}^2$ ($a = b = \acute{a}$). It has been reported that the ratio of the change in area ΔS to the original area of the patch S is related to the Q of the uncut antenna Q_0 computed using equation (2.51) by[43]

$$\frac{\Delta S}{S} = \frac{1}{2Q_0} \tag{2.58}$$

The area to be cut from each corner of the unperturbed patch, as shown in Figure 2-15(III), is half of the perturbation area S calculated using equation (2.58) or $\Delta S/2S$. In terms of the length along each edge which is cut off we have

$$\Delta_L = \frac{\acute{a}}{\sqrt{Q_0}} \tag{2.59}$$

Figure 2-15(IV) uses a diagonal slot to produce circular polarization. A guideline for choosing the slot area is to make it equal to $\Delta S/S$.

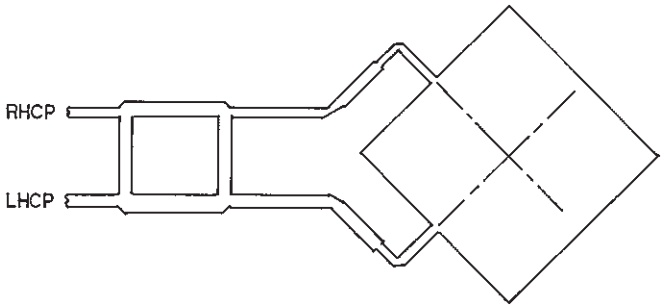

Figure 2-21 (a) Circular polarization may be synthesized using a 90° branchline hybrid.

2.6.2 Dual-Feed Circularly Polarized Rectangular Microstrip Antenna Design

Figure 2-21(a) shows the use of a 90° branchline hybrid to feed a microstrip antenna and create circular polarization. In this case, one begins with a square microstrip antenna. The TM_{01} and TM_{10} modes will have the same resonant frequency and are orthogonal. Each mode is fed independently using the branchline hybrid, which provides equal amplitude and the required 90° phase shift at the hybrid's center frequency to produce circular polarization. Figure 2-21(a) shows the branchline hybrid inputs that will produce LHCP and RHCP. In practice, if the antenna is fed RHCP, the LHCP port is terminated in a matched load, and vice versa.

The branchline hybrid will enforce equal amplitudes and nearly correct phase over a wide bandwidth, but as the patch edge impedance mismatches with frequency, the rejected power will appear at the terminated port, and power is lost to maintain good circular polarization compared with a single-feed design. The input impedance bandwidth and axial ratio bandwidth are far greater than the single-feed design, but when antenna efficiency is taken into account, the amount of power lost into the load of the hybrid is approximately the same as the power lost from impedance and polarization mismatch in a single-feed circular polarization antenna design. This design can also be implemented using a pair of probe feeds (one for the TM_{10} mode and one for the TM_{01} mode), and an external branchline 90° hybrid realized with coaxial cable.

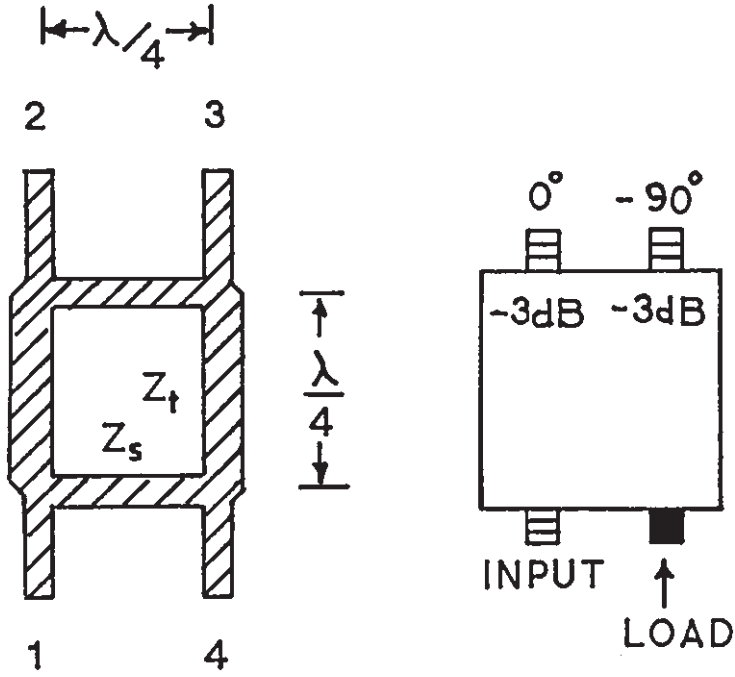

Figure 2-21 (b) A 90° branchline hybrid realized in microstrip or stripline and as often packaged commercially.

2.6.3 Quadrature (90°) Hybrid

The design of a rectangular patch with circular polarization (Section 2.6.2) requires a branchline hybrid, also known as a quadrature hybrid. A branchline quadrature hybrid provides a 3 dB power split between a pair of output ports with a 90° difference between them. The left-hand illustration of Figure 2-21(b) shows a branchline hybrid as it would appear realized in stripline or microstrip. The shunt branches have a characteristic impedance Z_s and the through or series branch has a characteristic impedance of Z_t.

At the branchline hybrid design frequency, the scattering parameters are[44]

$$S_{21} = -j\frac{Z_t}{Z_0} \tag{2.60a}$$

$$S_{31} = -\frac{Z_t}{Z_s} \tag{2.60b}$$

$$S_{11} = 0.0 \tag{2.60c}$$

$$S_{41} = 0.0 \tag{2.60d}$$

The illustration on the right of Figure 2-21(b) shows how a commercial hybrid appears with coaxial connectors. Some hybrids have a built-in load on one port, as shown, while others require the user to provide a load. This allows one to have one input that produces RHCP and another that produces LHCP, as shown in Figure 2-21(a). This allows a system to switch between polarization if desired.

When a 3 dB split between ports is desired with a reference impedance of Z_0 (generally 50 Ω), the shunt branches should have $Z_s = Z_0$ and the through branches $Z_t = Z_0/\sqrt{2}$ (35.4 Ω for a 50 Ω system). The lengths of the branches are all λ/4. When port 1 is used as an input port, then port 2 receives half of the input power and is the phase reference for port 3. Port 3 receives half of the input port power with a phase that is 90° behind port 2. The split waves cancel at port 4, which is called the isolated port. A load is generally placed on this port to absorb any imbalance, which stabilizes the phase difference between port 2 and 3. If port 4 is the input port, port 1 becomes the isolation port, port 3 is the 0° phase port with half the power, and port 2 becomes the –90° port.

In practice, there is often a slight imbalance in the power split between ports 2 and 3. We note that equation (2.60b) has Z_s in its denominator. This allows one to change the characteristic impedance of the shunt branches slightly and obtain a more even power split.

The bandwidth of a branchline hybrid is limited by the quarter-wave length requirement on the branches to 10–20%. One must also take the discontinuities at the transmission line junctions into account to produce a design which operates as desired. One can increase the bandwidth of a branchline coupler by adding cascading sections.[45] Recently Qing added an extra section to produce a three-stub hybrid coupler and created a microstrip antenna design with 32.3% 2:1 voltage standing wave ratio (VSWR) bandwidth and 42.6% 3 dB

axial ratio bandwidth.[46] Quadrature hybrids that have unequal power division and/or unequal characteristic impedances at each port can also be designed.[47]

2.7 Impedance and Axial Ratio Bandwidth

The impedance bandwidth of a rectangular microstrip antenna can be determined with the total Q used in the cavity model. For a linear rectangular microstrip antenna, driven in a single mode, the normalized impedance bandwidth is related to the total Q by[48]

$$BW_{Linear} = \frac{S-1}{Q_T\sqrt{S}} \quad \text{(S:1 VSWR)} \tag{2.61}$$

When a linear microstrip antenna design is very close to achieving an impedance bandwidth design goal, one can obtain a tiny amount of extra impedance bandwidth by designing the antenna to have a 65 Ω driving point resistance at resonance rather than a perfectly matched 50 Ω input resistance. The perfect match at one frequency is traded for a larger overall 2:1 VSWR bandwidth.[49] The impedance bandwidth also increases slightly when the width of the rectangular microstrip antenna is increased. The largest bandwidth increase occurs as the substrate dielectric constant ε_r is decreased and/or the substrate thickness is increased. The effect substrate thickness and dielectric constant have on impedance bandwidth as computed with the cavity model is illustrated in Figure 2-22 for a square linearly polarized microstrip antenna.

One must recall that as the substrate thickness is increased, higher order modes provide a larger and larger contribution to an equivalent series inductance, which in turn produces a larger and larger driving point mismatch. A desirable driving point impedance must be traded for impedance bandwidth. Equation (2.62) and equation (2.63) have been developed to relate the impedance bandwidth of a rectangular patch antenna radiating circular polarization to total Q as well as its expected axial ratio bandwidth. We can substitute $S = 2$ in equation (2.61) and equation (2.62), forming the ratio of circular to linear bandwidth. This reveals that the impedance bandwidth of a circularly

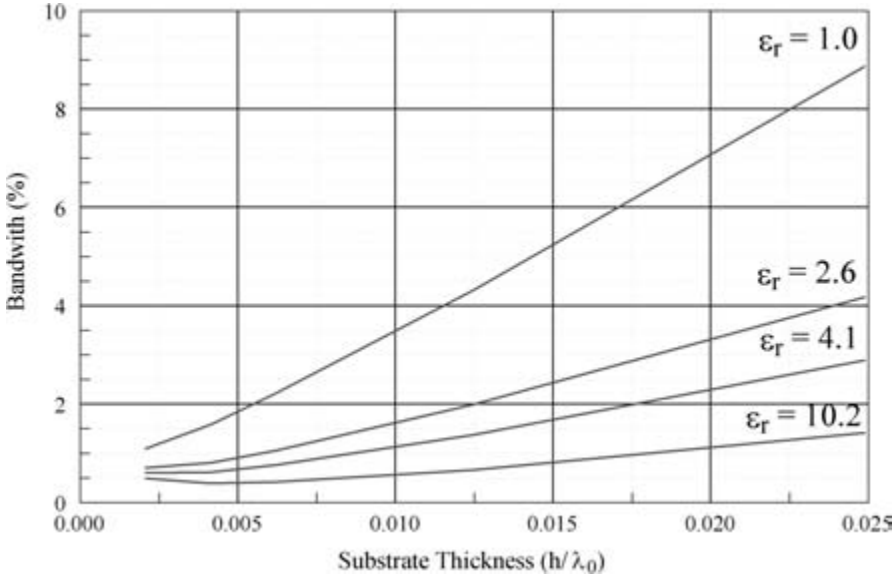

Figure 2-22 Normalized bandwidth of a square microstrip antenna as a function of substrate thickness and relative dielectric constant predicted by the cavity model.

polarized microstrip antenna compared to a linear antenna is larger by a factor of two. The two detuned resonances which sum to create circular polarization increase the total impedance bandwidth.

$$BW_{circular} = \frac{\sqrt{2(S-1)}}{Q_T} \tag{2.62}$$

$$BW_{axialratio} = \frac{AR-1}{Q_T\sqrt{AR}} \tag{2.63}$$

The received power (P_R) bandwidth of a patch is independent of polarization and given by

$$BW_{P_R} = \frac{2}{Q_T}\sqrt{\frac{1-p_{min}}{p_{min}}} \tag{2.64}$$

where p is the fraction of power received by a matched load (load resistance is equal to driving point resistance at resonance), to the power received by the antenna at its resonant frequency ($0 < p < 1$). The received power reaches maximum when $p = 1$ and becomes zero when $p = 0$. In equation (2.64), p_{min} is the minimum acceptable receive power coefficient for a given design.

Langston and Jackson have written the above expressions in terms of a normalized frequency variable for comparison.[50] The axial ratio bandwidth is the smallest for a transmitting single-feed circularly polarized patch. The receive power bandwidth is larger than the axial ratio or impedance bandwidth.

2.8 Efficiency

The antenna efficiency e relates the gain and directivity of an antenna:

$$G = eD \tag{2.65}$$

where G is the antenna gain and D is directivity.

The efficiency of a rectangular microstrip antenna can be calculated from the cavity model in terms of the cavity Qs.[51] The radiated efficiency is the power radiated divided by the total power, which is the sum of the radiated, surface wave, conductor loss, and dielectric loss. The stored energy is identical for all the cavity Qs. This allows us to write:

$$e = \frac{Q_T}{Q_r} \tag{2.66}$$

which expanded out is

$$e = \frac{Q_d Q_c Q_{sw}}{Q_{sw} Q_c Q_d + Q_{sw} Q_c Q_r + Q_{sw} Q_r Q_d + Q_r Q_d Q_c} \tag{2.67}$$

When multiplied by 100%, equation (2.66) gives the antenna efficiency in percent as predicted by the cavity model. We can readily see from equation

Table 2-6 Losses in a square linear microstrip antenna versus h (2.45 GHz, $a = b =$ 56.46 mm, $\tan\delta = 0.0025$, $\varepsilon_r = 1.1$).

h		η_r	η_{sw}	η_c	η_d
(0.030″)	0.762 mm	83.41%	0.01%	6.86%	9.71%
(0.060″)	1.524 mm	92.67%	0.03%	1.91%	5.39%
(0.090″)	2.286 mm	95.38%	0.05%	0.87%	3.70%
(0.120″)	3.048 mm	96.63%	0.06%	0.50%	2.81%

2.67 that as Q_{sw}, Q_c, and Q_d become large compared with Q_r, the antenna's efficiency approaches 100%. In other words, we desire to minimize the radiation Q and maximize Q_{sw}, Q_c, and Q_d, the surface wave Q, conductor Q, and dielectric Q, respectively, for maximum efficiency.

It is instructive to calculate the losses from each of the mechanisms separately. We can calculate $\eta_r = Q_T/Q_r$ for radiation efficiency, $\eta_{sw} = Q_T/Q_{sw}$ for the surface wave efficiency, $\eta_c = Q_T/Q_c$ for the conductor efficiency, and $\eta_d = Q_T/Q_d$ for the dielectric efficiency. When these are added together, we are able to account for 100% of the power in the antenna.

In order to obtain some understanding of the contribution of each of the loss mechanisms of a rectangular microstrip antenna with respect to substrate thickness h and dielectric constant ε_r, we have computed these for three typical dielectric values ($\varepsilon_r = 1.1$, 2.6, and 10.2).

Table 2-6 shows the efficiency components η_r (radiation), η_{sw} (surface wave), η_c (conductor), and η_d (dielectric) for a square linear microstrip antenna operated at 2.45 GHz with a very low dielectric constant substrate ($\varepsilon_r = 1.1$). We note the loss contribution from surface waves is insignificant in this case. The next largest loss is that due to the dielectric, and then the conductors. As the thickness h of the antenna is increased, the radiation efficiency increases.

The next analysis case is for $\varepsilon_r = 2.6$ (Table 2-7), where we can see the surface wave contribution has increased significantly compared with $\varepsilon_r = 1.1$ in Table 2-6. The surface wave loss increases in proportion to the thickness of the substrate; the conductor and dielectric losses decrease as the thickness increases. If a designer wants to maximize the space wave contribution in this case, then the 2.286 mm substrate would appear to be a good choice.

Table 2-7 Losses in a square linear microstrip antenna versus h (2.45 GHz, $a = b = 37.62$ mm, $\tan\delta = 0.0025$, $\varepsilon_r = 2.6$).

h		η_r	η_{sw}	η_c	η_d
(0.030″)	0.762 mm	76.28%	2.43%	8.82%	12.47%
(0.060″)	1.524 mm	85.15%	5.43%	2.46%	6.96%
(0.090″)	2.286 mm	85.96%	8.25%	1.10%	4.68%
(0.120″)	3.048 mm	84.99%	10.93%	0.61%	3.47%

Table 2-8 Losses in a square linear microstrip antenna versus h (2.45 GHz, $a = b = 19.28$ mm, $\tan\delta = 0.0025$, $\varepsilon_r = 10.2$)

h		η_r	η_{sw}	η_c	η_d
(0.030″)	0.762 mm	53.75%	24.71%	17.47%	4.07%
(0.060″)	1.524 mm	68.09%	10.73%	5.53%	15.65%
(0.090″)	2.286 mm	69.31%	17.56%	2.50%	10.62%
(0.120″)	3.048 mm	66.27%	24.76%	1.35%	7.62%

When the dielectric constant is increased to $\varepsilon_r = 10.2$ (Table 2-8), we see the surface wave power increases significantly compared with the $\varepsilon_r = 2.6$ case in Table 2-7. The thinnest substrate only radiates 53.75% into the space wave. As h increases from 0.762 mm to 1.524 mm, the amount lost to the conductor and dielectric loss approximately reverse contributions. The best compromise to maximize the losses due to the space wave, and minimize the conductor and dielectric losses, is the 2.286 mm thickness. Computing the losses separately can be very useful to a designer when evaluating the choice of substrate thickness for a given design. This is often a good design path to use because of the difficulty involved in making experimental efficiency measurements.[52]

2.9 Design of a Linearly Polarized Microstrip Antenna with Dielectric Cover

Microstrip antennas are often enclosed in dielectric covers (i.e., radomes) to protect them from harsh environments. These can range from vacuum-molded

or injection-molded plastic enclosures which leave an air gap between the radiating patch and the radome, to bonding a plastic material directly to the antenna.

Bonding dielectric material directly to the antenna can provide a high degree of hermetic sealing. When the substrate material is Teflon based, the bonding process to produce good adhesion can be very involved. In some commercial applications, the injection molding of a plastic radome which surrounds the antenna element and seals it has been implemented. In these cases, the use of a full-wave simulator such as Ansoft HFSS is best for the refinement of a design prior to prototyping, but the use of a quick quasi-static analysis can provide initial design geometry for refinement and design sensitivity prior to optimization.

A number of approaches have been forwarded to analyze a microstrip antenna with a dielectric cover.[53–56] Here we will utilize the transmission line model to analyze a rectangular microstrip antenna with a dielectric cover. A quasi-static analysis of a microstrip transmission line with a dielectric cover forms the basis of this analysis.[57] An effective dielectric constant for the geometry shown in Figure 2-23 is defined in equation (2.68) and the characteristic impedance is related in equation (2.69).

$$\varepsilon_e = \frac{C_{\varepsilon_r}}{C_0} \tag{2.68}$$

$$Z_0 = \frac{Z_{air}}{\sqrt{\varepsilon_e}} \tag{2.69}$$

$$Z_{air} = \frac{1}{cC_0} \tag{2.70}$$

where

ε_e = effective dielectric constant of microstrip line
Z_0 = characteristic impedance of microstrip line
Z_{air} = characteristic impedance of microstrip line with no dielectrics present

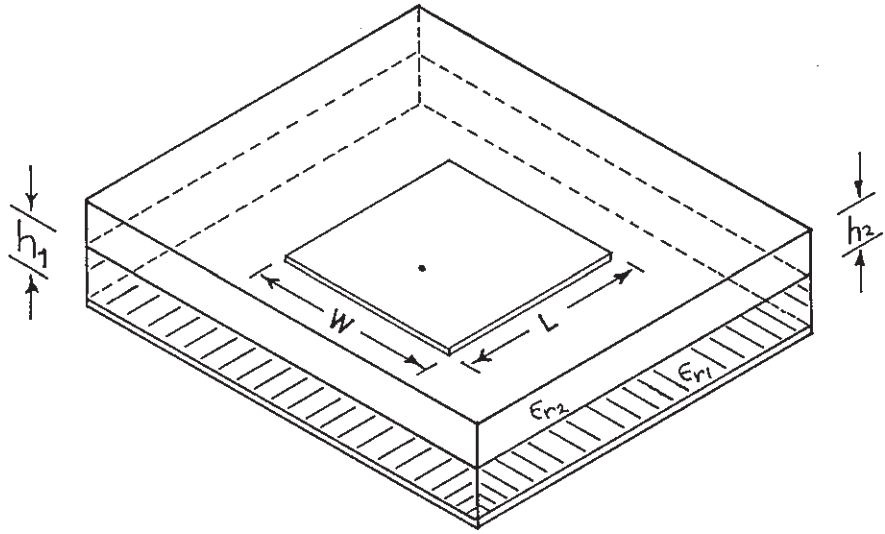

Figure 2-23 Rectangular microstrip patch geometry of a dielectric covered microstrip antenna analyzed with the transmission line model. The patch antenna is fed along the centerline of the antenna's width (i.e., $W/2$). The feed point is represented by the black dot.

C_{ε_r} = capacitance per unit length with dielectrics present
C_0 = capacitance per unit length with only free space present
c = speed of light in a vacuum.

Using the substitution of $\alpha = \beta h_1$ in Bahl et al.[58], we are able to write the capacitance as

$$\frac{1}{C} = \frac{1}{\pi\varepsilon_0}\int_0^{\infty}\left(1.6\frac{\sin(\alpha W/2h_1)}{(\alpha W/2h_1)} + 2.4(\alpha W/2h_1)^{-2}\cdot \left[\cos(\alpha W/2h_1) - \frac{2\sin(\alpha W/2h_1)}{(\alpha W/2h_1)} + \sin^2(\alpha W/4h_1)\cdot(\alpha W/4h_1)^{-2}\right]\right)^2 \cdot \left(\left[\varepsilon_{r_2}\frac{\varepsilon_{r_2}\tanh(\alpha h_2/h_1)+1}{\varepsilon_{r_2}+\tanh(\alpha h_2/h_1)} + \varepsilon_{r_1}\coth(\alpha)\right]\alpha\right)^{-1} d\alpha \tag{2.71}$$

where

W = width of microstrip transmission line (patch width)
h_1 = thickness of dielectric substrate
ε_{r1} = relative dielectric constant of substrate
h_2 = thickness of dielectric superstrate (dielectric cover/radome)
ε_{r2} = relative dielectric constant of radome dielectric superstrate (dielectric cover/radome).

The integration of equation (2.71) is efficiently computed using Gaussian quadrature, as presented in Appendix B. The slot admittance is modified when a dielectric cover is added to a rectangular microstrip antenna design. The modification is slight and is best computed using equation (2.4), when compared with the accuracy of more complicated alternatives.[59,60] The edge susceptance may be written as

$$B_e = jwC_{slot} \tag{2.72a}$$

The capacitance of the radiating slot for a rectangular microstrip antenna with a cover layer is obtained using

$$C_{slot} = \frac{W}{2}\left[\frac{\varepsilon_e(L)}{cZ_{air}(L)} - \varepsilon_0\varepsilon_r\frac{L}{h_1}\right] \tag{2.72b}$$

$\varepsilon_e(L)$ and $Z_{air}(L)$ are the effective dielectric constant with dielectrics present and the characteristic impedance of a microstrip line of width L with only air, respectively. Equation (2.72a) provides the edge capacitance of a microstrip transmission line with a dielectric superstrate of width L rather than W. The left-hand term inside of equation (2.72b) is the transmission line capacitance and the right-hand term is the capacitance per unit length of a parallel plate capacitor of width L. The fringing field capacitance is computed by the difference, which is used as an approximation of the slot capacitance.

When a microstrip antenna is covered with a dielectric substrate in practice, an air gap may exist. This air gap has a strong effect on the effective dielectric

constant of the patch, which in turn affects the characteristic impedance and resonant frequency of the antenna.

The resonant frequency of the microstrip antenna with a dielectric cover is computed using

$$f = \frac{c}{2(L + 2\Delta l)\sqrt{\varepsilon_e}} \tag{2.73a}$$

$$\Delta l = 0.412 h_1 \frac{(\varepsilon_e + 0.3)(W/h_1 + 0.264)}{(\varepsilon_e - 0.258)(W/h_1 + 0.8)} \tag{2.73b}$$

2.10 Design Guidelines for a Linearly Polarized Rectangular Microstrip Antenna

There are a number of antenna performance trade-offs with respect to substrate dielectric constant and thickness to consider when designing a linear rectangular microstrip antenna.[61] Clearly if one needs to feed a patch with a coaxial transmission line, then a probe feed is a good choice. If the design requires a microstrip feed, a nonradiating edge feed may make sense, but the patch needs to be narrow enough to decrease any excitation of a secondary mode. A narrower patch has slightly decreased bandwidth compared with a wide patch. If the impedance bandwidth requirement is greater than a narrow patch can provide, then one can turn to a feed along a radiating edge. A quarter-wave transformer feed on a radiating edge produces the least amount of perturbation of the patch radiation, but if the design constraints do not allow for enough area to implement the transformer, an inset feed can be utilized. In either case, if the patch is fed along a centerline which drives the lowest order mode, the driving point impedance presented by the next dominant mode is along a shorting plane for that next mode and mismatched (not driven), even if the patch is square.

A useful beginning patch width for a linear microstrip antenna is

$$W = \frac{c}{2f_r}\left(\frac{\varepsilon_r + 1}{2}\right)^{-1/2} \tag{2.74}$$

Patch thickness is an important parameter to consider. If the patch thickness is too thin, the efficiency and impedance bandwidth are decreased. When the patch is too thick, it can efficiently generate surface waves and produce a series inductive mismatch at the driving point from higher order cavity modes.

The lowest order surface wave (TM_0), which can propagate in any direction along a conducting sheet coated with a dielectric slab, has no cutoff frequency for dielectric substrates with $\varepsilon_r > 1$. This means there will always be some amount of power in the lowest order surface wave mode independent of frequency when $\varepsilon_r > 1$. For a given maximum frequency of operation, a good compromise between these conflicting parameters is to choose the substrate thickness according to

$$h \leq \frac{0.3c}{2\pi f_{max}\sqrt{\varepsilon_r}} \tag{2.75}$$

At higher frequencies, Gopinath has presented an analysis which allows one to choose a substrate thickness that maximizes the Q of a microstrip line at a given frequency.[62] When a very thick substrate or a dielectric cover layer (radome) is present, more efficient generation of surface waves is possible than in the normal microstrip antenna geometry with a thin substrate and no cover layer over the patch.

The resonant length of a rectangular microstrip antenna is computed with

$$L = \frac{c}{2f_r\sqrt{\varepsilon_e}} - 2\Delta l \tag{2.76}$$

When designing a square microstrip patch one can use

$$L_0 = \frac{c}{2f_r\sqrt{\varepsilon_r}} \tag{2.77}$$

to provide an initial length L_0. This value can then be equated to the width of the antenna, W, to produce a new resonant length L_1 using equation (2.76), equation (2.6), and equation (2.7). This process is continued until the value

becomes fixed. The solution generally becomes fixed by the fifth iteration [L_5] (Appendix B, Section B.3).

If electrostatic discharge (ESD) is a consideration, one can place an electrical short at the center of the patch using a via or soldered shorting pin. Gold flashing can be used to protect a copper element from many environmental hazards. Tin immersion is another alternative which is useful in some situations to prevent copper degradation.

In some designs, a higher frequency resonance of a rectangular microstrip antenna may coincide with a band which is to be isolated for system design reasons. This problem can sometimes be resolved by using a circular microstrip patch which has resonances with different spacings than those of a rectangular patch.

The desired feed point impedance may be located using the transmission line model with a root finding algorithm such as the bisection method (Appendix B, Section B.4). Experience indicates the relationships used to compute the wall admittance, equation (2.4) and equation (2.5), predict accurate values for the feed point location when the dielectric constant is $2.2 < \varepsilon_r < 3.8$, which is often encountered in practice, and have proven more accurate than alternative expressions for uncovered rectangular microstrip antennas. In other situations, the feed point will require experimental determination. One can also use the cavity model to predict the location of a desired driving point impedance, but its results are somewhat sensitive to the effective probe diameter used in the computation.

The directivity of a linear rectangular microstrip antenna can be estimated using equation (2.43), which is generally within 1 to 2 dB of measurement for most groundplane sizes. A more accurate directivity can be computed with a more powerful technique such as FDTD or FEM. The antenna efficiency can be computed from equation (2.66) and used to calculate the antenna gain.

As discussed previously, the directivity of a linear rectangular microstrip antenna depends on the substrate's relative dielectric constant, ε_r. Directivity increases as the dielectric constant decreases and will decrease, in an asymptotic fashion, as the dielectric constant is increased (see Table 2-3).

In some design environments, a microstrip antenna must survive a considerable amount of shock and vibration. When a patch is probe fed, the solder joint on the top of a microstrip patch that connects the feed probe to the patch is vulnerable to failure. Under large vibrational shock, the probe can punch itself

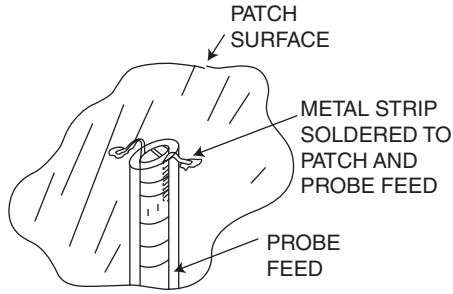

Figure 2-24 Vulnerability of a probe feed to shock and vibration can be mitigated by the use of two (or more) small metal strips. Each strip is soldered to the feed pin, extending through a minute gap along the pin, which is provided by a slightly larger than required hole in the dielectric substrate. The strips are then soldered to the patch with a small radius of slack. This slack allows the feed pin to move up and down without solder failure.

through the upper solder joint, leaving a microscopic ring-shaped gap between the solder and the feed probe. Often this ring-shaped gap is too small to be seen without a microscope, but will produce antenna failure. One solution to this problem is to use a pair of thin metal strips soldered along the feed probe and whose ends are bent at right angles with a small amount of slack and soldered to the patch. The feed pin with soldered strips on either side pass through a hole that is large enough to allow the feed pin to move axially without interference. The small amount of extra slack that is left as a small radius at the right-angle bend of the strip before the end of the strip is soldered allows for movement. This is illustrated in Figure 2-24.

Cross-polarization is produced by the existence of higher order modes on the patch. This is discussed in greater detail in Chapter 3.

In the case of a linearly polarized rectangular microstrip antenna, we generally feed the antenna in the center ($x = 0$). This will drive the TM_{01} mode and theoretically not excite the TM_{10} mode, which is mismatched.

When a square patch is used to produce circular polarization with two orthogonal (microstrip or probe) feeds, any error in centering the feeds along the y-axis and x-axis will increase cross-polarization. A square microstrip antenna has the property that both TM_{01} and TM_{10} modes have the same resonant frequency and the undesired mode may be readily excited by error in the driving point location.

A resonant cavity model may be used to estimate the amount of cross-polarization produced by probe placement error.[63] These computations were undertaken by Mishra and Milligan.[64] For a square patch to have no less than 25 dB cross-polarization, the feed probe must not vary more than 0.75% of the antenna width (a). A square patch designed on a substrate with a 2.32 relative dielectric constant and a 3.0 GHz operating frequency with an approximately 3 cm width must be within 0.22 mm to achieve 25 dB cross-polarization.

When only linear polarization is desired, one can increase the 25 dB cross-polarization driving point location tolerance by using a rectangular patch ($a > b$). By shifting the TM_{10} resonance to a frequency twice that of the 2:1 VSWR band-edge location, the tolerance increases from 0.75% to 2% of the patch width (a).

These examples demonstrate that when feeding a patch with a probe feed, the feed point location tolerance for low cross-polarization is very tight and small location errors will quickly increase cross-polarization levels.

2.11 Design Guidelines for a Circularly Polarized Rectangular Microstrip Antenna

The design of a circularly polarized microstrip antenna that uses a rectangular patch with an aspect ratio begins with designing a square microstrip antenna. Equation (2.8) and equation (2.6) may be iterated (Appendix B, Section B.3) to create a square patch. The resonant frequency tends to be slightly low when the iterated converged value is used. The cavity model may be used to refine the patch size and make it more accurate. The Q of a single mode, TM_{01} or TM_{10}, of a square patch can be determined with measurement or computed using the cavity model to determine Q_T. The cavity model can then be used to compute a driving point location that has an input resistance at resonance of about 88 Ω. Equation (2.52) is then used to compute the patch dimensions to produce circular polarization.

Experimental optimization is generally required to complete the design of a circularly polarized rectangular patch antenna. The Smith chart of Figure 2-18 illustrates the impedance trace one needs in order to achieve circular polarization. The frequency which exists at the vertex of a kink in the Smith chart impedance, which forms a 90° angle, is the point at which the optimum circular polarization occurs. The polarization sense of the antenna may be determined

by consulting Figure 2-15(I). Often the impedance at the kink of the impedance trace is not well matched and frequently has a capacitive component. In the case of a probe fed circularly polarized rectangular microstrip antenna, one can move the driving point location off the patch diagonal and often match the antenna at the circular polarization frequency.

When a dielectric superstrate (radome) covers a microstrip antenna (Figure 2-23) that generates circular polarization, the axial ratio bandwidth will remain unchanged.[65]

A variety of Global Positioning System (GPS) RHCP rectangular microstrip antenna designs that use high dielectric constant ceramic material as a substrate are offered by a number of manufacturers. A common GPS antenna design has substrate dimensions of 25 mm × 25 mm × 4 mm with $\varepsilon_r = 20$ which are optimized to operate on a 70 mm × 70 mm groundplane. This antenna design is electrically small at 1.575 GHz and its performance is strongly affected by electrically small groundplane dimensions. The groundplane dimensions affect the resonant frequency and radiation patterns adversely and these effects must be included in the design. The limitations of electrically small antennas are discussed in Chapter 7, Section 7.3.1.

2.12 Electromagnetically Coupled Rectangular Microstrip Antenna

One may use a rectangular microstrip patch that is fed with a microstrip transmission line which is electromagnetically coupled to the patch. The geometry of this design is defined in Figure 2-25. Microstrip antennas of this configuration are very difficult to directly analyze and most designs are empirical or designed by trial and error with a full-wave simulator.[66] One can use equations (2.68) through (2.71) to determine the width that corresponds to a 50 Ω microstrip line embedded between two dielectrics, ε_{r1} and ε_{r2}. Alternatively, many full-wave electromagnetic simulation programs allow one to compute the characteristic impedance of an embedded microstrip transmission line. Altering the width of a patch generally allows one to match the antenna to the transmission line, and patch length determines the resonant frequency.

An example electromagnetically coupled patch designed to operate at 2.45 GHz has substrate heights of $h_1 = h_2 = 1.524$ mm. The dielectric constant

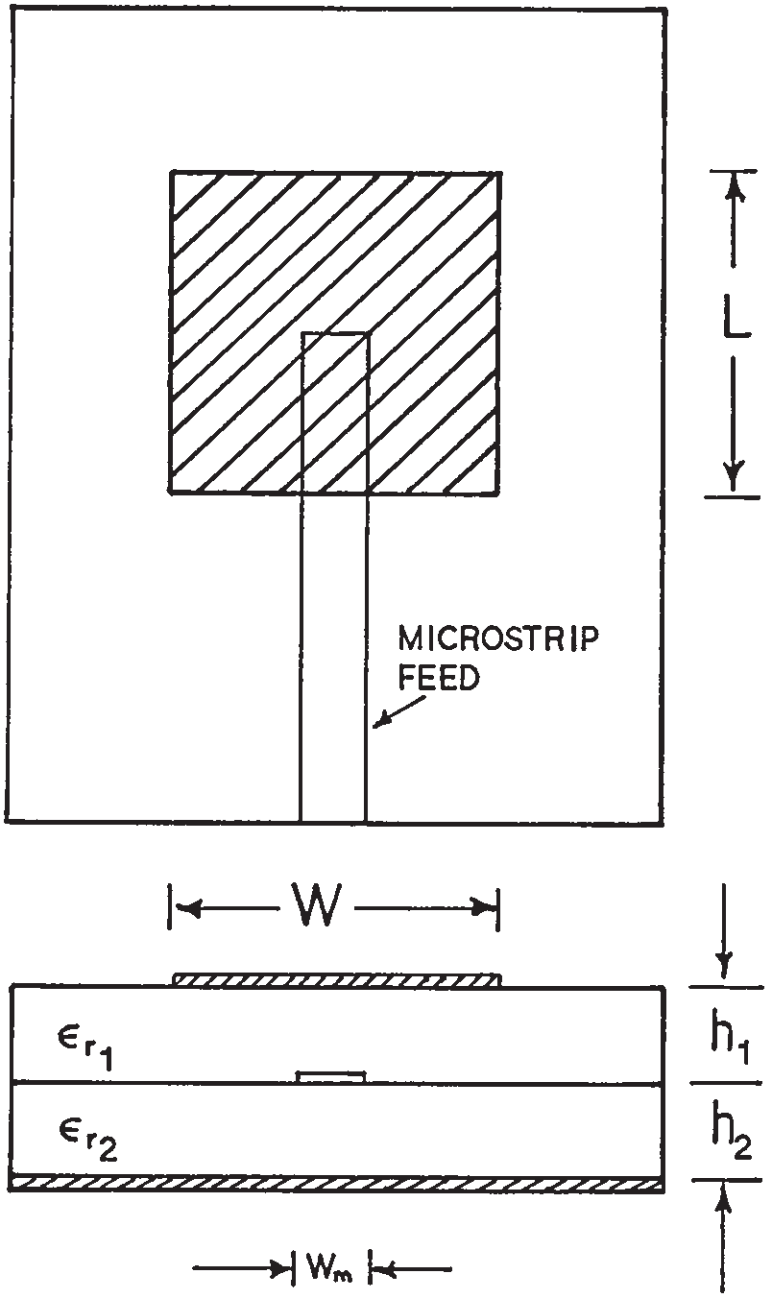

Figure 2-25 Rectangular microstrip patch with an electromagnetically coupled feed.

of both layers ε_{r1} and ε_{r2} = 2.6, with tan δ = 0.0025. The patch width is W = 44.0 mm and the resonant length is L = 34.0 mm. The width of the 50 Ω microstrip feed line is W_m = 4.0 mm. The groundplane width and length are 128.0 mm and 130.0 mm. respectively. The patch is centered on the substrate and the feed line extends under the patch to the patch center. The antenna has about 3.2% impedance bandwidth, with 7.3 dBi gain. We can see from this design example that another advantage of this geometry is the ability to feed a rectangular microstrip antenna directly with a 50 Ω microstrip transmission line.

2.13 Ultrawide Rectangular Microstrip Antennas

In Chapter 4 we will investigate the use of a matching network to broadband a microstrip antenna. The example used requires a microstrip antenna with an edge resistance of 92.5 Ω. This antenna is obtained by increasing the width of the patch beyond that generally suggested.[67] The symmetry of the feed is such that driving a mode along the length of the patch does not occur when it is driven at the frequency of the TM_{01} mode. Rectangular microstrip antennas that are very wide compared with their resonant length are referred to as ultrawide rectangular microstrip antennas (UWMSAs).

Ultrawide microstrip antennas have useful properties compared with microstrip antennas that possess typical widths. First, one can control the edge resistance at resonance to make the development of a broadband matching network easier. Second, one can choose a patch width that produces an edge resistance of 50 Ω and vanquishes the need for matching when the patch is fed with a 50 Ω microstrip transmission line. Third, the gain of a wide microstrip antenna is very large compared with typical microstrip antennas.

A special case of a UWMSA is the 50 Ω microstrip patch. This patch has a width that is chosen so the edge resistance at resonance is 50 Ω. A 50 Ω transmission line can be used to directly feed a radiating edge so that no matching network (e.g., quarter-wave transformer) is required. The patch aperture is larger than a conventional patch and so has enhanced gain when compared with a typical patch antenna design.

The geometry of a UWMSA 50 Ω patch is presented in Figure 2-26. The antenna has a width W_{50} and length L. The patch is fed with a 50 Ω microstrip

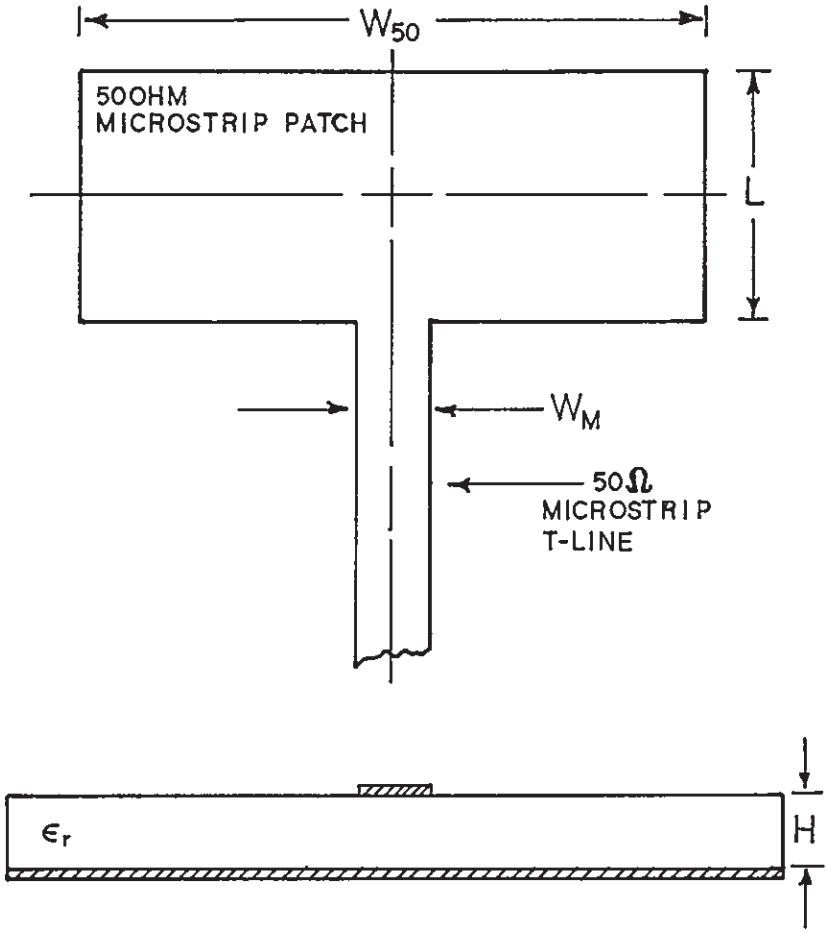

Figure 2-26 A 50 Ω ultrawide microstrip antenna geometry.

transmission line whose width is designated as W_M. As was discussed previously, the gain of a microstrip antenna is dependent upon the relative dielectric constant ε_r of the substrate. We will examine the radiation patterns and bandwidth of the UWMSA for $\varepsilon_r = 1.0$ and 2.6 and the special case of a 50 Ω patch. The substrate thickness is 2.286 mm (0.090 inches). The operating frequency is 5.25 GHz. For $\varepsilon_r = 1.0$, $W_{50} = 68.0$ mm, $L = 24.76$ mm, and $W_M = 11.0$ mm, and when $\varepsilon_r = 2.6$, $W_{50} = 54.0$ mm, $L = 15.10$ mm, and $W_M = 6.2$ mm.

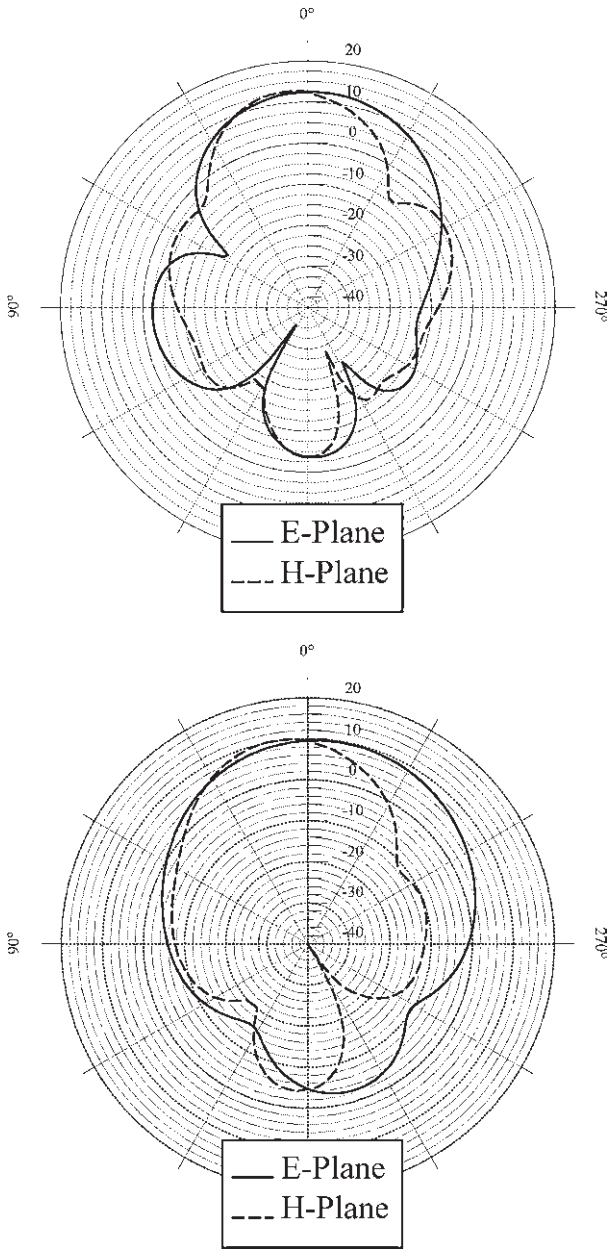

Figure 2-27 Predicted radiation pattern of the 2.45 GHz 50 Ω UWMSA of Table 2-9 using FDTD analysis for $\varepsilon_r = 1.0$ (top) and $\varepsilon_r = 2.6$ (bottom).

Table 2-9 Single-element gain of the UWMSA examples.

ε_r	Gain (dBi)
1.00	12.84
2.60	10.29

The computed radiation patterns of the ultrawide microstrip antenna are presented in Figure 2-27. The top polar plot is of a patch with an air dielectric ($\varepsilon_r = 1.0$). The bottom patch has a dielectric substrate with ($\varepsilon_r = 2.6$). Table 2-9 presents the single element gain of UWMSA examples. The air loaded UWMSA has as much gain as a typical 2×2 rectangular patch array on a dielectric substrate.

References

[1] Hildebrand, L. T., and McNamara, D. A., "A guide to implementational aspects of the spacial-domain integral equation analysis of microstrip antennas," *Applied Computational Electromagnetics Journal*, March 1995, Vol. 10, No. 1, ISSN 1054-4887, pp. 40–51.

[2] Mosig, J. R., and Gardiol, F. E. "Analytical and numerical techniques in the Green's function treatment of microstrip antennas and scatterers," *IEE Proceedings*, March 1983, Vol. 130, Pt. H, No. 2, pp. 175–182.

[3] Mosig, J. R., and Gardiol, F. E., "General integral equation formulation for microstrip antennas and scatterers," *IEE Proceedings*, December 1985, Vol. 132, Pt. H, No. 7, pp. 424–432.

[4] Mosig, J. R., "Arbitrarily Shaped microstrip structures and their analysis with a mixed potential integral equation," *IEEE Transactions on Microwave Theory and Techniques*, February 1988, Vol. 36, No. 2, pp. 314–323.

[5] Pues, H., and Van de Capelle, A., "Accurate transmission-line model for the rectangular microstrip antenna," *IEE Proceedings*, December 1984, Vol. 131, Pt. H, No. 6, pp. 334–340.

[6] Dearnley, R. W., and Barel, A. R. F., "A broad-band transmission line model for a rectangular microstrip antenna," *IEEE Transactions on Antennas and Propagations*, January 1989, Vol. 37, No. 1, pp. 6–15.

[7] Bhattacharyya, A. K., and Garg, R., "Generalized transmission line model for microstrip patches," *IEE Proceedings*, April 1985, Vol. 132, Pt. H, pp. 93–98.

[8] Derneryd, A., "Linearly polarized microstrip antennas," *IEEE Transactions on Antennas and Propagations*, November 1976, Vol. AP-24, pp. 846–851.

[9] Munsen, R. E., "Conformal microstrip antennas and microstrip phased arrays," *IEEE Transactions on Antennas and Propagations*, January 1974, Vol. AP-22, pp. 74–78.

[10] Bahl, I. J., and Bhartia, P., *Microstrip Antennas*, London: Artech House, 1980, p. 46.

[11] Basilio, L., Khayat, M., Williams, J., and Long, S., "The dependence of the input impedance on feed position of probe and microstrip line-fed patch antennas," *IEEE Transactions on Antennas and Propagation*, January 2001, Vol. 49, No. 1, pp. 45–47.

[12] Derneryd, A. G., "A theoretical investigation of the rectangular microstrip antenna element," *IEEE Transactions on Antennas and Propagations*, July 1978, Vol. AP-26, pp. 532–535.

[13] Augustine, C. F., "Field detector works in real time," *Electronics*, June 24, 1968, pp. 118–122.

[14] Fergason, J. L., "Liquid crystals," *Scientific American*, August 1964, Vol. 211, No. 2, pp. 77–85.

[15] Yang, K., Gerhard, D., Yook, J. G., Papapolymerou, I., Katehi, L. P. B., and Whitaker, J. F., "Electrooptic mapping and finite-element modeling of the near-field pattern of a microstrip patch antenna," *IEEE Transactions on Microwave Theory and Techniques*, February 2000, Vol. 48, No. 2, pp. 288–294.

[16] Bokhari, S. A., Zurcher, J.-F., Mosig, J. R., and Gardiol, F. E., "Near fields of microstrip antennas," *IEEE Transactions on Antennas and Propagation*, February 1995, Vol. 43, No. 2, pp. 188–197.

[17] Levine, E., "Special measurement techniques for printed antennas," in *Handbook of Microstrip Antennas*, James, J. R., and Hall, P. S., eds. Stevenage, UK: Peter Peregrinus, Ltd., 1989.

[18] Frayne, P. G., "Microstrip field diagnostics," in *Handbook of Microstrip Antennas*, James, J. R., and Hall, P. S., eds. Stevenage, UK: Peter Peregrinus, Ltd., 1989.

[19] Lo, Y. T., Solomon, D., and Richards, W. F., "Theory and experiment on microstrip antennas," *IEEE Transactions on Antennas and Propagations*, March 1979, Vol. AP-27, pp. 137–149.

[20] Richards, W. F., Lo, Y. T., and Harrison, D. D., "An improved theory for microstrip antennas and applications," *IEEE Transactions on Antennas and Propagations*, January 1981, Vol. AP-29, pp. 38–46.

[21] Lee, H. F., and Chen, W., eds., *Advances in Microstrip and Printed Antennas*, New York: John Wiley and Sons, 1997, pp. 223–242.

[22] Gan, Y.-B., Chua, C.-P., and Li, L.-W., "An enhanced cavity model for microstrip antennas," *Microwave and Optical Technology Letters*, March 2004, Vol. 40, No. 6, pp. 520–523.

[23] Thouroude, D., Himdi, M., and Daniel, J. P., "CAD-oriented cavity model for rectangular patches," *Electronics Letters*, June 1990, Vol. 26, No. 13, pp. 842–844.

[24] Pozar, D. M., "Rigorous closed-form expressions for the surface wave loss of printed antennas," *Electronics Letters*, June 1990, Vol. 26, No. 13, pp. 954–956.

[25] Schaubert, D. H., Pozar, D. M., and Adrian, A., "Effect of microstrip antenna substrate thickness and permittivity: comparison of theories with experiment," *IEEE Transactions on Antennas and Propagation*, June 1989, Vol. 37, No. 6, pp. 677–682.

[26] Cabedo-Fabres, M., Antonino-Daviu, E., Valero-Nogueira, A., and Bataller, M. F., "The theory of characteristic modes revisited: a contribution to the design of antennas for modern applications," *IEEE Antennas and Propagation Magazine*, October 2007, Vol. 49, No. 5, pp. 52–67.

[27] Schaubert, D. H., Pozar, D. M., and Adrian, A., "Effect of microstrip antenna substrate thickness and permittivity: comparison of theories with experiment," *IEEE Transactions on Antennas and Propagation*, June 1989, Vol. 37, No. 6, pp. 677–682.

[28] Bahl, I. J., and Bhartia, P., *Microstrip Antennas*, London: Artech House, 1980, pp. 48–50.

[29] Bahl, I. J., and Bhartia, P., *Microstrip Antennas*, London: Artech House, 1980, p. 64.

[30] Tavlov, A., *Computational Electrodynamics: The Finite-Difference Time Domain Method*, London: Artech House, 1995, pp. 213–218.

[31] Kunz, K. S., and Luebbers, R. J., *The Finite Difference Time Domain Method for Electromagnetics*, Boca Raton, FL: CRC Press, 1993, p. 109.

[32] Sanford, G. E, and Klein, L., "Recent developments in the design of conformal microstrip phased arrays," IEE Conference on Maritime and Aeronautical Satellites for Communication and Navigation, IEE Conference Publication 160, London, pp. 105–108.

[33] Post, R. E., and Stephenson, D. T., "The design of microstrip antenna array for a UHF space telemetry link," *IEEE Transactions on Antennas and Propagations*, January 1981, Vol. AP-29, pp. 129–134.

[34] James, J. R., Hall, P. S., and Wood, C., *Microstrip Antenna Theory and Design*, Stevenage, UK: Peter Peregrinus, Ltd., 1981, p. 106.

[35] Milligan, T., *Modern Antenna Design*, New York: McGraw Hill, 1985, p. 118.

[36] Bancroft, R., Unpublished Witnessed/Notarized Engineering Notebook, October 23, 1998.

[37] Lu, J.-H., and Yang, K.-P., "A simple design for single-feed circularly polarized microstrip antennas," *Proceedings of the National Science Council ROC(A)*, 2000, Vol. 24, No. 2, pp. 130–133.

[38] Richards, W. F., Lo Y. T., and Harrison, D. D., "An improved theory for microstrip antennas and applications," *IEEE Transactions on Antennas and Propagation*, January 1981, Vol. AP-29, pp. 38–46.

[39] Lumini, F., Cividanes, L., and Lacava, J. C. S., "Computer aided design algorithm for singly fed circularly polarized rectangular microstrip patch antennas," *International Journal of RF & Microwave Computer-Aided Engineering*, January 1999, Vol. 9, No. 1, pp. 32–41.

[40] Balanis, C. A., *Antenna Theory Analysis and Design*, New York: Harper & Row, 1982, p. 51.

[41] Lumini, F., Cividanes, L., and Lacava, J. C. S., "Computer aided design algorithm for singly fed circularly polarized rectangular microstrip patch antennas," *International Journal of RF and Microwave Computer-Aided Engineering*, January 1999, Vol. 9, No. 1, pp. 32–41.

[42] Lee, D., and Lee, S., "Design of a coaxially fed circularly polarized rectangular microstrip antenna using a genetic algorithm," *Microwave and Optical Technology Letters*, September 2000, Vol. 26, No. 5, pp. 288–291.

[43] Suzuki, Y., "Key points in the design and measurement of microstrip antennas," in *Analysis, Design, and Measurement of Small and Low-Profile Antennas*, Hirasawa, K., and Haneishi, M., eds., London: Artech House, 1992, pp. 144–145.

[44] Mongia, R., Bahl, I., and Bhartia, P., *RF and Microwave Coupled-Line Circuits*, London: Artech House, 1999, pp. 244–247.

[45] Malherbe, J. A. G., *Microwave Transmission Line Coupler*, London: Artech House, 1988.

[46] Qing, X. M., "Broadband aperture-coupled circularly polarized microstrip antenna fed by a three-stub hybrid coupler," *Microwave and Optical Technology Letters*, January 2004, Vol. 40, No. 1, pp. 38–41.

[47] Sainati, R. A., *CAD of Microstrip Antennas for Wireless Applications*, London: Artech House, 1996, pp. 124–129.

[48] Langston, W. L., and Jackson, D. R., "Impedance, axial ratio, and receive power bandwidths of microstrip antennas," IEEE International Symposium, San Antonio, Texas, June 16–21 2002, pp. 882–885.

[49] Milligan, T., *Modern Antenna Design*, New York: McGraw Hill, 1985, p. 104.

[50] Langston, W. L., and Jackson, D. R., "Impedance, axial ratio, and receive power bandwidths of microstrip antennas," *IEEE Transactions on Antennas and Propagation*, October 2004, Vol. 52, No. 10, pp. 2769–2773.

[51] Sainati, R. A., *CAD of Microstrip Antennas for Wireless Applications*, London: Artech House, 1996, p. 54.

[52] Pozar, D., "Comparison of three methods for the measurement of printed antenna efficiency," *IEEE Transactions on Antennas and Propagation*, January 1988, Vol. 36, No. 1, pp. 136–139.

[53] Roudot, B., Mosig, J. R., and Gardiol, F. E., "Radome effects on microstrip antenna parameters," 17th European Microwave Conference, Rome, Italy, September 1987, pp. 771–777.

[54] Verma, A. K., Bhupal, A., Rostamy, Z., and Srivastava, G. P., "Analysis of rectangular patch antenna with dielectric cover," *IEICE Transactions*, May 1991, Vol. E-74, No. 5, pp. 1270–1276.

[55] Bernhard, J. T., and Tousignant, C. J., "Resonant frequencies of rectangular microstrip antennas with flush and spaced dielectric substrates," *IEEE Transactions on Antennas and Propagation*, February 1999, Vol. 47, No. 2, pp. 302–308.

[56] Zhong, S. Z., Liu, G., and Qasim, G., "Closed form expressions for resonant frequency of rectangular patch antennas with multidielectric layers," *IEEE Transactions on Antennas and Propagation*, September 1994, Vol. 42, No. 9, pp. 1360–1363.

[57] Bahl, I. J., and Stuchly, S. S., "Variational method for the analysis of microstrip-like transmission lines," *IEEE Transactions on Microwave Theory and Techniques*, August 1968, Vol. MTT-16, No. 8, pp. 529–535.

[58] Bahl, I. J., and Stuchly, S. S., "Analysis of a microstrip covered with a lossy dielectric," *IEEE Transactions on Microwave Theory and Techniques*, February 1980, Vol. MTT-28, No. 2, pp. 104–109.

[59] Shavit, R., "Dielectric cover effect on rectangular microstrip antenna array," *IEEE Transactions on Antennas and Propagation*, August 1994, Vol. 42, No. 8, pp. 1180–1184.

[60] Sainati, R. A., *CAD of Microstrip Antennas for Wireless Applications*, London: Artech House, 1996, pp. 70–71.

[61] James, J. R., Henderson, A., and Hall, P. S., "Microstrip antenna performance is determined by substrate constraints," *Microwave System News (MSN)*, August 1982, pp. 73–84.

[62] Gopinath, A., "Maximum *Q*-factor of microstrip resonators," *IEEE Transactions on Microwave Theory and Techniques*, February 1981, Vol. MTT-29, No. 2, pp. 128–131.

[63] Benalia, A., and Gupta, K. C., "Faster computation of *Z*-matrices for rectangular segments in planar microstrip circuits," *IEEE Transactions on Microwave Theory and Techniques*, June 1986, Vol. MTT-34, No. 6, pp. 733–736.

[64] Mishra, R. K., and Milligan, T., "Cross-polarization tolerance requirements of square microstrip patches," *IEEE Antennas and Propagation Magazine*, April 1996, Vol. 38, No. 2, pp. 56–58.

[65] Chen, W., Wong, K., and Row, J., "Superstrate loading effects on the circular polarization and crosspolarization characteristics of a rectangular microstrip antenna," *IEEE Transactions on Antennas and Propagation*, February 1994, Vol. 42, No. 2, pp. 260–264.

[66] Waterhouse, R. B., ed., *Microstrip Antennas: A Designer's Guide*, Boston: Kluwer Academic Publishers, 2003, pp. 52–54.

[67] Bahl, I. J., and Bhartia, P., *Microstrip Antennas*, London: Artech House, 1980, p. 57.

Chapter 3

Circular Microstrip Antennas

3.1 Circular Microstrip Antenna Properties

In Chapter 2 we saw that the rectangular microstrip antenna has a number of useful designs. The circular microstrip antenna offers a number of radiation pattern options not readily implemented using a rectangular patch. The fundamental mode of the circular microstrip patch antenna is the TM_{11}. This mode produces a radiation pattern that is very similar to the lowest order mode of a rectangular microstrip antenna. The next higher order mode is the $TM_{21,}$ which can be driven to produce circularly polarized radiation with a monopole-type pattern. This is followed in frequency by the TM_{02} mode, which radiates a monopole pattern with linear polarization. In the late 1970s, liquid crystals were used to experimentally map the electric field of the driven modes surrounding a circular microstrip antenna and optimize them.[1]

In Figure 3-1, the geometry of a circular microstrip antenna is defined. The circular metallic patch has a radius a and a driving point located at r at an angle ϕ measured from the $\hat{x}$ axis. As with the rectangular microstrip antenna, the patch is spaced a distance h from a groundplane. A substrate of ε_r separates the patch and the groundplane.

An analysis of the circular microstrip antenna, which is very useful for engineering purposes, has been undertaken by Derneryd and will be utilized here.[2] The electric field under the circular microstrip antenna is described by:

$$E_z = E_0 J_n(kr)\cos(n\phi) \tag{3.1}$$

The magnetic field components are described as

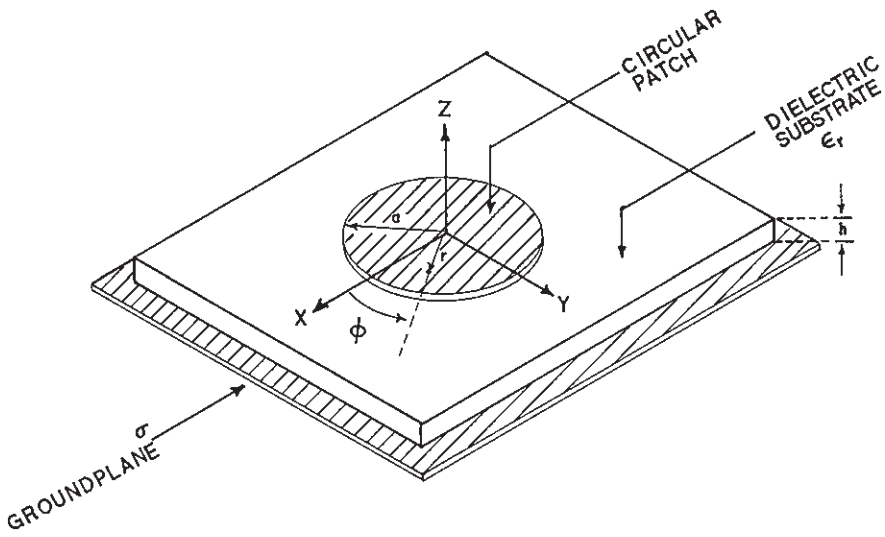

Figure 3-1 Circular microstrip antenna geometry. The circular microstrip antenna is a metal disk of radius a and has a driving point location at r which makes an angle ϕ with the $\hat{x}$ axis. The thickness of the substrate is h, where $h \ll \lambda_0$, which has a relative dielectric constant of ε_r.

$$H_r = -\frac{j\omega\varepsilon n}{k^2 r} E_0 J_n(kr) \sin n\phi \tag{3.2}$$

$$H_\phi = -\frac{j\omega\varepsilon}{k} E_0 \acute{J}_n(kr) \cos n\phi \tag{3.3}$$

where k is the propagation constant in the dielectric which has a dielectric constant $\varepsilon = \varepsilon_0\varepsilon_r$. J_n is the Bessel function of the first kind of order n. $\acute{J}_n$ is the derivative of the Bessel function with respect to its argument, ω is the angular frequency ($\omega = 2\pi f$). The open circuited edge condition requires that $\acute{J}_n(ka) = 0$. For each mode of a circular microstrip antenna there is an associated radius which is dependent on the zeros of the derivative of the Bessel function. Bessel functions in this analysis are analogous to sine and cosine functions in rectangular coordinates. E_0 is the value of the electric field at the edge of the patch across the gap.

Table 3-1 First four Bessel function zeros used with equation (3.4).

A_{nm}	TM_{nm}
1.84118	1,1
3.05424	2,1
3.83171	0,2
4.20119	3,1

The resonant frequency, f_{nm}, for each TM mode of a circular microstrip antenna is given by

$$f_{nm} = \frac{A_{nm} \cdot c}{2\pi a_{eff}\sqrt{\varepsilon_r}} \tag{3.4}$$

where A_{nm} is the mth zero of the derivative of the Bessel function of order n. The constant c is the speed of light in free space and a_{eff} is the effective radius of the patch. A list of the first four Bessel function zeros used with equation (3.4) are presented in Table 3-1. (In the case of a rectangular microstrip antenna, the modes are designated by TM_{mn}, where m is related to x and n is related to y. The modes for a circular microstrip antenna were introduced as TM_{nm}, where n is related to ϕ and m is related to r (often designated ρ). The reversal of indices can be a source of confusion.)

a_{eff} is the effective radius of the circular patch, which is given by

$$a_{eff} = a \cdot \left[1 + \frac{2h}{\pi a \varepsilon_r}\left(\ln\left\{\frac{\pi a}{2h}\right\} + 1.7726\right)\right]^{1/2} \tag{3.5}$$

$$a/h >> 1$$

where a is the physical radius of the antenna.

Equation (3.4) and equation (3.5) can be combined to produce:

$$a = \frac{A_{nm} \cdot c}{2\pi\sqrt{\varepsilon_r}}\left[1 + \frac{2h}{\pi a \varepsilon_r}\left(\ln\left\{\frac{\pi a}{2 f_{nm} h}\right\} + 1.7726\right)\right]^{-1/2} \tag{3.6}$$

The form of equation (3.6) is

$$a = f(a) \tag{3.7}$$

which can be solved using fixed point iteration (Appendix B, Section B.3) to compute a design radius given a desired value of A_{nm} from Table 3-1, which determines the mode TM_{nm}, and given the desired resonant frequency f_{nm} at which the antenna is to operate.[3]

An initial approximation for the radius a_0 to begin the iteration is

$$a_0 = \frac{A_{nm} \cdot c}{2\pi f_{nm}\sqrt{\varepsilon_r}} \tag{3.8}$$

The initial value a_0 is placed into the right-hand side of equation (3.6) to produce a value for a. This value is designated a_1, then is placed into the right-hand side to produce a second, more refined value for a designated a_2, and so on. Experience indicates that no more than five iterations are required to produce a stable solution.

The lowest order mode, TM_{11}, is the bipolar mode, which is analogous to the lowest order mode of a rectangular microstrip antenna. In Figure 3-2 we can see the electric field concentrated at each end of the antenna for the n = 1 mode with a sign reversal. The mode number n corresponds to the number of sign reversals in π radians of ϕ.

The next resonant mode is the TM_{21} mode, which is called the quadrapolar mode. Figure 3-2 shows the electric field distribution for the $n = 2$ mode. Note the four concentrations of electric field with alternating signs. This mode is the first of a family of modes that may be used to create a circularly polarized monopole-type pattern.

The third mode is the TM_{02} unipolar mode. In this situation, the mode index n is zero, which implies that no sign reversals occur because the cosine in equation (3.1) becomes unity for all values of ϕ, and it therefore is independent of the angle ϕ. Figure 3-2 shows the $n = 0$ mode and illustrates the uniform electric field around the edge of the circular antenna. This mode radiates a monopole-type pattern. Following the introduction of the mathematical

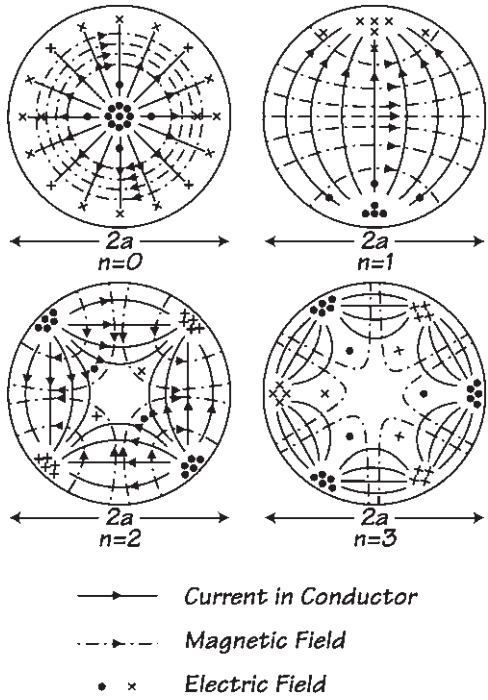

Figure 3-2 Electric and magnetic field patterns of a circular microstrip antenna at resonance.

analysis equations for directivity, driving point impedance, and efficiency, we will examine these modes in more detail.

3.2 Directivity

A very useful formulation for the directivity of the fundamental mode of a circular microstrip antenna was presented by Derneryd.[4] The radiation conductance of a circular microstrip antenna is given by

$$G_{rad} = \varepsilon_{n0} \frac{(k_0 a)^2}{480} \int_0^{\frac{\pi}{2}} [B_M^2(k_0 a \sin\theta) + B_P^2(k_0 a \sin\theta)\cos^2\theta] \sin\theta d\theta \qquad (3.9)$$

where

$$\varepsilon_{n0} = \begin{cases} 2 \ (n = 0) \\ 1 \ (n \neq 0) \end{cases}$$

and

$$B_P(X) = J_{n-1}(X) + J_{n+1}(X)$$

$$B_M(X) = J_{n-1}(X) - J_{n+1}(X)$$

The directivity of a circular patch for the $n = 1$ mode is expressed as

$$D = \frac{(k_0 a)^2}{120 G_{rad}} \tag{3.10}$$

The losses associated with the dielectric may be expressed as

$$G_{\varepsilon_r} = \frac{\varepsilon_{n0} \tan \delta}{4 \mu_0 h f_{mn}} [(ka)^2 - n^2] \tag{3.11}$$

The ohmic loss associated with the conductors is

$$G_{cu} = \frac{\varepsilon_{n0} \cdot \pi (\pi f_{mn} \mu_0)^{(-3/2)}}{4 h^2 \sqrt{\sigma}} [(ka)^2 - n^2] \tag{3.12}$$

The total conductance is

$$G = G_{rad} + G_{\varepsilon_r} + G_{cu} \tag{3.13}$$

3.3 Input Resistance and Impedance Bandwidth

The input resistance at resonance as a function of radius r is

$$Z_{in}(r) = \frac{1}{G} \frac{J_n^2(kr)}{J_n^2(ka)} \tag{3.14}$$

The cavity Q's, which allow us to compute the impedance bandwidth of a circular microstrip antenna, may be defined as the following:
The radiation Q is

$$Q_R = \frac{240[(ka)^2 - n^2]}{h\mu f_r (k_0 a)^2 I_1} \tag{3.15}$$

where

$$I_1 = \int_0^{\pi} [\{J_{n+1}(k_0 a \sin\theta) - J_{n-1}(k_0 a \sin\theta)\}^2 + \cos^2\theta \{J_{n+1}(k_0 a \sin\theta) - J_{n-1}(k_0 a \sin\theta)\}^2] \sin\theta d\theta \tag{3.16}$$

The dielectric Q is

$$Q_D = \frac{1}{\tan\delta} \tag{3.17}$$

The conductor Q is

$$Q_C = h\sqrt{\mu_0 \pi f_r \sigma_c} \tag{3.18}$$

As related previously:

$$\frac{1}{Q_T} = \frac{1}{Q_R} + \frac{1}{Q_D} + \frac{1}{Q_C}$$

The impedance bandwidth [S:1 voltage standing wave ratio (VSWR)] of a circular microstrip antenna is given by

$$BW = \frac{100(S-1)}{Q_T \sqrt{S}}\% \tag{3.19}$$

3.3.1 Gain, Radiation Pattern, and Efficiency

The antenna efficiency is

$$e = \frac{Q_C Q_D}{Q_C Q_D + Q_C Q_R + Q_D Q_R} \tag{3.20}$$

The radiation patterns may be calculated using

$$E_\theta = j^n \frac{Vak_0}{2} \frac{e^{-jk_0 r}}{r} \cos n\phi [J_{n+1}(k_0 a \sin\theta) - J_{n-1}(k_0 a \sin\theta)] \tag{3.21}$$

$$E_\phi = j^n \frac{Vak_0}{2} \frac{e^{-jk_0 r}}{r} \cos\theta \sin n\phi [J_{n+1}(k_0 a \sin\theta) + J_{n-1}(k_0 a \sin\theta)] \tag{3.22}$$

where V is the edge voltage at $\phi = 0$:

$$V = hE_0 J_n(ka) \tag{3.23}$$

when $n = 1$ [equation (3.10)] may be used to compute the antenna directivity. One must numerically integrate equation (3.21) and equation (3.22) to obtain directivity estimates of a circular patch when $n \neq 1$. The efficiency obtained from equation (3.20) allows one to compute the gain of a circular microstrip antenna.

3.4 Circular Microstrip Antenna Radiation Modes

3.4.1 The TM_{11} Bipolar Mode

The TM_{11} mode of a circular microstrip antenna is analogous to the lowest order mode of a rectangular patch antenna. This can be seen in Figure 3-2 for the $n = 1$ mode. This mode is essentially similar in design utility to a rectangular microstrip antenna driven in the TM_{10} mode. The impedance bandwidth is slightly smaller for a circular patch than its rectangular counterpart. The center of a circular patch driven in the TM_{11} mode may be shorted if a direct current (DC) short is required.

We will use a circular microstrip antenna with a radius of 21.21 mm on a dielectric substrate that is 1.524 mm thick and has a relative dielectric constant of $\varepsilon_r = 2.6$ and $\tan\delta = 0.0025$ to illustrate the properties of the TM_{11} mode. A finite difference time domain (FDTD) analysis of this antenna placed on a circular groundplane that has a 33.43 mm radius produces a resonant frequency of 2.435 GHz. Equation (3.4) predicts the resonant frequency to be 2.467 GHz

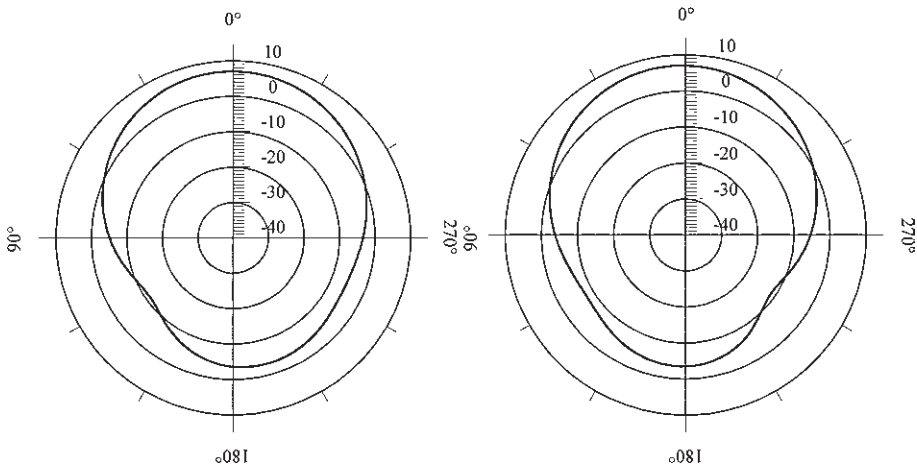

Figure 3-3 E-plane and H-plane patterns of a circular microstrip antenna driven in the TM_{11} mode.

for the TM_{11} mode. The antenna is fed 7 mm from the center of the antenna at $\phi = 0$. Figure 3-3 shows the E-plane and H-plane radiation patterns. The directivity of the antenna is computed to be 7.12 dB by FDTD analysis. Using equation (3.20), the antenna efficiency is computed to be 78.37%, which reduces the directivity peak by 1.06 dB for a gain of 6.06 dBi. As is the case with the rectangular patch, the pattern directivity of a TM_{11} circular patch antenna decreases as the relative dielectric constant of the substrate increases.

The TM_{11} bipolar mode has a virtual short at a plane along its center in the same way a rectangular microstrip patch has one. This allows one to place a shorting plane in the center of the circular patch antenna and create a half-patch circular antenna.[5] This antenna is analogous to the quarter-wave patch antenna of Section 2.4 in Chapter 2.

3.4.2 TM_{11} Bipolar Mode Circular Polarized Antenna Design

Lo and Richards developed a perturbation relationship to design circularly polarized rectangular and circular microstrip antennas using the TM_{11} mode.[6] They extended their work on rectangular microstrip antennas and demonstrated that a circular microstrip antenna may be stretched into an ellipse,

which will produce circular polarization from the superposition of the radiation of a pair of orthogonal modes when it is fed at $\phi = \pm 45^{\circ}$. The ratio of the semimajor to semiminor axes that will produce circular polarization is given by equation (3.24). As with the design of a circularly polarized rectangular microstrip antenna, the Q of the unperturbed circular patch is first obtained to compute the a/b ratio of a patch which will produce circular polarization.

$$\frac{a}{b} = 1 + \frac{1.0887}{Q} \tag{3.24}$$

The value of antenna Q can be computed using the cavity model equation (3.15), equation (3.17), and equation (3.18) with equation (3.25).

$$\frac{1}{Q} = \frac{1}{Q_R} + \frac{1}{Q_D} + \frac{1}{Q_C} \tag{3.25}$$

One can also measure the Q of the antenna experimentally, or use results from a full-wave analysis such as FDTD with equation (3.26) to estimate Q:[7]

$$Q \approx \frac{f_0}{\Delta f} = \frac{(\text{resonance frequency})}{(\text{bandwidth})3\text{dB}} \tag{3.26}$$

where

f_0 is the resonant frequency of the patch antenna, and

Δf is the bandwidth between 3 dB return loss points.

The antenna must have a single apparent resonance with reasonable symmetry for this equation to apply.

If the radius of the unperturbed circular patch which operates at the desired design frequency f_0 is designated as $\acute{a}$, the semimajor axis a and semiminor axis b of the ellipse which produce circular polarization (Figure 3-4) may be written as

$$a = \acute{a} + \Delta_L \tag{3.27}$$

$$b = \acute{a} - \Delta_L \tag{3.28}$$

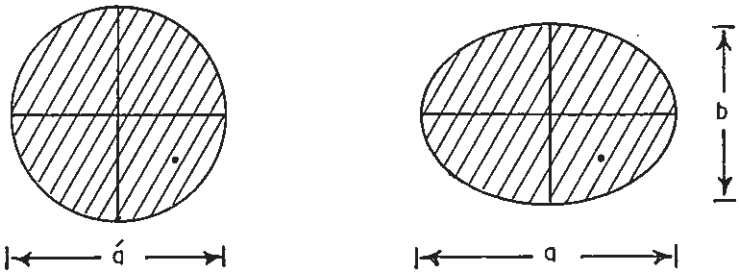

Figure 3-4 Circular microstrip antenna and the antenna perturbed into an ellipse to produce circular polarization (heavy dot is RHCP feed).

Using equation (3.27) and equation (3.28) with equation (3.24), we can write

$$\Delta_L = \frac{\acute{a}}{\left(\frac{2Q}{1.0887}\right)+1} \tag{3.29}$$

The FDTD analysis of the circular patch example produced a negative return loss plot from which we use equation (3.26) to obtain a value of 13.08 for Q. We can compute Δ_L as

$$\Delta_L = \frac{21.21\,\text{mm}}{\left(\frac{2\cdot(13.08)}{1.0887}+1\right)} = 0.84742\,\text{mm}$$

and from equation (3.27) and equation (3.28), because we used the radius we obtain the semimajor and semiminor axis values:

$$a/2 = 21.21\,\text{mm} + 0.84742\,\text{mm} = 22.057\,\text{mm}$$

$$b/2 = 21.21\,\text{mm} - 0.84742\,\text{mm} = 20.363\,\text{mm}$$

An FDTD analysis was undertaken to evaluate the circular polarization produced using equation (3.24). The patch feed point location is x = 15.0 mm

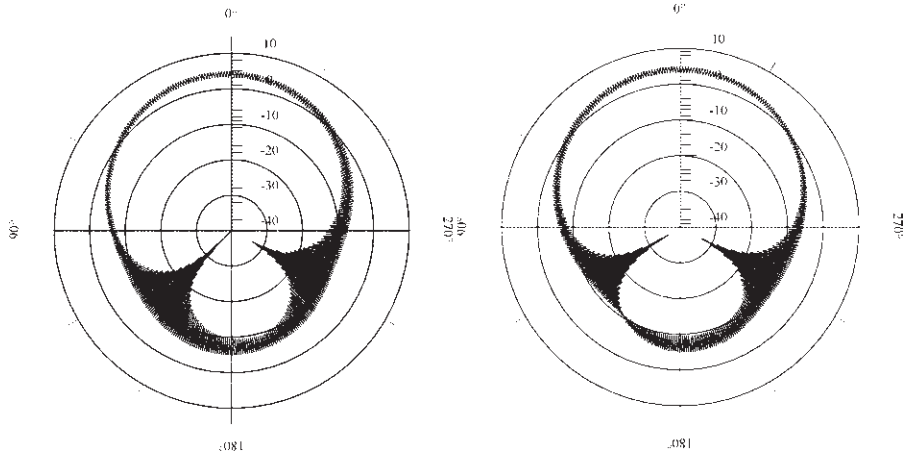

Figure 3-5 Rotating linear plots of an elliptical patch antenna which produces circular polarization designed using equation (3.24). On the left is a cut through the minor axis of the ellipse (x-z) and on the right is a cut through the major axis of the ellipse (y-z). The axial ratio at $\theta = 0$ is 2 dB.

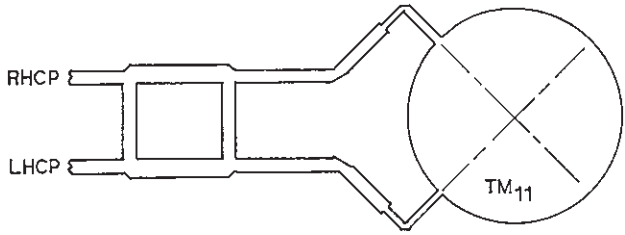

Figure 3-6 (a) Circular polarization using a TM_{11} mode circular patch may be synthesized using a 90° branchline hybrid feeding the patch edges at a spatial angle of 90°.

and $y = -15.0$ mm with the ellipse centered in the x-y plane, with a circular groundplane with a 33.43 mm radius.

Figure 3-5 provides synthesized rotating linear principle plane patterns from an FDTD analysis driven with a sinusoidal source with a square coaxial probe at 2.45 GHz.[8] The performance of the antenna is very good, and in a practical design one could further optimize the antenna experimentally.

A branchline hybrid is an alternative method one may use to generate circular polarization from a circular patch. Figure 3-6 shows a TM_{11} mode

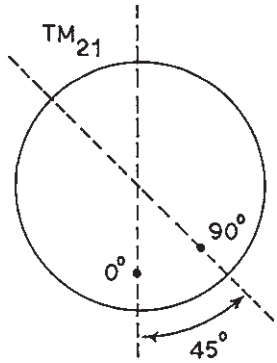

Figure 3-7 A TM_{21} mode circular microstrip antenna driven with two probe feeds (heavy dots) 90° out of phase with equal amplitudes spatially separated by 45°. This antenna produces a monopole pattern with circular polarization.

patch fed at orthogonal points to create circular polarization. This is analogous to the use of a branchline hybrid to generate circular polarization with a square patch. The right- and left-hand circular polarization (RHCP and LHCP) inputs are labeled. In practice, the unused port would be terminated with a load.

3.4.3 The TM_{21} Quadrapolar Mode

The TM_{21} mode has the next highest frequency of operation (after TM_{11}). This particular mode is useful in creating a monopole radiation pattern that has circular polarization, as described by Huang.[9] The electric field pattern for the $n = 2$ mode in Figure 3-2 shows the four electric field reversals which give this mode its name. One can produce circular polarization from this mode by providing two probe feeds to the patch; one is physically located at $\phi = 0^o$ and the other at $\phi = 45^o$. The feed at $\phi = 0^o$ is fed with zero electrical phase. The feed at $\phi = 45^o$ is fed with a 90° electrical phase with an identical amplitude (Figure 3-7). This angular spacing produces two modes driven orthogonal to each other, as is their radiation. The 90° phase difference with identical amplitude using orthogonal modes is the usual manner of creating circular polarization. The combination of these feeds produces a resultant quadrapolar electric field, as seen in Figure 3-2, which rotates about the center of the patch antenna. This has been verified with FDTD simulation.

One may obtain better circular polarization (axial ratio) by feeding the antenna in four probe locations rather than two. These locations are diametrically across from the two original feed points. In the case of an even mode, $n = 2, 4, 6, \ldots$ (TM_{21}, TM_{41}, TM_{61}, . . .), the diametric feeds have the same phase as their original counterparts. The feeds have a phase arrangement around the patch counterclockwise of 0°, 90°, 0°, 90°. In the case of an odd mode, $n = 1, 3, 5, \ldots$ (TM_{11}, TM_{31}, TM_{51}, . . .) the diametric feeds have a phase arrangement around the patch counterclockwise starting at the top of the patch of 0°, 90°, 180°, 270°. These relationships are related in detail by Huang.[9]

As the resonant mode index n increases ($n > 1$) with $m = 1$, the peak directivity of the radiation pattern becomes more and more broadside. The pattern will also move further broadside with increasing relative dielectric constant. Huang has reported the pattern peak may be moved from broadside over a range of 35° to 74° by use of a combination of a chosen higher order mode and substrate relative dielectric constant adjustment.

In commercial applications, a complex feed structure with its required feed network may be untenable as a design. It is possible to drive a patch in the TM_{21} mode with a single feed which will produce circular polarization.[10] One may cut a pair of notches in a circular microstrip antenna driven in the TM_{21} mode in accordance with:

$$\left|\frac{\Delta S}{S}\right| = \frac{1}{2.5014 \cdot Q}$$

$$|\Delta S| = \frac{\pi a^2}{2.5014 \cdot Q} \tag{3.30}$$

We will use a patch of radius 20.26 mm as a design example. Each notch area is $\Delta S/2$ for each of the notches in Figure 3-8(a). The substrate thickness is 1.524 mm, $\varepsilon_r = 2.6$, $\tan\delta = 0.0025$, with a resonate frequency of 4.25 GHz computed using FDTD analysis. The feed point radius is 16.0 mm. Equation (3.4) predicts 4.278 GHz for the TM_{21} mode. FDTD was used to analyze a circular patch antenna with the previous parameters and produce a negative return loss plot. The Q was computed to be 22.83 from the negative return loss plot –3 dB points using (3.26). We then find $|\Delta S|$ using (3.30)

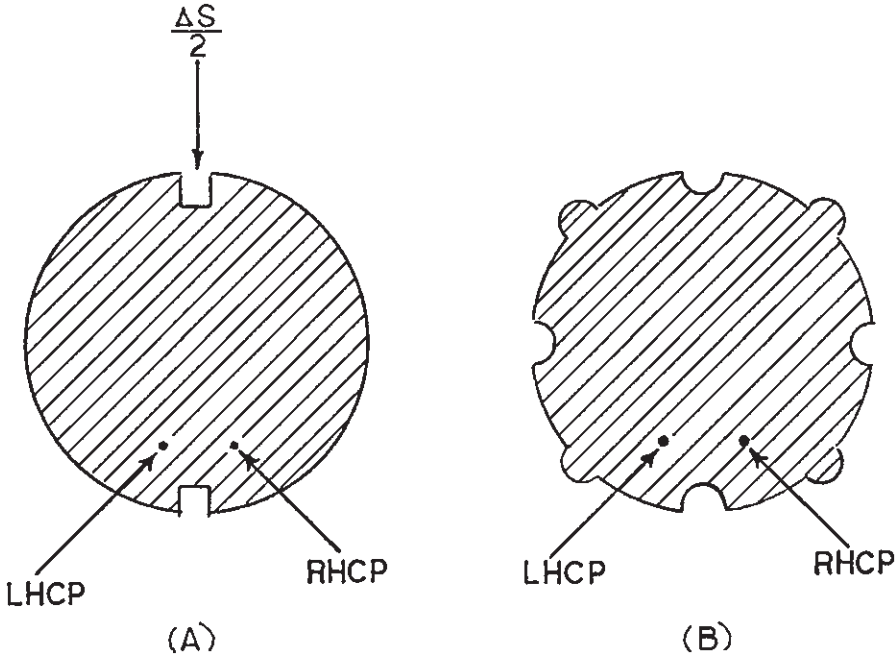

Figure 3-8 (a) A TM_{21} circular microstrip antenna is modified with a pair of slots using equation (3.30) with a single probe feed (heavy dots) at $\phi = \pm 22.5^{o}$. This antenna produces a monopole pattern with circular polarization. (b) A TM_{21} circular microstrip antenna with indents and tabs spaced 45° apart. The feed is at $\phi = \pm 22.5^{o}$, which also produces a monopole pattern with circular polarization.

$$|\Delta S| = \frac{\pi(20.26\,\text{mm})}{2.5014 \cdot 22.83} = 0.022578\,\text{mm}^2$$

which is a square with sides of length $L = 4.75$ mm. Each notch in this example is $L/2 \times L$, which corresponds to $|\Delta S|/2$ for each notch in Figure 3.8(a). The radiation patterns computed with an FDTD simulation of this design is presented in Figure 3-9. The patterns are synthesized rotating linear plots. Figure 3.8(b) shows an alternative method using tabs and indents which perturb the patch to produce circular polarization from the TM_{21} mode.

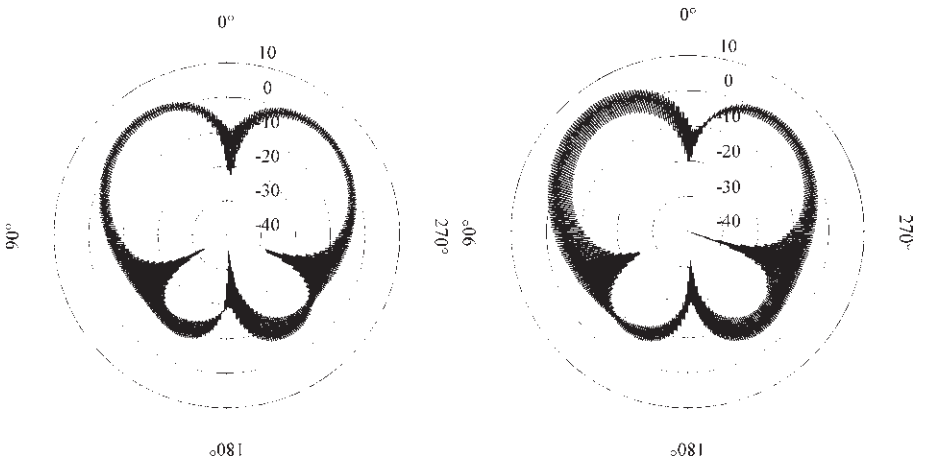

Figure 3-9 Synthesized rotating linear radiation patterns of TM_{21} circular microstrip antenna modified with a pair of slots using equation (3.30) with a single probe feed.

3.4.4 The TM_{02} Unipolar Mode

The next mode in order of increasing frequency is the TM_{02} mode. This mode has the useful characteristic that the electric field around the circular microstrip antenna is uniform. This is seen in Figure 3-2 for the $n = 0$ mode, which we note has no electric field reversal [$(\cos(0\phi) = 1$ for all ϕ in equation (3.21)]. The TM_{02} mode has the useful property that it produces a vertically polarized ($\vec{E}_\theta$) monopole-type pattern. This can be very useful for replacing a quarter-wave monopole antenna, which can be easily damaged in a hostile mechanical environment, with a conformal version.

We will use a patch of radius 21.21 mm as an example. The substrate thickness is 1.524 mm, $\varepsilon_r = 2.6$, $\tan\delta = 0.0025$, on a circular groundplane of radius 33.43 mm with a resonate frequency of 5.02 GHz computed using FDTD analysis. The patch is probe fed with a square coaxial transmission line. Equation (3.4) predicts 5.13 GHz for the TM_{02} mode. The feed point radius is 7.52 mm. The maximum directivity computed by FDTD analysis is 5.30 dB. The efficiency computed using equation (3.20) is 87.88%, which is a loss of 0.561 dB, for a predicted antenna gain of 4.74 dBi. The computed radiation patterns are presented in Figure 3-10.

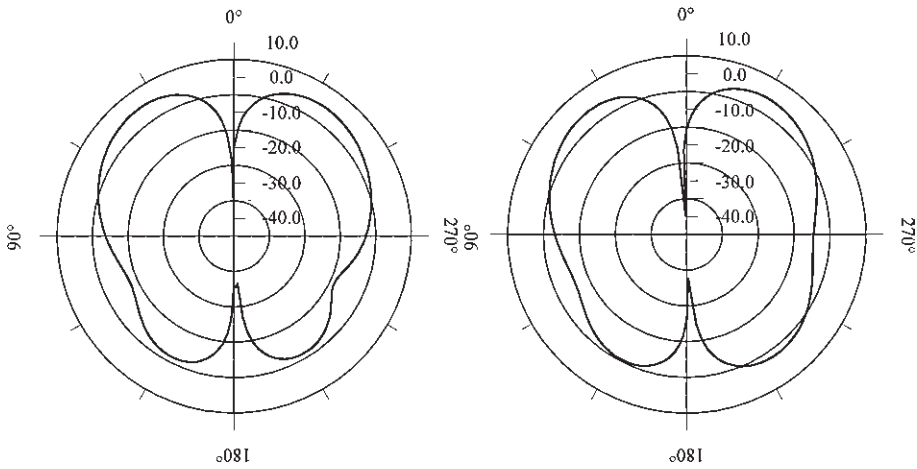

Figure 3-10 A TM_{02} circular microstrip antenna pattern as computed by FDTD analysis. The pattern on the left is a cut in a plane perpendicular to the plane which contains the probe feed. On the right is a cut through the plane of the probe. The maximum pattern directivity is 5.30 dB.

A thermal plot of the total electric field just above the circular patch element is presented in Figure 3-11. We see the electric field is uniform around the edge of the element, which is consistent with Figure 3-2 for $n = 0$. The small square is the probe feed.

The description of driving point impedance is given in equation (3.14). The driving point impedance for the TM_{02} mode passes through a short at a radial position where the Bessel function $J_0(kr)$ passes through zero and then increases to the edge resistance value at $r = a$. Figure 3-12 presents a thermal plot of the total electric field just below the circular patch element. We see a ring of zero field corresponding to the short in the driving point impedance predicted by equation (3.14).

3.5 Microstrip Antenna Cross-Polarization

The cross-polarization performance of microstrip antennas is considered to be rather poor. The permittivity and thickness of the substrate used to create a microstrip antenna determines its cross-polarization performance. It has been

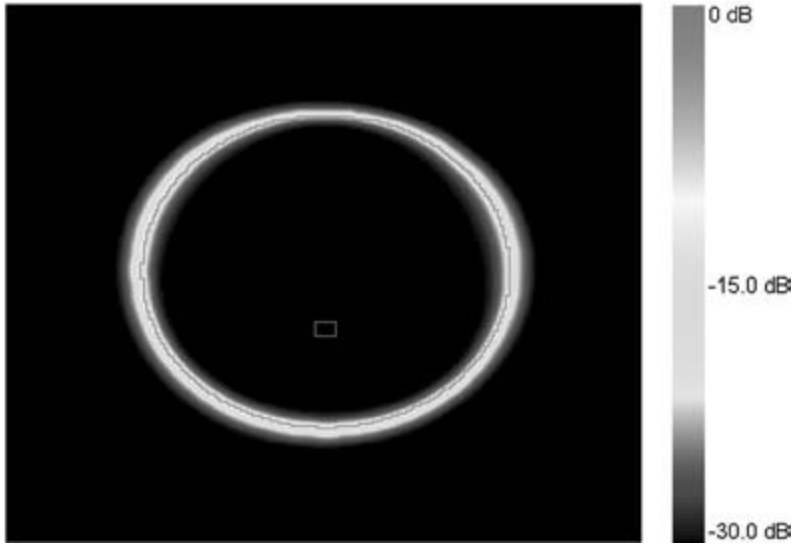

Figure 3-11 A TM_{02} circular microstrip antenna thermal plot of the total electric field just above the element (computed with FDTD analysis). One can see the uniform electric field distribution which is consistent with the $n = 0$ mode of Figure 3-2.

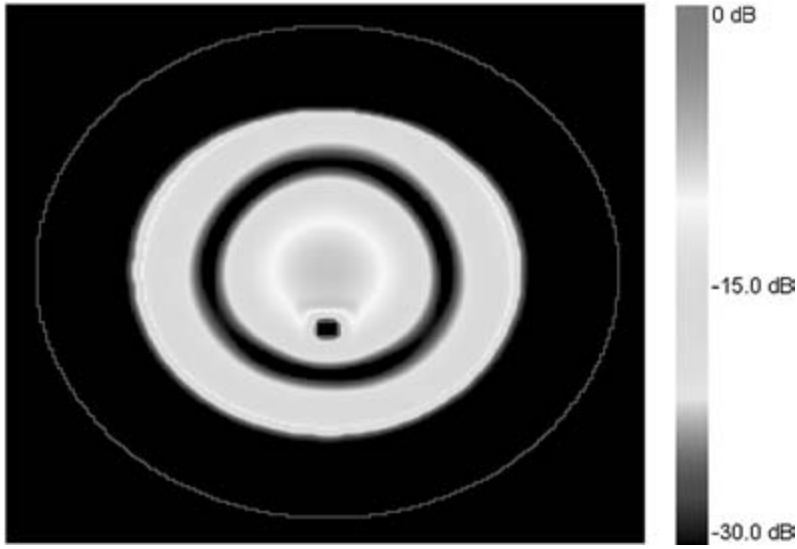

Figure 3-12 A TM_{02} circular microstrip antenna thermal plot of the total electric field distribution just below the element (computed by FDTD analysis). The ring of zero electric field is consistent with the electric field as predicted by Derneryd [2].

related previously that the gain and impedance bandwidth of a microstrip antenna can be increased by decreasing the permittivity of the substrate. When a low dielectric constant is used to design a microstrip antenna element, it also increases the radiated cross-polarization level.[11] A higher permittivity substrate will produce better cross-polarization performance, but at the expense of impedance bandwidth. The cross-polarization performance of a linearly polarized patch is dependent on substrate thickness, feed point location, and substrate permittivity.

The origin of the radiated cross-polarization is associated with the generation of higher order modes on the patch.[12] When a circular microstrip patch is driven in the TM_{11} with a single driving point, the next highest frequency TM_{21} mode is consistent with the measured cross-polarization patterns.[13] Table 3-1 shows the modes occur in order of increasing frequency as TM_{11}, TM_{21}, TM_{01}, etc. Garcia-Garcia states that when an antenna is driven in the fundamental mode TM_{11}, this mode is mostly perturbed by the TM_{21} mode. When a patch is designed to be driven in the TM_{21} mode, the radiation purity is disturbed by the dominant TM_{11} and next higher TM_{01} mode.

Figure 3-13 presents sketches of the current of (a) a TM_{21} mode circular patch antenna and (b) a TM_{11} mode circular patch antenna. When a patch is driven in the fundamental TM_{11} mode, and the majority of the cross-polarization radiation is due to TM_{21}, we note that in the x-z plane (H-plane), the copolarized radiation $\vec{E}_y$ dominates the pattern. The cross-polarized pattern in the H-plane $\vec{E}_z$ has two lobes approximately –15 dB below the copolarized pattern maximum. The cross-polarization pattern is consistent with the pattern shape expected from the TM_{21} mode. In the E-plane, the radiated field of the driven TM_{11} and the TM_{21} mode are in parallel, which means whatever cross-polarization exists is of uncertain origin. It could be from an imperfect generation of the TM_{21} mode, other modes, or due to a different mechanism.

An illustrative example was analyzed with the FDTD method. The substrate is vacuum $\varepsilon_r = 1$ with a thickness of $h = 1.524$ mm (0.060 inches). The patch has a radius of $a = 14.71$ mm. The probe feed is 5.5 mm below the center of the patch, which has a resonant frequency of 5.35 GHz. The FDTD analysis results are presented in Figure 3-14(a) and (b). We note the H-plane pattern has the expected TM_{21} mode pattern shape. The E-plane pattern has a small

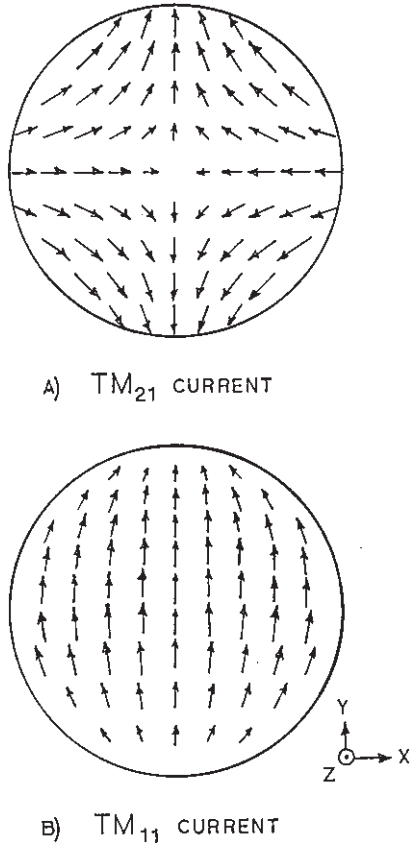

Figure 3-13 (a) Sketch of the theoretical current distribution of the TM_{21} mode of a circular patch antenna. (b) Sketch of the theoretical current distribution of the TM_{11} mode of a circular patch antenna.

amount of cross-polarized radiation which has a peak magnitude that is approximately –30 dB below the copolarized maximum. The E-plane cross-polarized pattern has a shape consistent with the TM_{11} mode. The geometry of a circular patch does not enforce a single direction for the TM_{11} mode as a square patch does for the TM_{10} mode. It is very possible the computed cross-polarization is from the generation of a TM_{11} mode with very small amplitude.

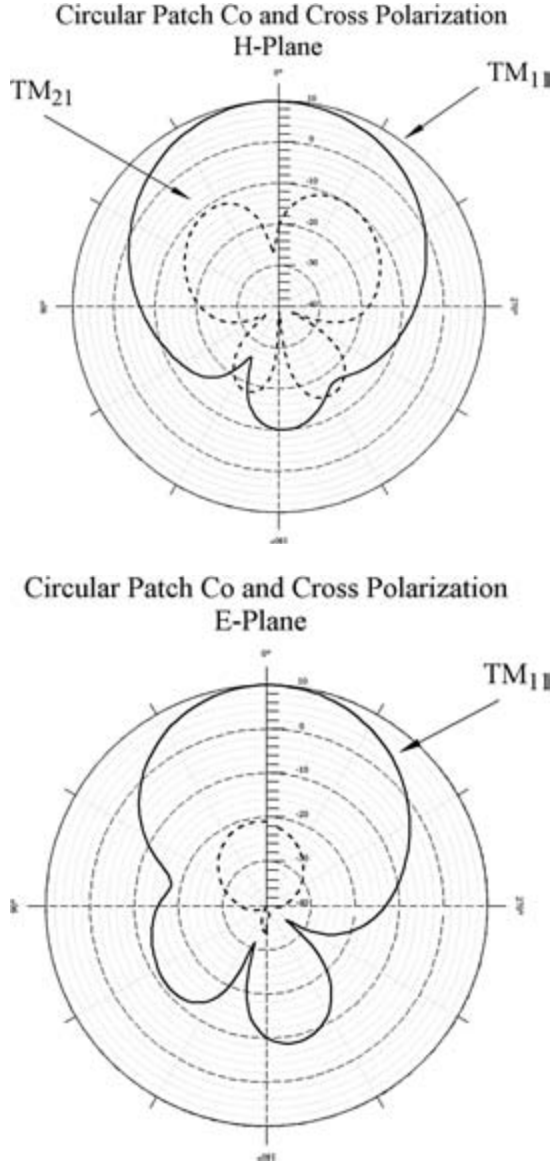

Figure 3-14 Circular patch co- and cross-polarization of the (a) H-plane and (b) E-plane.

3.6 Annular Microstrip Antenna

When a concentric circle of conductor is removed from the interior of a circular microstrip antenna it forms an annulus. The ring-shaped microstrip conductor which is formed has its geometry defined in Figure 3-15. We assume the

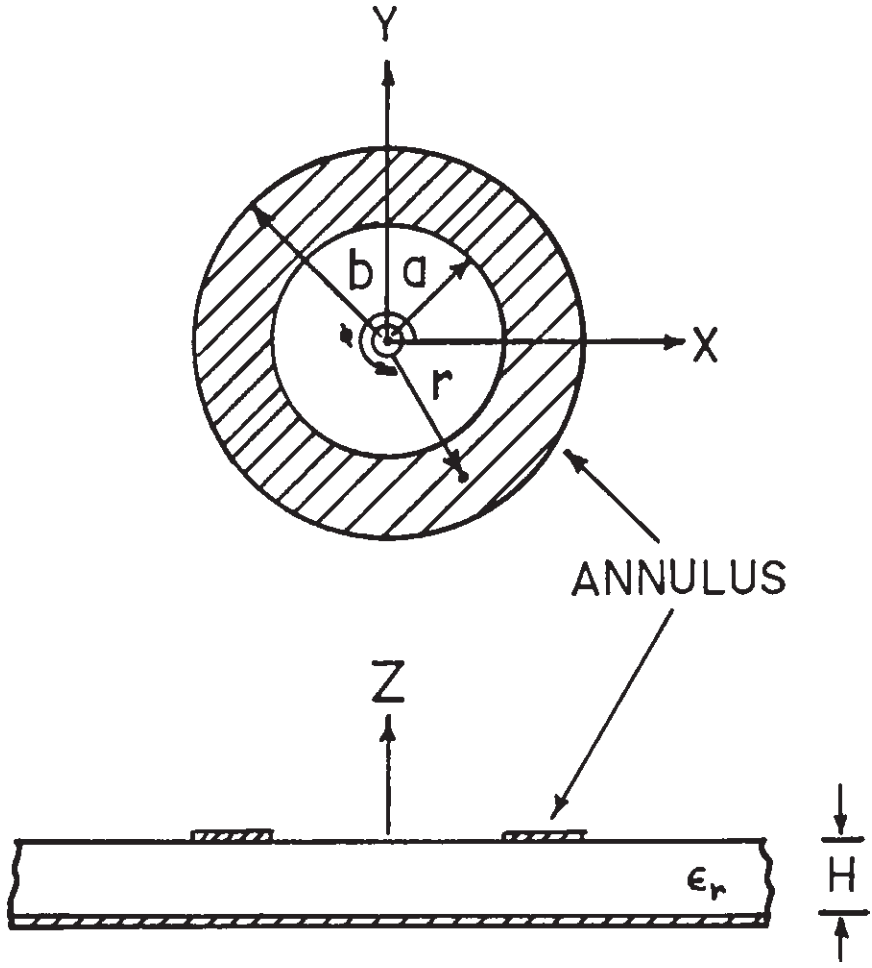

Figure 3-15 Annular microstrip antenna geometry. The outer radius is b, the inner radius is a, with a probe feed at radius r at angle ϕ.

thickness of the substrate is small compared with a wavelength $H \ll \lambda_0$, which implies no variation of the electric field in the z direction. The cavity model with magnetic walls on the edges of the annulus may be used to obtain solutions for the fields beneath the annulus. The fields are assumed to be TM_{nm} in cylindrical coordinates:[14,15]

$$E_z = E_0[J_n(kr)\acute{Y}_n(ka) - \acute{J}_n(ka)Y_n(kr)]\cos n\phi \tag{3.31}$$

$$H_r = \frac{j\omega\varepsilon}{k^2 r}\frac{\partial E_z}{\partial \phi} \tag{3.32}$$

$$H_\phi = \frac{-j\omega\varepsilon}{k^2}\frac{\partial E_z}{\partial r} \tag{3.33}$$

The Bessel functions (J_n and Y_n) are of the first and second kind of order n. The prime signs signify the first derivative of the Bessel functions. The wave number k is in the dielectric substrate $k = \dfrac{2\pi\sqrt{\varepsilon_r}}{\lambda_0}$, where ε is the substrate permittivity and λ_0 is the wavelength in free space. The mode integer n is associated with the variation along ϕ, and mode integer m is associated with the variation of fields along the radial direction.

The surface currents on the annulus may be computed using $K_\phi = -H_r$ and $K_r = H_\phi$. The radial component of the surface current will disappear at an edge:

$$K_r(r = b) = H_\phi(r = b) = 0 \tag{3.34}$$

It follows from equation (3.31), equation (3.33), and equation (3.34) that the wave number must obey:

$$[\acute{J}_n(kb)\acute{Y}_n(ka) - \acute{J}_n(ka)\acute{Y}_n(kb)] = 0 \tag{3.35}$$

Equation (3.35) may be solved to obtain the modes associated with a given inner radius a and outer radius b. $\acute{J}_n$ and $\acute{Y}_n$ are the derivatives of the

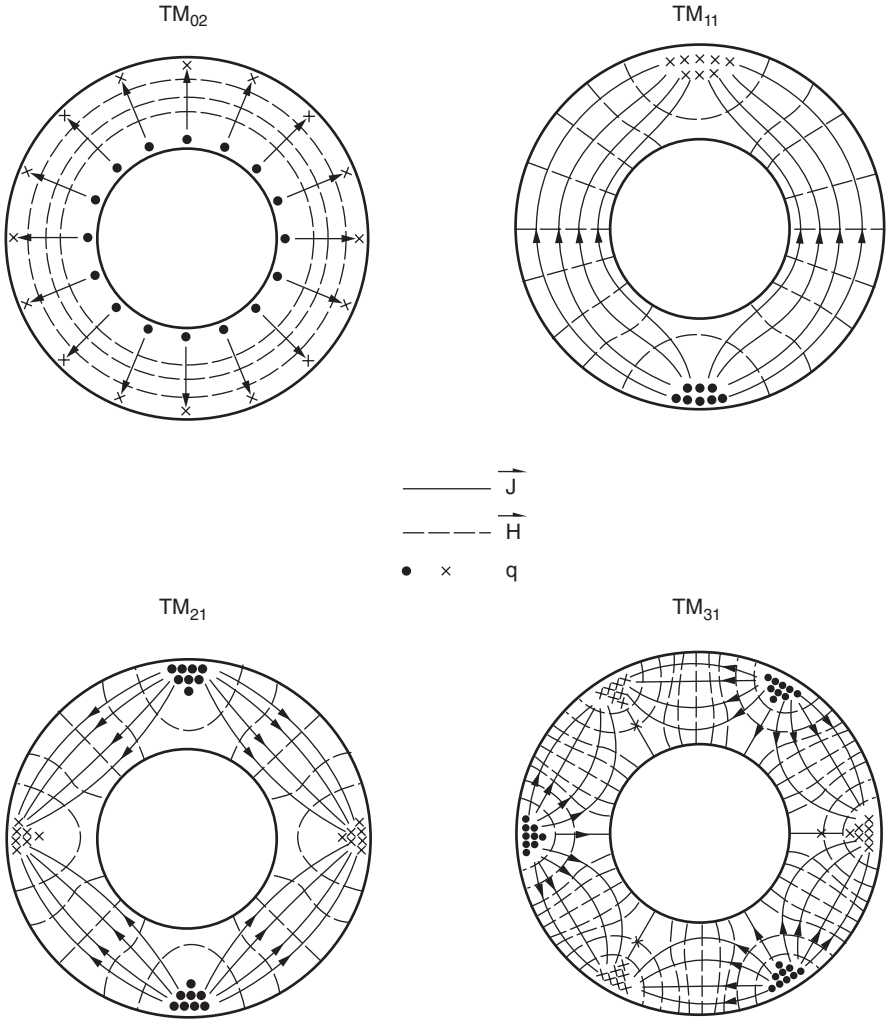

Figure 3-16 (a) Sketch of the theoretical current distribution of the TM_{21} mode of a circular patch antenna. (b) Sketch of the theoretical current distribution of the TM_{11} mode of a circular patch antenna. (From [14], copyright 1973, IEEE. Reprinted with permission.)

Bessel functions with respect to kr. Approximate values for k may be obtained with

$$k \approx \frac{2n}{a+b} \tag{3.36}$$

where $(b - a)/(b + a) \leq 0.35$ and $n \leq 5$.

The resonant frequency of the annular microstrip antenna may be computed with

$$f_r = \frac{ck}{2\pi\sqrt{\varepsilon_e}} \tag{3.37}$$

The effective dielectric constant ε_e is for a microstrip transmission line of conductor width $W = b - a$ (Appendix C). The resonant frequencies predicted by equation (3.37) are within 3% of experimental values.

The first few modes of an annular microstrip antenna are presented in Figure 3-16. We note they are very similar to the modes of a circular microstrip, as shown in Figure 3-2. The patterns produced by the modes are also very similar to those produced by a circular microstrip antenna. Slot insets may be used to create circular polarization in the same manner as in Section 3.4.2.[16]

While the rectangular patch antenna is perhaps the most commonly implemented microstrip antenna, the circular patch antenna can offer pattern options that are generally much more flexible in a single element. We have seen that it is possible to have a broadside radiation pattern with linear or circular polarization, a monopole-like pattern with linear polarization, or a monopole-like pattern which is circularly polarized.

References

[1] Kernweis, N. P., and McIlvenna, J. F., "Liquid crystal diagnostic techniques an antenna design aid," *Microwave Journal*, October 1977, Vol. 20, pp. 47–58.

[2] Derneryd, A. G., "Analysis of the microstrip disk antenna element," *IEEE Transactions on Antennas and Propagation*, September 1979, Vol. AP-27, No. 5, pp. 660–664.

[3] Burden, R. L., Faires, J. D., and Reynolds, A. C., *Numerical Analysis*, Boston: Prindle, Weber, and Schmidt, 1978, pp. 31–38.

[4] Derneryd, A. G., "Analysis of the microstrip disk antenna element," *IEEE Transactions on Antennas and Propagation*, September 1979, Vol. AP-27, No. 5, pp. 660–664.

[5] Hirasawa, K., and Haneishi, M., eds., *Analysis, Design, and Measurement of Small and Low-Profile Antennas*, London: Artech House, 1992, p. 69.

[6] Lo, Y. T., and Richards, W. F., "Perturbation approach to design of circularly polarized microstrip antennas," *Electronics Letters*, May 28, 1981, pp. 383–385.

[7] *Reference Data for Radio Engineers*, 6th ed., Indianapolis, IN: Howard W. Sams & Co., 1982, p. 9–7.

[8] Marino, R. A., and Hearst, W., "Computation and measurement of the polarization ellipse," *Microwave Journal*, November 1999, Vol. 42, pp. 132–140.

[9] Huang, J., "Circularly polarized conical patterns from circular microstrip antennas," *IEEE Transactions on Antennas and Propagation*, September 1984, Vol. AP-32, No. 9, pp. 991–994.

[10] Du, B., and Yung, E., "A single-feed TM_{21}-mode circular patch antenna with circular polarization," *Microwave Optics Technology Letters*, May 2002, Vol. 33, No. 3, pp. 154–156.

[11] Hanson, R. C., "Cross polarization of microstrip patch antennas," *IEEE Transactions on Antennas and Propagation*, June 1987, Vol. AP-35, No. 6, pp. 731–732.

[12] Lee, K. F., Luk, K. M., and Tam, P. Y., "Crosspolarization characteristics of circular patch antennas," *Electronics Letters*, March 1992, Vol. 28, No. 6, pp. 587–589.

[13] Garcia-Garcia, Q., "Radiated cross-polar levels and mutual coupling in patch radiators," *International Journal of RF and Microwave Computer-Aided Design*, December 2000, Vol. 10, No. 6, pp. 342–352.

[14] Wu, Y. S., and Rosenbaum, F. J., "Mode chart for microstrip ring resonators," *IEEE Transactions on Microwave Theory and Techniques*, July 1973, Vol. MTT-21, No. No. 7, pp. 487–489.

[15] Bahl, I. J., Stuchly, S. S., and Stuchly, M. A., "A new microstrip radiator for medical applications," *IEEE Transactions on Microwave Theory and Techniques*, December 1980, Vol. MTT-28, No. 12, pp. 1464–1468.

[16] Licul, S., Petros, A., and Zafar, I., "Reviewing SDARS antenna requirements," *Microwaves & RF* September 2003, Vol. 43, pp. 51–62.

Chapter 4

Broadband Microstrip Antennas

4.1 Broadband Microstrip Antennas

Microstrip antennas are inherently narrowband. The typical bandwidth of a microstrip antenna is around 4% to 7%. A considerable number of experimental approaches have been undertaken to develop microstrip antennas that have a broader impedance bandwidth than a single microstrip element achieves without external matching.

The methods employed to increase impedance bandwidth are essentially variations of three approaches: 1) Increasing the antenna volume. This is accomplished by geometry changes that increase the volume under the patch (e.g., increasing the thickness h), decreasing the substrate dielectric constant, or adding additional coupled resonators. 2) The implementation of a matching network. 3) Perturbing the antenna geometry to create or relocate resonances using shorts and slots in the antenna. Kumar and Ray have compiled a considerable number of microstrip antenna design variations that utilize these approaches[1], as has Wong.[2]

One approach is the use of a groundplane slot, which is excited by a microstrip line below the groundplane, which in turn couples to a microstrip patch which is above the groundplane. This configuration can be adjusted to produce an elegant matching network, low dielectric constant substrate for the patch, and maximized substrate thickness which provides a broadband input impedance match and a large impedance bandwidth. One implementation of this type of antenna is called a strip slot foam inverted patch (SSFIP), developed by Zurcher and Gardiol in the mid-1990s. The design of these antennas is experimental in nature. The researchers state: “Since the various parts of the antenna interact, determining the best design is a long and tedious process, even when carried out systematically.” The parameters which may be used to

guide this type of design are found in the literature.[3–5] Some possible alternatives to SSFIP matching network/thick patch design are explored in this chapter.

4.2 Microstrip Antenna Broadbanding

The broadbanding of a microstrip antenna is often accomplished by increasing the thickness of a microstrip antenna. This broadbanding reaches a limit when the series inductance produced by higher order modes produces an unacceptable mismatch in the driving point impedance. One can also use a matching network to increase the impedance bandwidth of a microstrip antenna.

The normalized bandwidth of a microstrip antenna can be written as

$$BW = \frac{f_H - f_L}{f_R} \tag{4.1}$$

where f_H is the upper frequency where the impedance match is S:1 voltage standing wave ratio (VSWR) and f_L is the lower frequency where the impedance match is also S:1 VSWR. The VSWR is less than S:1 over $(f_H - f_L)$. f_R is the resonant frequency of the patch. Generally $S = 2$ for most practical applications.

At the resonant frequency of a patch, the driving point impedance is pure real. This resistance is designated as R_0. When the patch is connected to a transmission line of characteristic impedance Z_0, the impedance bandwidth is predicted using

$$BW = \frac{1}{Q}\sqrt{\frac{(TS-1)(S-T)}{S}} \tag{4.2}$$

where Q is the total Q of the patch antenna, S is the VSWR S:1 value, and $T = R_0/Z_0$. When a microstrip antenna is fed with a transmission line where $R_0 = Z_0$, the bandwidth equation reduces to the bandwidth equation for a linear patch antenna [equation (2.61)]:

$$BW_{Linear} = \frac{S-1}{Q_T\sqrt{S}} \quad (S{:}1 \text{ VSWR})$$

To maximize the impedance bandwidth for a given $S{:}1$ VSWR mismatch between the resonant resistance R_0 and the feeding transmission line characteristic impedance Z_0 we must satisfy this relationship:

$$T_{\text{opt}} = \frac{1}{2}\left(S + \frac{1}{S}\right) \tag{4.3}$$

For example, in the case of a 50 Ω coaxial transmission line probe feeding a rectangular microstrip patch antenna, we can compute the driving point impedance we must choose for a maximized 2:1 VSWR bandwidth. To obtain this value we compute the optimum T value:

$$T_{\text{opt}} = \frac{1}{2}\left(2 + \frac{1}{2}\right) = 1.25 = \frac{R_0}{Z_0} \tag{4.4}$$

which implies the resonant driving point impedance R_0 = 1.25, Z_0 = 62.5 Ω, or the driving point location should be chosen where 62.5 Ω exists. This value is near the approximate optimum value of 65 Ω reported by Milligan.[6]

When we use equation (4.4), we trade a perfect match at a single frequency for wider bandwidth at the expense of a larger mismatch. The equation describes an elementary form of a broadband matching network. The bandwidth obtained when T_{opt} is used may be related to the $S{:}1$ bandwidth by

$$BW_{T_{\text{opt}}} = \frac{1}{2Q}\frac{\sqrt{S^4-1}}{S} \tag{4.5}$$

For the case of 2:1 VSWR, we can take the ratio of equation (4.5) to equation (2.61) to obtain a bandwidth increase factor. The 2:1 VSWR bandwidth is computed to be 1.38 times larger than the bandwidth of a perfectly matched microstrip antenna. Experiment, FDTD, and cavity model data all indicate that in practice the best increase in bandwidth is about 1.1 times the original band-

width of the matched element. This bandwidth increase produced using simple impedance mismatch is often so small it is not of practical use.

If we allow the use of a perfect matching network, with an unrestricted extent, the maximum impedance bandwidth obtainable is

$$BW_{\max} = \frac{1}{Q}\frac{\pi}{\ln[(S+1)/(S-1)]} \tag{4.6}$$

This relationship allows us to compare the maximum bandwidth attainable using a broadband matching network with the normally obtained bandwidth of equation (2.61) by taking the ratio of equation (2.61) to equation (4.6) which produces a bandwidth increase factor F:

$$F = \frac{\pi\sqrt{S}}{(S-1)\ln[(S+1)/(S-1)]} \tag{4.7}$$

For the case of 2:1 VSWR, the bandwidth increase factor F is 4.044, or approximately four times the bandwidth of a single element without matching. This provides a fundamental limit against which we can compare designs.

4.2.1 Microstrip Antenna Matching with Capacitive Slot

Increasing the thickness of a microstrip antenna increases its impedance bandwidth. As the thickness increases, higher order modes produce an equivalent series inductance which mismatches a rectangular microstrip antenna. The straightforward solution to this problem is to introduce series capacitance to cancel the inductive reactance that appears at the driving point. A cost-effective method is to provide capacitance by modifying the patch geometry. Researchers have used a rectangular or circular slot surrounding the feed probe (Figure 4-1(a)) to provide the required series matching capacitance.[7,8] The values of the slot dimensions for the circular or rectangular slots which bound the probe feed are determined experimentally.

Another approach used to provide series capacitance is to place a narrow slot directly in front of the feed point and adjust its length until a match is provided (Figure 4-1(b)).

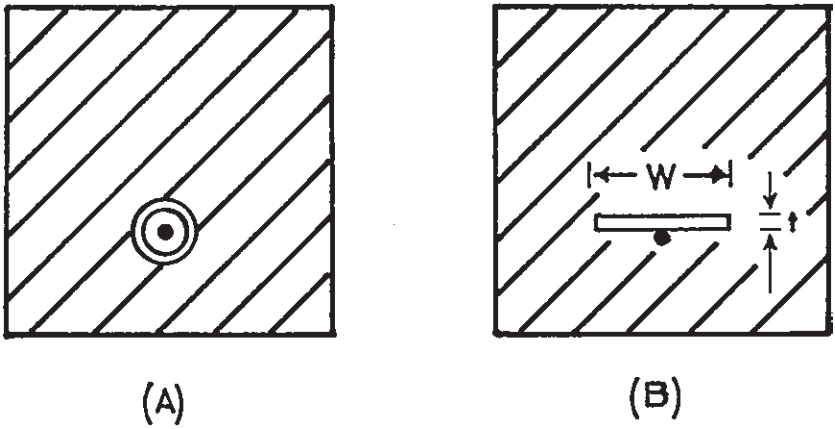

Figure 4-1 (a) Series matching capacitance provided using a circular slot. (b) Series matching capacitance created using a rectangular slot near the driving point.

As an example of the use of matching with a slot, we will use a rectangular microstrip antenna that has a substrate thickness of 6.096 mm, a relative dielectric constant of $\varepsilon_r = 2.6$, and a $\tan\delta = 0.0025$. The patch dimensions are $a = 38.0$ mm by $b = 34.72$ mm. The 50 Ω driving point location is 6.0 mm from the patch center along the centerline of the width. FDTD analysis computes a resonance at 2.31 GHz (maximum real impedance) with a driving point impedance of $46 + j35.35\ \Omega$. $h/\lambda_0 = 0.047$, which is electrically thick for a patch antenna. A narrow slot, $t = 1$ mm across and $W = 14$ mm in width, matches the antenna with a driving point impedance of $49.71 + j5.79\ \Omega$ at 2.31 GHz. The impedance with and without slot matching is plotted on a Smith chart in Figure 4-2. After matching, the antenna has a respectable 7% impedance bandwidth.

4.2.2 Microstrip Antenna Broadband Matching with Bandpass Filter

It must be noted up front, that generally, the design of a broadband impedance matching network is a very difficult network synthesis problem. The prototype element values used in this section for creating an impedance matching network using lumped elements are taken from previous work.[9] The synthesis presented works better for lower frequency microstrip antennas where lumped

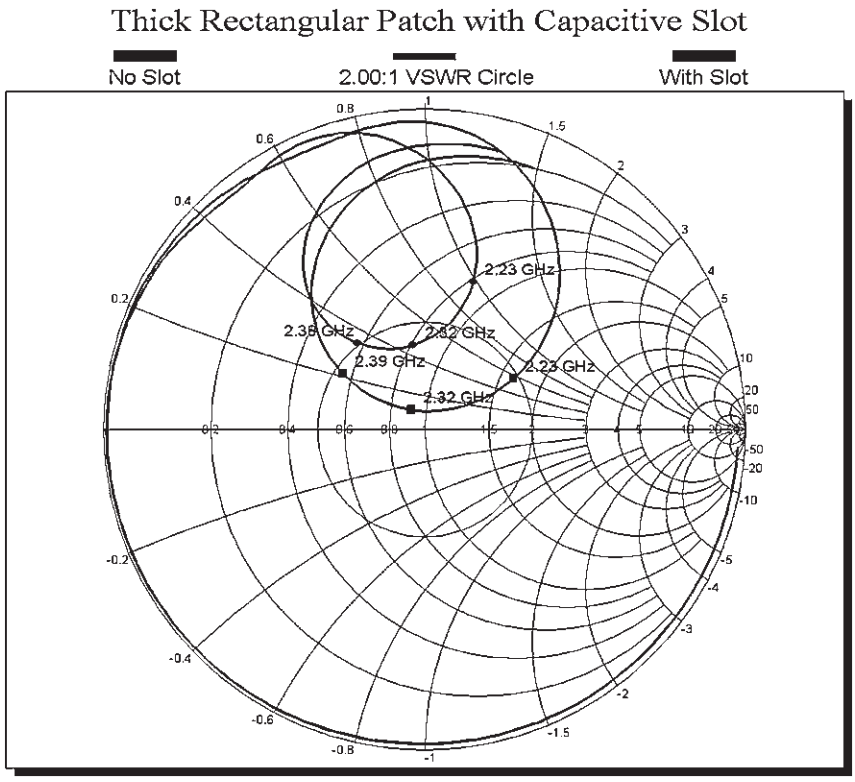

Figure 4-2 (a) Driving point impedance without (circles) and with (squares) a capacitive slot. The series capacitance provided by the rectangular slot cancels the inductive reactance of thick microstrip antennas.

elements may be incorporated with relative ease. It will be demonstrated that the realization of lumped element models using microwave transmission line structures is quite challenging, but not insurmountable.

A rectangular microstrip antenna fed to excite only one dominant mode (TM_{10} or TM_{01}) has a single resonance which may be modeled as a parallel RLC circuit. These values are designated R_a, L_a, and C_a in Figure 4-3. When the patch is probe fed and becomes electrically thick, a series inductor must also be taken into account, which is designated L_s. In some rare cases, feed geometries can produce a series capacitance C_s rather than L_s, but generally it is L_s that

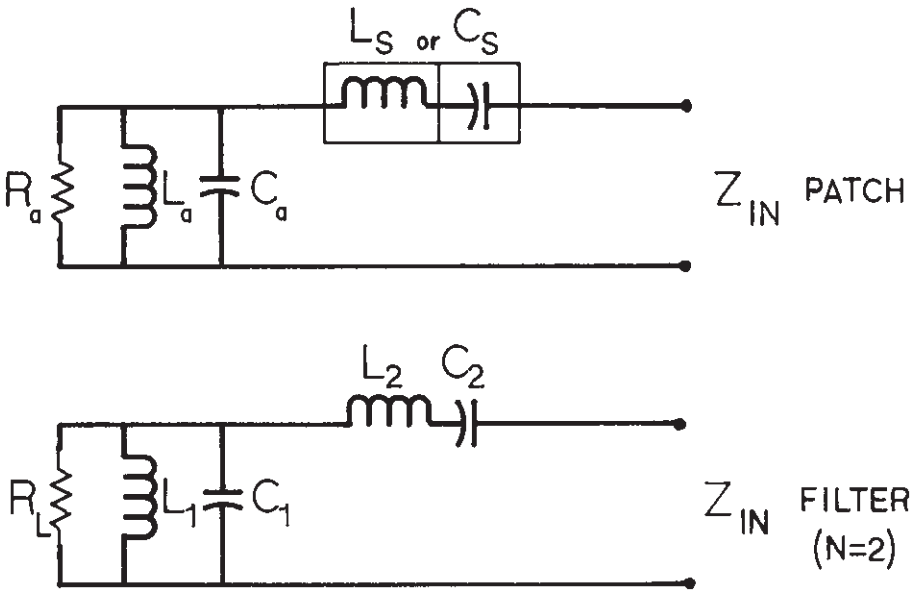

Figure 4-3 (a) A microstrip antenna may be modeled as a parallel RLC circuit with a series inductance or capacitance. (b) A bandpass filter has a similar model and may be used to impedance match a microstrip antenna over a larger frequency range than that covered by a single element.

exists for a typical patch. The resonant angular frequency, ω_0, is the frequency at which the maximum value of the real part of the driving point impedance occurs. The maximum value of the real part at resonance can be obtained directly from a measured impedance plot or a full-wave analysis method. At resonance, the relationship between the resonant angular frequency ω_0 and the patch model values L_a and C_a is

$$\omega_0^2 = \frac{1}{L_a C_a} \tag{4.8}$$

When the patch is resonant, the inductive and capacitive reactance of L_a and C_a cancel each other, and the maximum value of resistance occurs. If the patch is probe fed and thick, the impedance at resonance will have a series inductive reactance term L_s:

$$Z_{\text{in}} = R_a + j\omega_0 L_s \tag{4.9}$$

In order to obtain the values of C_a and L_a from measured or computed data one must subtract the series inductive reactance from the impedance. Choose two points on either side of ω_0 in frequency:

$$\omega_1 = \omega_0 - \Delta\omega_1 \tag{4.10}$$

$$\omega_2 = \omega_0 + \Delta\omega_2 \tag{4.11}$$

With the subtraction of the series inductance, the reactance now changes sign on either side of ω_0. The admittance at each frequency may be expressed as

$$Y_1 = \frac{1}{R_a} + j\omega_1 C_a + \frac{1}{j\omega_1 L_a} = G_1 + jB_1 \tag{4.12}$$

$$Y_2 = \frac{1}{R_a} + j\omega_2 C_a + \frac{1}{j\omega_2 L_a} = G_2 + jB_2 \tag{4.13}$$

The susceptance at each frequency is

$$B_1 = \omega_1 C_a - \frac{1}{\omega_1 L_a} \tag{4.14}$$

$$B_2 = \omega_2 C_a - \frac{1}{\omega_2 L_a} \tag{4.15}$$

Solving the equations for C we obtain

$$C_a = \frac{\omega_1 B_1 - \omega_2 B_2}{\omega_1^2 - \omega_2^2} \tag{4.16}$$

Solving the equations for L we obtain

$$L_a = \frac{1}{\omega_1^2 C_a - \omega_1 B_1} \tag{4.17}$$

We have now computed R_a, L_a, C_a, and L_s (or C_s in some rare cases). The similarity of the model to a bandpass filter allows one to use filter synthesis techniques to evaluate optimal component values for broadband matching. This method was first articulated by Paschen.[10] Optimum values may be found in the literature.[11] With a requirement of 1.8:1 VSWR (0.35 dB insertion loss) the g_i values for an $N = 2$ bandpass filter network are

$$g_1 = 1.50$$

$$g_2 = 0.455$$

$$g_3 = 1.85$$

The component values of the bandpass filter are given by

$$C_1 = \frac{g_1}{R_L(\omega_U - \omega_L)} \tag{4.18}$$

where ω_U is the upper radian frequency band limit and ω_L is the lower radian frequency band limit. The filter bandwidth is

$$F_{bw} = \omega_U - \omega_L.$$

$$L_1 = \frac{1}{\omega_0^2 C_1} \tag{4.19}$$

$$L_2 = \frac{g_2 R_L}{(\omega_U - \omega_L)} \tag{4.20}$$

$$C_2 = \frac{1}{\omega_0^2 L_2} \tag{4.21}$$

$$R_{\text{in}} = R_L/g_3 \tag{4.22}$$

We desire a 50 Ω input resistance, which requires that the load resistance $R_L = g_3 \cdot 50\ \Omega = 92.5\ \Omega$ for this case. We now have all the equations required to compute a matching example.

We need to provide $R_a = 92.5\ \Omega$, which is then equated with R_L of the filter circuit. We will do this by using a patch fed in the center of a radiating edge with a microstrip transmission line. The patch width is adjusted to provide a 92.5 Ω edge resistance at resonance. We can compute the value of L_s from measured or simulated data using the inductive reactance value X_L:

$$L_s = \frac{X_L}{\omega_0} \tag{4.23}$$

When the inductive reactance is subtracted from two frequencies on either side of resonance, we use equation (4.16) and equation (4.17) to compute C_a and L_a. The value of C_a is equated with C_1, which allows one to determine the expected filter bandwidth F_{bw} using equation (4.18):

$$F_{\text{bw}} = \frac{g_1}{R_a C_a} \tag{4.24}$$

This computation can be used to decide if the bandwidth is acceptable for a given design requirement. If the bandwidth is within the design requirement, we next compute L_2 using equation (4.20). This value needs to be larger than the series inductance of the microstrip antenna L_s to realize the design. The series inductance consists of two components, L_m and L_p. which are the series inductance attributable to higher order modes and feed probe self-inductance, respectively. While the majority of the series inductance L_s is due to the excitation of higher order modes, a coaxial probe feed also contributes its self-inductance L_p to the total series inductance. In some cases the diameter of this probe may be used to adjust the series inductance to conform to a realizable design.[12] Next, the value of C_2 is computed from equation (4.21).

4.2.3 Example Microstrip Antenna Broadband Matching with Lumped Elements

A microstrip antenna was designed, analyzed, and refined using FDTD to create an element fed at a radiating edge with a 50 Ω microstrip transmission line that has a 94.16 Ω impedance at resonance. This resistance is close enough to realize an impedance matching design as detailed previously. The

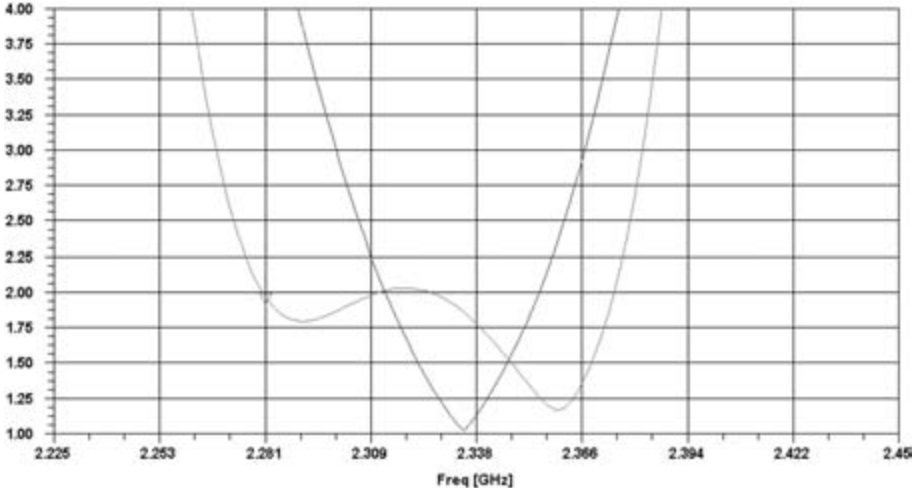

Figure 4-4 Bandwidth of the original element matched using a quarter-wave transformer and matched using lumped element matching (marked with triangle).

antenna dimensions are $a = 100.0$ mm and $b = 37.16$ mm, the substrate thickness is $h = 1.524$ mm, $\varepsilon_r = 2.6$, and $\tan\delta = 0.0025$, with a 130 mm $\times$ 75 mm groundplane.

The FDTD data have a maximum resistance value at 2.3317 GHz and an input impedance of $94.61 + j7.54\ \Omega$. Figure 4-5 shows the impedance plot for the antenna which is to be matched. At resonance we can compute an equivalent series inductance to be $L_s = 0.5147$ nH using equation (4.23).

The effectiveness of this matching method is dependent upon how well the load can be modeled as a parallel RLC circuit. Equation (4.16) and equation (4.17) provide values of $C_a = 26.67$ pF and $L_a = 175.195$ pH. When plotted with the FDTD data on a Smith chart, the computed RLC circuit can be improved upon. Computer optimization using a random search computes a very good fit to the FDTD data. This is illustrated in Figure 4-6. The computer optimized values are $R_a = 95.55\ \Omega$, $C_a = 28.64$ pF, $L_a = 163.04$ pH, and the series inductance is $L_s = 1.017$ nH. These values clearly model the FDTD data better than the curve fit values. These values are used with equation (4.20) and equation (4.21) to compute $L_2 = 77.39$ nH and $C_2 = 0.0602$ pF. The value of C_2 is clearly very difficult to realistically implement with a lumped element. We can still use

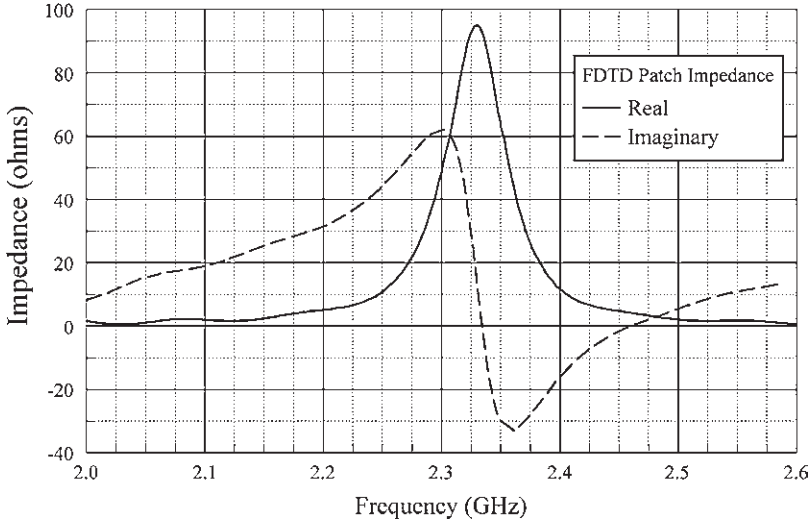

Figure 4-5 Rectangular impedance plot of a rectangular microstrip antenna used to illustrate matching network design.

these values to illustrate the theoretical match produced by this analysis compared with a single frequency match using a quarter-wave transformer.

The expected bandwidth from equation (4.24) is 88.1 MHz. In Figure 4-4, the bandwidth using a quarter-wave transformer is 41 MHz and the computed bandwidth using the synthesized impedance matching network implemented with discrete elements produces a bandwidth of 92 MHz. The bandwidth increase factor F is a respectable 2.24 in this implementation. The value of C_2 is unrealizable in this example, however, we will continue with the implementation of this method for illustration. One must also keep in mind this method is sensitive to the tolerance of the components used.

4.2.4 Lumped Elements to Transmission Line Section Conversion

At microwave frequencies, it is often desirable to implement a matching network using microstrip transmission line sections in place of lumped elements. One may use admittance and impedance inverters to realize the design of the example in Section 4.2.3 with transmission line.

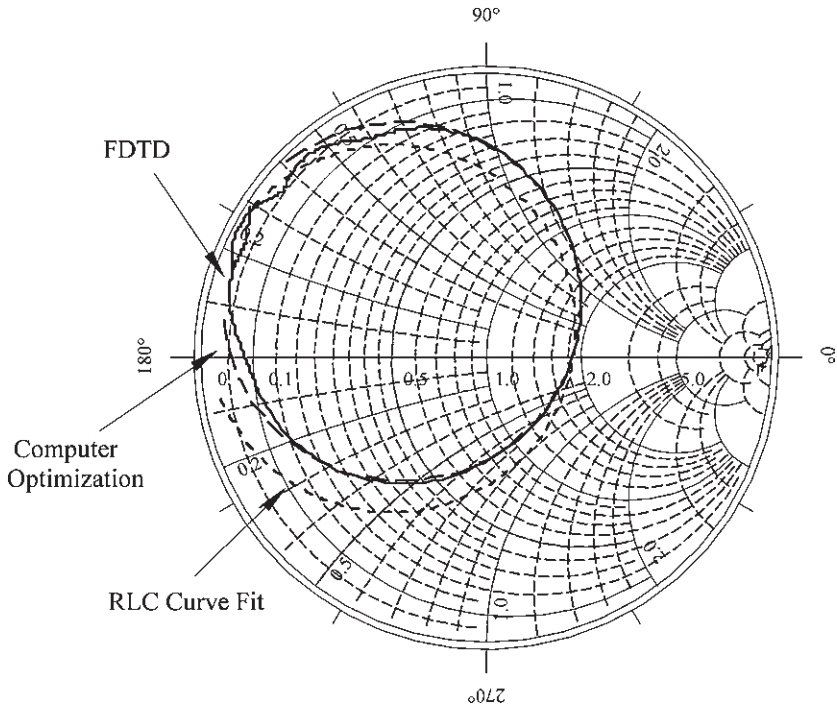

Figure 4-6 Rectangular microstrip antenna impedance from FDTD analysis with a curve fit RLC circuit and a computer optimized fit.

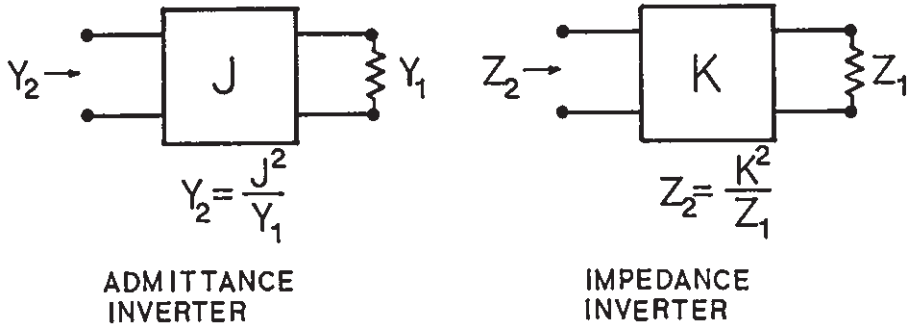

Figure 4-7 Admittance inverter and impedance inverter.

An admittance inverter is an ideal quarter-wave transmission line section of characteristic admittance J and an impedance inverter is an ideal quarter-wave transmission line section of characteristic impedance K.

$$Y_2 = \frac{J^2}{Y_1} \quad \text{(admittance inverter)}$$

$$Z_2 = \frac{K^2}{Z_1} \quad \text{(impedance inverter)}$$

A series admittance may be represented with a shunt admittance sandwiched between two J inverters. This is illustrated in Figure 4-8. A shunt impedance may be represented with a series impedance sandwiched between two K inverters, as shown in Figure 4-9. This property of J and K inverters

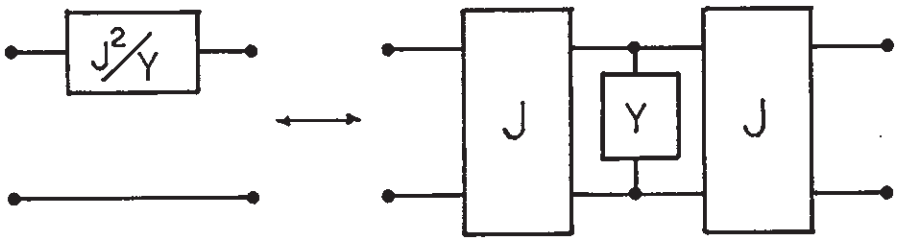

Figure 4-8 Series admittance and its equivalent circuit as a shunt admittance sandwiched between a pair of admittance inverters.

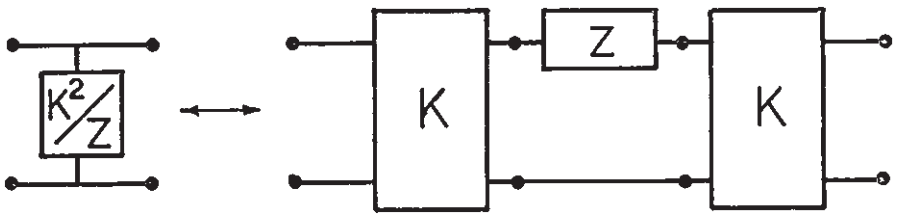

Figure 4-9 Shunt impedance and its equivalent circuit as a series impedance sandwiched between a pair of impedance transformers.

allows us to take series inductances and capacitances and convert them into shunt capacitances and inductances between a pair of quarter-wave transformers.

Once the series elements have been converted into shunt elements, the shunt capacitance and inductance can be approximated with transmission line sections. Lengths of transmission line provide reactance which is an approximation to a capacitor or inductor, but over a narrower bandwidth than the original elements. The bandwidth of the matching network is decreased because of this difference between transmission line sections and lumped elements. Often these transmission line sections are realized using microstrip transmission line. One must further compensate for physical microstrip transmission line discontinuities that produce deviations from idealized transmission line theory (Appendix C). With all these factors which can introduce error included, often considerable experimental optimizing must be undertaken to realize a design, which decreases the utility of this matching method considerably. This technique is most useful at low frequencies where lumped elements may be used to implement the matching network directly, as in the example in Section 4.2.3.

Figure 4-10(a) shows a microstrip patch antenna which is ideally designed to have a resonant edge resistance of 92.5 Ω. The example we have been using has an input impedance of 94.16 Ω at a reference plane 1 mm from a radiating edge along a 50 Ω microstrip transmission line as computed using FDTD analysis ($\Delta = 1$ mm). The patch width $W = 100.0$ mm, the patch length $L = 37.16$ mm, substrate thickness $h = 1.524$ mm, $\varepsilon_r = 2.6$, and $W_T = 4.12$ mm (50 Ω). The physical values for the transmission line matching network computed with FDTD refinement are

$$L_1 = 26.56 \text{ mm}$$

$$L_2 = 11.44 \text{ mm}$$

$$L_3 = 53.08 \text{ mm}$$

$$L_4 = 52.84 \text{ mm}$$

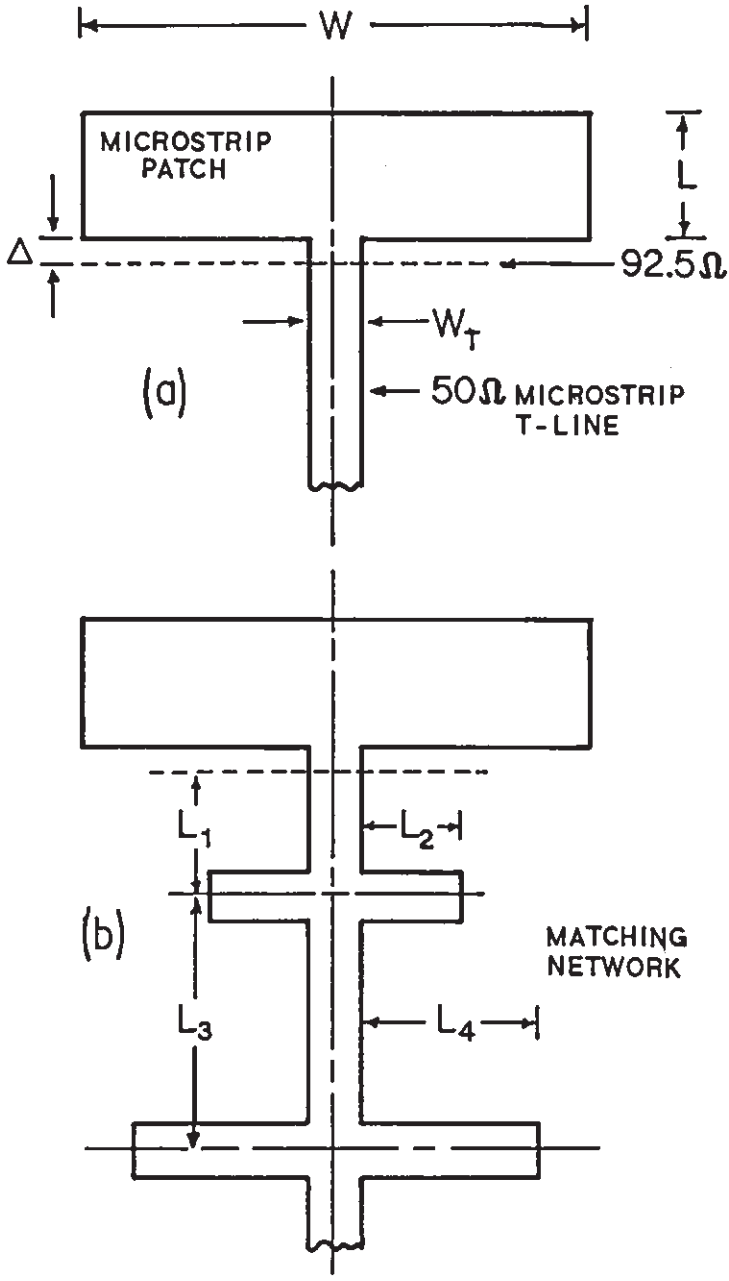

Figure 4-10 (a) Microstrip patch antenna that has a 92.5 Ω reference plane a very short electrical distance from the patch edge impedance. (b) Matching network topology synthesized using J-inverters.

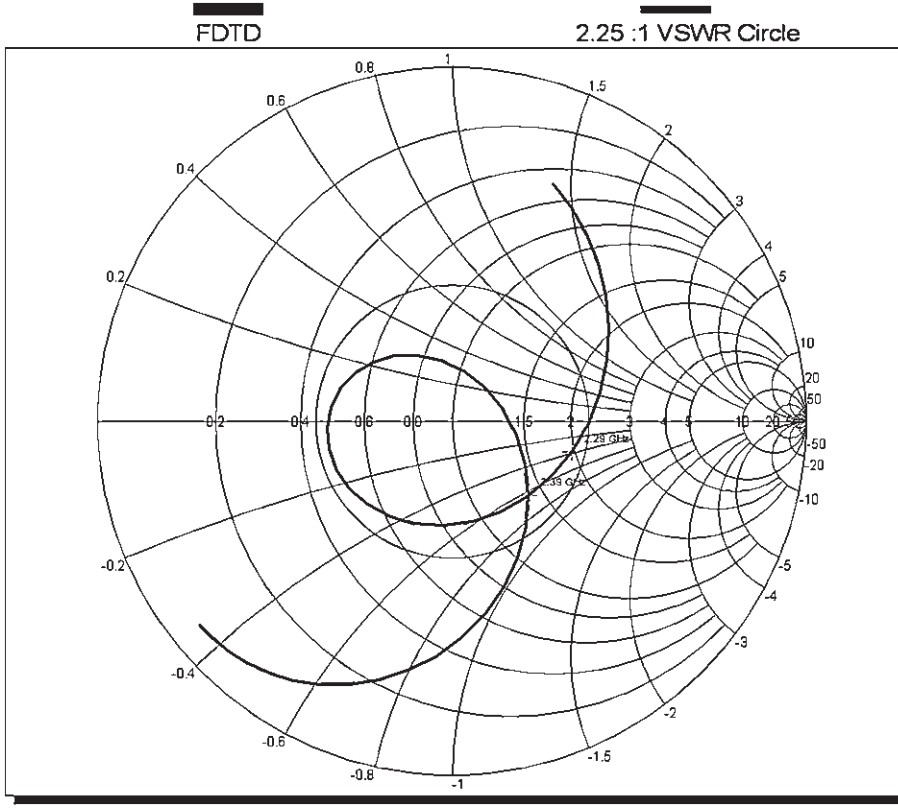

Figure 4-11 Microstrip transmission line matching network design FDTD analysis. The design is below 2.25:1 VSWR over 100 MHz.

These values were obtained by using the transmission line topology developed in this section (synthesized using J and K inverters with the lumped element solution) with the use of computer optimization to develop an improved transmission line realization, which requires less experimental intervention than a direct application of J inverters to realize a matching network. A small lengthening of the microstrip transmission line stubs compared with prediction allowed for the development of a design which when analyzed with FDTD has less than 2.25:1 VSWR over a 100 MHz bandwidth. A Smith chart plot of the analysis results is found in Figure 4-11.

4.2.5 Real Frequency Technique Broadband Matching

Another powerful matching method is the real frequency technique. Carlin realized and demonstrated that traditional broadband matching methods involving Chebyshev functions are optimum for purely resistive loads, but are not optimum for complex loads.[13] Carlin and Yarman introduced an alternate version known as the simplified real frequency technique (SRFT), which they demonstrated to be a very powerful method for the matching of microwave circuits.[14]

The SRFT is much more flexible than using bandpass filter theory as a matching method. With filter theory, one must choose the value of the resistance in the RLC circuit based on achieving a 50 Ω input. The SRFT has the flexibility that it can match any complex load whether it is a theoretical or measured load impedance. Implementation of the SRFT is very involved.[15] It produces lumped element networks which are very effective, but conversion to a transmission line realization remains very difficult. The SRFT has been used to match microstrip antennas by Hongming et al.[16]

4.2.6 Matching Network Optimization Using Genetic Algorithms

When computer optimization is chosen as a method to develop a broadband impedance matching network for a microstrip antenna, the choice of driving point impedance of the patch antenna can be arbitrary. A popular contemporary optimization method is the use of genetic algorithms.[17] This optimization method has the advantage that it is not difficult to implement and is conceptually accessible to the average designer. In an analogy with evolution, the limits of the parameters to be optimized are coded into binary “genes” and concatenated to form “chromosomes.” A population of chromosomes is created with the bits (ones and zeros) chosen by a random number generator. Generally a random number generator produces numbers between zero and one. If the value is below 0.5, the bit is set to zero, if it is greater than or equal to 0.5, the bit is set to one. Each of the members of this initial population is evaluated and assigned a normalized fitness value. The chromosomes are sorted and ranked. An arbitrary percentage of chromosomes with the highest values of fitness are retained. The chromosome with the highest fitness is “mated” with

Table 4-2 Matching network designs.

Optimization	L_2	L_4
Random	12.65 mm	56.07 mm
Genetic	55.92 mm	11.63 mm

the other chromosomes with lower fitness values. A point is randomly chosen along each binary string which represents each gene. This point is called a crossover. The crossover point is used as a boundary at which the bit strings of the two mated genes exchange bits. A percentage of the lower ranked population has their bits mutated or randomized. The new population is ranked and then mated to produce a number of generations. The difficult decision is what normalized "fitness" function best describes the parameters to be optimized which will produce a desired outcome. One can directly implement the optimization of a transmission line matching network with little difficulty.

When implemented with our previous example, the transmission line values for a matching network generated by a genetic algorithm, and using random optimization, are presented in Table 4-2. A plot of the theoretical VSWR from each of these optimizations is presented in Figure 4-12. In order to make a fair comparison, the quarter-wave sections (J inverters) were kept constant and only the length of the matching stubs were varied in both optimizations. The two methods produced different matching stub lengths (L_2 and L_4).

4.3 Patch Shape for Optimized Bandwidth

We noted in Chapter 2, section 2.7 that rectangular microstrip antennas that are linearly polarized have an impedance bandwidth that is half of the impedance bandwidth of a circularly polarized rectangular microstrip antenna. The superposition of two detuned TM_{10} and TM_{01} modes stretch out the bandwidth when compared with a single TM_{10} or TM_{01} mode. In general, a microstrip patch antenna may be of any shape: oval, rectangular, star, cross, circle with slot, pentagon, etc. Consideration of this property of microstrip antennas leads one to a basic question about microstrip antennas which has not been answered by theory: What microstrip patch shape provides maximum impedance bandwidth? Subsets of this question are

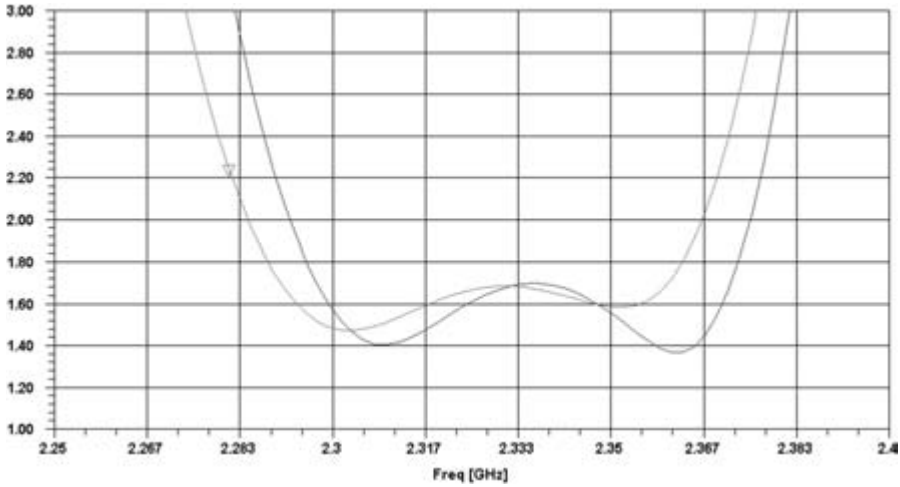

Figure 4-12 VSWR versus frequency using a genetic algorithm (marked with triangle) and using a random search method to produce a matching network for the example microstrip antenna. The quarter-wave sections were kept constant and only the length of the transmission line stubs were varied in both cases.

- What microstrip patch shape provides maximum impedance bandwidth with maximum linear polarization bandwidth allowing the linear polarization to vary in direction over the bandwidth?
- What microstrip patch shape provides maximum impedance bandwidth with maximum linear polarization bandwidth without rotation?
- What microstrip patch shape provides maximum impedance bandwidth with maximum axial ratio bandwidth for a circularly polarized antenna.

One restriction on shape is to have a single continuous patch without apertures (holes). One can relax this restriction and apply the same questions previously stated.

4.3.1 Patch Shape Bandwidth Optimization Using Genetic Algorithms

Delabie et al. proposed sectioning a plane in which a microstrip patch antenna is to be created into a set of small square subpatches.[18] Each subpatch is metalized if represented by a one and no metal is present if represented by a

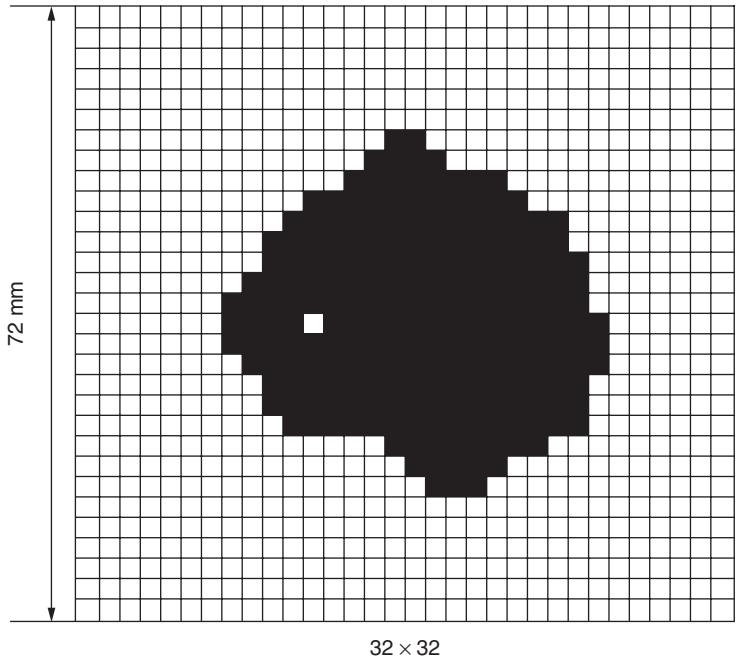

Figure 4-13 Patch shape produced by a genetic algorithm using a 32 × 32 grid of squares on a 72 mm × 72 mm groundplane. The substrate is 1.6 mm thick FR-4. (From [19], copyright 2000, IEE. Reprinted with permission.)

zero. A set of chromosome representations of candidate patches are selected, mated, and mutated using appropriate electromagnetic analysis technique.

The use of genetic algorithms to develop shapes which have increased impedance bandwidths compared with a square microstrip patch has been investigated by Choo et al.[19] Each antenna is described by a grid of connected squares with no internal voids. The patch antennas they developed use 1.6 mm thick FR-4 substrate. Their groundplane size is 72 mm × 72 mm. Two cases were examined, one using a 16 × 16 grid of squares; the second is a 32 × 32 grid of squares. The latter case is shown in Figure 4-13.

This patch is reported to have a fourfold increase in bandwidth improvement when compared with a square microstrip antenna. This increase in bandwidth is very close to the fundamental limit of increased bandwidth factor (Section 4.1) when a matching network is implemented (Section 4.2).

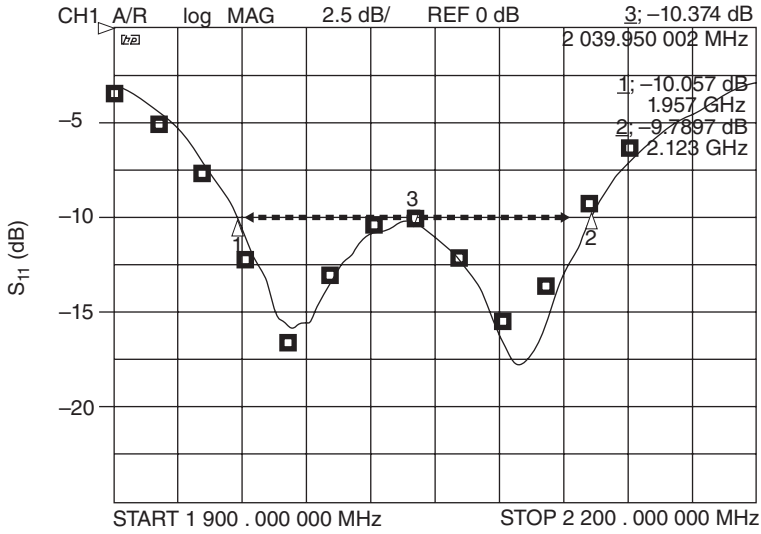

Figure 4-14 S_{11} versus frequency of the patch in Figure 4-13. (From [19], copyright 2000, IEE. Reprinted with permission.)

The center frequency of the design bandwidth is 2.0 GHz. Simulation by the method of moments predicted 8.04% bandwidth, and 8.10% was measured as seen in Figure 4-14.

An FDTD analysis reveals this antenna combines two separate resonances and creates circular polarization (LHCP) at 2.0 GHz. It is interesting to note the genetic algorithm selected circular polarization. It was related in Chapter 2, Section 2.7, that the impedance bandwidth of a patch with circular polarization is two times that of a linear antenna. The patch shaping and area apparently contribute to produce a further doubling of the impedance bandwidth.

References

[1] Kumar, G., and Ray, K. P., *Broadband Microstrip Antennas*, London: Artech House, 2003.

[2] Wong, K.-L., *Compact and Broadband Microstrip Antennas*, New York: John Wiley & Sons, 2002.

[3] Zurcher, J.-F., and Gardiol, F. E., *Broadband Patch Antennas*, London: Artech House, 1995.

[4] Zurcher, J.-F., "The SSFIP: a global concept for high-performance broadband planar antennas," *Electronics Letters*, November 10, 1988, Vol. 24, No. 23, pp. 1433–1435.

[5] Zurcher, B., Zurcher, J.-F., and Gardiol, F. E., "Broadband microstrip radiators: the SSFIP concept," *Electromagnetics*, November 1989, Vol. 9, No. 4, pp. 385–393.

[6] Milligan, T., *Modern Antenna Design*, New York: McGraw-Hill, 1985, p. 104.

[7] Hall, P. S., "Probe compensation in thick microstrip patch antennas," *Electronics Letters*, May 21, 1987, Vol. 23, No. 11, pp. 606–607.

[8] Bernard, R., Tchanguiz, R., and Papiernik, A., "Capacitors provide input matching of microstrip antennas," *Microwaves & RF*, July 1994, Vol. 33, No. 7, pp. 103–106.

[9] Matthaei, G., Young, L., and Jones, E. M. T., *Microwave Filters, Impedance-Matching Networks, and Coupling Structures*, New York: McGraw Hill, 1964, pp. 120–130, 681–686.

[10] Paschen, D. A., "Practical examples of integral broadband matching of microstrip elements," Proceedings of the 1986 Antenna Applications Symposium, Monticello, Illinois, September 17–19, 1986, pp. 199–217.

[11] Matthaei, G. L., Young, L., and Jones, G. M. T., *Microwave Filters, Impedance-Matching Networks, and Coupling Structures*, New York: McGraw Hill, 1964, pp. 123–129.

[12] Schaubert, D. H., Pozar, D. M., and Adrian, A., "Effect of microstrip antenna substrate thickness and permittivity: comparison of theories with experiment," *IEEE Transactions on Antennas and Propagation*, June 1989, Vol. 37, No. 6, pp. 677–682.

[13] Carlin, H. J., and Amstutz, P., "On optimum broad-band matching," *IEEE Transactions of Circuits and Systems*, May 1981, Vol. CAS-28, No. 5, pp. 401–405.

[14] Yarman, B. S., "A simplified real frequency technique for broadband matching a complex generator to a complex load," *RCA Review*, September 1982, Vol. 43, pp. 529–541.

[15] Gerkis, A. N., "Broadband impedance matching using the 'real frequency' network synthesis technique," *Applied Microwave & Wireless*, July/August 1998, pp. 26–36.

[16] Hongming, A., Nauwelaers, B. K. J. C., and Van de Capelle, A. R., "Broadband microstrip antenna design with the simplified real frequency technique," *IEEE Transactions on Antennas and Propagation*, February 1994, Vol. 42, No. 2, pp. 129–136.

[17] Rahmat-Samii, Y., and Michielssen, E., eds., *Electromagnetic Optimization by Genetic Algorithms*, New York: John Wiley & Sons, 1999.

[18] Delabie, C., Villegas, M., and Picon, O., "Creation of new shapes for resonant microstrip structures by means of genetic algorithms," *Electronics Letters*, August 28, 1997, Vol. 33, No. 18, pp. 1509–1510.

[19] Choo, H., Hutani, A., Trintinalia, L. C., and Ling, H., "Shape optimization of broadband microstrip antennas using genetic algorithm," *Electronics Letters*, December 7, 2000, Vol. 36, No. 25, pp. 2057–2058.

Chapter 5

Dual-Band Microstrip Antennas

5.0 Dual-Band Microstrip Antennas

Dual-band microstrip antennas are generally of two types: 1) separate microstrip resonators coupled to a transmission line, or 2) perturbed microstrip resonators where their original resonant frequencies are shifted by geometrical alteration of a basic resonator.[1,2] Dual-band microstrip antenna designs which allow for independent frequency selection have the most design utility. A good overview of dual-band microstrip antennas is given by Maci and Gentili.[3]

5.1 Single-Resonator Rectangular Microstrip Dual-Band Antenna

If one requires a single element, dual-band microstrip antenna that has a broadside radiation pattern at each of the dual-band design frequencies with the same polarization, one must drive the TM_{10} and TM_{30} modes. When these restrictions are chosen, the upper frequency must be approximately three times the lower frequency of operation. For a rectangular microstrip antenna, the pattern and polarization restrictions which have been previously imposed, severely limit the number of applications for which this design may be utilized.

In Section 2.6.1, a rectangular microstrip antenna is used to create circular polarization by allowing the TM_{10} and TM_{01} modes to overlap in frequency. A similar approach can be used to create a single resonator (element), dual-band microstrip antenna by separating the modes until they are isolated. If a designer can allow orthogonal linear polarization for each of the dual-band frequencies, and desires broadside radiation patterns, one can choose rectangular patch

dimensions a and b so the TM_{10} and TM_{01} modes correspond to a desired upper and lower frequency pair (F_U, F_L). This allows one to choose the two frequencies of operation in an independent fashion. One can choose the patch dimensions a and b to produce the desired frequency pair using methods from Chapter 2. The feed point location (X_p, Y_p) is the place which will optimally match the two modes simultaneously. The transmission line model of a rectangular microstrip antenna allows one to feed a patch antenna anywhere along a plane that is 50 Ω. A 50 Ω driving point impedance plane exists for each of the two modes generated. Where the impedance planes intersect is an optimum point to feed a dual-band patch of this type.[4] The geometry of a dual-band patch antenna of this type is illustrated in Figure 5-1.

In order to avoid the inaccuracies that can occur using the transmission line model, one can use the cavity model with genetic optimization to design a dual-band patch based on the use of TM_{01} and TM_{10}. This approach allows us to study the feasibility of designs using different frequency separations.

For ease of analysis, we can define a midpoint frequency F_m which is centered between the dual-band frequencies F_L and F_U:

$$F_m = \frac{F_L + F_U}{2}$$

We can define a frequency separation factor:

$$F_s = \left| \frac{F_m + \Delta_F}{F_m - \Delta_F} \right|$$

with

$$\Delta_F = \frac{F_U - F_L}{2} = F_m \frac{(F_s - 1)}{(F_s + 1)}$$

Multiplying the lower frequency by this factor produces the upper frequency:

$$F_U = F_s \cdot F_L = F_m + \Delta_F$$

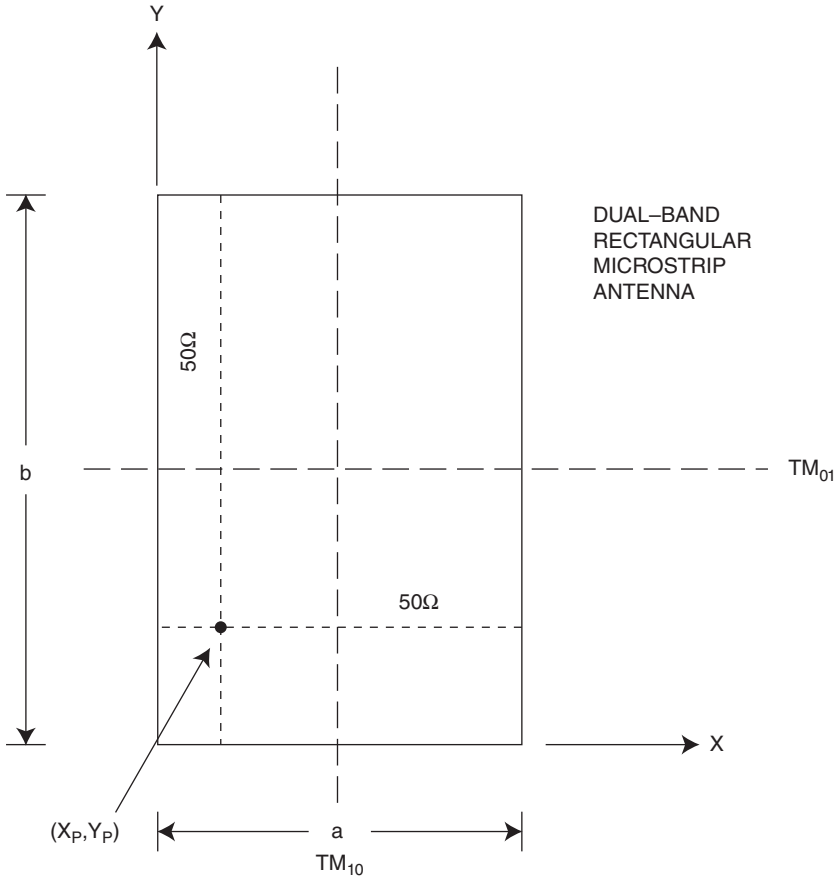

Figure 5-1 Optimization using a genetic algorithm with the cavity model allows for the design of a rectangular dual-band antenna with a single feed point by matching the TM_{10} and TM_{01} modes with the desired upper and lower design frequencies and simultaneously determining a matched driving point location at (X_p,Y_p).

$$F_L = F_m - \Delta_F$$

As a design example, we choose a midpoint frequency (F_m) of 2.0 GHz and use a genetic algorithm optimization with the cavity model to obtain designs for F_s = 1.05, 1.1, 1.2 with $\varepsilon = 4.1$ and h = 1.524 mm. The fitness function used for the genetic optimization is

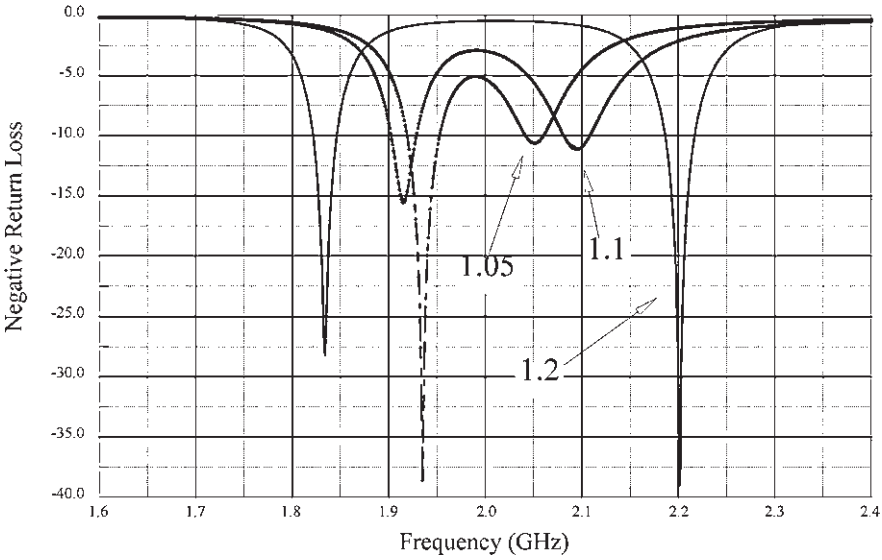

Figure 5-2 Single-feed dual-band solutions for a rectangular microstrip antenna using a genetic algorithm optimization with the cavity model.

$$Fit = \frac{|\text{Min}(\Gamma_L, \Gamma_U)|}{|\text{Max}(\Gamma_L, \Gamma_U)|} \cdot [(1 - |\Gamma_L|) + (1 - |\Gamma_U|)]$$

where

$|\Gamma_L|$ = magnitude of the driving point reflection coefficient at the lower center frequency

$|\Gamma_U|$ = magnitude of the driving point reflection coefficient at the upper center frequency.

We note in Figure 5-2 that as the frequency separation becomes larger, the genetic algorithm produces designs that are very close to the desired design frequencies and well matched (>20 dB return loss). An F_s of 1.05 is a design in which genetic optimization is unable to match both frequencies. When $F_s > 1.2$, genetic optimization produces well-matched dual-band designs for the rectangular patch geometry.

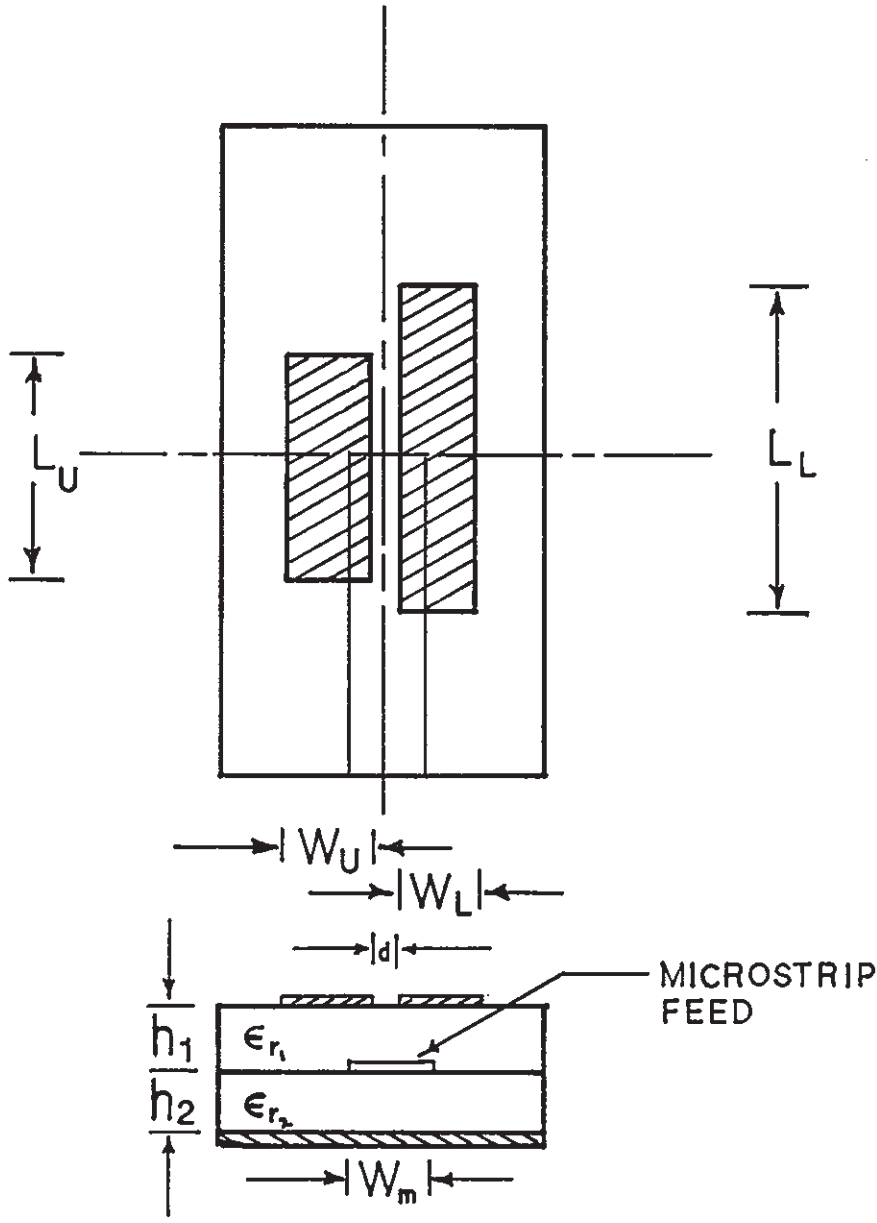

Figure 5-3 Two microstrip dipoles coupled to an imbedded microstrip transmission line.

5.2 Multiple Resonator Dual-Band Antennas

5.2.1 Coupled Microstrip Dipoles

A second dual-band antenna design option is to place a pair of parallel narrow microstrip elements (microstrip dipoles) in close proximity with a separation of d and feed them with a single coupled microstrip line, as illustrated in Figure 5-3. The two resonators are in the same plane, which makes this a coplanar dual-band design. This type of design allows one to more easily control F_L and F_U and maintain a good match. A microstrip line extends under the microstrip dipoles ending at the center of each microstrip dipole (i.e., at $L_U/2$ and $L_I/2$). The width of each dipole affects the match of each antenna. The lengths L_U and L_L change the upper and lower frequencies. The match is fairly stable as the resonator lengths are altered when compared to the sensitive nature of a single resonator, dual-band antenna. This is illustrated by the negative return loss plot of Figure 5-4 and Table 5-1, which describes the design. The length of each element can be adjusted to produce frequency separations F_s from 1.25 to 2.0 without altering other dimensions. The antenna patterns at each frequency are squinted by the presence of the nondriven element, which is the trade-off one must accept when using this antenna design.

5.2.2 Stacked Rectangular Microstrip Antennas

One can stack microstrip resonators to produce a dual-band antenna. The geometry of this design is illustrated in Figure 5-5. The upper patch is the high-frequency element of the dual-band antenna. The lower patch is larger than the upper patch and acts as a groundplane for the upper patch when it is resonant at F_U. When the lower patch is excited at the lower dual-band frequency (F_L), the upper patch has little affect on the lower patch. The groundplane of the structure acts as the groundplane for the lower patch.

Generally, a single feed probe passes through the bottom patch without connection (a small circle of the lower patch is removed for this purpose) and connects to the upper patch. This excitation geometry is sometimes called a common feed. When the upper patch is resonant, the lower patch produces negligible reactance, and vice versa. Another approach is parasitic feeding. The

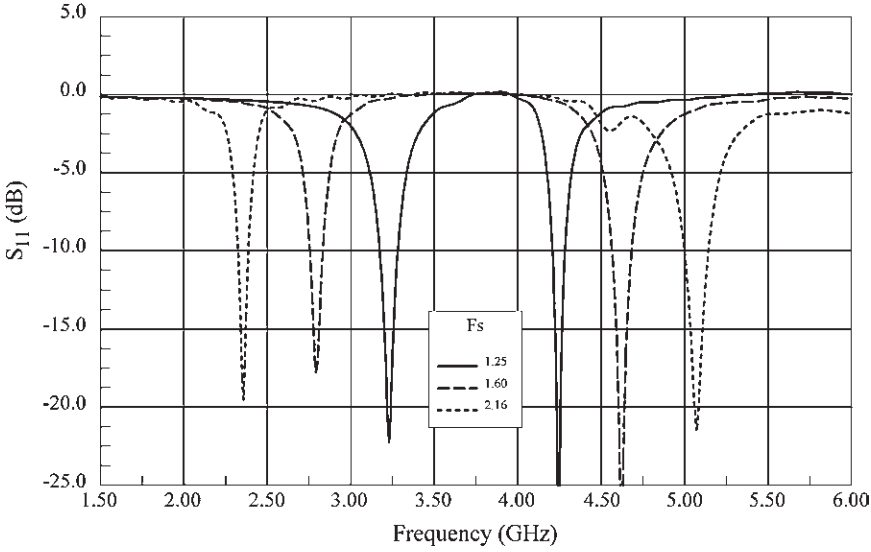

Figure 5-4 Microstrip dipole dual-band designs of Table 5-1 analyzed with FDTD.

Table 5-1 Coupled dual-band microstrip antenna parameters.

F_s	L_L (mm)	L_U (mm)	W_L (mm)	W_U (mm)
2.15	31.20	13.52	9.50	6.20
1.60	25.73	15.00	9.50	6.20
1.25	21.78	16.83	9.50	6.20

$\varepsilon_{r_1} = \varepsilon_{r_2} = 4.1$ $\tan\delta = 0.005$ $h_1 = h_2 = 1.524$ mm $d = 2$ mm
Microstrip Line Width = 2.98 mm

feed probe connects to the lower patch, and the upper patch is electromagnetically coupled. Parasitic feeding is often used to broaden the bandwidth of the upper patch rather than produce a dual-band antenna. When used to broaden antenna bandwidth, the upper patch is larger than the lower patch.[5]

When the upper patch is directly fed, the feed point location for a set of stacked linear rectangular microstrip antennas is close to the location of each patch separately. A shorting pin can be placed through the center of both

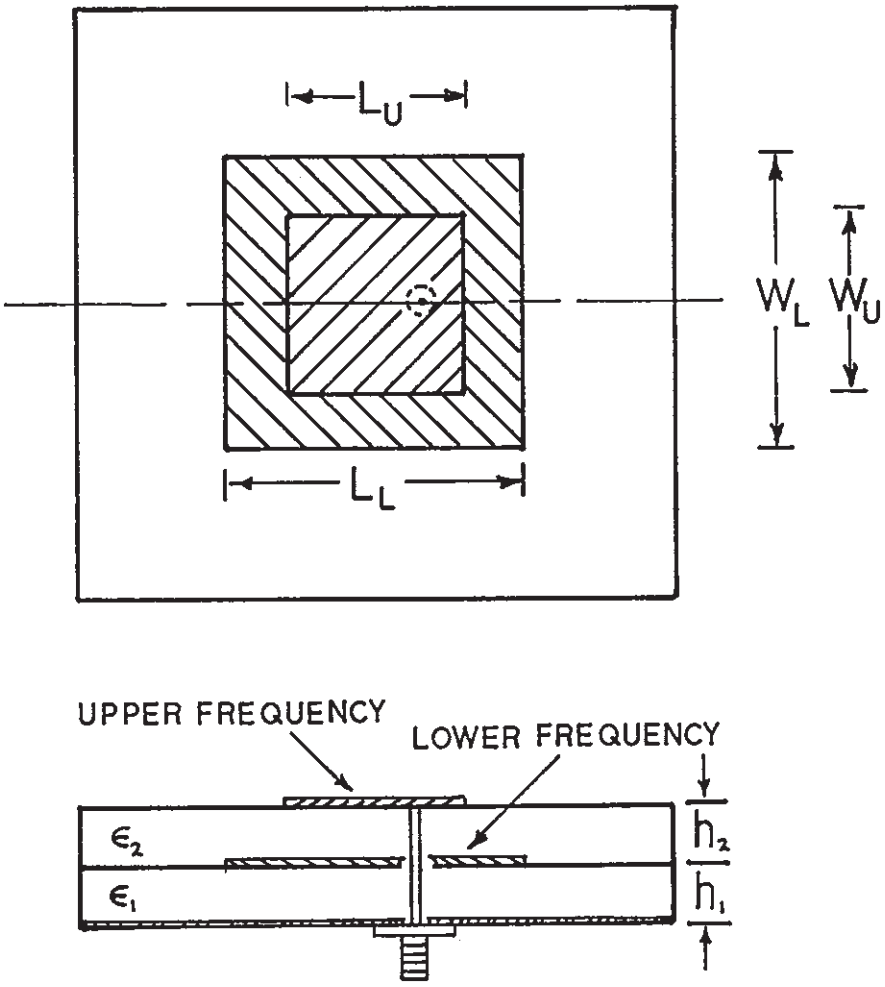

Figure 5-5 Stacked patch antennas.

patches to the groundplane. This helps to enforce the driven mode and eliminate many electrostatic discharge (ESD) problems.

The upper and lower patches may have their aspect ratios adjusted to produce circular polarization at each of the two dual-band frequencies. One can also stack quarter-wave patch elements to create dual-band stacked

element configurations with a smaller footprint than required by half-wave elements.

As stated previously, the upper and lower patches may have their aspect ratios adjusted so the upper and lower patches can have their TM_{01} and TM_{10} modes driven at distinct frequencies. This allows one to create a pair of stacked patches that will operate at four separate frequencies.

One can create a quad-band stacked patch antenna using the cavity model with genetic algorithms, as detailed in Section 5.1. A dual-band patch design, as shown in Figure 5-1, is the starting point. The two lowest frequencies are assigned to the bottom patch antenna and the two highest frequencies are assigned to the upper rectangular patch antenna. Lengths a_L and b_L are chosen to resonate the TM_{10} and TM_{01} of the lower patch at the desired lower set of design frequencies. Lengths a_H and b_H are chosen to resonate the TM_{10} and TM_{01} of the upper patch at the desired high set of design frequencies.

A pair of 50 Ω impedance planes, as shown in Figure 5-1, will exist for each of the two antennas. The point of intersection of the impedance planes of the upper patch antenna (X_{PU},Y_{PU}) is aligned with the lower patch's intersection point (X_{PL},Y_{PL}). The two points are colocated as (X_P,Y_P) in Figure 5-6. Experimental optimizing of the antenna is required to produce a final design.

5.3 Dual-Band Microstrip Antenna Design Using a Diplexer

An alternative to using a stacked patch to create a dual-band microstrip antenna is to use a diplexer with two single-frequency elements. A diplexer separates a pair of frequency bands that are originally combined at the input port and presents each frequency at each of a pair of output ports which are isolated from one another. The classic lumped element version of a diplexer consists of a high-pass filter and low-pass filter with a common input.

The exact and approximate design of diplexers and multiplexers is presented in the literature.[6,7] This design process can be rather extensive when developing microwave diplexers. If the frequency ratio between bands is approximately 2:1, one can use a diplexer circuit, introduced by de Haaij et al. and presented in Figure 5-7.[8]

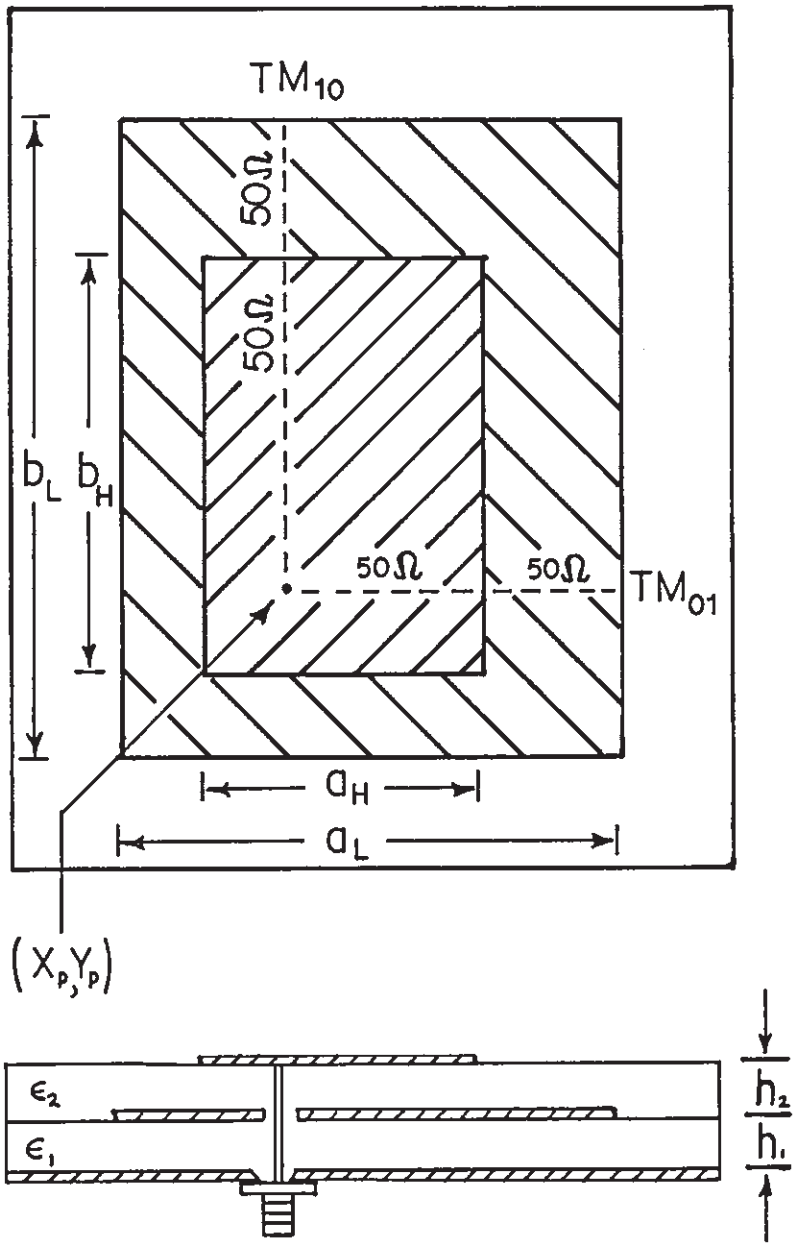

Figure 5-6 Stacked patch antenna fed to drive four separate modes to create a quad-band antenna.

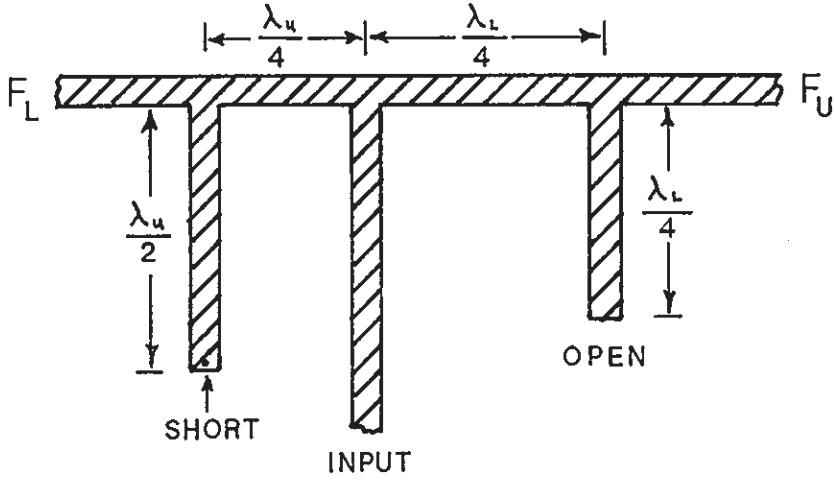

Figure 5-7 Diplexer for combining two bands which have an approximate 2:1 center frequency ratio.

The three-port microstrip circuit has a 50 Ω input port with a length of transmission line that forms a T-junction with a pair of 50 Ω transmission lines. The upper and lower frequency ports are designated F_U and F_L for the upper and lower frequency bands, respectively.

When the center frequency F_L of the lower frequency band is presented to the input port, the quarter-wavelength open circuit stub ($\lambda_L/4$) produces a short circuit one quarter-wavelength ($\lambda_L/4$) from the T-junction, which becomes an open circuit at the T-junction. λ_L is the guide wavelength of the microstrip transmission line at the center of the lower frequency band. The short circuited stub at the lower frequency band becomes an open circuit at the microstrip transmission line. This allows the low-frequency signal to pass through to the F_L port unrestricted. This occurs because $\lambda_U/2 = \lambda_L/4$ when a 2:1 frequency ratio is assumed.

When the center frequency F_U of the upper frequency band is presented to the diplexer's input port, the open circuit stub on the right-hand side is one-half guide wavelength ($\lambda_L/4 = \lambda_U/2$) and presents an open circuit to the transmission line. This allows the signal to pass to the F_U output port. The short-circuited stub becomes a short circuit at the microstrip transmission line at a location

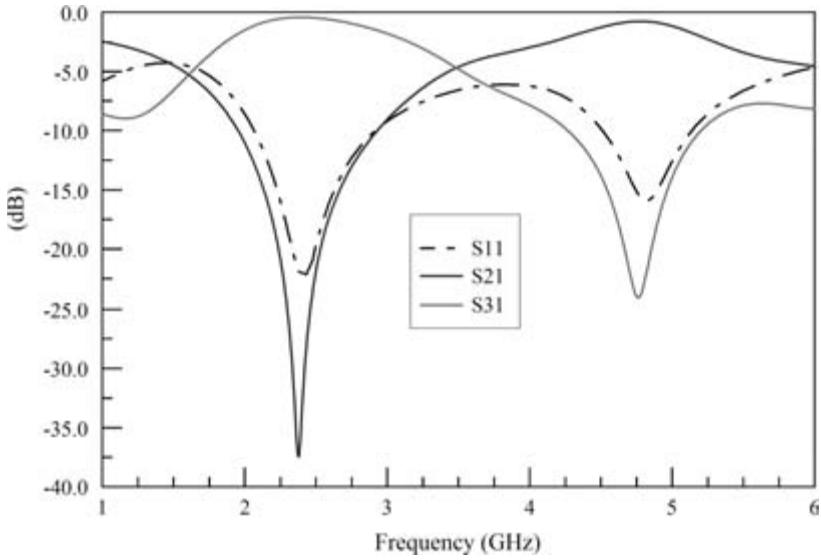

Figure 5-8 Diplexer designed to feed a pair of rectangular patches to produce a dual-band radiating structure for Example 5.3.1.

one-quarter wavelength from the T-junction, which produces an open circuit at the T-junction.

5.3.1 Example Dual-Band Microstrip Antenna Design Using a Diplexer

In Figure 5-8, a diplexer of the form found in Figure 5-7 is realized using Ansoft HFSS and passes 2.38 and 4.77 GHz. This diplexer has limited utility in practice, but offers a succinct design for illustration of the use of a diplexer in a dual-band microstrip antenna design. The diplexer is used to feed a pair of rectangular microstrip antennas that are wide enough to directly match a 50 Ω microstrip transmission line. Two ultrawide rectangular microstrip antennas with 50 Ω edge resistance were designed to have resonant frequencies of 2.38 and 4.77 GHz, respectively.

The two patches integrated with the diplexer are shown in Figure 5-9. The physical values of the distance from the low frequency (F_L) port to the input

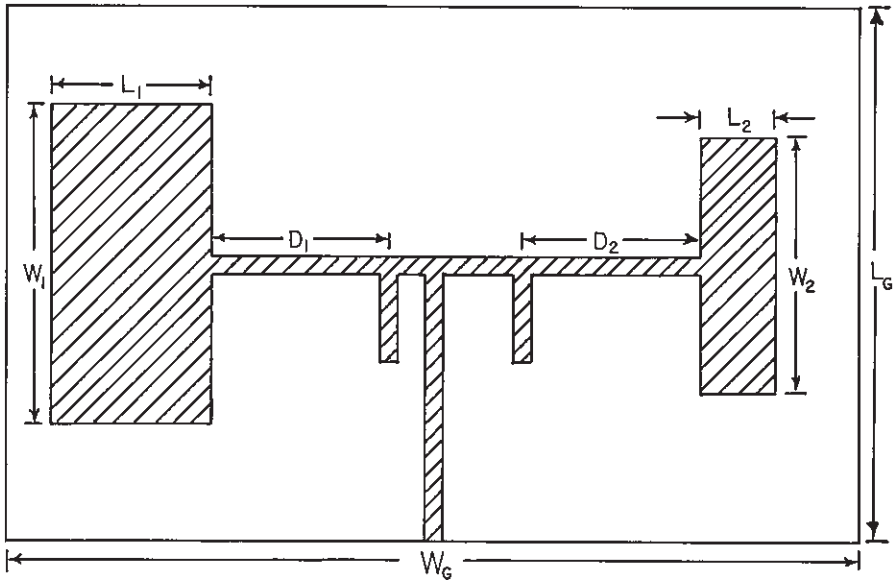

Figure 5-9 Geometry of a diplexer with integrated rectangular patch antennas used to produce a dual-band structure.

port (D_1) of the low-frequency patch is 41.7 mm. The low-frequency patch has a width $W_1 = 75.0$ mm and length of $L_L = 37.576$ mm. The length from the upper frequency (F_U) port to the input port (D_2) of the high-frequency patch is 35.0 mm. The high-frequency patch has a width of $W_2 = 60$ mm and length of $L_2 = 17.86$ mm, and $\lambda_L = 83.4$ mm and $\lambda_U = 41.7$ mm. The width of the interconnecting 50 Ω transmission lines is 4.17 mm. The substrate parameters are $\varepsilon_r = 2.6$ with $\tan\delta = 0.0019$ and the substrate thickness is 1.524 mm. The length and width of the substrate is $L_G = 125$ mm and $W_G = 200$ mm.

The gain values predicted by Ansoft HFSS are 6.7 dBi for the low-frequency patch and 9.52 dBi for the high-frequency patch. The negative return loss plot of the ultrawide elements separately and integrated with the example diplexer as predicted by HFSS is shown in Figure 5-10.

More complex diplexers have larger and more flexible passbands which allow for an easier antenna design implementation. The previous example illustrates a simple diplexer design that can be used to produce a dual-band planar antenna with frequency separation of approximately 2.0 which is useful for illustration. When a more elaborate diplexer design is used, broad band-

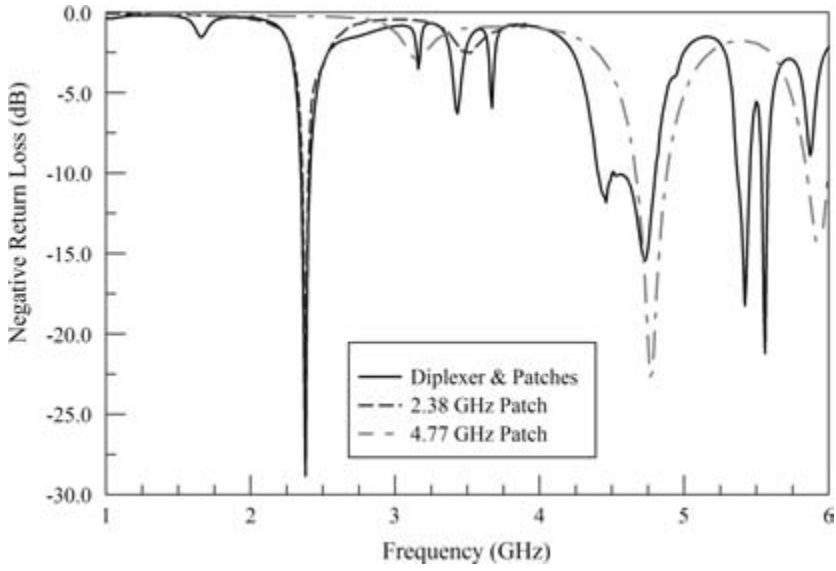

Figure 5-10 (a) Negative return loss plots of high- and low-frequency patches analyzed separately and the response of the diplexer and patches predicted by HFSS.

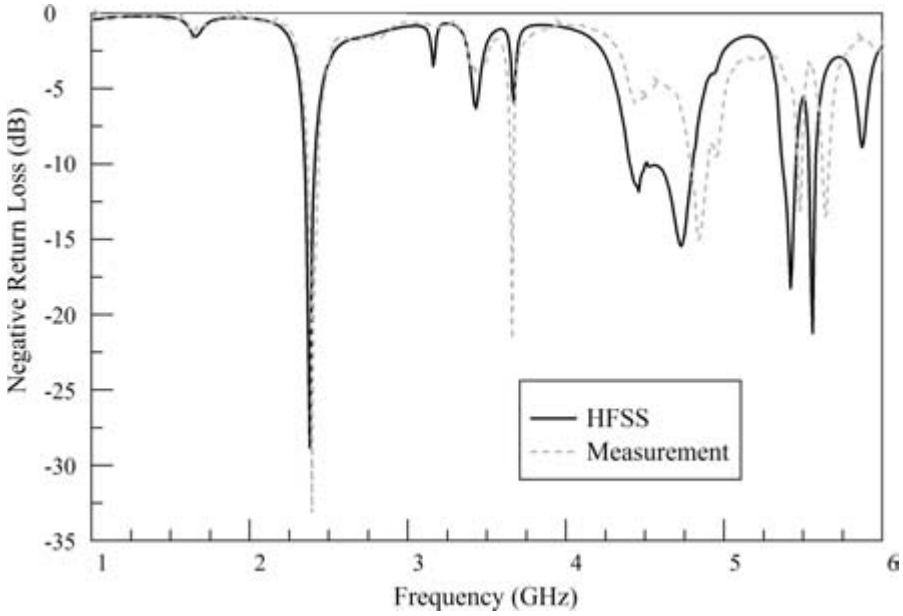

Figure 5-10 (b) Negative return loss plots predicted by HFSS and measured.

width planar antenna element designs allow one to develop designs with up to 20% bandwidth per band by using planar antennas (i.e., monopole-type elements).

5.4 Multiband Microstrip Design Using Patch Shaping and a Genetic Algorithm

In Section 4.3, the creation of microstrip antennas with a large impedance bandwidth using patch shaping guided with a genetic algorithm was discussed. This method has been used by Choo and Ling to design a microstrip antenna patch shape using the method of moments, which produces multiband antennas on FR-4.[9,10] An antenna shape was created which operates at 900 MHz (GSM), 1.6 GHz (GPS/L1), 1.8 GHz (DCS), and 2.45 GHz (ISM/Bluetooth). This design is reproduced in Figure 5-11. This method offers the possibility

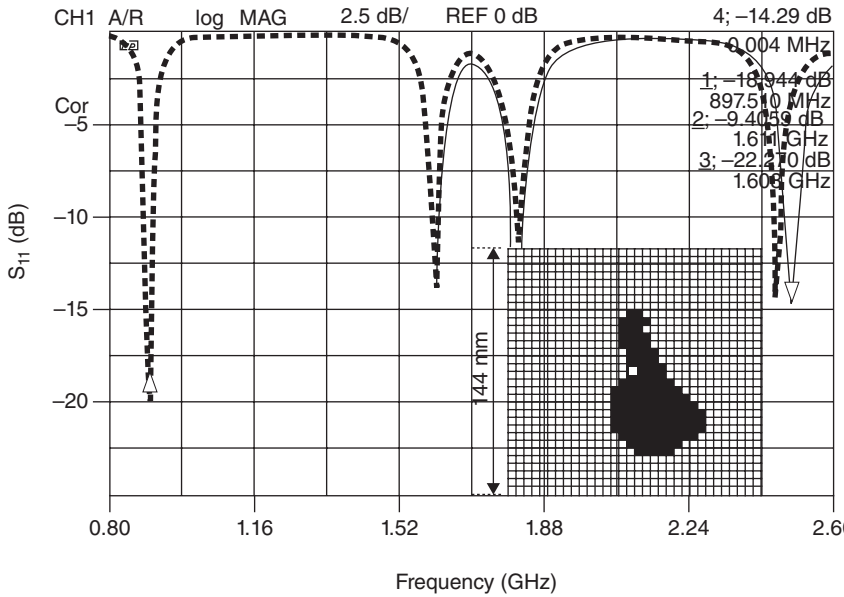

Figure 5-11 Patch shape of a microstrip antenna that has been optimized for quad-band operation. The dashed lines are simulation and the solid line is measurement. (From [9], copyright 2002, IEEE. Reprinted with permission.)

of developing low-cost single-layer multiband antennas with arbitrary frequencies.

References

[1] Kumar, G., and Ray, K. P., *Broadband Microstrip Antennas*, London: Artech House, 2003.

[2] Wong, K.-L., *Compact and Broadband Microstrip Antennas*, New York: John Wiley & Sons, 2002.

[3] Maci, S., and Gentili, G. B., "Dual-frequency patch antennas," *IEEE Antennas and Propagation Magazine*, December 1997, Vol. 39, No. 6, pp. 13–20.

[4] Chen, J.-S., and Wong, K.-L., "A single-layer dual-frequency rectangular microstrip patch antenna using a single probe feed," *Microwave and Optical Technology Letters*, February 5, 1996, Vol. 11, No. 2, pp. 83–84.

[5] James, J. R., and Hall, P. S., *Handbook of Microstrip Antennas*, Vol. 1, Stevenage, UK: Peter Peregrinus, Ltd., 1989, pp. 324–325.

[6] White, J. F., *High Frequency Techniques*, New York: John Wiley & Sons, 2004, pp. 364–369.

[7] Malherbe, J. A. G., *Microwave Transmission Line Filters*, London: Artech House, 1979, chap. 7.

[8] de Haaij, D. M., Joubert, J., and Odendaal, J. W., "Diplexing feed network for wideband dual-frequency stacked microstrip patch antenna," *Microwave and Optical Technology Letters*, January 20, 2003, Vol. 36, No. 2, pp. 100–103.

[9] Choo, H., and Ling, H., "Design of multiband microstrip antennas using a genetic algorithm," *IEEE Microwave and Wireless Components Letters*, September 2002, Vol. 12, No. 9, pp. 345–347.

[10] Choo, H., and Ling, H., "Design of dual-band microstrip antennas using the genetic algorithm," *Proceedings of the 17th Annual Review of Progress in Applied Computational Electromagnetics*, Session 15, Monterey, CA, May 19–23, 2001, pp. 600–605.

Chapter 6

Microstrip Arrays

6.0 Microstrip Arrays

A single microstrip antenna utilizing an air dielectric substrate ($\varepsilon_r \approx 1$) is able to provide a maximum gain of about 10 dBi. When larger gains are required, and a microstrip antenna solution is the best choice, a number of microstrip elements may be connected together to form an array of antennas. An array of elements provides a much larger effective aperture and therefore gain compared to a single microstrip element. This chapter will discuss elementary methods used to design microstrip antenna arrays.

6.1 Planar Array Theory

Classic linear and planar array analysis papers were presented by Elliot in the early 1960s which are very useful for the analysis of rectangular microstrip antenna arrays.[1–3] In Figure 6-1, a number of rectangular microstrip antennas are located in the x-y plane. The z axis is directed out from the paper. Each microstrip antenna can be modeled as a pair of radiating slots in a groundplane. Assuming a TM_{01} mode, the antennas are polarized along the y axis. A patch with its center located at (X_n,Y_n) is effectively modeled as a pair of slots located at $(X_n,Y_n + L/2)$ and $(X_n,Y_n - L/2)$ of width W and thickness H and identical excitation amplitude for each pair as shown in Figure 6-2.

The array factor for a number of point sources (N_p) in free space is

$$A(\theta,\phi) = \sum_{n=1}^{N_p} I_n e^{jk\sin\theta[X_n\cos\phi + Y_n\sin\phi]} \tag{6.1}$$

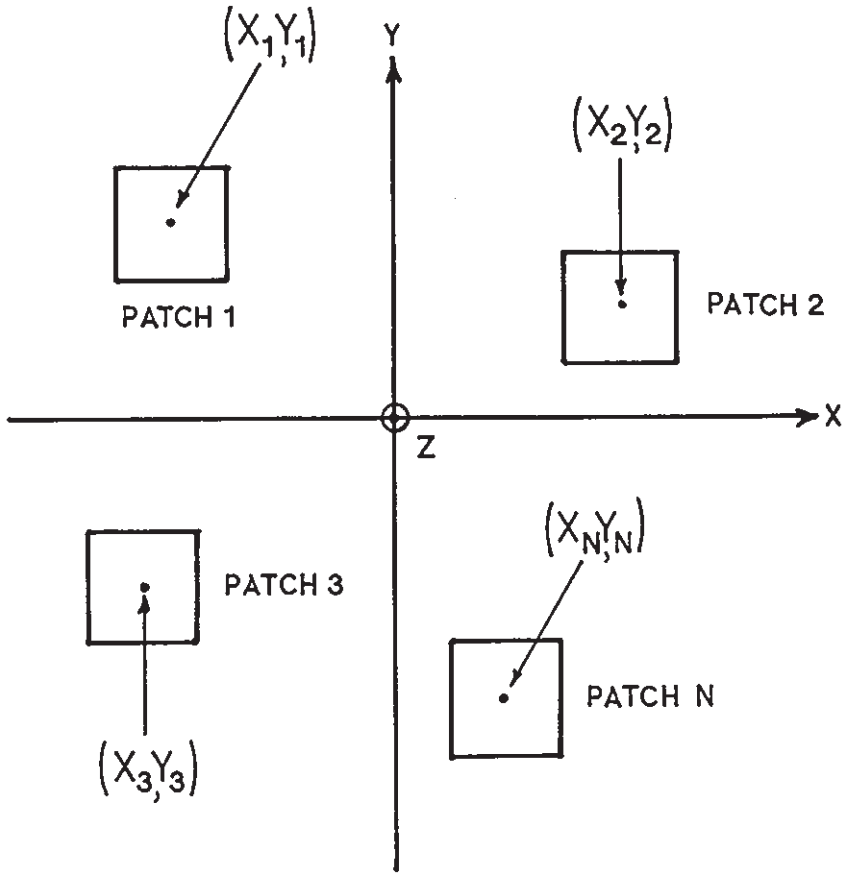

Figure 6-1 Geometry of a set of rectangular microstrip antennas 1,2,3, . . . , N in the x-y plane. The center of each patch is used for reference to locate a pair of equivalent slots.

To analyze the radiation pattern of a rectangular microstrip array we sum the array factor over all the slots, taking into account the excitation factor of each slot: $I_n = E_n \cdot w \cdot h$, where E_n is the electric field across each slot of patch n, w is the patch width, and h is the substrate thickness. θ is measured from the z axis. The electric field radiated is proportional to the array factor multiplied by an element (antenna) factor $R(\theta,\phi)$. The electric field decreases by $1/r$:

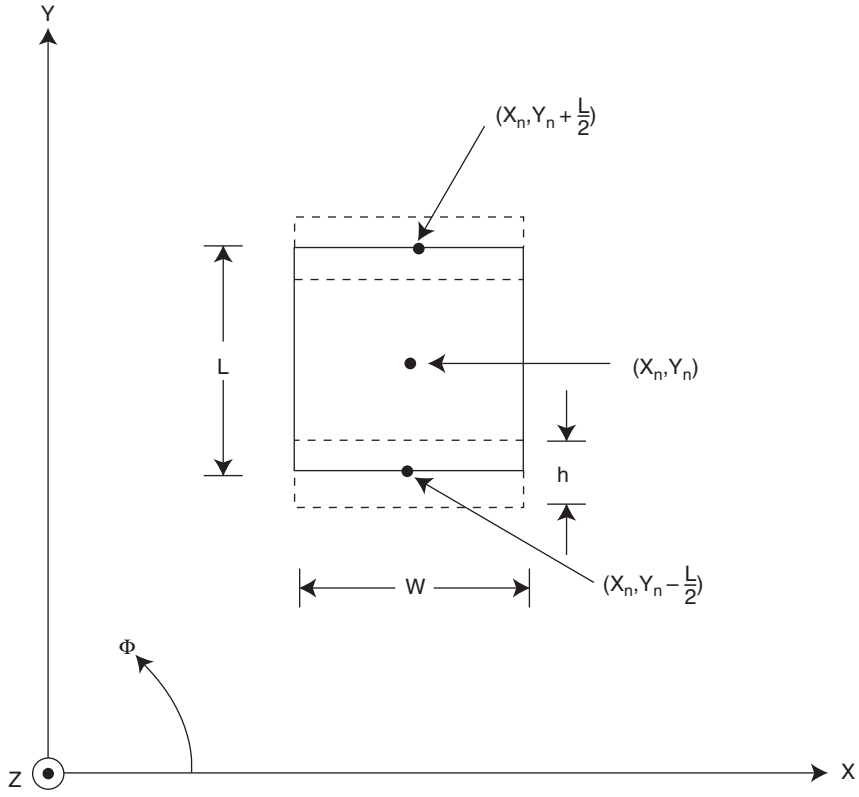

Figure 6-2 The radiation from each patch of Figure 6-1 is modeled as a pair of slots.

$$\vec{E}(\theta, \phi) = A(\theta, \phi) \cdot R(\theta, \phi) \tag{6.2}$$

The θ and ϕ components of the electric field are

$$\vec{E}_\theta(\theta, \phi) = A(\theta, \phi) \sin\phi \cdot R(\theta, \phi) \tag{6.3}$$

$$\vec{E}_\phi(\theta, \phi) = A(\theta, \phi) \cos\theta \cos\phi \cdot R(\theta, \phi) \tag{6.4}$$

The element factor for a rectangular aperture is[4]

$$R(\theta,\phi)=\frac{\sin[(kw/2)u]}{(kw/2)u}\frac{\sin[(kh/2)v]}{(kh/2)v} \tag{6.5}$$

where

$$u=\sin\theta\cos\phi \tag{6.6}$$

$$v=\sin\theta\cos\phi \tag{6.7}$$

The power at any point in space is

$$P(\theta,\phi,r)=\frac{|E_\theta|^2}{r^2}+\frac{|E_\phi|^2}{r^2} \tag{6.8}$$

We can multiply equation (6.8) by r^2, which gives us the power per unit solid angle or the radiation intensity U:

$$U(\theta,\phi)=|E_\theta|^2+|E_\phi|^2 \tag{6.9}$$

The expression for radiation intensity can be used to compute the array directivity using numerical techniques:[5]

$$D_0=\frac{4\pi U_{max}}{P_{rad}} \tag{6.10}$$

$$P_{rad}=\left(\frac{\pi}{N}\right)\left(\frac{2\pi}{M}\right)\sum_{j=1}^{M}\left[\sum_{i=1}^{N}U(\theta_i,\phi_j)\sin\theta_i\right] \tag{6.11}$$

where

$$\theta_i=i\left(\frac{\pi}{N}\right) \tag{6.12}$$

$$\theta_j=j\left(\frac{2\pi}{M}\right) \tag{6.13}$$

The radiation sphere is divided into N and M sections. Microstrip antennas only radiate into the upper half of the space ($\theta < \pi/2$), so the radiation intensity is zero for $\theta > \pi/2$. These equations produce reliable estimates of the directivity of a planar microstrip array.

6.2 Rectangular Microstrip Antenna Array Modeled Using Slots

The gain of an antenna is directly proportional to its effective aperture. As the gain of an antenna increases, so does its effective aperture. When microstrip antennas are arranged in an x-y plane, one can assume each of the separate antennas radiate only into the region above the x-y plane. If we have a single microstrip antenna with a gain of, say, 6.0 dBi and then connect a second identical antenna that is spaced at one wavelength center to center (approximately 0.5 wavelength edge to edge, $\varepsilon_r = 1$), we will increase the effective aperture by approximately a factor of 2. This aperture doubling translates into approximately a 3 dB increase in the maximum gain of the two elements. The gain of the two antennas is approximately 9.0 dBi. If we continue this line of reasoning we have a rule of thumb to predict the approximate gain of a planar array of microstrip antennas. If a single element has 8.0 dBi of gain, then a pair of these elements can have approximately 11.0 dBi maximum gain. We need to double the aperture again to increase the gain by 3 dB, so we add two more elements for a total of four. This 4×4 array should have up to 14.0 dBi gain. To obtain 3 dB more, we double from four elements to eight elements to obtain 17.0 dBi. One can quickly estimate the maximum theoretical gain (or directivity) of a uniformly fed microstrip array by noting the approximate gain of a single element and adding 3 dB for each doubling of the number of elements until one reaches the total number of elements. This procedure is illustrated in Figure 6-3.

As an example, we will use the equations of Section 6.1 to compute the directivity of the array configurations depicted in Figure 6-3. The frequency chosen is 5.3 GHz with a patch width and length (W and L) of 15.70 mm. The center to center distance between patches is 29.66 mm. The substrate thickness (h) is 1.524 mm.

In Table 6-1 we have computed and estimated the directivity of the arrays of Figure 6-3. The direction of the E-plane of the antennas is from top to bottom

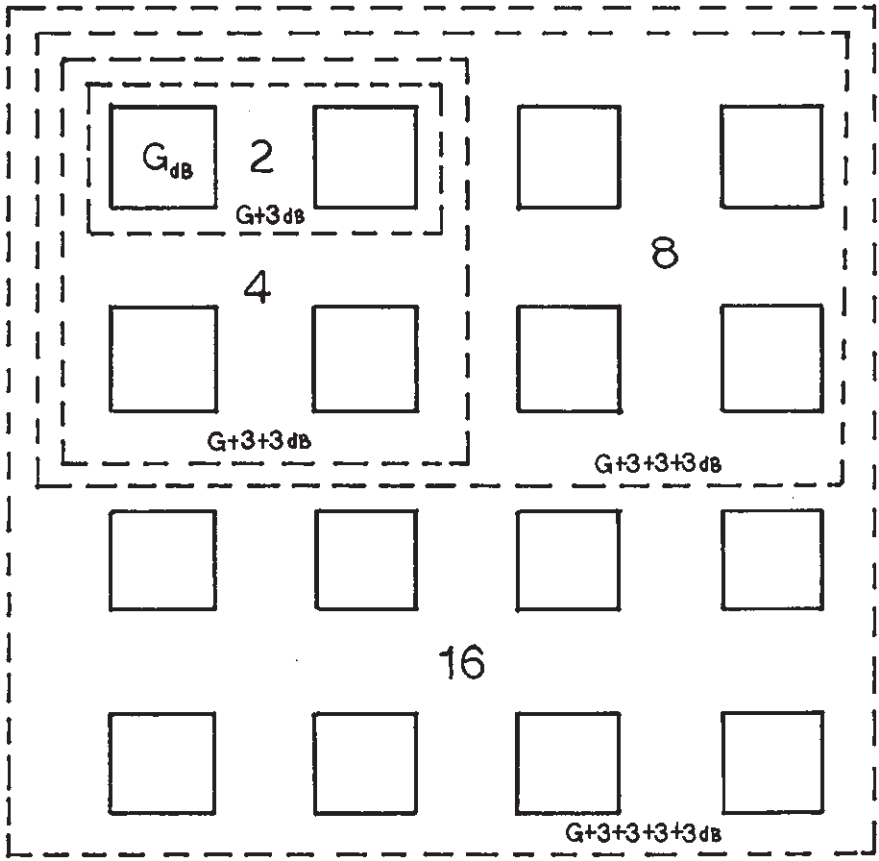

Figure 6-3 Relationship between array aperture and directivity. Each time the aperture is doubled (for a properly spaced array) the directivity is increased by approximately 3 dB.

Table 6-1 Computed directivity versus estimated directivity.

Elements	Directivity (dB)	Estimate (dB)
1	6.25	6.25
2	8.32	9.25
4	11.81	12.25
8	14.67	15.25
16	17.64	18.25
32	20.57	21.25

of the page. The H-plane is from left to right, as illustrated in Figure 6-2. The difference between the directivity computations for a uniformly illuminated planar array and the estimates based on aperture are less than 1 dB.

The computed patterns of Figure 6-4 offer some insight into how microstrip antennas array. Pattern (a) is a single element. The E-plane pattern is hemispherical and the H-plane diminishes to zero as θ approaches 90°. In (b), when two elements are placed side by side along the antennas' H-planes, we note they array along the H-plane and narrow the beamwidth. The E-plane pattern remains unchanged. When two more patch antennas are added below along the E-plane, for a total of four, we see the E-plane now arrays leaving the H-plane unchanged in (c). Repeating the same selections in (d), (e), and finally (f), we get an understanding of how element and array factors interact to narrow the beamwidth as the effective aperture increases, which increases the antenna gain.

6.3 Aperture Excitation Distribution

Figure 6-4 shows that a number of sidelobes appear in an array of 32 elements with equal amounts of current (or equivalent voltage) driven in each element. This type of distribution is often referred to as uniform. When the array excitation distribution of a planar microstrip array is uniform and electrically large, the gain of the main beam of the array is maximized, and the first sidelobe is 13.2 dB below the gain of the main beam. The value of the gain of the first sidelobe below the gain of the main beam of an array is known as the first sidelobe level. The maximum sidelobe value compared with the main beam is the sidelobe level of the array.

In many applications, a –13.2 dB sidelobe level is not acceptable. The sidelobe level of an array can be controlled by tapering the excitation amplitudes of the array elements from a maximum value in the center to lower levels as one reaches the outside.

When the array excitation values are chosen to correspond with binomial coefficients, all sidelobes can be completely suppressed, in theory. The beamwidth of the main beam of the array will widen, which decreases the gain of the array. Between the maximum gain of a uniform array with –13.2 dB sidelobes

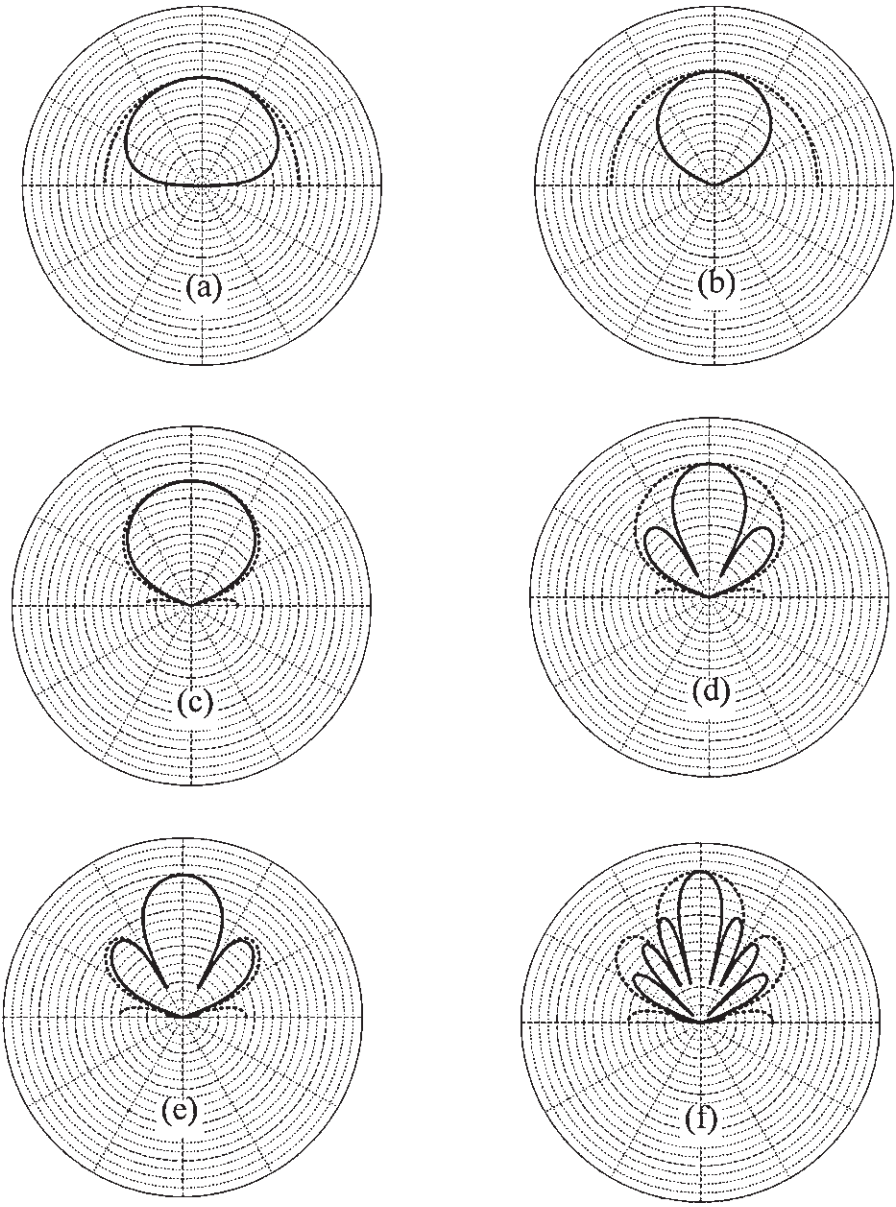

Figure 6-4 The computed patterns for the geometry of Figure 6-3. The E-plane patterns have dashed lines, the H-plane patterns are solid. (a) Single antenna element. (b) Two antenna elements. (c) Four antenna elements. (d) Eight antenna elements. (e) Sixteen antenna elements. (f) Thirty-two antenna elements.

and the minimized gain of a binomial array with $-\infty$ dB sidelobes is an optimum choice known as a Dolph-Chebyshev distribution.[6] The realization of a Dolph-Chebyshev distribution, however, can prove to be very challenging. Often, in practice, nonoptimum aperture distributions relinquish only a small amount of gain and are more readily realizable than an optimum distribution. A normalized linear taper on a pedestal is one which has a maximum value of one at the center of the array and tapers to a value of C at the maximum extent of the array. Because the distribution tapers to a nonzero value at its edge, it is said to be on a pedestal. A cosine on a pedestal distribution superimposes a cosine curve which has a nonzero value of C at the edges of an array. The expressions that describe these distributions are summarized below:

- Uniform

$$I_n = 1 \tag{6.14}$$

- Linear taper on a pedestal

$$I_n = C + (1-C)\left[1 - \frac{|x_n|}{L_A}\right] \tag{6.15}$$

- Cosine taper on a pedestal

$$I_n = C + (1-C)\cos\left[\frac{\pi}{2}\frac{x_n}{L_A}\right] \tag{6.16}$$

- Cosine squared taper on a pedestal

$$I_n = C + (1-C)\cos^2\left[\frac{\pi}{2}\frac{x_n}{L_A}\right] \tag{6.17}$$

- Quadratic taper on a pedestal

$$I_n = C + (1-C)\left[1 - \left(\frac{x_n}{L_A}\right)^2\right] \tag{6.18}$$

x_n is the location of the nth element along the x axis, as shown in Figure 6-6 for a linear taper. The length of the array is $2L_A$. I_n is the excitation value for each element n. For an array with an odd number of elements, the element at the center of the array is located at x_0 and has a normalized value equal to one ($I_0 = 1$). When an array has an even number of elements, the I_0 element is removed and only the even elements remain. Figure 6-6 illustrates a linear taper on a pedestal of value C. The excitation distribution is linear in Figure 6-6 and is on a pedestal of value C. The value of C may be expressed as a decibel level with respect to the unity excitation value in the center:

$$C = 10^{(C_{dB}/20.0)} \tag{6.19}$$

For a –16 dB taper we compute $C = 0.1585$, which may be used in equations (6.15) through (6.18). Figure 6-5 contains patterns computed with a uniform, linear, and cosine taper computed with equation (6.15) and equation (6.16) and using the values of the 5.3 GHz patches in the previous section. We can see that for a 64-element, 8×8 array, the uniform distribution provides the maximum main beam gain of 23.60 dBi (assuming 100% efficiency). We can reduce the sidelobe level to –21.7 dB with a –16 dB linear taper, and the gain of the main beam decreases by 0.70 dB, which is the trade-off one makes for a lower sidelobe level. A –16 dB cosine squared on a pedestal reduces the main beam gain by –1.20 dB compared with a uniform distribution, but the sidelobe level is now approximately –26 dB. Figure 6-6 presents an illustration of how the aperture functions are sampled to determine the excitation values, I_n. The origin of the coordinate system is on the center of patch 1. A vector to the center-most patch is formed. For an even array—2×2, 4×4, etc.—$\vec{r}_c$ is a vector to the center of the array. In the geometry of Figure 6-7, equation (6.20) describes the location of $\vec{r}_c$. The vector from each patch to the array center patch, $\vec{r}_d$ [equation (6.21)], is used to provide the distance $d_n (= x_n)$ [equation (6.22)]. The value L_A is defined with equation (6.23). The values of d_n and L_A are placed into equation (6.15) for a linear taper on a pedestal and equation (6.16) for a cosine taper on a pedestal for each n patch element.

$$\vec{r}_c = \frac{L_x}{2}\hat{i} + \frac{L_y}{2}\hat{j} \tag{6.20}$$

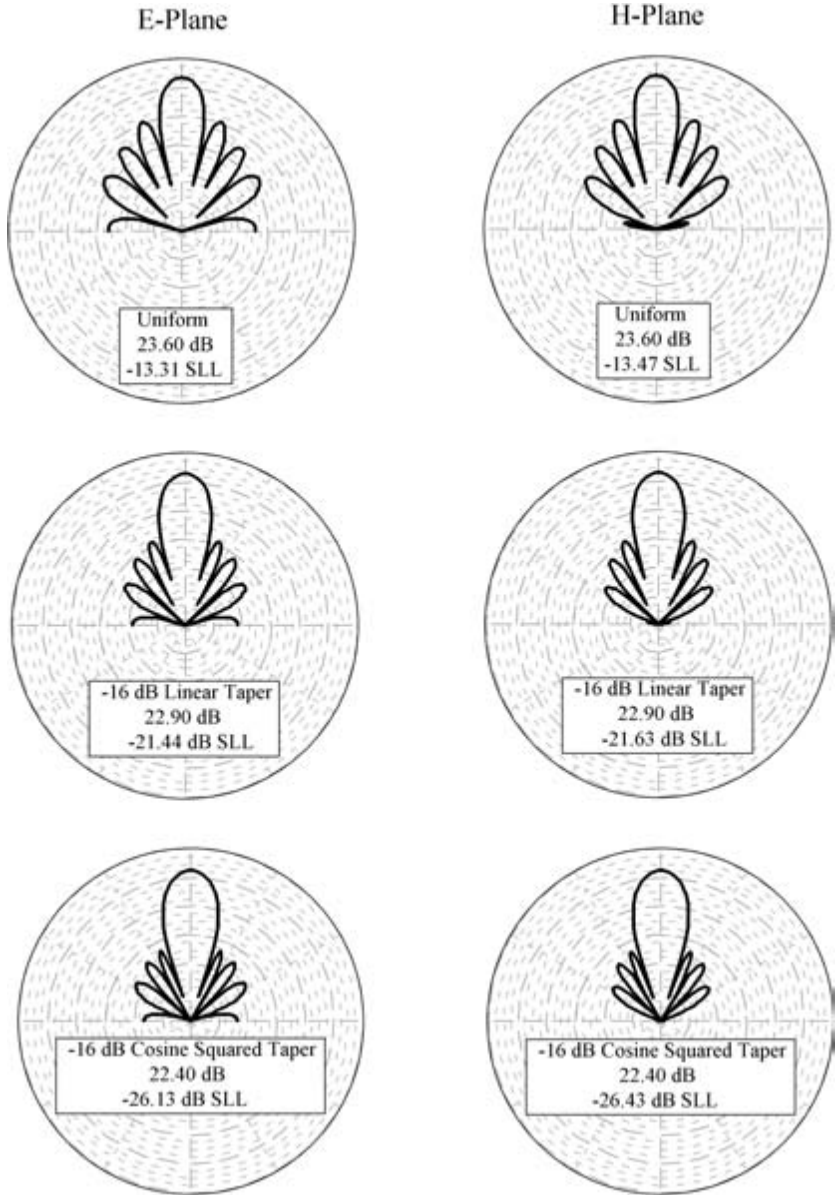

Figure 6-5 The computed E- and H-plane patterns for a 64-element antenna array (8×8) with uniform, −16 dB linear taper on a pedestal and −16 dB cosine squared taper on a pedestal.

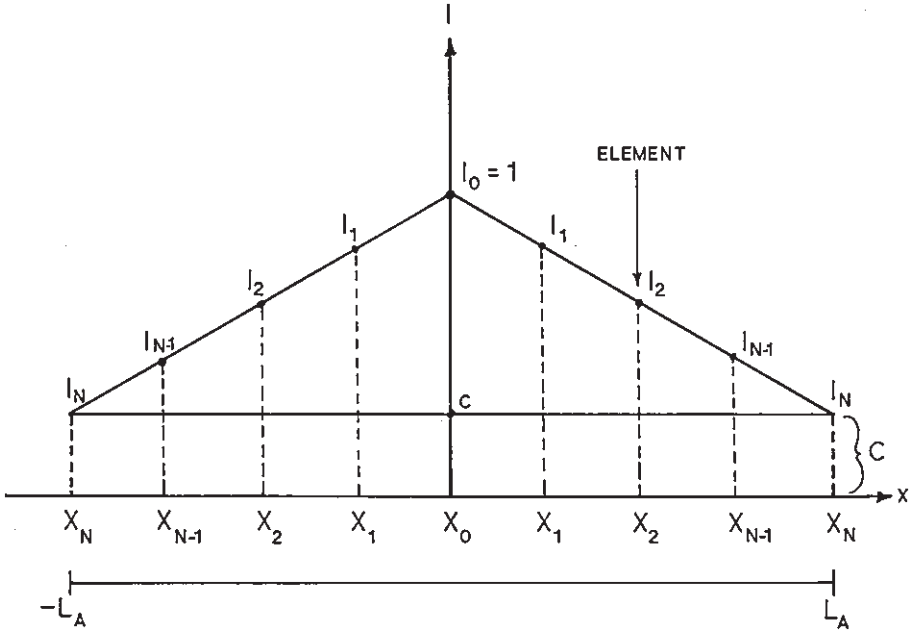

Figure 6-6 Linear taper on a pedestal.

$$\vec{r}_d = \vec{r}_c - \vec{r}_n \tag{6.21}$$

$$d_n = |\vec{r}_d| \tag{6.22}$$

$$L_A = |\vec{r}_c| \tag{6.23}$$

The distributions of equations (6.14) through (6.18) are useful for most array implementations. When choosing a distribution, one first obtains designs that meet the directivity and sidelobe requirements. The pedestal value C determines the sidelobe level of the array in each case. Generally it is easiest to realize a distribution with the minimum taper which meets the pattern requirements. This choice also minimizes the beamwidth which keeps the pattern directivity maximized. The quadratic and cosine squared distributions have the most gentle variation of the non-uniform distributions presented. The linear distribution has an aperture taper which decreases at the highest rate of the given distributions.

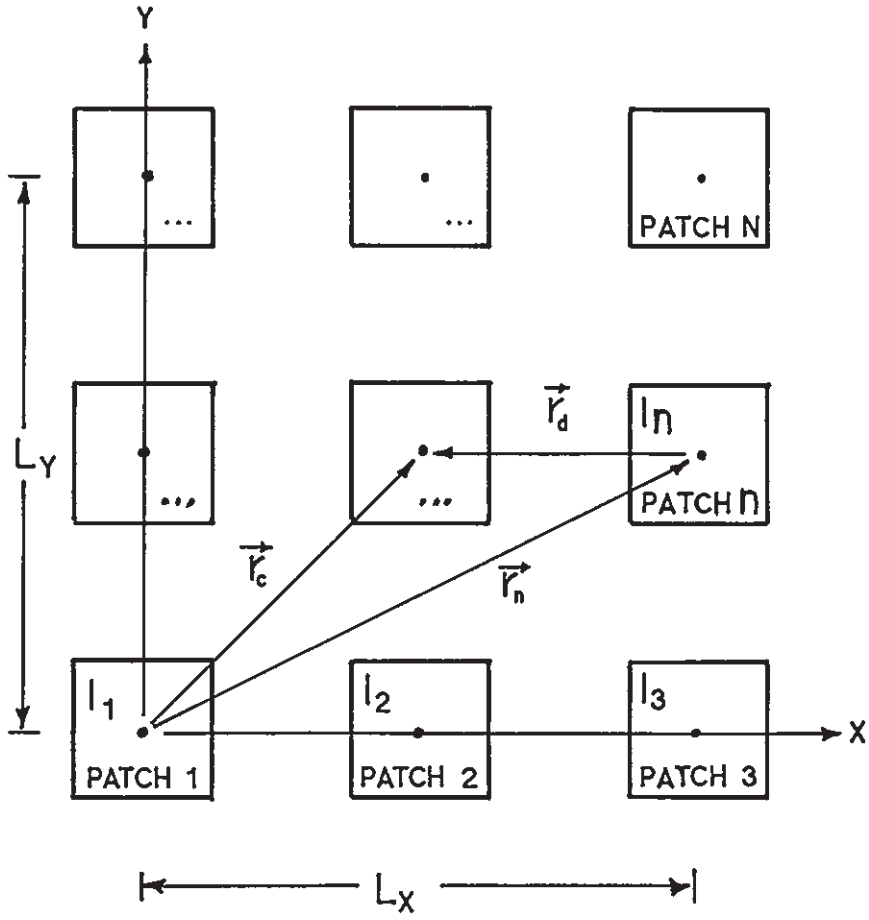

Figure 6-7 The distribution values I_n for a linear taper on a pedestal and cosine on a pedestal may be obtained by using equation (6.15) and equation (6.16). The distance from the center of the array $\vec{r}_c$ to the center of patch n ($\vec{r}_n$) determines the scalar value $d_n = |\vec{r}_c - \vec{r}_n|$ the value of $L_A = \vec{r}_c$.

6.4 Microstrip Array Feeding Methods

6.4.1 Corporate Fed Microstrip Array

The array feed methods that are most popular are corporate feeding and series feeding. Series feeding has a number of difficulties involved in its implementation. The beam direction is sensitive to frequency, and producing a desired

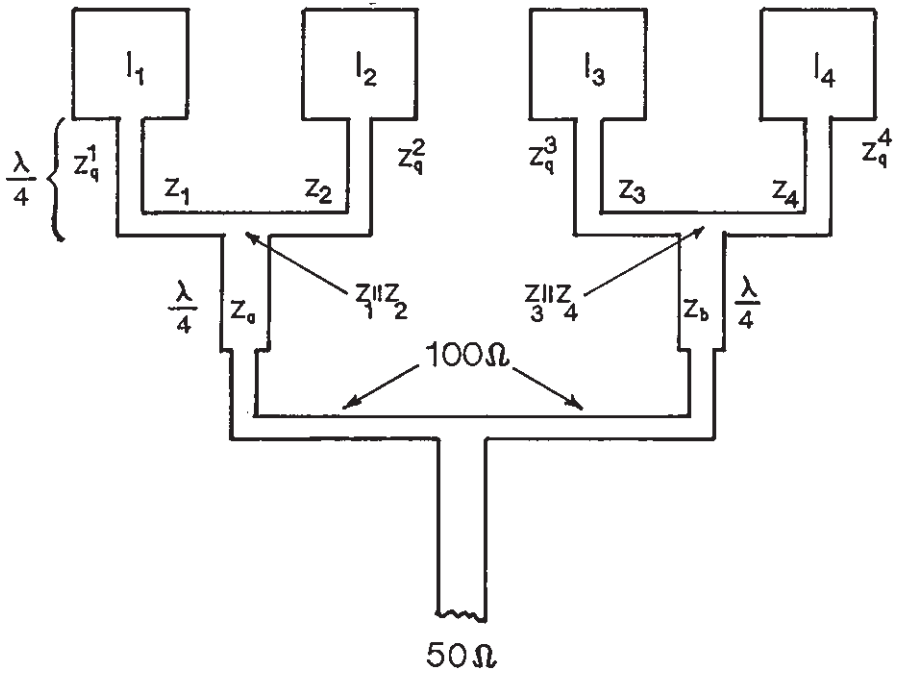

Figure 6-8 Four patch linear array fed with a microstrip corporate feed network.

amplitude taper can prove to be difficult. The design details of series fed arrays will be addressed in the next section.[7]

To illustrate an elementary corporate feed network we will feed a linear array of four patch antennas, as illustrated in Figure 6-8. Each of the identical square patch antennas has an element input resistance R_{in} at resonance [$R_{in} = R_e/2 = 1/(2G_e)$]. This element resistance at each patch may be matched to connecting transmission line impedances Z_1, Z_2, Z_3, Z_4, which will be used to provide a desired power split. This is accomplished with a number of quarter-wave transformers: Z_q^1, Z_q^2, Z_q^3, Z_q^4.

To simplify this design we will feed the linear array with a 50 Ω microstrip transmission line into a pair of 100 Ω lines. This will split the power in an equal manner to Z_a and Z_b quarter-wave transformers. These transformers are used to match between the 100 Ω feed line and the pair of transmission lines used to divide the incident power between each pair of patches (i.e., 1 and 2, 3 and 4). In the case of patch 1 and patch 2, we wish to provide them with current

I_1 and I_2. We obtain these desired currents by realizing that the voltage at the junction of Z_1 and Z_2 is common. The power propagated in each transmission line can be equated to the power in each patch to produce the desired current I_1 and I_2:

$$\frac{I_1^2 R_e}{I_2^2 R_e} = \frac{V_0^2/Z_1}{V_0^2/Z_2} \tag{6.24}$$

The ratio of I_1 to I_2 is controlled by the ratio of Z_2 and Z_1:

$$\frac{I_1^2}{I_2^2} = \frac{Z_2}{Z_1} \tag{6.25}$$

Once we have chosen the desired ratio of the current we can choose the ratio of the transmission line impedances.

As an example, let us choose an operating frequency of 5.25 GHz. A square patch with $a = b = 15.7$ mm on a 1.524 mm thick substrate $\varepsilon_r = 2.6$ has an element edge resistance of $R_{in} \approx 271.21\ \Omega$.

When etching microstrip circuits, most printed circuit board shops do not like to have line widths smaller than 152 μm (0.006 inches). This provides us with a maximum line impedance that may be used. For this substrate this value is 180 Ω. If $I_1 = I_4 = 0.50$ and $I_2 = I_3 = 0.75$:

$$\frac{Z_2}{Z_1} = \frac{(0.50)^2}{(0.75)^2} = \frac{1}{2.25}$$

We know the element resistance of the patch antenna at resonance (R_{in}) and may choose the quarter-wave transformer for patch 1 (Z_q^1) to be the maximum impedance of 180 Ω, thus we can compute the value of Z_1:

$$\frac{(Z_q^1)^2}{R_{in}} = Z_1 = 119.5\,\Omega$$

This allows us to compute $Z_2 = 53.11\ \Omega$ with equation (6.25), which then may be used to compute Z_q^2:

$$Z_q^2 = \sqrt{Z_2 \cdot R_{in}} = \sqrt{53.11 \cdot 271.21} = 120.02\,\Omega.$$

The impedance at the power split is $Z_1 \| Z_2 = 36.77\ \Omega$. The quarter-wave transformer Z_a is found as $\sqrt{36.77 \cdot 100.0} = 60.64\ \Omega$.

In this case we have chosen a symmetric array distribution so the values of the impedances for both sides have been evaluated. The loss in a corporate fed array will increase as substrate height increases and dielectric constant decreases. The loss also increases as the feed line impedances decrease.[8] As the dimensions of an array increase, the length of the corporate feed network extends further and further. The microstrip line losses increase and decrease the realized gain of the array and also add to the antenna noise figure. One can reach a point of diminishing return. As the number of array elements (and thus the effective aperture) are increased, the losses from the feed network become larger and larger. The increase in gain produced by a larger aperture can be balanced by the losses in the feed lines or overtaken.

This method of creating a feed network can be used to design the feed network of a planar array. Figure 6-9 has a 4×4 (16 elements) planar array fed with a corporate network. This antenna can be sectioned into four 2×2 subarrays. The distribution can be computed for a subarray and the subarrays can be arrayed to create a planar array.

6.4.2 Series Fed Microstrip Array

A set of microstrip patches may be fed in series with microstrip transmission line connecting their radiating edges.[9,10] This is illustrated in Figure 6-10(a). The microstrip realization of the series array is on the left in Figure 6-10. The patches are separated by microstrip transmission line which has a $\lambda/2$ guide wavelength. In theory the characteristic impedance of the transmission line is not critical because each of the loads created by the edges of a microstrip radiator are all one-half wavelength in spacing. This is shown in the illustration of Figure 6-10(b). At resonance, the pair of slots of each rectangular microstrip element may be combined to form an equivalent admittance. A load that represents each patch is separated by half-wavelength sections of microstrip transmission line. This is illustrated in Figure 6-10(c). This separation allows one to compute the input resistance of the series fed array at resonance as

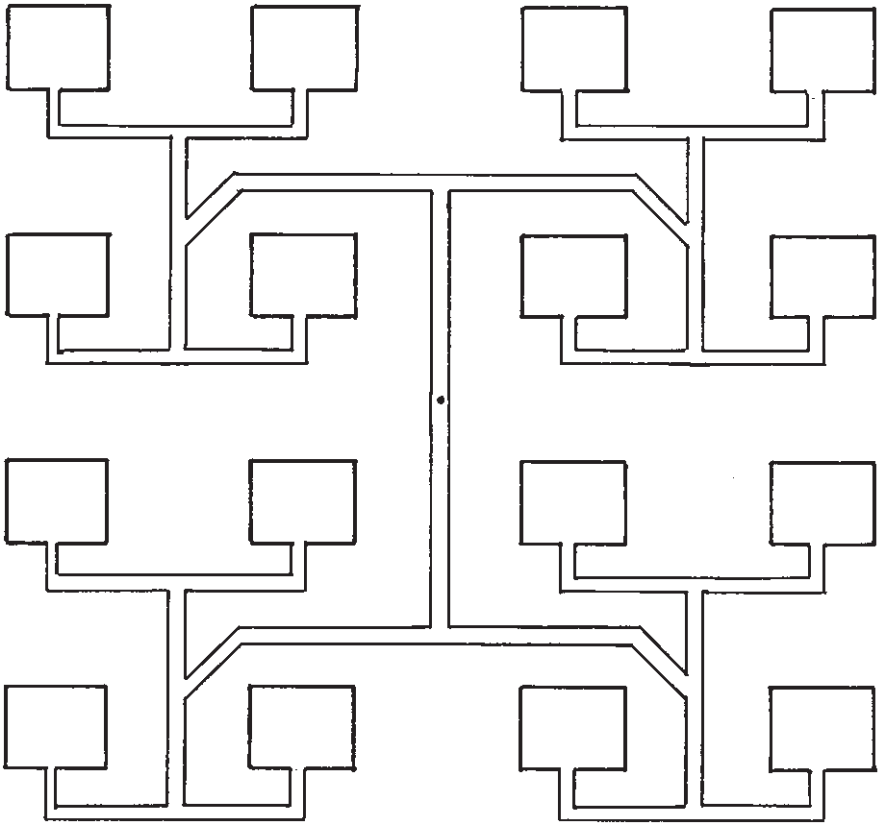

Figure 6-9 Four-by-four patch planar array fed with a microstrip corporate feed network. Heavy dot in the center is the feed point.

$$R_{in} = \left(2 \sum_{n=1}^{N} G_n \right)^{-1} \tag{6.26}$$

where G_n is the edge conductance at each edge of each patch. For example, if all the patches in a series fed array have the same slot conductance G_e at resonance, we may express the input resistance as

$$R_{in} = \frac{1}{2NG_e} \tag{6.27}$$

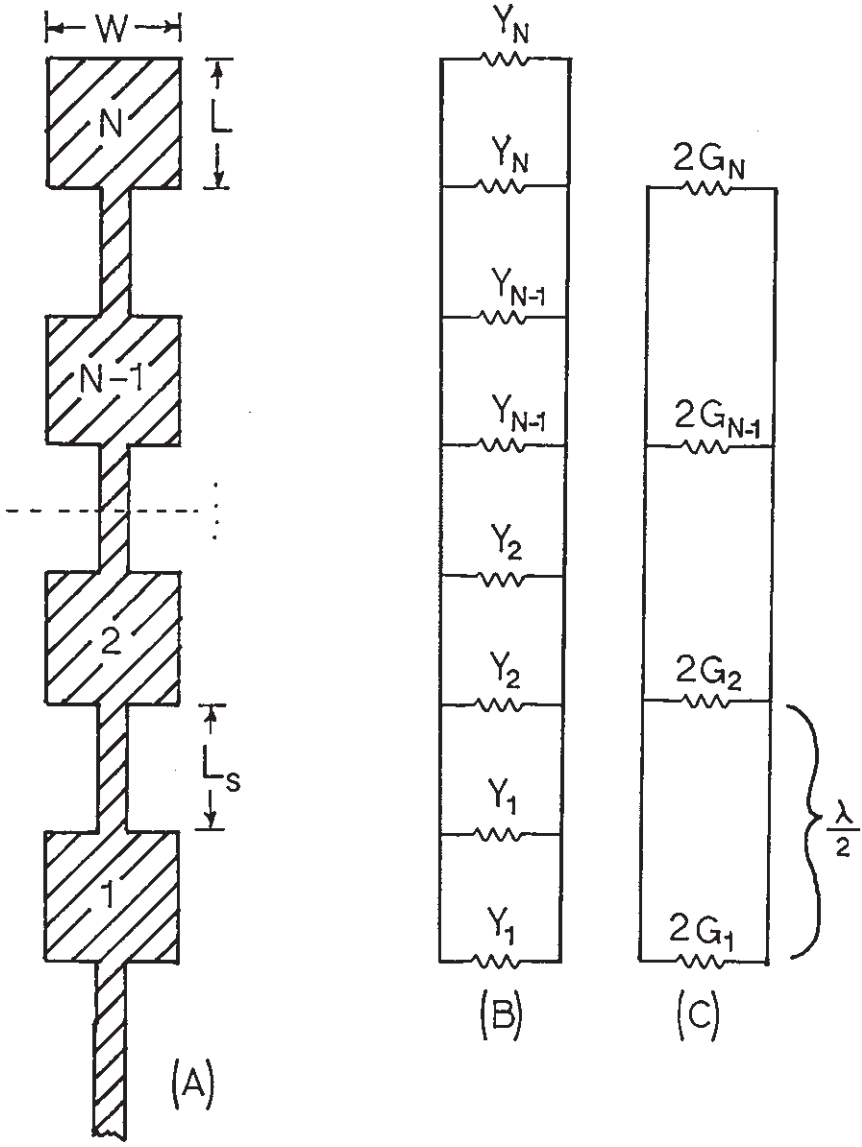

Figure 6-10 (a) Series fed microstrip array. (b) Transmission line representation of series microstrip array. (c) Microstrip elements represented as lumped resistive loads between half-wave sections of transmission line.

This expression allows one to choose a value of G_e that allows for the design of a series fed array with uniform distribution that has a desired input resistance.

As an example, we choose a series fed array with four elements ($N = 4$). When a 50 Ω input resistance is chosen, the edge resistance of each slot ($R_e = 1/G_e$) is 400 Ω. We can then use equation (2.4) to approximate the width of a patch that produces this edge resistance. One can use full-wave analysis methods to refine this patch width to produce an element that has an edge resistance closer to the desired value of 400 Ω ($R_{in} = 200$ Ω) than these approximate expressions can provide. When the antennas are connected, there will be a slight shift in frequency from the loading of the radiating edges.

For the example above we use a dielectric substrate with $\varepsilon_r = 2.6$ and a substrate thickness of $H = 1.524$ mm. The width (W) of each patch is 19.4 mm with a resonant length of 17.0 mm. The patches are interconnected with 100 Ω transmission line. This is done to minimize the influence of the interconnects on the design.

The design of a single patch was accomplished using the finite difference time domain (FDTD). A single patch antenna was developed which was of an approximate size to produce a 200 Ω element resistance ($R_e = 400$ Ω, $R_{in} = R_e/2 = 1/2G_e$). This was connected through a 100 Ω quarter-wave transformer to a 50 Ω feed line. When this patch is well matched to the transformer and feed line it should have a 200 Ω element resistance R_{in}.

A four patch series array was designed using the patch design obtained using FDTD analysis. The array is matched at 5.09 GHz with a 1.35% (2:1) voltage standing wave ratio (VSWR) bandwidth. The substrate thickness is 1.524 mm (0.060 inches) with $\varepsilon_r = 2.6$ and $\tan\delta = 0.0025$. The length of each patch is L =17.0 mm with a width W = 19.4 mm. The four patches are connected with 0.8 mm wide ($Z_0 = 100$ Ω) microstrip transmission line of length 19.08 mm. The bottom-most patch is fed with one of these line sections, which are $\lambda/2$ and fed with a 4.12 mm ($Z_0 = 50$ Ω) feed line. The groundplane is 44 mm × 128 mm.

The E-plane and H-plane patterns computed using FDTD analysis are presented in Figure 6-11. The maximum directivity is 12.74 dB. One can see the elements array along the E-plane and maintain their individual element patterns in the H-plane.

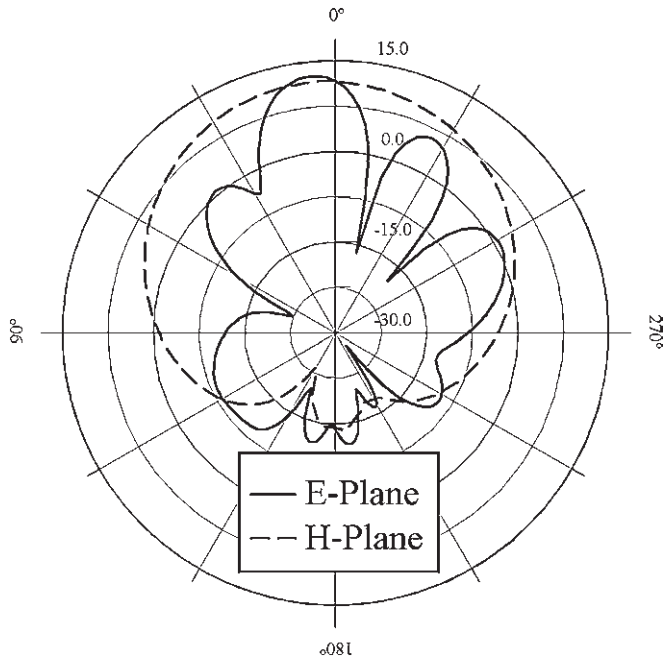

Figure 6-11 Four-by-four patch with uniform element excitation planar array.

The main beam of a series array is broadside to the array at resonance with proper spacing. The main beam will squint from broadside with frequency. The bandwidth of this type of array is rather narrow and in general only about 1 % to 2%.[11] As additional patches are added, the impedance bandwidth of a series array narrows.

The previous design example has patches of identical width. When this is the case, all the elements have the same excitation amplitude.

If we wish to produce an amplitude taper to decrease the array sidelobe level we can change the widths of each patch to accept a designated amount of power. The power accepted by the nth element of a series array is

$$P_n = 2g_n V^2 \tag{6.28}$$

The value g_n is the conductance of each antenna n normalized to the desired driving point resistance, which in this case is 50 Ω:

$$g_n = 2G_n \cdot Z_{drv} = \frac{2G_n}{G_{drv}} \tag{6.29}$$

V is the voltage across each element. The power radiated by an element is proportional to the square of the electric field. The electric field is proportional to the excitation coefficient I_n. We can produce an amplitude distribution along a series fed array by choosing the patch conductivities proportional to the amplitude excitation coefficients:

$$g_n = K I_n^2 \tag{6.30}$$

where K is a constant of proportionality. The elements are all spaced between half-wavelength microstrip transmission line sections so the input conductance (normalized) of the array is the sum of the element conductances:

$$g_{in} = \sum_{n=1}^{N} g_n \tag{6.31}$$

where $g_n = 2.0 \cdot 50.0\ \Omega \cdot G_{e_n}$ and N is the number of elements in the series array. For normalized conductances the condition for input match is

$$g_{in} = \sum_{n=1}^{N} g_n = 1 \tag{6.32}$$

We can substitute equation (6.30) into equation (6.32) and obtain K as

$$K = \left(\sum_{n=1}^{N} I_n^2 \right)^{-1} \tag{6.33}$$

The value of K allows one to compute the element conductances g_n using the desired amplitude values I_n. The element conductances allow one to compute the patch widths required to present these desired conductances and in turn the designated amplitude distribution values.

A simple illustration of how to introduce an aperture taper into a series array is to begin with the uniform array example examined previously. The uniform array has four elements, each element contributes the same conductance (i.e.,

G_n = constant). A realistic taper for the physical realization of a four-element series array is to widen the two center elements by a factor of 1.5 and reduce the outer elements to one-half of the original width. When this is done, the sum of the conductances remains constant and the series array remains matched as it was in the uniform conductance example. FDTD analysis results demonstrate the input match and the resonant frequency of 5.09 GHz remain constant when the array is modified in this way. The modified array is shown in Figure 6-12. This tapering of the patch widths translates to a –4.04 dB linear taper. The array directivity is 12.86 dB.

The pattern computed by FDTD analysis is shown in Figure 6-13. We can see the sidelobe on the left side at approximately 45° has all but vanished, and the sidelobe on the right at approximately 30° has been reduced considerably. If one chooses to widen the inner two patches further and narrow the outer two patches so a 50 Ω driving point impedance is maintained, the narrow patches will be more affected by the feed lines as their dimension decreases.

A second option for a series fed array is to feed the antennas along nonradiating edges. One can choose the position of each input and output location on each patch to provide a desired amplitude taper. The design of this type of array is very involved mathematically and details may be found in the literature.[12–14]

6.5 Phase and Amplitude Error

The arrays examined in this chapter all assume the currents in the radiating elements of an array are excited in phase (i.e., $I_n \angle 0^\circ$) with the proper amplitudes. In any physically realized array, the phase of the excitation current of the elements in the array will deviate from the desired phase values. The sources of error are numerous. The dielectric constant and thickness of a substrate material can vary with location in a given sheet. This changes the propagation constant of the microstrip lines as well as their impedance values. The driving point impedance of elements will be affected as well. When elements are closely located, mutual coupling can introduce amplitude and phase error. A good introduction to the effects encountered because of mutual coupling is given by Malherbe.[15] Although corrections for microstrip discontinuities are presented in Appendix C, their relative accuracy can produce phase

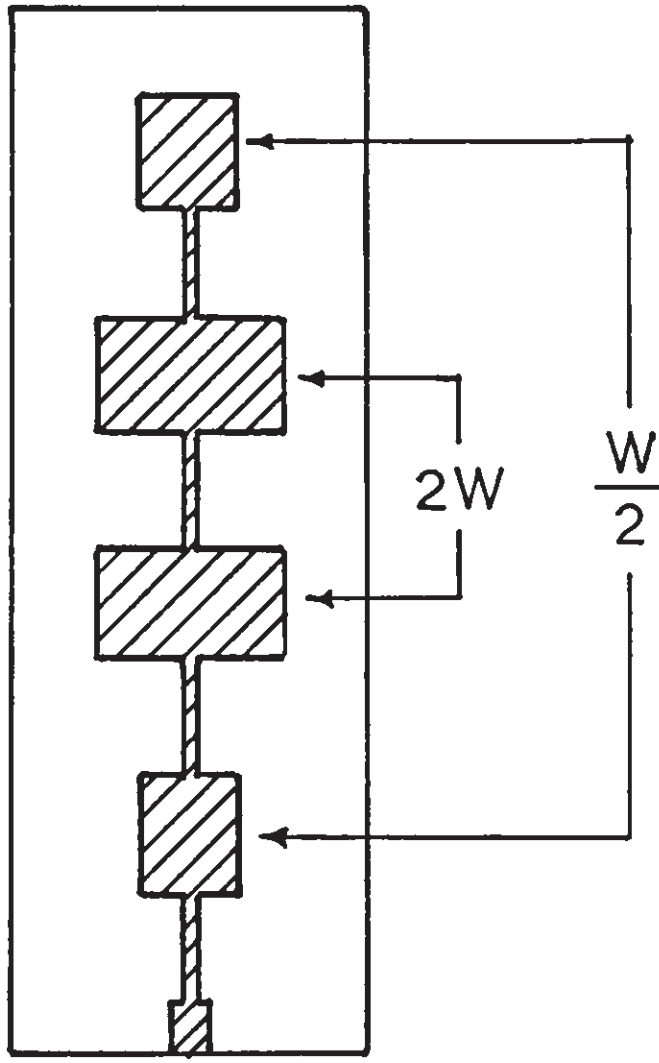

Figure 6-12 Four patch series fed planar array of Figure 6-10 with the center two elements widened to 2*W* and the outer-most elements reduced to a width of *W*/2. This modification creates a –4.04 dB amplitude taper. The radiation patterns of this array are presented in Figure 6-13.

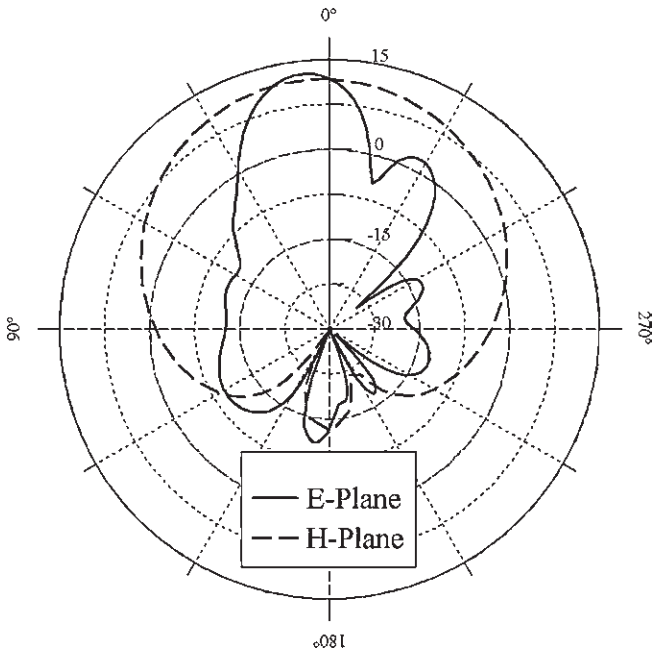

Figure 6-13 Four-by-four patch planar array modified to have a –4.04 dB linear taper.

and amplitude errors for different power splits in a corporate fed array. Deterministic amplitude errors generally fill in pattern nulls and increase sidelobe level. Random amplitude and phase errors are associated with a minor increase in sidelobe level and a decrease in gain. Large corporate fed microstrip phased arrays have numerous junctions and bends which can be sources of undesired radiation that can increase sidelobes. One must also use elements that are matched as perfectly as possible to maintain the best phase and amplitude relationship to theory as possible.

6.6 Mutual Coupling

When multiple microstrip antenna elements are arrayed, the elements will couple to one another. One mechanism by which coupling occurs is surface

wave generation. One can use the analysis presented in Section 2.8 to minimize surface wave generation.

Often with element spacings encountered in practice, the amount of coupling between microstrip elements is small enough to be neglected. When interelement coupling is significant enough to be included, often in practice, measured values of coupling are used in place of analysis. The availability of full-wave analysis methods allow one to compute mutual coupling with relative ease compared with the approximate analysis offered here.

One can analyze the effects of mutual coupling using network methods. The voltage and current at the driving point of each element in an antenna array with the coupling of all the other elements included is related by equation (6.34).

$$\begin{vmatrix} V_1 \\ V_2 \\ V_3 \\ \vdots \\ V_{N-1} \\ V_N \end{vmatrix} = \begin{vmatrix} Z_{11} & Z_{12} & Z_{13} & \cdots & Z_{1N} \\ Z_{21} & Z_{22} & Z_{23} & \vdots & Z_{2N} \\ Z_{31} & Z_{32} & Z_{33} & \vdots & Z_{3N} \\ \vdots & \vdots & \vdots & \vdots & \vdots \\ Z_{N,1} & Z_{N,2} & Z_{N,3} & \cdots & Z_{N,N} \end{vmatrix} \begin{vmatrix} I_1 \\ I_2 \\ I_3 \\ \vdots \\ I_{N-1} \\ I_N \end{vmatrix} \tag{6.34}$$

Each row of the matrix equation can be written out. The voltage at the driving point of element 1 of an array of N elements becomes

$$V_1 = Z_{11}I_1 + Z_{12}I_2 + Z_{13}I_3 + \ldots + Z_{1N}I_N \tag{6.35}$$

We can divide both sides of equation (6.35) by I_1, which produces an equation that relates the driving point impedance of element 1 in terms of the ratio of currents in each of the other elements to the current in element 1. This equation is called the active impedance of element 1 (Za_1):

$$Za_1 = Z_{11} + Z_{12}\frac{I_2}{I_1} + Z_{13}\frac{I_3}{I_1} + \ldots + Z_{1N}\frac{I_N}{I_1} \tag{6.36}$$

In general, for each element n with $m = 1, 2, 3, \ldots \acute{N}$ we write

$$Za_n = \frac{V_n}{I_n} = \sum_{m=1}^{\acute{N}} \frac{I_m}{I_n} Z_{mn} + Z_{nn} \tag{6.37}$$

The $\acute{N}$ in equation (6.37) means the sum which excludes the $m = n$ term.

The currents at each of the elements is unknown initially, but we can use equation (6.37) to iterate to a solution starting with an initial guess at the driving point currents. The starting current for the array can be computed by dividing the driving point voltages by each antenna's self-impedance neglecting coupling:

$$\left|I_n^{s1}\right| = \left|\frac{E_n}{Z_{nn} + Z_0}\right| \tag{6.38}$$

We can then use equation (6.37) to calculate a new active impedance. After the active impedance has been calculated, we calculate a new current distribution, keeping the voltage distribution constant. The current at the kth iteration is

$$\left|I_n^{fk}\right| = \left|\frac{E_n}{Z_{an} + Z_0}\right| \tag{6.39}$$

The superscript f is the final current for iteration k and which drives element n.

A new starting current for iteration $k + 1$ is found with

$$\left|I_n^{s(k+1)}\right| = \frac{1}{2}\left|I_n^{sk} + I_n^{fk}\right| \tag{6.40}$$

At each iteration an error is evaluated using

$$\text{Error} = \sum_{i=1}^{N} \left|Re[I_i^{fk}] - Re[I_i^{sk}]\right|^2 + \left|Im[I_i^{fk}] - Im[I_i^{sk}]\right|^2 \tag{6.41}$$

The mutual coupling terms may be computed using the cavity model as related in Section 6.6.1 After the currents have been calculated, the techniques of sections 6.1, 6.2, and 6.3 are used to compute the radiation pattern of the array.

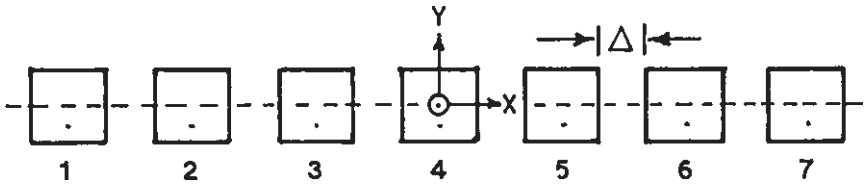

Figure 6-14 Seven-element rectangular microstrip array with H-plane mutual coupling (electric field in y direction) (dots show feed points).

Example: We will use a seven-element linear array of rectangular microstrip antennas to illustrate the effects of mutual coupling.

The geometry of the elements is illustrated in Figure 6-14. The polarization is directed along the y axis. The patches all have identical dimensions. The resonant length of each patch is $a = 50.0$ mm with a width of $b = 60.0$ mm. The substrate thickness is $H = 1.575$ mm with $\varepsilon_r = 2.50$ and $\tan\delta = 0.0018$. The frequency is 1.560 GHz. These values are consistent with those presented by Jedlinka and Carver.

The computation of mutual coupling between rectangular microstrip elements using the cavity model is very sensitive to the value of the wall admittance used in the computation. In many practical cases one can measure the mutual coupling of a fabricated prototype array or employ a full-wave analysis method to determine more accurate mutual coupling values.

We will illustrate the effects of mutual coupling on the radiation pattern of a seven-element array using the cavity model. Section 6.6.1 provides an outline of the computation of mutual coupling between a pair of rectangular microstrip antennas using the cavity model.

In Figure 6-15(a), the seven-element array is excited with a uniform voltage distribution. When no mutual coupling is present, the directivity is maximum. When mutual coupling is included with an edge-to-edge spacing of $\Delta = 0.8a$ (where a is the patch width), the directivity decreases, as does the sidelobe level. This trend continues as the spacing between nonradiating edges is decreased to $0.6a$.

Figure 6-15(b) presents the patterns of the seven-element array with a voltage excitation that has a –6 dB linear taper on a pedestal. The pattern computed with no mutual coupling is shown, and when the coupling has

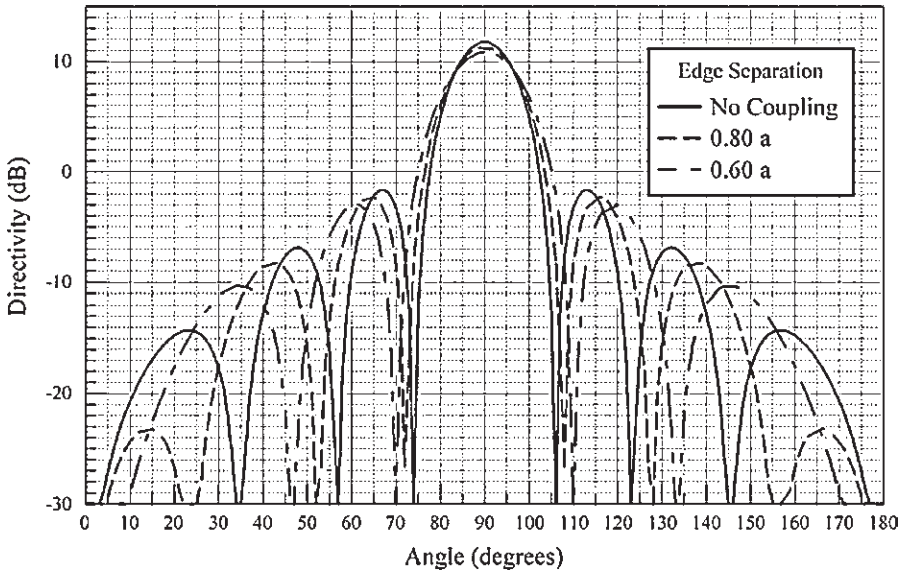

Figure 6-15 (a) Seven patch rectangular microstrip array with uniform excitation with effects of mutual coupling computed with the cavity model.

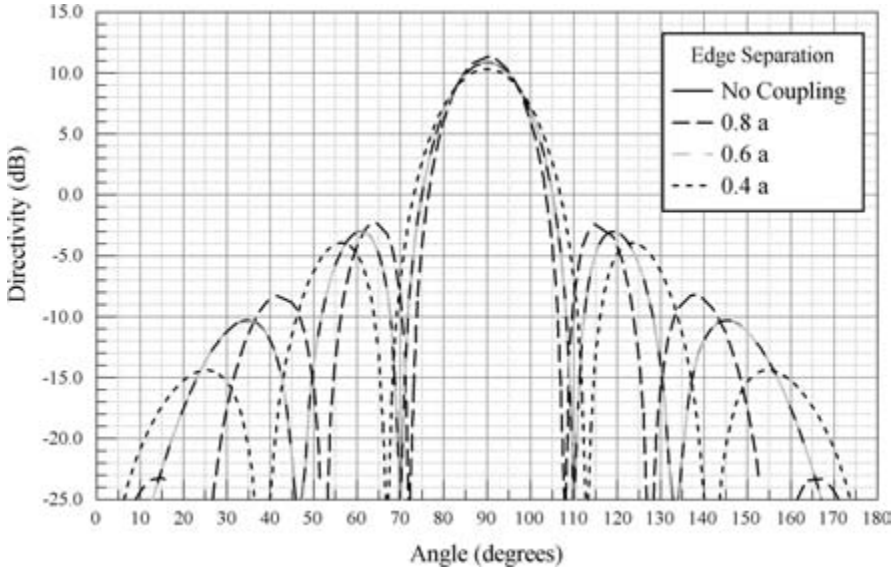

Figure 6-15 (b) Seven patch rectangular microstrip array with –6 dB tapered excitation with effects of mutual coupling computed with the cavity model.

an edge-to-edge separation of $0.8a$ we see that, as before, the directivity decreases but the sidelobe level increases. At $\Delta = 0.6a$, the coupling is such that the current distribution is almost identical to that without mutual coupling. When the spacing is decreased to $0.4a$, the directivity decreases.

6.6.1 Mutual Coupling Between Square Microstrip Antennas

The mutual coupling between two microstrip antennas may be calculated using the following relationship:[16]

$$Z_{21} = \frac{1}{I_1 I_2} \oint \vec{H}^{patch1} \bullet \vec{M}^{patch2} dl_2 \tag{6.42}$$

One can use the cavity model with equation (6.42) to obtain the mutual impedance between probe fed microstrip antennas. I_1 and I_2 are the currents at the feeds of the patches. $\vec{H}^{patch1}$ is the magnetic field on antenna 2 produced by antenna number 1. $\vec{M}^{patch2}$ is the linear magnetic current density on antenna 2 when it has been self-excited. The integration is over the perimeter of antenna 2. The dimensions for this analysis are defined in Figure 6-16.

The patches are located in the x-y plane. The center of patch 1 is the origin of the coordinate system. The center of patch two is at $\vec{r}_0 = X_0\hat{i} + Y_0\hat{j}$. We calculate $\vec{H}^{patch1}$ from the magnetic current at the edge of patch 1. The equivalent magnetic line currents at the edge of the cavity are related to the field at the boundary of the cavity by

$$\vec{M}^{patch2} = 2HE_z(x, y)\hat{z} \times \hat{n} \tag{6.43}$$

The unit vector $\hat{n}$ is an outward normal at the cavity boundary and H is the substrate thickness. The interior electric field is calculated using the cavity model. This relationship is given by

$$E_z(x, y) = \frac{2jI_0\omega \cos\dfrac{\pi y}{b} \cos\dfrac{\pi y_p}{b}}{\varepsilon^* ab[\omega^2 - (\omega_r + j\omega_i)^2]} \tag{6.44}$$

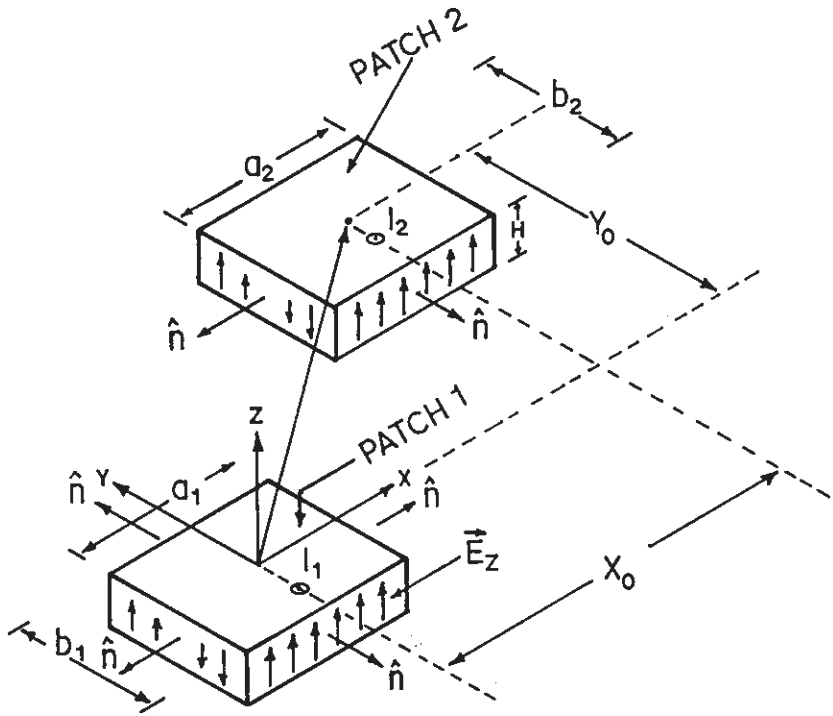

Figure 6-16 Geometry of the cavity model of two rectangular microstrip patch antennas in the x-y plane, with distance between antenna centers, used to compute the mutual coupling using the cavity model.

where

$\varepsilon^* = \varepsilon_r(1 - j\tan\delta)$

ω = angular frequency (radians/sec)

a = width of patch in x plane

b = width of patch in y plane

y_p = y coordinate of feed probe position

I_0 = driving point (i.e., feed point) current

$(\omega_r + j\omega_i)$ = complex resonant frequency.

The normal vectors, magnetic current directions, and numbering of patch edges is illustrated in Figure 6-16. The resulting magnetic current about the patches is shown in Figure 6-17.

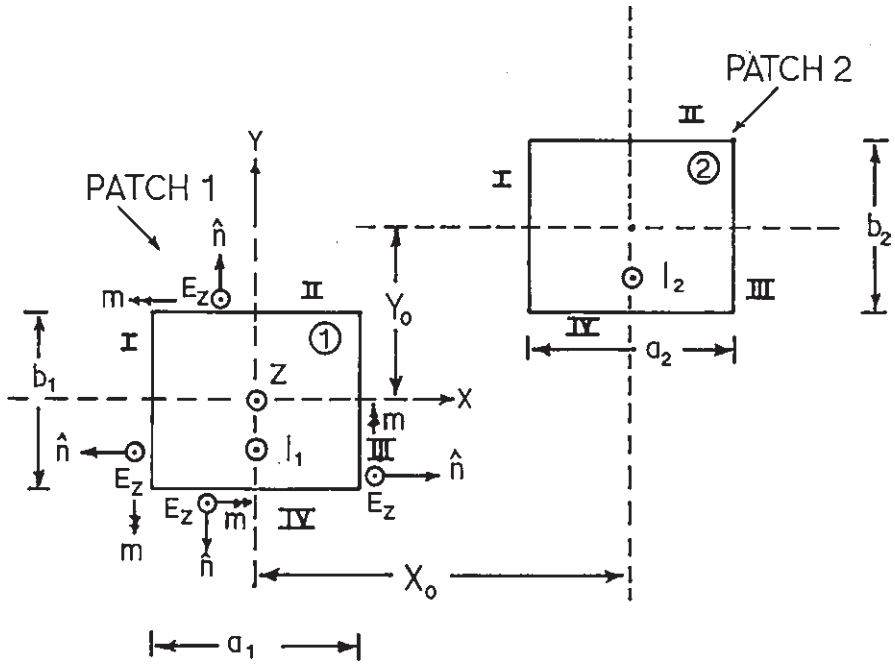

Figure 6-17 Direction of magnetic current on each side of a rectangular microstrip patch antenna defined by equation (6.43) with the cavity model.

The magnetic field radiated by a small $\hat{z}$ directed magnetic current $\vec{M}$ of length Δz is given by[17]

$$\vec{H}(r,\theta) = jw\varepsilon\frac{\vec{M}\Delta z}{4\pi}\left[1+\frac{1}{jkr}+\frac{1}{(jkr)^2}\right]\frac{e^{-jkr}}{r}\sin\theta\hat{\theta}+$$
$$j\omega\varepsilon\frac{\vec{M}\Delta z}{2\pi}\left[1+\frac{1}{(jkr)^2}\right]\frac{e^{-jkr}}{r}\cos\theta\hat{r} \qquad (6.45)$$

For a magnetic current of differential length dz, the differential magnetic field simply becomes

$$d\vec{H}(r,\theta) = jw\varepsilon\frac{\vec{M}dz}{4\pi}\left[1+\frac{1}{jkr}+\frac{1}{(jkr)^2}\right]\frac{e^{-jkr}}{r}\sin\theta\hat{\theta}+$$
$$j\omega\varepsilon\frac{\vec{M}dz}{2\pi}\left[1+\frac{1}{(jkr)^2}\right]\frac{e^{-jkr}}{r}\cos\theta\hat{r} \qquad (6.46)$$

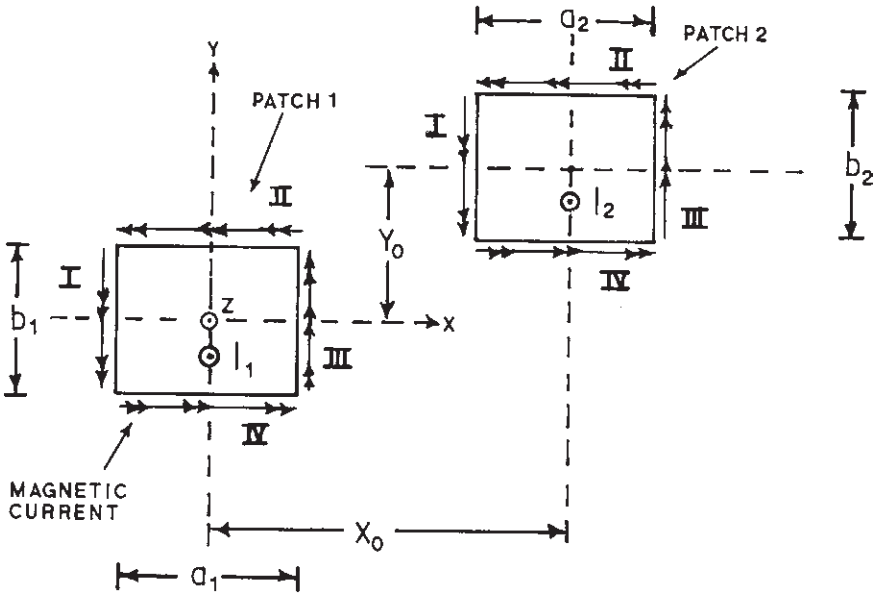

Figure 6-18 Magnetic current around rectangular patch 1, which with equation (6.37) describes the magnetic field at any point along the perimeter of patch 2. With the magnetic field at patch 2 due to patch 1 and the magnetic current of patch 2, equation (6.42) is used to compute Z_{21}.

The magnetic field radiated by patch 1 along some vector $\vec{r}$ may be calculated by integrating the field contributions of the magnetic current from each of its sides:

$$\vec{H}(r,\theta) = j\frac{w\varepsilon}{4\pi}\int_{patch\ 1\ edges} \vec{M}(z)\left[1+\frac{1}{jkr}+\frac{1}{(jkr)^2}\right]\frac{e^{-jkr}}{r}\sin\theta dz\hat{\theta} + j\frac{\omega\varepsilon}{2\pi}\int_{patch\ 1\ edges} \vec{M}(z)\left[1+\frac{1}{(jkr)^2}\right]\frac{e^{-jkr}}{r}\cos\theta dz\hat{r} \qquad (6.47)$$

The $\hat{z}$ directed current has fields expressed in spherical coordinates. In order to facilitate the dot product with the magnetic current around patch 2, rectangular coordinate values are calculated using the expressions below (with $H_\phi = 0$ and $\phi = 90$ when $\vec{r}$ is in the magnetic currents $\hat{z} - \hat{y}$ plane):

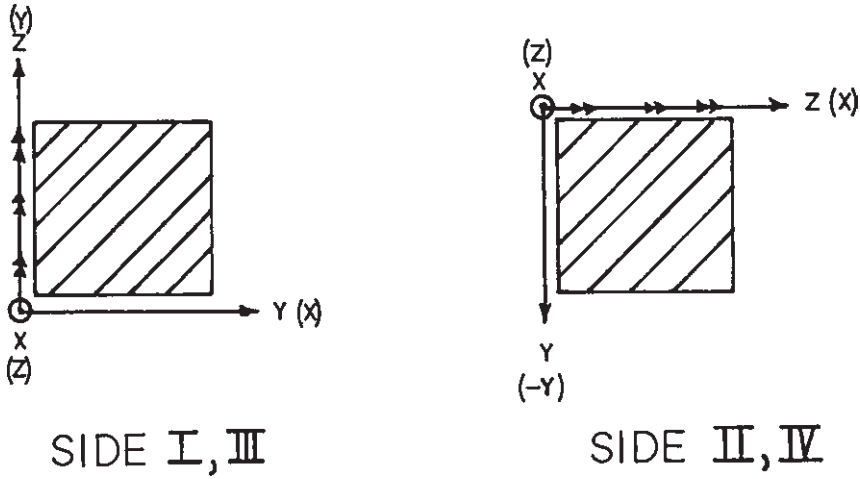

Figure 6-19 Coordinate transformations that facilitate the computation of mutual coupling using equation (6.42).

$$H_y = H_r \sin\theta + H_\theta \cos\theta \tag{6.48a}$$

$$H_z = H_r \cos\theta + H_\theta \sin\theta \tag{6.48b}$$

For side I or III of patch 1, the $\hat{z}$ directed current is placed along the edge in the direction of the $\hat{y}$ axis of the coordinate system for patch 1. In this situation,

$$\vec{H}_x^{\vec{M}} \rightarrow \vec{H}_z$$

$$\vec{H}_y^{\vec{M}} \rightarrow \vec{H}_x$$

$$\vec{H}_z^{\vec{M}} \rightarrow \vec{H}_y$$

For side II or IV of patch 1, the $\hat{z}$ directed current is placed along the $\hat{x}$ axis of the coordinate system of patch 1. In this situation the transformation to the patch coordinate system is accomplished using

$$\vec{H}_x^{\vec{M}} \rightarrow \vec{H}_z$$

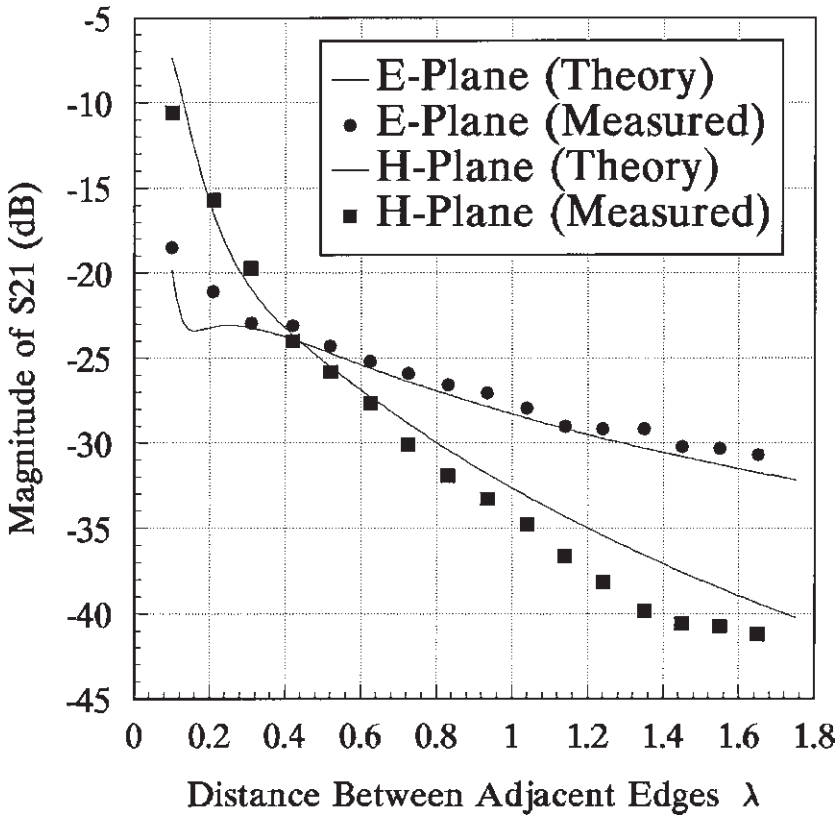

Figure 6-20 Comparison of experimental results of Jedlicka and Carver [16] with those computed with equation (6.42) using the cavity model: $f = 1.56$ GHz, $\varepsilon_r = 2.50$, $a_1 = a_2 = 50.0$ mm, $b_1 = b_2 = 60.0$ mm, $H = 1.57$ mm. The probe feed is located at the center $x = a/2$ of each patch with the probe fed at 8.25 mm from the center ($R_{in} = 50.125\ \Omega$).

$$-\vec{H}_y^{\vec{M}} \rightarrow \vec{H}_y$$

$$\vec{H}_z^{\vec{M}} \rightarrow \vec{H}_x$$

Now that we have calculated the magnetic field from the center of patch 1 at any given distance $\vec{r}$, we may now dot it with the magnetic current around the edge of patch 2 and integrate the resulting function. This completes the evaluation of equation (6.42).

The coupling between a pair of rectangular microstrip antennas has been evaluated and compared with the experimental results of Jedlicka and Carver.[18] The theoretical results are plotted with the experimental results of Jedlicka and Carver in Figure 6-20. The correlation between experiment and theory is good overall and very good from 0.3 to 0.6 λ edge separation.

References

[1] Elliot, R. S., "Bandwidth and directivity of large scanning arrays, first of two parts," *Microwave Journal*, December 1963, Vol. 6, No. 12, pp. 53–60.

[2] Elliot, R. S., "Beamwidth and directivity of large scanning arrays, last of two parts," *Microwave Journal*, January 1964, Vol. 7, No. 1, pp. 74–82.

[3] Hansen, R. C., *Significant Phased Array Papers*, London: Artech House, 1973.

[4] Stutzman, W. L., and Thiele, G. A., *Antenna Theory and Design*, John Wiley & Sons, 1981, pp. 385–391.

[5] Balanis, C. A., *Antenna Theory Analysis and Design*, New York: Harper & Row, 1982, pp. 37–42.

[6] Dolph, C. L., "A current distribution for broadside arrays which optimizes the relationship between beamwidth and sidelobe level," *Proceedings IRE*, June 1946, Vol. 34, No. 6, pp. 335–348.

[7] Sainati, R. A., *CAD of Microstrip Antennas for Wireless Applications*, London: Artech House, 1996, pp. 191–199.

[8] Hall, P. S., and Hall, C. M., "Coplanar corporate feed effects in microstrip patch array design" *IEE Proceedings*, June 1988, Vol. 135, Pt. H, No. 3, pp. 180–186.

[9] Sainati, R. A., *CAD of Microstrip Antennas for Wireless Applications*, London: Artech House, 1996, pp. 210–220.

[10] Collin, R. E., *Antennas and Radiowave Propagation*, New York: McGraw-Hill, 1985, pp. 266–268.

[11] Derneryd, A. G., "Linearly polarized microstrip antennas," *IEEE Transactions on Antennas and Propagation*, November 1976, Vol. 24, No. 6, pp. 846–851.

[12] Derneryd, A. G., "A two port rectangular microstrip antenna element," Scientific Report No. 90, Electromagnetics Laboratory, University of Colorado, Boulder, CO, July 1987.

[13] Gupta, K. C., and Benalla, A., "Transmission-line model for two-port rectangular microstrip patches with ports at the nonradiating edges," *Electronics Letters*, August 13, 1987, Vol. 23, No. 17, pp. 882–884.

[14] Gupta, K. C., and Benalla, A., "Two-port transmission characteristics of circular microstrip patch antennas," *Antennas and Propagation Society International Symposium*, June 1986, Vol. 24, pp. 821–824.

[15] Malherbe, A., and Johannes, G., "Analysis of a linear antenna array including the effects of mutual coupling," *IEEE Transactions on Education*, February 1989, Vol. 32, No. 1, pp. 29–34.

[16] Huynh, T., Lee, K. F., and Chebolu, S. R., "Mutual coupling between rectangular microstrip patch antennas," *Microwave and Optical Technology Letters*, October 1992, Vol. 5, No. 11, pp. 572–576.

[17] Stutzman, W. L., and Thiele, G., *Antenna Theory and Design*, New York: John Wiley & Sons, 1981, p. 98.

[18] Jedlicka, R. P., and Carver, K. R., "Mutual coupling between microstrip antennas," Workshop on Printed Circuit Antenna Technology, Physical Science Laboratory, New Mexico State University, Las Cruces, NM, October 17–19, 1979.

Chapter 7

Printed Antennas

7.0 Printed Antennas

Microstrip antennas have a large number of applications despite their limitations. In some cases, pattern or bandwidth requirements can only be met with planar antennas, which are not a traditional microstrip configuration. These are generally referred to as printed or planar antennas. In some cases, microstrip transmission line may be integrated with an antenna, and often these are still called microstrip antennas. In this chapter we will investigate a number of useful printed/microstrip antenna designs.

7.1 Omnidirectional Microstrip Antenna

An antenna with an omnidirectional pattern is desired for a number of wireless applications.[1] An omnidirectional antenna design which is easily scaled to produce a range of gain values, does not require a balun when fed with a coaxial transmission line, and has a 50 Ω driving point impedance was presented by Bancroft and Bateman.[2] Design details for dual-shorted rectangular omnidirectional microstrip antennas (OMAs) are presented in the literature.[3] Aspects of this design were anticipated by Jasik et al.[4,5] in the early 1970s and by Hill[6], as a traveling wave antenna, in the late 1970s. A similar geometry was related by Ono et al. in 1980.[7]

The geometry of the OMA is presented in Figure 7-1. The antenna consists of a bottom trace that begins with width W_e and length L_e. The trace narrows to W_m and length L_m and alternates between wide and narrow until the final wide section. Both wide end sections are shorted in their center to the upper trace. The upper trace begins at the bottom short with a narrow trace that is

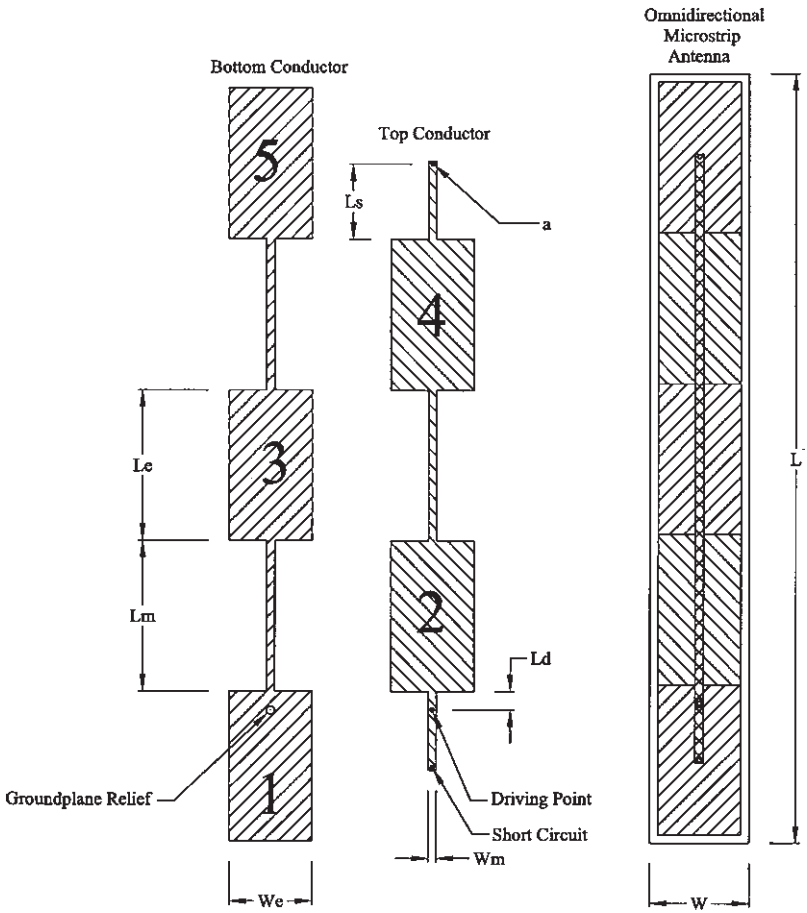

Figure 7-1 Five section rectangular dual-short OMA.

of width W_m which alternates between wide and narrow sections complementing the upper trace. The final upper trace terminates at the upper short. The short at each end connects the upper and lower trace. The driving point is shown in Figure 7-1. The outer shield of a coaxial line is soldered to the wide bottom trace and the center conductor drives the upper trace.

The OMA may be viewed as a set of $\lambda/2$ microstrip transmission lines, which is illustrated in Figure 7-2. The top illustration is of a microstrip transmission

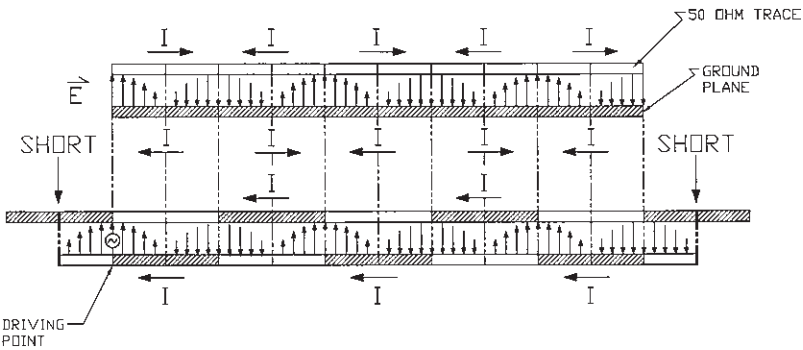

Figure 7-2 Current on a microstrip transmission line (top). Current on flipped sections of microstrip transmission line which make up a seven section OMA (bottom).

line with its currents. Each half-wavelength section of microstrip transmission line is flipped so the groundplane is connected to the trace and the trace is connected to the groundplane of the next section. Each section is a 50 Ω microstrip transmission line, but at each junction the reversal of the groundplane and trace produces a mismatch of the field mode desired by each section. This set of discontinuities encourages radiation. The electric field is maximum at each of the junctions, and the surface current is maximum in the center of each wide section (along the groundplane edges).

The shorting pin at the bottom of the antenna adds a negative 180° phase shift to a downward traveling wave produced by the voltage source ($L_d = 0$) which is 90° behind the driving point phase at the short. As it travels back to the driving point it adds another 90° (360° total) which causes the wave reflected from the lower short to arrive in phase with a wave that is traveling upward along the antenna generated at the driving point. The upper short operates in the same manner so that upward and downward traveling waves are in phase. This creates a resonant structure where the current on each wide groundplane (and the traces) are all in phase, which produces an omnidirectional antenna pattern.

The shorting pins also minimize the amount of current that appears below the short on the driving point end. The outer shield of the coaxial feed line is generally soldered from the driving point edge on the groundplane side to the

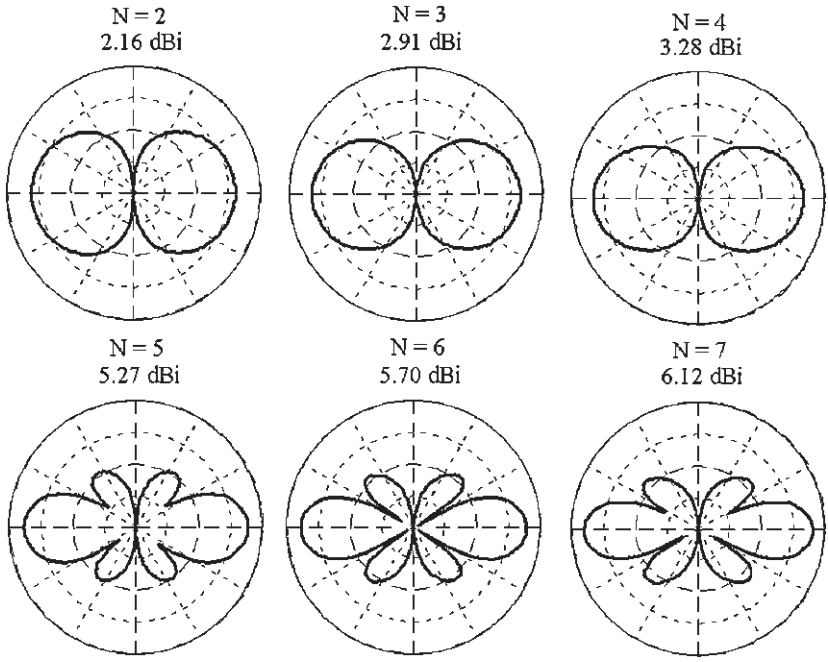

Figure 7-3 Gain of 10 mm wide (W_E) elements.

short. This short decouples the feed line from the antenna below the short (single conductor) so that only a minute amount of current is driven on the outer conductor of the coaxial cable and no balun is required.

The driving point impedance is maximum at the junction of elements 1 and 2 in Figure 7-1. The magnitude of this maximum impedance is inversely proportional to the width (W_e) of the elements. As the width of the elements is decreased, the maximum impedance at the junction increases; when W_e is increased, the impedance maximum decreases. Generally one can find a 50 Ω driving location between the bottom short (0 Ω) and the maximum driving point resistance at the junction.

The total number of sections making up the total length of the antenna may be altered to provide a desired gain. The gain of a rectangular dual-short OMA versus the number of elements for W_e = 10 mm and 20 mm is shown in Figure 7-3 and Figure 7-4, respectively. The antennas were analyzed using Ansoft

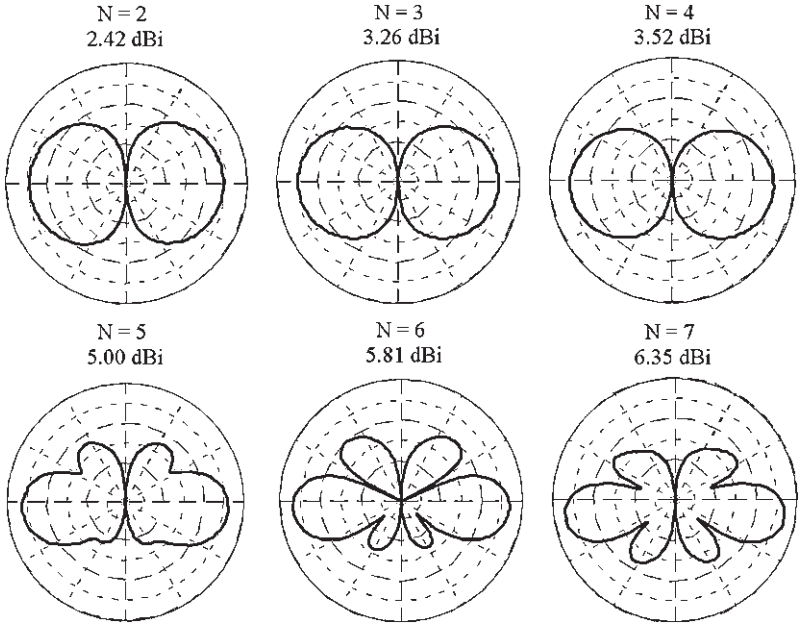

Figure 7-4 Gain of 20 mm wide (W_E) elements.

HFSS with H = 0.762 mm, ε_r = 2.6, W_m = 2 mm, and a = 0.5 mm operating at 2.45 GHz. One can see the gain steadily increases as the total number of elements increases.

The wider the elements, the higher the antenna efficiency, but at the expense of pattern shape. When the antenna elements are narrow (10 mm), the antenna patterns are symmetric and omnidirectional. As the width is increased (20 mm), a lower frequency resonance moves upward and produces a superposition of modes. The lower frequency mode has a butterfly type of radiation pattern which increases the sidelobe level of the design. This is illustrated in Figure 7-3 and Figure 7-4.

The impedance bandwidth for the dual-short rectangular OMA driven in a pure omnidirectional mode is about 3% to 4%, almost independent of the length.

The antenna efficiency is very stable for W_e = 20 mm versus the number of elements (96.5% for N = 2 and 94.7% for N = 7 as predicted by HFSS), but drops

with length as the number of elements is increased for $W_e = 10$ mm (91.3% for $N = 2$ and 87.6% for $N = 7$).

A seven-section OMA was designed to operate at 2.45 GHz on 0.762 mm (0.030 inches) laminate material. The relative dielectric constant of the substrate is $\varepsilon_r = 2.6$ with $\tan\delta = 0.0025$. The dimensions of the antenna are $W_m = 2.06$ mm, $W_e = 16.25$ mm, $L_e = L_m = 36.58$ mm. Shorting pins located on either end of the antenna have a 0.5 mm radius (a). The antenna is fed with a probe at the junction where the first narrow line and the next wide section meet (i.e., $L_d = 0$) in Figure 7-1. The dielectric material extends out 2.0 mm from each side and 2.0 mm from each end.

The finite difference time domain (FDTD) method was used to compute the expected radiation patterns.[8] A sinusoidal 2.586 GHz source was utilized to compute the radiation patterns of the antenna. They are presented in Figures 7-5(a–c) with corresponding measured radiation patterns. The best antenna

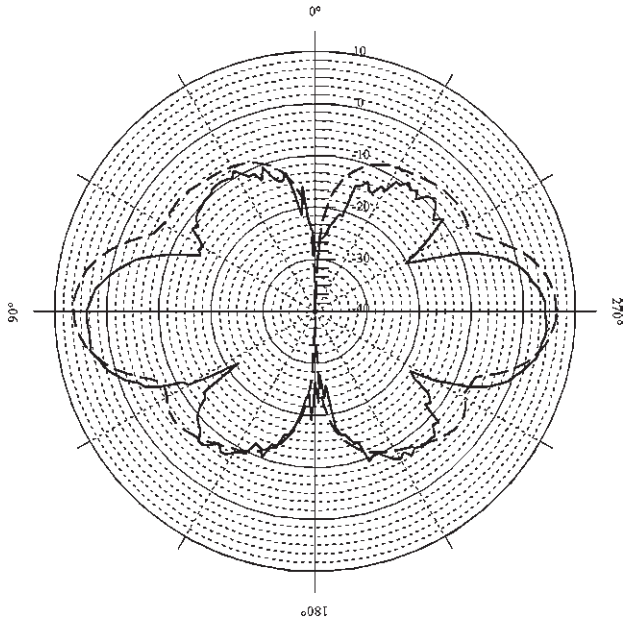

Figure 7-5 (a) The *y-z* plane radiation patterns of an OMA computed using FDTD analysis (dashed) and measured (solid) for 2.586 GHz.

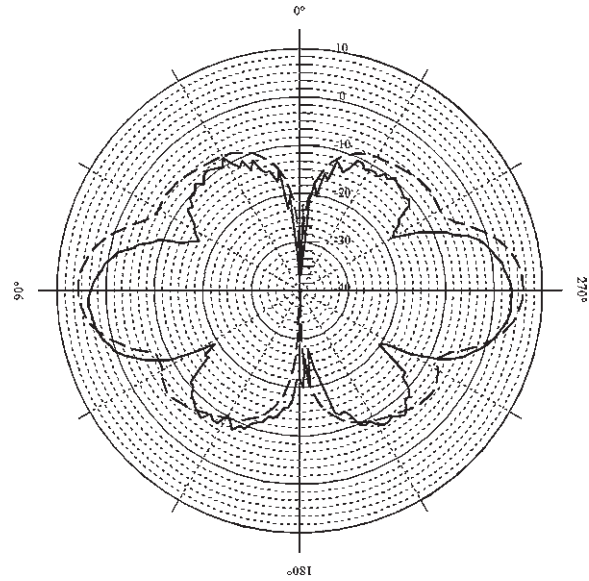

Figure 7-5 (b) The *x-y* plane radiation patterns of an OMA computed using FDTD analysis (dashed) and measured (solid) for 2.586 GHz.

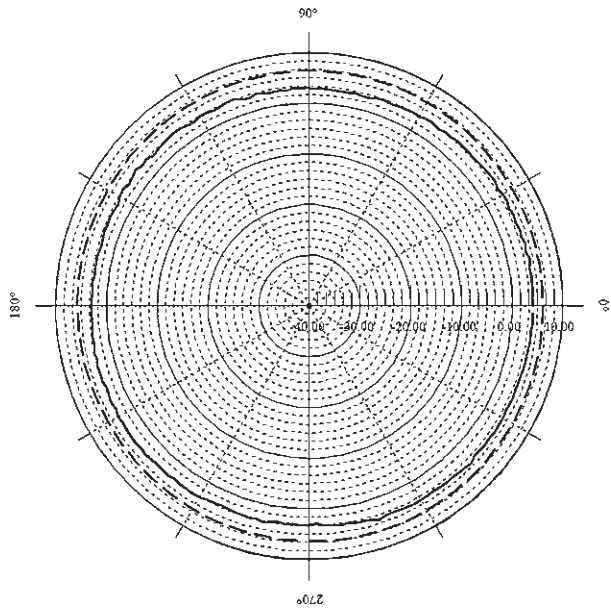

Figure 7-5 (c) The *x-z* plane radiation patterns of an OMA computed using FDTD analysis (dashed) and measured (solid) for 2.586 GHz.

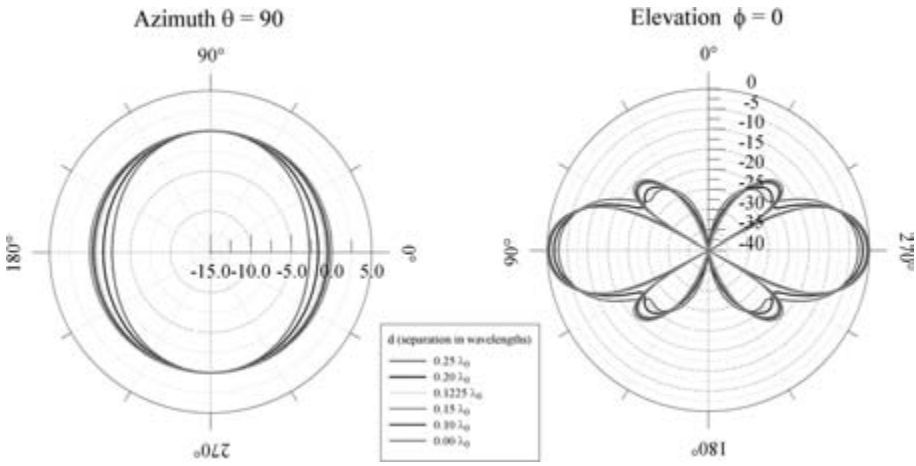

Figure 7-6 The effect of W_e on the pattern variation of an OMA in the azimuth (omni) and elevation plane modeled with uniform amplitude sinusoids. The gain variation changes from 0.0 dB to 2.77 dB as W_e varies from $0.0\lambda_0$ to $0.25\lambda_0$.

performance is at the high end of the band. The measured patterns are slightly squinted downward compared with the FDTD analysis. It appears the attached feeding cable slightly affects the phase relationship along the array and is the cause of this beam squint. The small cable used to feed the array was impractical to model with FDTD. The maximum gain was predicted to be 6.4 dBi versus 4.6 dBi measured at 2.586 GHz. The antenna sidelobes are approximately −11 dB below the main lobe.

The optimum match for the antenna is at 2.4 GHz with a 371 MHz 2 : 1 voltage standing wave ratio (VSWR) impedance bandwidth. The normalized bandwidth is 15.45%, which is very good for a printed antenna. However, the pattern bandwidth is only 5% to 6%. The driving point is unbalanced and thus balun is not required when feeding this antenna with a coaxial cable.

The radiation of the OMA originates from the currents at each edge of the rectangular elements. When W_e is small, the pair of currents become almost colinear and the antenna pattern has very little variation in the omniplane. As W_e becomes large, the two currents begin to array and the pattern deviates significantly from a circle. One can use a set of uniform amplitude sinusoids (UAS) to model the radiation from an OMA. The pattern results of this analysis are presented in Figure 7-6. The predicted pattern variation correlates well with

HFSS computations.[9] The predicted pattern variation value is 0.0 dB to 2.77 dB as W_e ranges from $0.0\lambda_0$ to $0.25\lambda_0$.

7.1.1 Low Sidelobe Omnidirectional Microstrip Antenna

The OMA presented in Section 7.1 has a uniform illumination along its length. A uniform amplitude distribution along an array produces sidelobes that are –13.2 dB below the main beam. The example uniform OMA has sidelobes that are as high as –11 dB. The uniform OMA has radiating elements of identical widths. We can control the amount of radiation from each of the elements by varying their widths.[10] Figure 7-7 shows a seven-section OMA that has elements of different widths. The relative width of each element corresponds with a –6 dB linear taper on a pedestal using equation (6.15).

Finite difference time domain analysis was used to vary the center width W_4 (with the other widths dependent upon W_4) until the desired distribution to produce a –22.5 dB sidelobe level is obtained. The design uses a 0.762 mm (0.030 inches) thick dielectric substrate with $\varepsilon_r = 2.6$ and $\tan\delta = 0.0025$. The element widths are $W_1 = 3.0$ mm, $W_2 = 7.32$ mm, $W_3 = 11.66$ mm, and $W_4 = 16.0$ mm with 50 Ω interconnects of 2.03 mm width. The length of each element is 36.15 mm. An antenna with the dimensions from the previous FDTD analysis (Section 7.1) was fabricated with the altered element widths. The antenna patterns were optimum at 2.628 GHz, but the input impedance has a slight series inductive reactance which produced an unacceptable mismatch (2.5 : 1 VSWR). A 1.0 pF capacitor was used as a via at the driving point to match the antenna with a return loss of better than 25 dB. The normalized impedance bandwidth of the matched –6 dB taper OMA is 3.8%, which is smaller than the 14.58% bandwidth of the uniform design.

The directivity predicted by FDTD analysis is 5.39 dB. The measured gain of the fabricated antenna is 5.0 dBi. The measured and predicted radiation patterns are presented in Figure 7-8(a) and Figure 7-8(b).

The FDTD patterns have a –22.5 dB sidelobe level. The measured patterns are close to the –20 dB sidelobe level. This is approximately a 9 dB improvement over the –11 dB sidelobe level of the uniform OMA design.

When designing an omnidirectional antenna, it is often useful to know the approximate directivity of an omnidirectional pattern versus the half-power

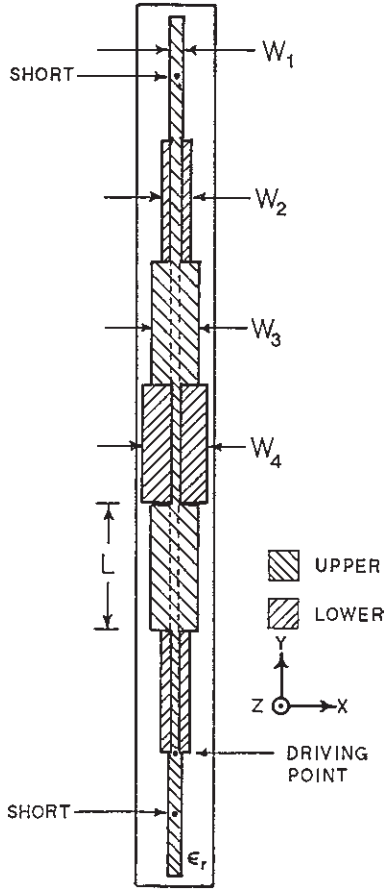

Figure 7-7 Seven section OMA with linear taper.

beamwidth (HPBW). Pozar developed a curve-fit equation based on a $\sin^N\theta$ pattern to relate the HPBW of an omnidirectional pattern without sidelobes to its directivity:[11]

$$D = 10\log_{10}\left(191.0\sqrt{0.818+\frac{1}{HPBW}}-172.4\right)\ \text{dB}$$

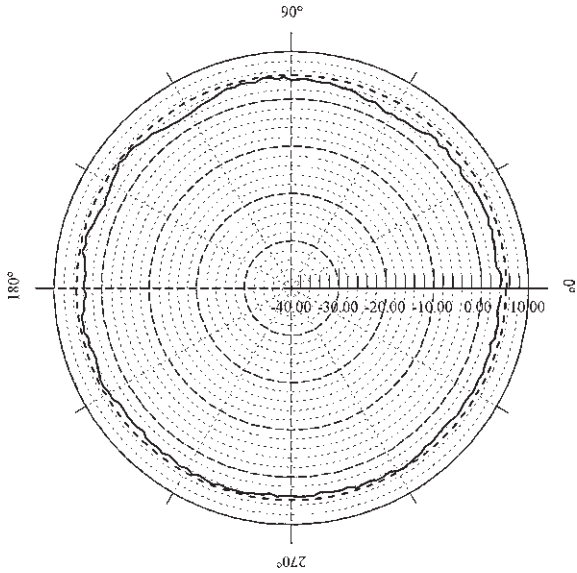

Figure 7-8 (a) Omniplane radiation patterns of a seven section OMA with linear taper. E_ϕ ($\phi = 0$) x-z plane. The dashed line is from FDTD analysis. The solid line is measured.

where HPBW is the elevation-plane half-power beamwidth (in degrees). This equation is valid up to a beamwidth of 140°. When sidelobes are present with an assumed uniform current distribution, McDonald has developed a relationship that uses a $\sin(b\theta)/(b\theta)$ pattern as its basis:[12]

$$D = 10\log_{10}\left(\frac{101.5}{HPBW - 0.00272(HPBW)^2}\right) \text{ dB}$$

7.1.2 Element Shaping of an Omnidirectional Microstrip Antenna

The OMAs discussed thus far all have rectangular elements. The use of other shapes can provide some advantages in the design of an OMA. Figure 7-9 shows five combinations of circular, rectangular, and elliptical elements.

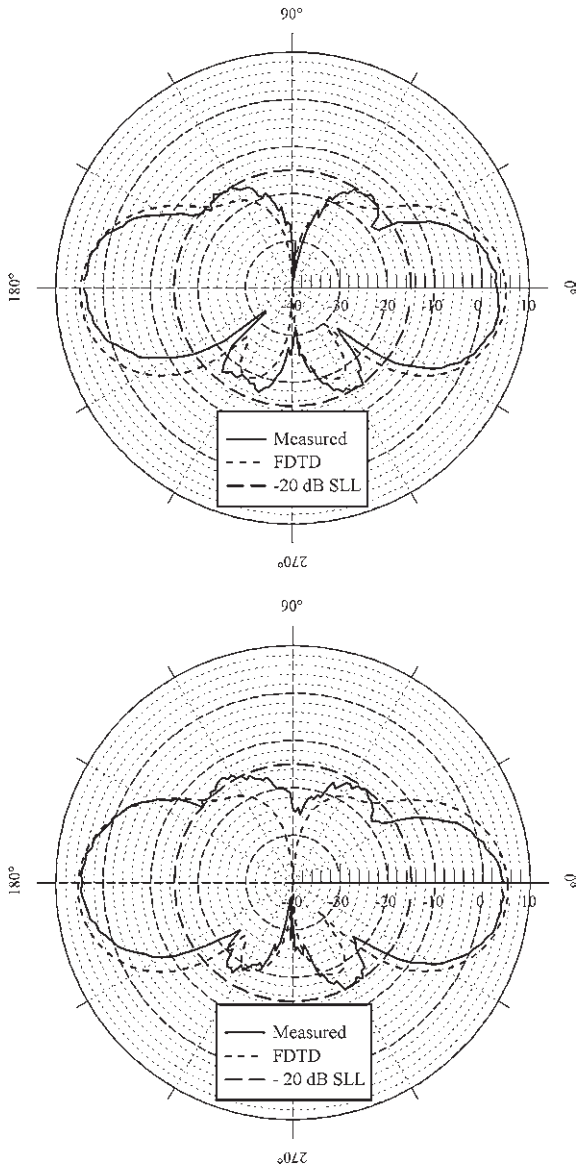

Figure 7-8 (b) Elevation plane radiation patterns of a seven section OMA with linear taper. Upper: E_ϕ ($\theta = 90^\circ$) *x-y* plane; lower: $E\theta$ ($\phi = 90^\circ$) *y-z* plane. The dashed line is from FDTD analysis. The solid line is measured.

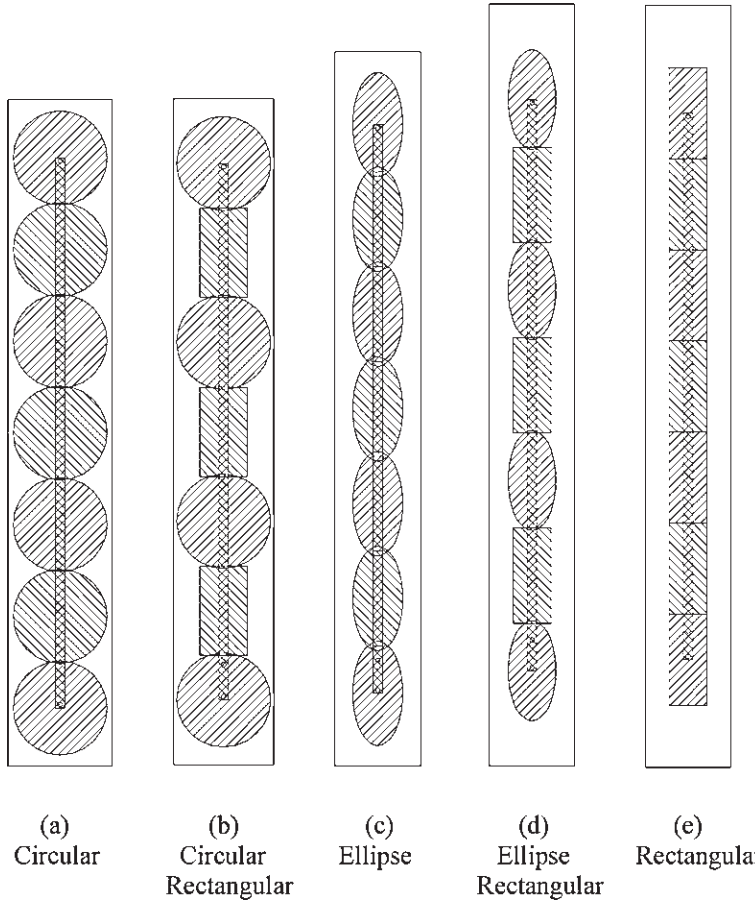

Figure 7-9 Seven-section dual-short shaped element OMA designs.

We have seen previously with rectangular elements that as the width of the element is increased, the efficiency of the antenna also increases. For a 4.9 GHz design, HFSS predicts that the efficiency of each design decreases from left to right in Figure 7-9. The efficiency of the circular OMA design (a) is 96.8%, (b) is 95.8%, (c) is 93.5%, (d) is 92.52%, and (e) is 92.5%, as predicted using HFSS. The efficiency change from the element shape changes is only 0.2 dB. The gain of the designs changes, decreasing from left to right in Figure 7-9. The gain of the circular OMA design (a) is 7.7 dBi, (b) is 6.7 dBi, (c) is 6.8 dBi, (d) is 6.7 dBi,

and (e) is 6.2 dBi. In all five cases the physical antenna length is approximately equal for equivalent operating frequency, but there appears to be approximately a 1.0 to 1.5 dB advantage in gain by using circular elements as opposed to all rectangular elements.

The sidelobe levels predicted by HFSS indicate that the combination of ellipses and rectangles produces the lowest sidelobe level with elements of uniform width. The predicted sidelobe levels for (a) is 11.8 dB, (b) is 11.3 dB, (c) is 13.1 dB, (d) is 14.5 dB, and (e) is 11.8 dB.

The driving point impedance is proportional to the element widths, as seen in the case of the rectangular designs. The driving point impedance at resonance is the lowest for the circular elements (a) and increases to a maximum value with the rectangular elements (d). The impedance bandwidth of the omnidirectional mode is approximately the same for all the element widths for a dual-short design.

7.1.3 Single-Short Omnidirectional Microstrip Antenna

The dual-short OMA design presented in Section 7.1 has the advantage that one can directly connect a coaxial transmission line and match the driving point impedance with the proper choice of element width and driving point location. A second option is to use a single short at the top of the antenna and use the bottom section of the antenna as a platform for broadband impedance matching.

An illustration of a single-short OMA with circular elements and a broadband impedance matching network is shown in Figure 7-10. A number of useful impedance matching techniques are presented in Appendix E. This design uses a theoretical driving point impedance with transmission line analysis software to design a broadband matching network. This network was input into a full-wave analysis package (HFSS) and optimized. A prototype antenna was realized and its VSWR and the prediction made by HFSS are plotted in Figure 7-11(a). This OMA has an impressive 25% 2:1 VSWR impedance bandwidth. This bandwidth covers many commercial frequency bands in a single antenna.

The theoretical antenna gain ranges from 6.4 dBi to 7.6 dBi. The elevation pattern of this antenna as predicted by HFSS is shown in Figure 7-11(b). The single-short OMA offers more design options than the dual-short antenna.

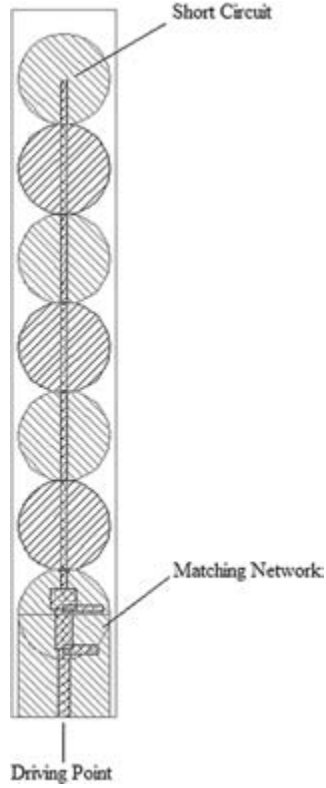

Figure 7-10 Single-short omnidirectional antenna with broadband matching network.

7.2 Stripline Fed Tapered Slot Antenna

A printed antenna with a very large impedance bandwidth (approximately 70%) is a stripline fed linear tapered slot antenna (LTSA). The geometry of this type of antenna is shown in Figure 7-12. The antenna has dual metallization which is etched away in an identical manner in the top and bottom metallization. A slot is used as a feed to the tapered elements on either side of the 50 Ω stripline feed. The 50 Ω stripline feed protrudes between and past the feed slots, which act as a transition from the stripline to the slots on each metallization plane.

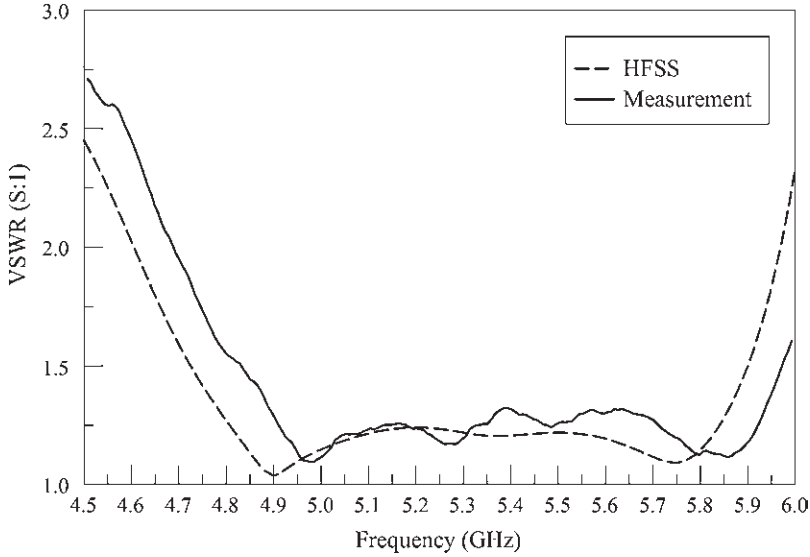

Figure 7-11 (a) VSWR of a single-short OMA with broadband matching network.

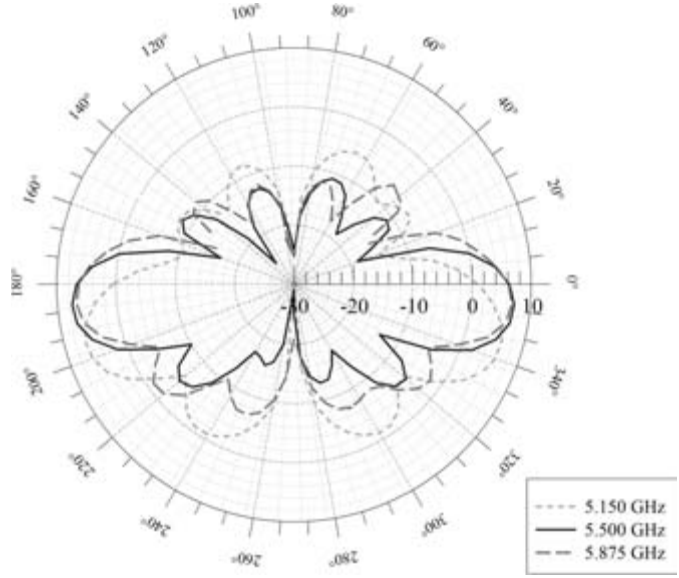

Figure 7-11 (b) Elevation pattern of a single-short OMA with broadband matching network.

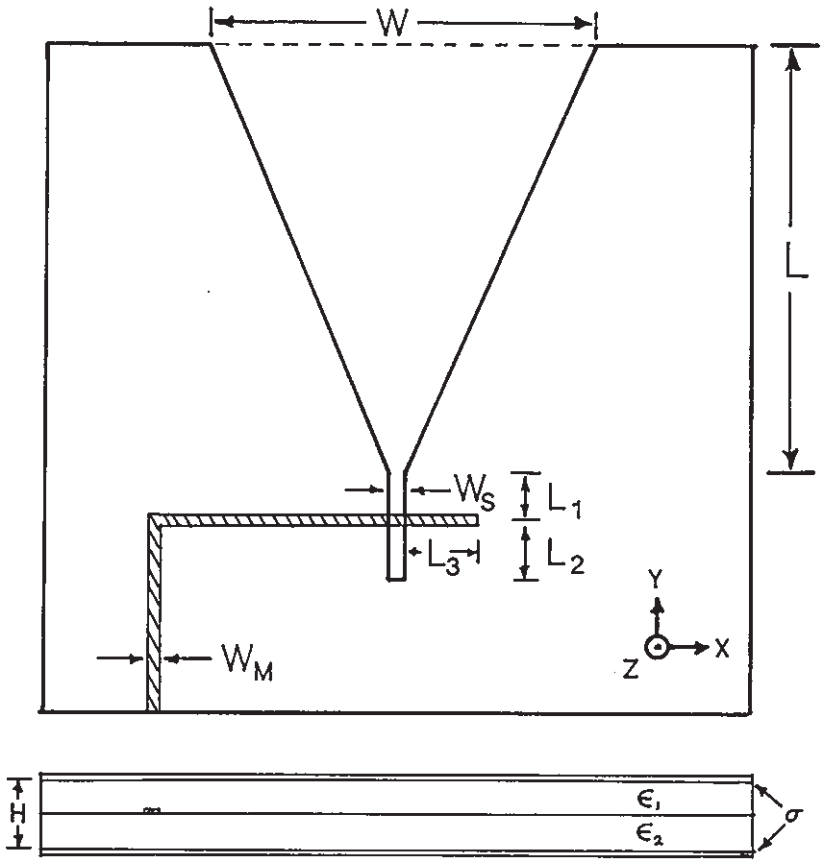

Figure 7-12 Stripline fed tapered slot antenna.

The values of the slot width and length to feed the tapered slot antenna are determined experimentally.

An illustrative design example of an LTSA has a stripline width of W_M = 0.6 mm with a slot width of W_S = 1.0 mm. The stripline passes through the slot at the point defined by $L_1 = L_2$ = 5.0 mm and extends past the slots by a length L_3 = 5.9 mm. The tapered antenna section has a length L = 40.0 mm and width W = 30.0 mm. The groundplane separation between the dielectric material is H = 1.524 mm, with dielectric constant $\varepsilon_1 = \varepsilon_2$ = 2.17. The ground-

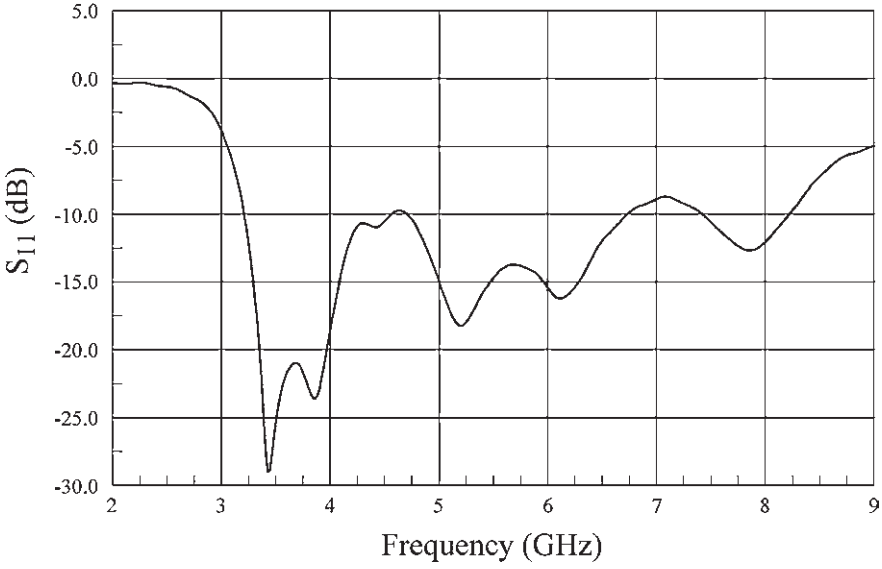

Figure 7-13 Negative return loss of stripline fed linear tapered slot antenna.

Table 7-1 Stripline linear tapered slot antenna example gain versus frequency.

Frequency (GHz)	Gain (dBi)
3.190	5.17
4.000	5.49
5.250	7.50
5.650	7.93
6.810	8.87

plane dimensions are 60 mm × 65 mm. The stripline is 10.7 mm from the left edge. FDTD analysis shows the antenna has a better than 2:1 VSWR [–9.54 dB negative return loss (NRL)] from 3.19 GHz to 6.81 GHz, as shown in Figure 7-13.

The gain of the stripline linear tapered slot antenna versus frequency is presented in Table 7-1. Over the band of operation in Figure 7-13, the gain ranges from 5.17 dBi to 8.87 dBi.

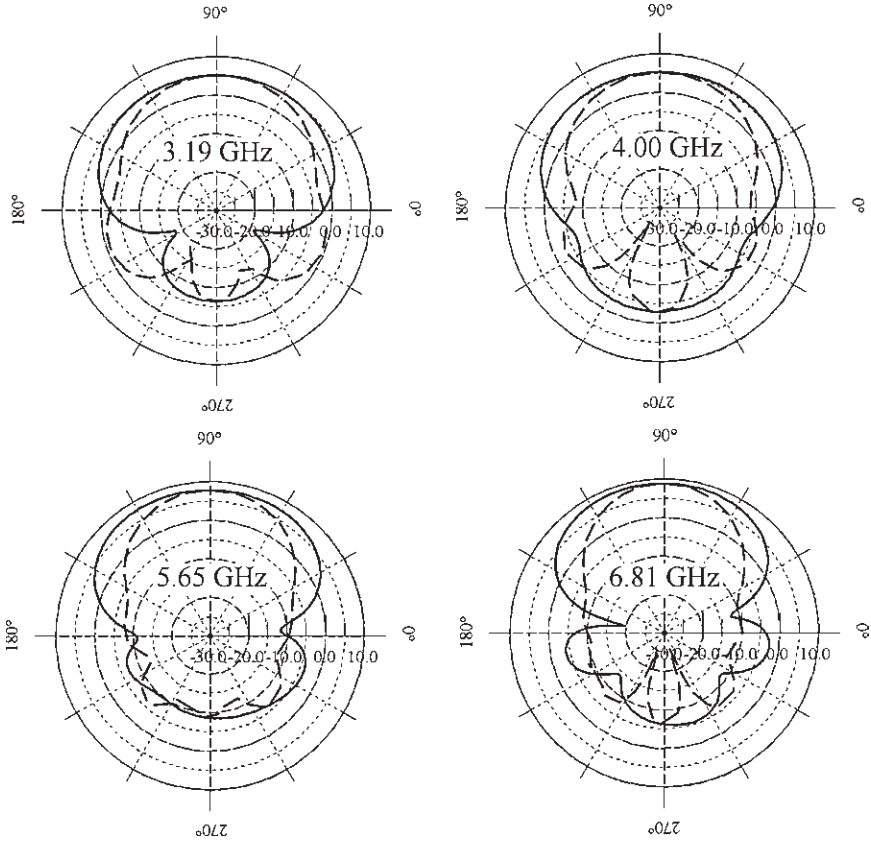

Figure 7-14 Radiation patterns of the tapered slot antenna example (FDTD). The dashed lines are E-plane patterns and the solid are H-plane patterns.

The tapered notch design is the simplest geometrical implementation of this type of design. A variation of this design is the use of an exponential taper rather than a linear one. Careful adjustment of the slot length and stripline overlap (extension past the center slot) with an optimized taper can produce an even larger bandwidth than that obtained with a linear taper.

Radiation patterns for our design example predicted with FDTD analysis at 3.19 GHz, 4.00 GHz, 5.65 GHz, and 6.81 GHz are presented in Figure 7-14.

7.2.1 Stripline Fed Vivaldi Antenna

The LTSA is a special case of an exponentially tapered slot antenna (ETSA) which was introduced by Gibson in 1979 and called the Vivaldi antenna.[13] Vivaldi antennas have been optimized for very large impedance bandwidths (6:1).

The taper that describes the limits of the ETSA or Vivaldi is

$$y = \pm Ae^{Bx}$$

where

$$A = \frac{S_w}{2}$$

$$B = \frac{\ln(a/S_w)}{L_a}$$

and a is the antenna aperture at L_a and S_w is the slot width at the antenna origin.

The exponential taper of a Vivaldi antenna is the common geometry of several designs which differ in their method of providing a transition from a driving point to the exponential slots. One geometry which is used to create Vivaldi elements is presented in Figure 7-15.[14] Metallization on either side of the substrate of thickness H is removed to create the transition and antenna element. A circular open circuit with a radius of R_0 is attached to a slot of length L_s and width S_w. The exponential taper begins after this slot and extends for length L_A, which is the length of the element. The aperture of the element is a. The board length and width are L and W, respectively. The stripline feed is of width W_s terminates in a radial stub with an angle of α and radius R_s.

Early work on Vivaldi antennas used simpler transitions, as shown in Figure 7-12 for the LTSA. Considerable work has been undertaken to maximize the impedance bandwidth of the Vivaldi antenna. Figure 7-15 is a refinement

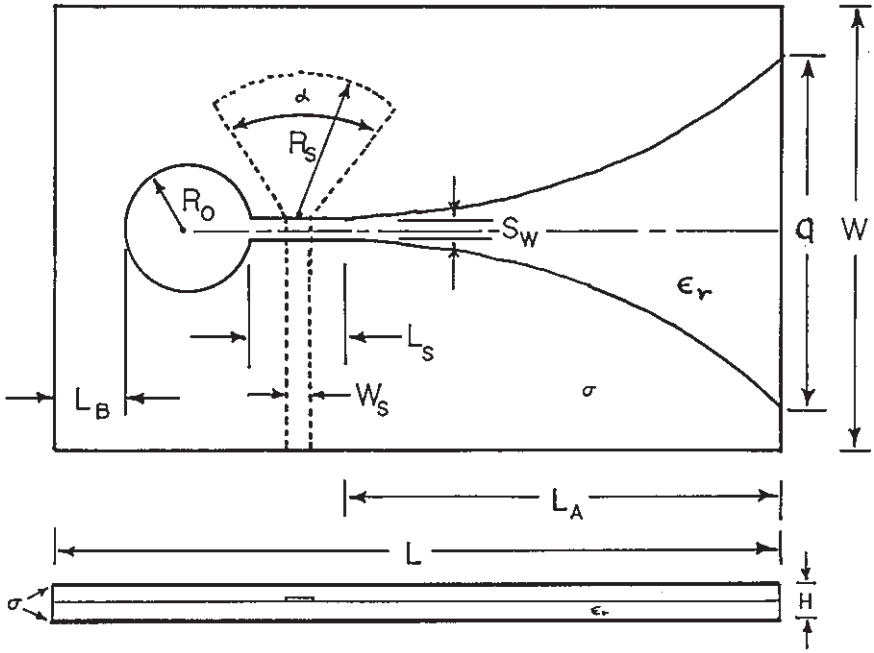

Figure 7-15 Geometry of a Vivaldi antenna (exponential tapered slot antenna).

of the original transition. Another approach has been to feed the antenna from the left side with microstrip along the centerline, narrow the microstrip groundplane to create a balun, and form a Vivaldi notch after the balun transition between the two layers.[15] This approach has created an antenna element with a very wide bandwidth. A large impedance bandwidth helps to preserve the shape of pulses required by ultra-wideband (UWB) systems. The design of Vivaldi antennas is empirical and is suited to the use of analysis to optimize their design prior to fabrication.

Figure 7-16 is a negative return loss plot from an FDTD analysis of a Vivaldi antenna with geometry as defined in Figure 7-15. The antenna parameters are $W = 30.0$ mm, $S_w = 1.0$ mm, $L_A = 45.0$ mm, $L_s = 5.0$ mm, $R_0 = 4.5$ mm, $R_s = 8.0$ mm, $\alpha = 80$ mm, $W_s = 0.5$ mm, $\varepsilon_r = 2.2$, $W = 40.0$ mm, $L = 63.0$ mm, and $H = 1.524$ mm. The antenna has better than 2:1 VSWR (–9.54 dB NRL) from 2.69 GHz to 10.18 GHz.

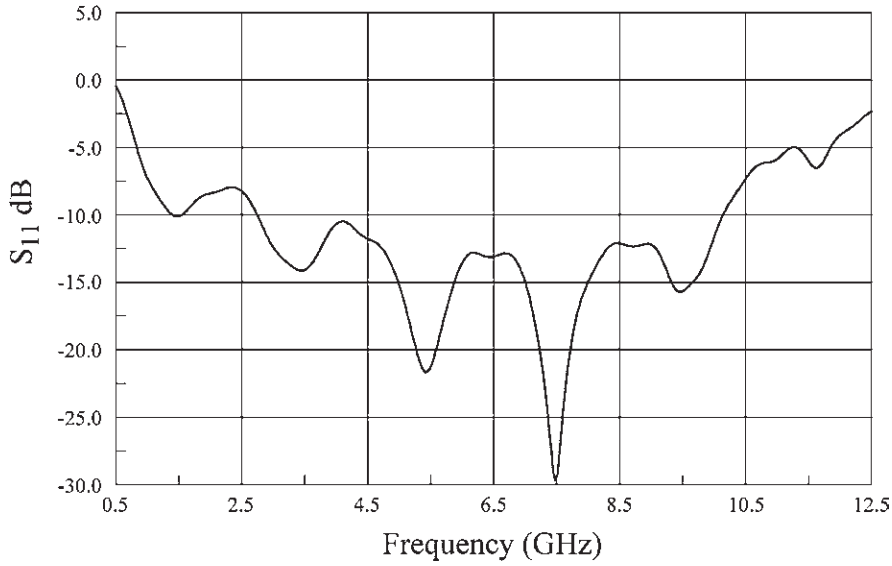

Figure 7-16 Negative return loss plot of the Vivaldi antenna example computed with FDTD analysis.

7.3 Meanderline Antennas

7.3.1 Electrically Small Antennas

In some applications, an electrically small planar antenna can be an appropriate solution. Electrically small antennas (ESAs) have fundamental limitations to their bandwidth. The definition of an ESA is an antenna whose maximum dimension is less than $\lambda/2\pi$.[16] This relation is often expressed as

$$ka < 1 \tag{7.1}$$

where

$k = 2\pi/\lambda$ (in radians/meter)

λ = free space wavelength (in meters)

a = radius of sphere enclosing the maximum dimension of the antenna (in meters).

An ESA has an inherent *minimum* value of Q. This places a limit on the attainable impedance bandwidth of an ESA. The higher the antenna Q, the smaller the impedance bandwidth.

The efficiency of an ESA is determined by the amount of losses in the conductors, dielectrics, and other materials of which the antenna is constructed compared with the radiation loss. This can be expressed as

$$\eta_a = \frac{R_r}{R_r + R_m} \tag{7.2}$$

where

η_a = efficiency of the ESA
R_r = radiation resistance (in Ω)
R_m = material loss resistance (in Ω).

The input impedance of an ESA is capacitive, and in order to provide the maximum transfer of power into the antenna's driving point, a matching network is required. The efficiency of the antenna and its matching network is expressed as

$$\eta_s = \eta_a \eta_m \tag{7.3}$$

where

η_s = efficiency of the system (i.e., antenna and matching network)
η_m = efficiency of the matching network.

Using common assumptions, the efficiency of the matching network is approximately

$$\eta_m \approx \frac{\eta_a}{1 + \dfrac{Q_a}{Q_m}} \tag{7.4}$$

where

Q_a = Q of the ESA
Q_m = Q of the matching network.

In 1996 McLean refined and corrected earlier work on the minimum Q of an ESA.[17] The minimum Q for an electrically small linear antenna in free space is expressed as

$$Q_L = \frac{1}{k^3 a^3} + \frac{1}{ka} \tag{7.5}$$

The minimum Q for an ESA that is circularly polarized is

$$Q_{cp} = \frac{1}{2}\left[\frac{1}{k^3 a^3} + \frac{2}{ka}\right] \tag{7.6}$$

Equation (7.5) and equation (7.6) assume a perfect lossless matching network.

The minimum Q relationship was originally derived for the case of an ESA in free space. In any practical environment an ESA is near some type of groundplane or other structure. In 2001 Sten et al. evaluated the limits on the fundamental Q of an ESA near a groundplane.[18] These relationships provide useful guidelines on theoretical limits to the development of an ESA with a desired impedance bandwidth.

The Q for the case of a horizontal current element and a vertical current element over a groundplane are analyzed as illustrated in Figure 7-17. The formulas for the Q of both instances are found in Sten et al.[18]

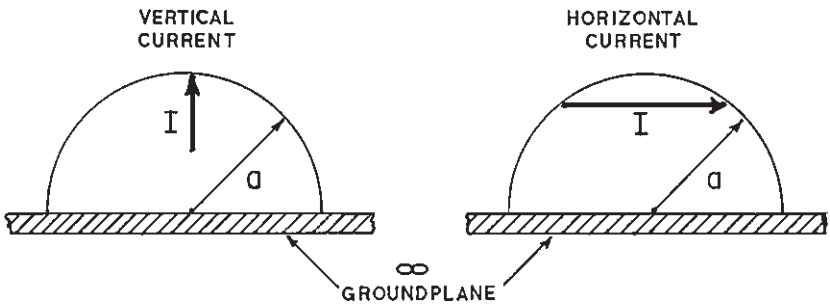

Figure 7-17 Vertical and horizontal ESAs (current) over a large groundplane and their enclosing spheres.

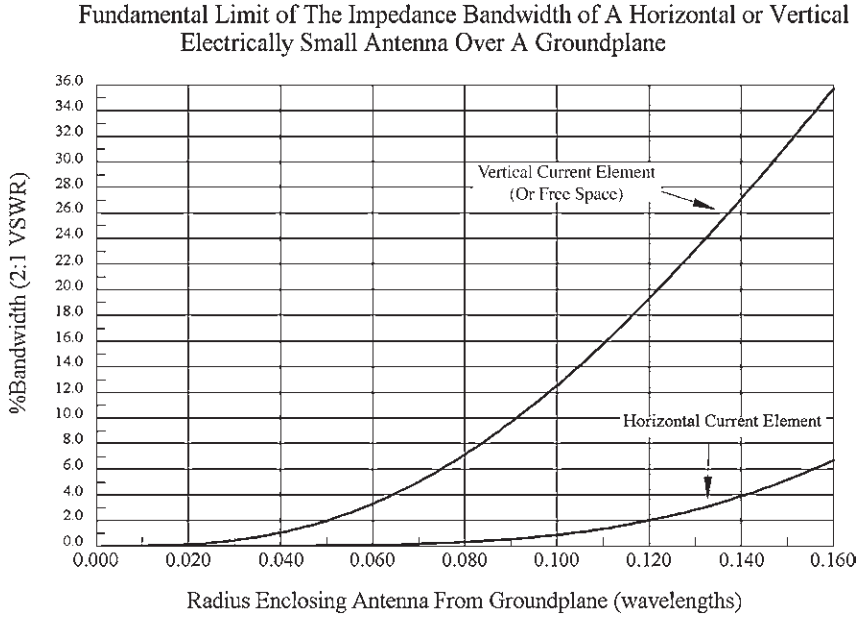

Figure 7-18 Fundamental bandwidth limits of a vertical and horizontal current.

The approximate bandwidth for an RLC-type circuit in terms of Q is

$$BW = \frac{S-1}{Q\sqrt{S}} \tag{7.7}$$

where

$S = S{:}1$ VSWR

BW = normalized bandwidth.

Figure 7-18 presents these impedance bandwidth results in a graphical form. The maximum (normalized) percent impedance bandwidth for the vertical and horizontal polarization cases with respect to the radius of a sphere which encloses the ESA can be determined with Figure 7-18. In the situation of a vertical ESA over a groundplane, we find its Q is equivalent to the free space case. When a horizontal current is over a groundplane the radiation efficiency is reduced. The tangential electric field at the surface of a perfect conductor

is zero. As a horizontal ESA is moved closer and closer to the surface of a conductor, the radiation decreases, the energy in the stored near fields increases, the Q becomes large, and the bandwidth becomes small. In many practical cases, the proximity of a groundplane will decrease the attainable bandwidth of an ESA.

7.3.2 Meanderline Antenna Design

7.3.2.1 Meanderline Antenna Impedance Bandwidth

Figure 7-19 shows the basic meanderline antenna geometry. The antenna itself is a rectangular meandering conductor trace of width W_c with separation W_s and is of overall length L and width W. An electrically small matching network ($\lambda/10$) using microstrip transmission line of length L_M and width W_M is just below the ESA's driving point. The characteristic impedance of this transmission line section can be determined using computer optimization to provide enough series inductive reactance to cancel the large capacitive reactance of the meanderline ESA. This matching section is attached to a 50 Ω microstrip line that is fed with a coaxial probe. The antenna is above a groundplane of width W_G and length L_G.

The meanderline antenna operates in a manner analogous to a self-resonant inductor. The capacitance between the windings of an inductor and the parallel inductance of each coil winding form an equivalent resonant LC circuit. When an inductor is driven at its self-resonant frequency it radiates electromagnetic waves. The meanderline antenna element's vertical sections act like inductors that are in parallel with each pair of horizontal traces which act like capacitors. The current on each pair of horizontal traces flows in opposite directions and cancels in the far field. The radiation is produced by each of the short vertical sections. The electric field polarization in the far field is along the Y axis.

We will assume that even though the meanderline resonator and groundplane section are thin, the minimum Q restrictions for a vertically polarized ESA over an infinite groundplane will approximately apply to this geometry. We will now use a 1.575 GHz ($\lambda = 190.48$ mm) meanderline antenna to estimate the best-case impedance bandwidth we can expect to obtain for this geometry. The substrate is $H = 0.762$ mm (0.030 inches) FR-4 with $\varepsilon_r = 3.9$ and $\tan\delta = 0.02$.

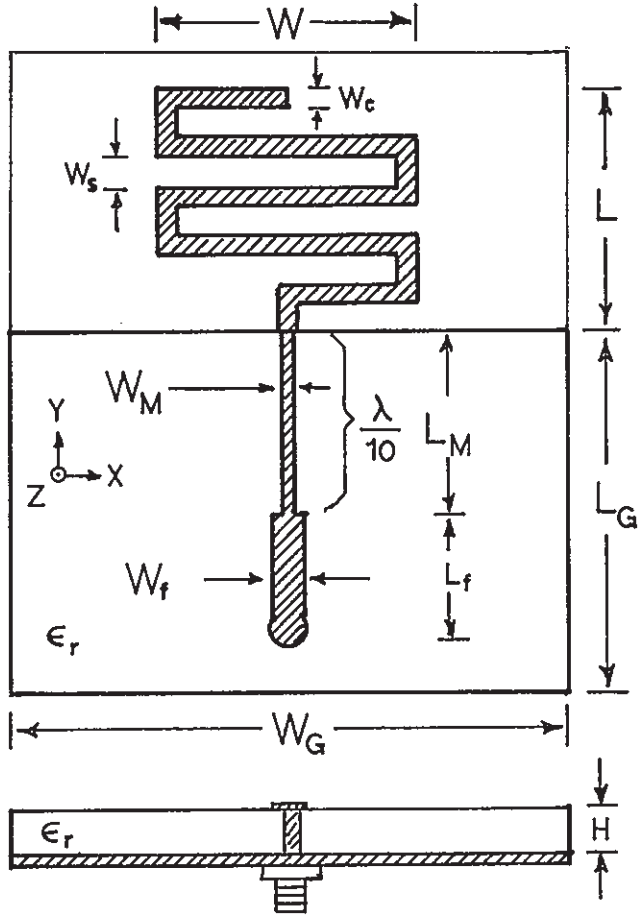

Figure 7-19 Electrically small meanderline antenna geometry.

The groundplane dimensions are W_G = 16.7 mm and L_G = 39.0 mm. The meanderline antenna dimensions are W_c = 1.07 mm and W_s = 1.71 mm (L = 13.91 mm and W = 14.552 mm). The matching network values are W_M = 0.660 mm and L_M = 10.27 mm. The 50 Ω microstrip transmission line dimensions are W_f = 1.65 mm and L_f = 8.02 mm.

The radius of a sphere that can enclose the meanderline antenna assuming an infinite groundplane is a = 15.63 mm. We calculate the free space wavelength and wave number which allows us to evaluate ka = 0.515.

We can see that ka is less than one and this 1.575 GHz meanderline antenna is by definition an ESA. This antenna is known to be linear and polarized vertically to the groundplane, so we easily calculate the radiation Q using equation (7.5) to be $Q_L = 9.22$.

We choose a 2:1 VSWR limit and compute the bandwidth:

$$BW = \frac{1}{Q_L\sqrt{2}} = (0.0291) = 7.66\%$$

Unfortunately this does not match with the computed percent bandwidth of 17.4% from FDTD analysis. At first glance this antenna appears to violate a fundamental limit of ESAs. We can better understand the situation by computing the Q value, which corresponds to a 17.4% (0.174) impedance bandwidth. We obtain $Q_L = 4.06$ for this bandwidth. We next determine what ka value is required to produce a 4.06 value for Q_L. The value is $ka \approx 0.72$, which is still electrically small and should be restricted by minimum Q. We know the value of k at 1.575 GHz. The value of the enclosing radius is

$$a = 0.72/(32.987 \cdot 10^{-3}\,\text{radians/mm}) = 21.83\,\text{mm}$$

In the case where we have an ESA with vertical polarization over a groundplane, the radius of the antenna appears to be expanded from 15.63 mm to 21.83 mm. The explanation for this is that the radiation of the meanderline structure includes about 6.2 mm of the groundplane. These extra currents are seen in the FDTD analysis results presented in Figure 7-20 on the upper left and upper right vertical edges of the groundplane. These patches of current are in phase with the four vertical high current radiating sections on the meander line. One can see the horizontal currents on the meander line sections cancel. The complement of currents on the groundplane cancel with the currents on the upper microstrip to form a transmission line.

If one increases the width of the meanderline antenna groundplane, the impedance bandwidth will decrease until it reaches a limit. When the bandwidth limit is reached, the dimensions of the groundplane have become large enough so that the vertical currents on the meanderline do not drive currents along the edges of the groundplane. FDTD analysis confirms this occurs. The

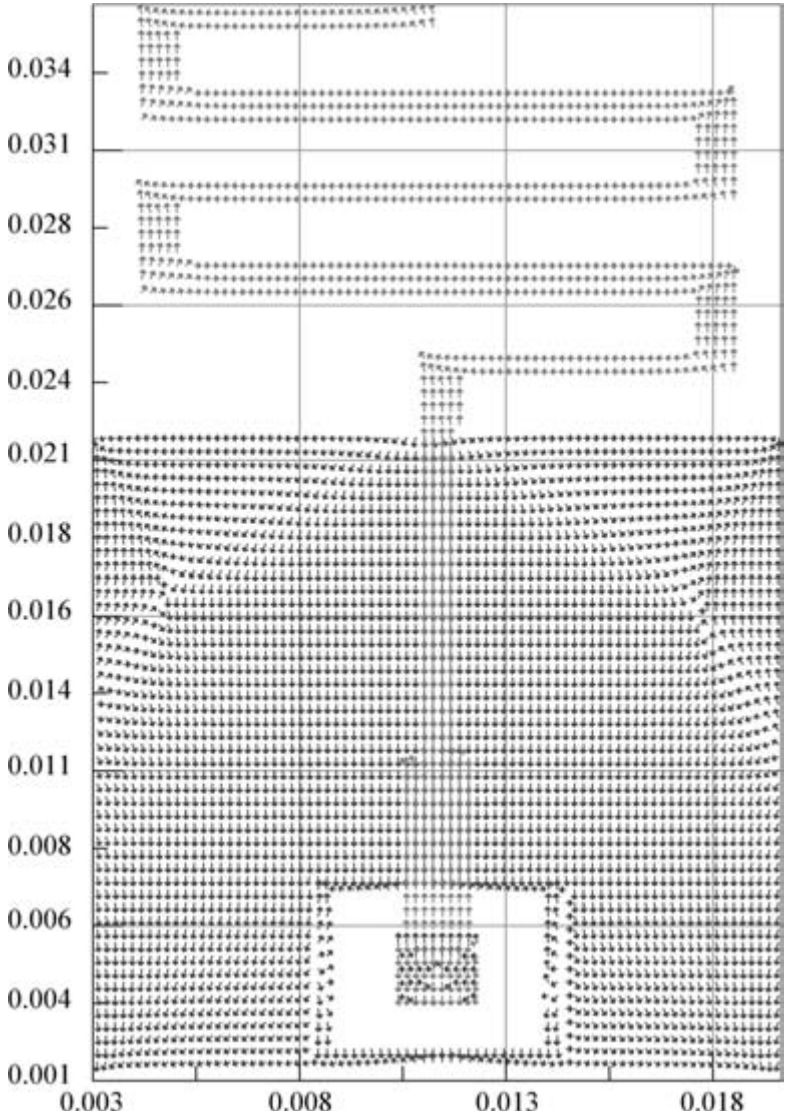

Figure 7-20 Surface current on the meanderline element and its groundplane as computed by FDTD analysis. The two sets of parasitically driven currents on the narrow groundplane are clearly visible. These are responsible for the measurement of a larger bandwidth than expected for a meanderline on a narrow groundplane ESA. The square section is a square coaxial probe feed.

FDTD results of Figure 7-21(a) and Figure 7-21(b) show the meanderline ESA with it's original groundplane width. The thermal plots show the magnitude of the edge current, which correlates to the direction shown in Figure 7-20 (W_G = 66.7 mm). One can see by comparison with Figure 7-21(d) that no significant currents exist on the edges when the groundplane is widened. The width of the electrically small matching section had to be increased (W_M = 4.8 mm) to cancel the increased capacitive reactance of the meanderline antenna driving point as the antenna's Q increased.

The main difference between the narrow and wide groundplane meanderline ESA antennas is the impedance bandwidth. When the groundplane width is increased to 66.7 mm, the bandwidth of the element decreases to 5.19% of the bandwidth. This value is in fair agreement with our computed estimate of 7.66%. Realizing the fundamental bandwidth limit in practice has proven elusive. Theoretical work by Thiele et al. suggests that this theoretical limit is based on a current distribution that is not obtainable in practice.[19]

Figure 7-22 shows the computed impedance bandwidth change for the baseline antenna groundplane width (W_G = 16.7 mm) and after 25 mm of extra groundplane are added to each side. The reduction in impedance bandwidth is clearly illustrated.

A pair of antennas were constructed using the dimensions obtained with FDTD analysis. Figure 7-23 shows the measured impedance bandwidth change for the baseline antenna and with 25 mm of extra groundplane. We note the measurements correlate very well with the predicted FDTD analysis. The measured antennas had a slightly higher resonant frequency than the analysis.

One must realize that when an ESA is used in an application, the groundplane and environment have a considerable affect on the bandwidth and what the extent of the actual antenna is versus what one might assume.

7.3.2.2 Meanderline Antenna Radiation Patterns

The antenna patterns computed using FDTD analysis are nearly equivalent for the small and large groundplane (2.0 dB directivity). Computed radiation patterns for the wide groundplane case are presented in Figure 7-24. The elevation plane radiation pattern in Figure 7-24 is similar to that of a dipole and matches the direction of the radiating currents of Figure 7-20. The pattern is omnidirectional in the x-z plane, consistent with the radiating current. FDTD modeling

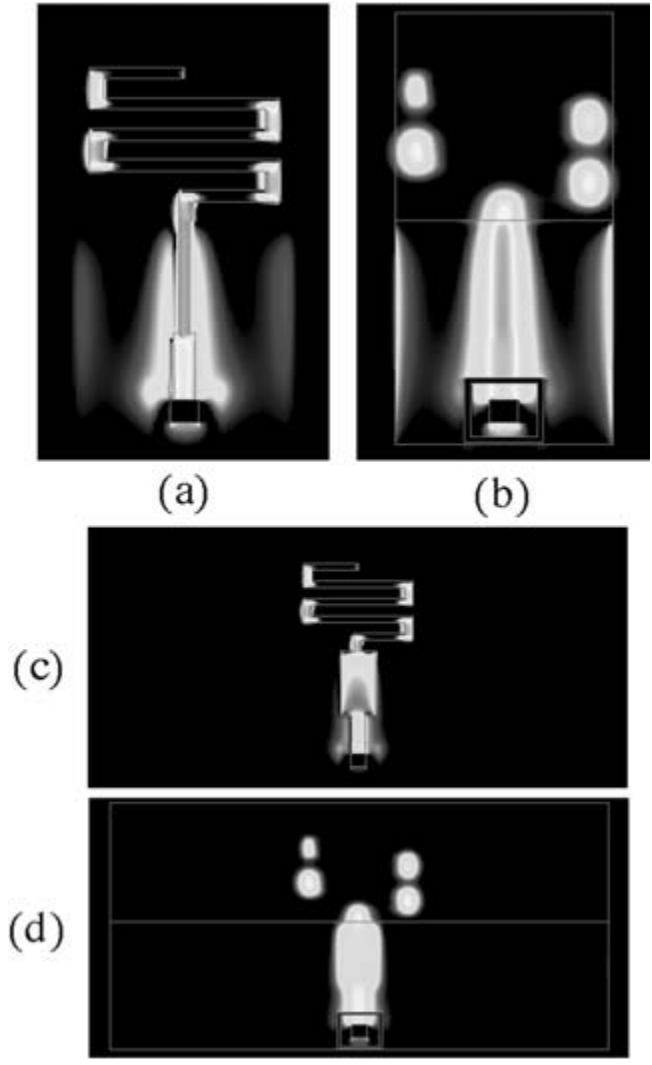

Figure 7-21 Magnitude of the surface current on (a) ESA conductor, (b) ESA groundplane, (c) ESA conductor + 25 mm groundplane, (d) ESA groundplane + 25 mm groundplane.

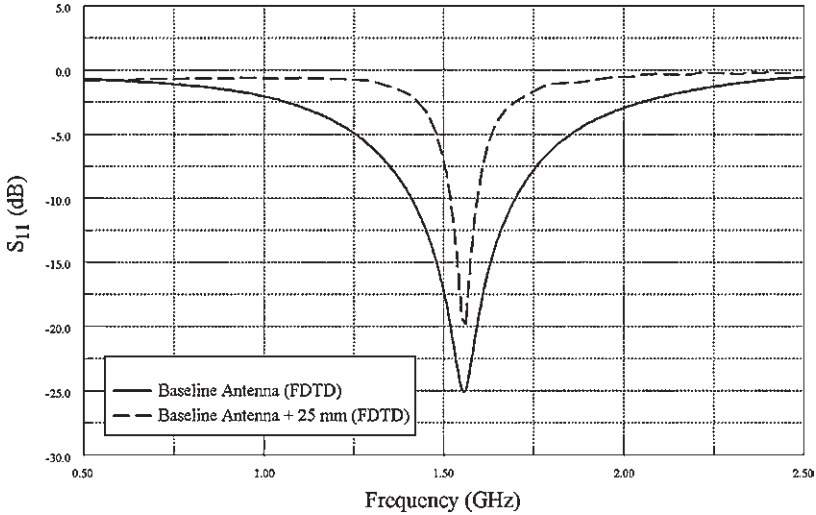

Figure 7-22 Meanderline baseline antenna S_{11} dB with baseline groundplane width and with 25 mm added to each side predicted by FDTD analysis. The plot demonstrates that as the width of the groundplane is increased, the sides no longer contribute to the radiation and the bandwidth reduces to that predicted by ESA fundamental limits.

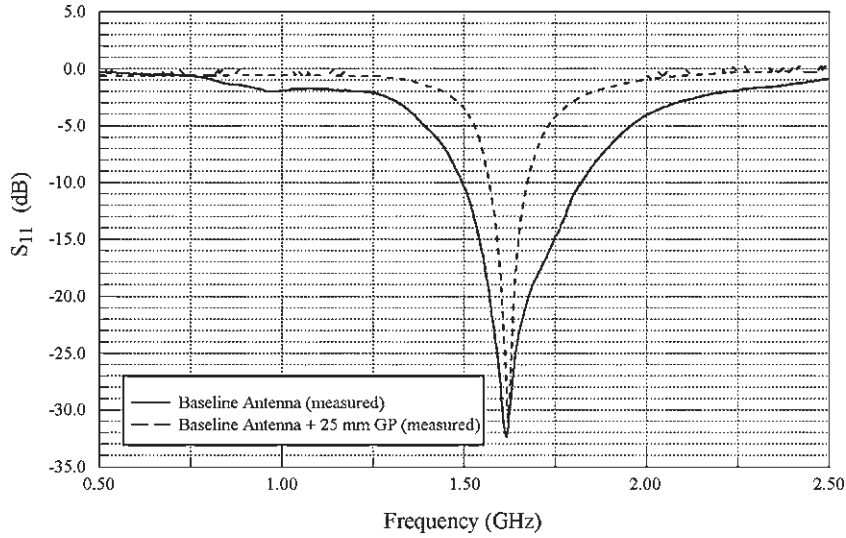

Figure 7-23 Meanderline baseline antenna S_{11} dB with baseline groundplane width and with 25 mm added to each side measured on a fabricated antenna. The bandwidth plot is consistent with Figure 7-22 which uses FDTD analysis.

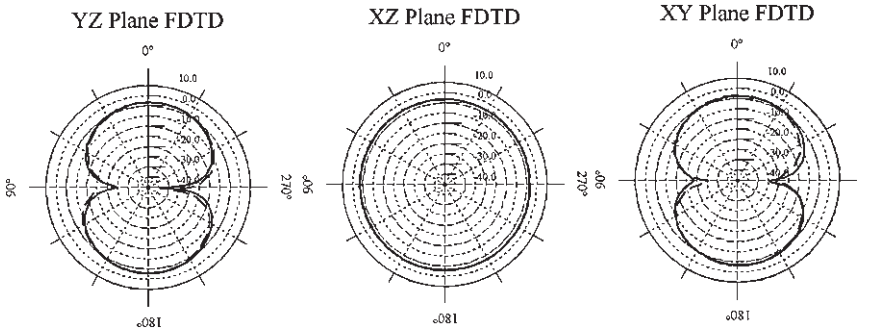

Figure 7-24 Radiation patterns of the narrow groundplane baseline (solid lines) meanderline ESA computed with FDTD analysis and the antenna with 25 mm wide groundplane width added (dashed lines).

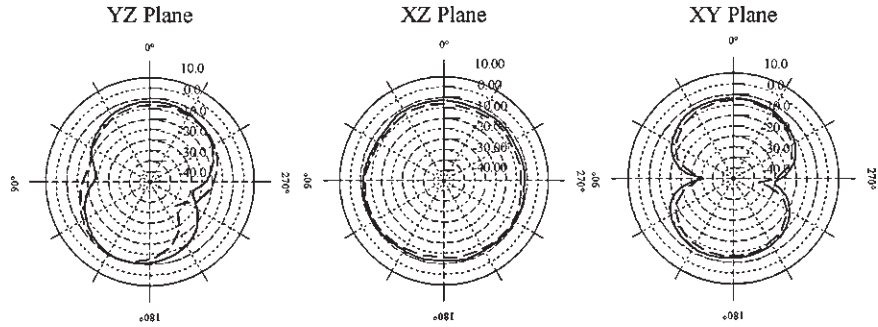

Figure 7-25 The measured radiation patterns of the baseline (narrow groundplane) meanderline ESA (dashed lines) and the antenna with 25 mm groundplane width added (solid lines).

allows for "perfect" feeding of the antenna, which minimizes perturbation from a coaxial feed line.

In practice, the gain of an ESA is bounded. This limitation has been expressed by Harrington as[20]

$$G = (ka)^2 + 2(ka) \tag{7.8}$$

When applied to the meanderline antenna, the maximum attainable gain for the antenna on a large groundplane (a = 15.63 mm) is 1.13 dBi; when the

groundplane is reduced (a = 21.83 mm) we have a maximum possible gain of 2.9 dBi.

Meanderline antennas were fabricated and found to match at 1.655 GHz (4.83% from 1.575 GHz). When measured, the maximum gain of the meanderline antenna with a large groundplane is 0.3 dBi. The measured gain value of the antenna with a smaller groundplane is 0.5 dBi. The smaller groundplane meanderline antenna generated more current along the coaxial cable that connects the antenna to the ESA than the wider antenna. This makes measuring the small groundplane antenna in isolation difficult and adds loss. This measurement problem has been noted and discussed by Staub et al.[21] An ESA has a combination of balanced and unbalanced modes which makes pattern measurement particularly problematic when using a coaxial (unbalanced) cable to feed the ESA.

7.4 Half-Patch with Reduced Short-Circuit Plane

In 1987 Taga et al. introduced a modified version of a half-patch ($\lambda/4$) microstrip antenna in which the width of the shorting plane was altered to reduce the resonant frequency of the antenna.[22] The geometry of a planar inverted-F (type) antenna (PIFA) is presented in Figure 7-26. The antenna is fed along one edge at location F. The short is reduced in width with respect to the edge opposite that of the feed to width W. The element is of dimensions L_1 and L_2 and thickness H. The original PIFA uses air as its dielectric substrate.[23]

When $W = L_1$, the antenna becomes a quarter-wave microstrip (half-patch) antenna (Figure 2-11). As the width W becomes small enough to be equivalent to a shorting post, the antenna has the appearance of an inverted-F antenna with a conductive plane attached to one side. The element was called a PIFA from this view of the geometry.

The resonant frequency of the antenna decreases as the value of W decreases. When $W/L_1 = 0.125$, it has been reported that the resonant frequency is about 40% of a half-patch. When $L_1/L_2 = 2.0$, for a ratio of $L_1/L_2 = 1.0$, the resonant frequency is about 60% of the half-patch. When $L_1/L_2 = 0.5$, it is lowered to about 70% of a normal quarter-wavelength patch antenna.

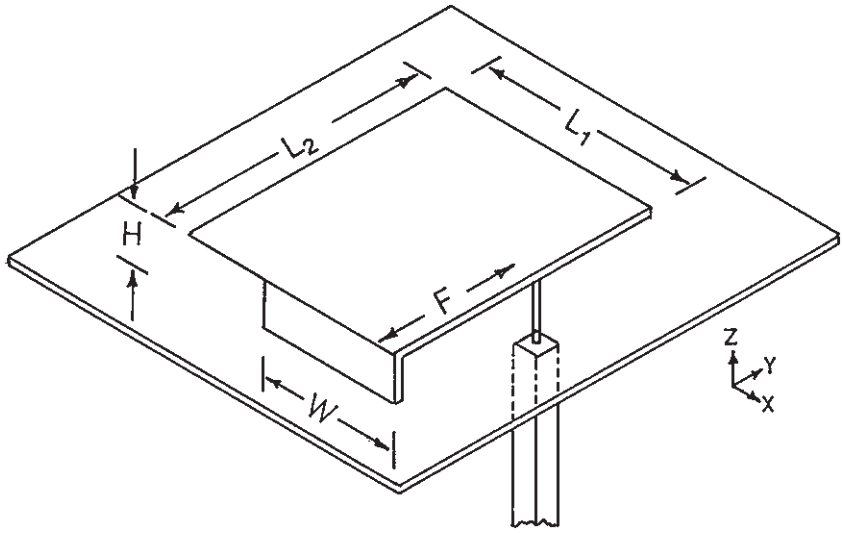

Figure 7-26 A PIFA version of a half-patch with a reduced short-circuit plane. One patch edge has a probe feed. This same patch edge is the termination of a short circuit of width *W*.

Taga computed the input impedance for a PIFA and then widened the short to create a quarter-wave microstrip antenna. In both cases the impedance was computed using an infinite groundplane. The antenna parameters are L_1 = 30.0 mm, L_2 = 45.0 mm, and H = 9.0 mm. The PIFA (case A) has a feed point at F = 3.0 mm and a shorting plane width of W = 6.0 mm. The quarter-wave microstrip antenna (QWMSA) has a feed point located at F = 15.0 mm and a shorting plane $W = L_1$ = 30.0 mm (case B).

The FDTD method was used to analyze these antennas. The resonant frequency of the QWMSA is 1.450 GHz, and the PIFA has a resonant frequency of 1.020 GHz. The frequency of the PIFA is 29.7% lower than the QWMSA. The negative return loss plot for each case is presented in Figure 7-27. We note that the QWMSA has a normalized impedance bandwidth of 10.35% and the PIFA has a 2.77% bandwidth. The reduction in resonant frequency comes at a considerable penalty in bandwidth.

One must keep in mind that these examples of a QWMSA and PIFA are both ESAs. The QWMSA has ka = 0.865 and the PIFA has ka = 0.608, which are both

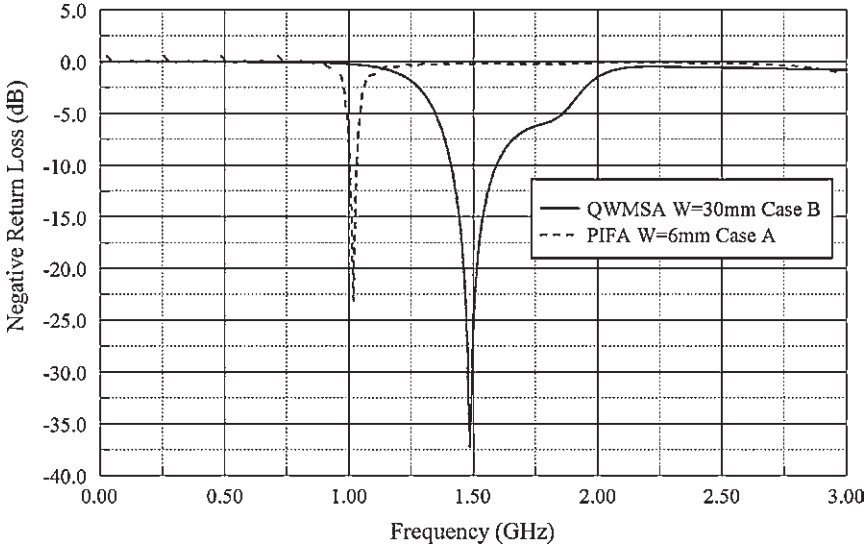

Figure 7-27 The negative return loss of a λ/4 microstrip antenna (baseline PIFA $W = L_1$) and PIFA ($W = 6$ mm) versus frequency.

less than one. The impedance bandwidth of a PIFA can be increased by increasing H, which increases the volume of the antenna.[24] One can decrease the size of the groundplane upon which the PIFA is constructed until the groundplane itself becomes part of the radiating structure and increases the impedance bandwidth.[25] This was illustrated earlier with the meanderline antenna. One must trade off the decrease in resonant frequency as W is decreased, with an associated decrease in impedance bandwidth for a given application.

One can create a PIFA-type structure where the back shorting plane is centered and the feed is positioned along the centerline (CPIFA). This is illustrated in Figure 7-28. If the width of the shorting plane is that of case A ($W = 6.0$ mm) with the CPIFA geometry, the resonant frequency is a slightly higher 1.112 GHz with 2.79% bandwidth.

When the shorting plane width is small ($W \ll L_1$), the resonant frequency of a PIFA ($\varepsilon_r = 1$) is approximately

$$F_r = \frac{c}{4(L_1 + L_2)} \tag{7.9}$$

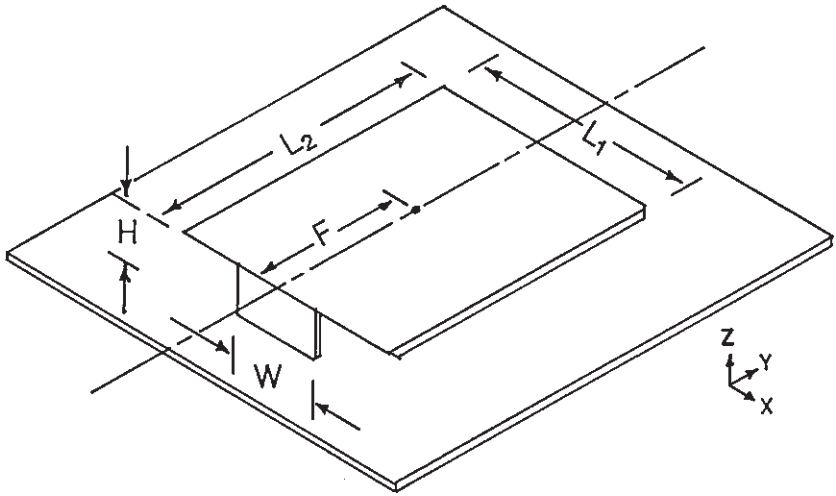

Figure 7-28 Centered short version of a half-patch with a reduced short-circuit plane. The probe feed is placed along the patch centerline. The short-circuit plane is of width *W*.

When the shorting plane width is large, correcting for the width produces a more accurate expression for resonant frequency:

$$F_r = \frac{c}{4(L_1 + L_2 - 0.978 \cdot W)} \tag{7.10}$$

A PIFA may be viewed as an LC circuit where the upper conductor is a capacitor and the shorting plane is an inductor. The inductance increases as the width of the shorting plane decreases, which lowers the resonant frequency of the circuit. A PIFA is also analogous to a microstrip antenna which has an edge resistance (see Section 2.4). The edge resistance increases as the electrical width of the antenna decreases. The position of the 50 Ω location thus moves toward the shorting plane in a manner consistent with the half-patch transmission line model of Figure 2-12. Figure 7-29 illustrates this driving point location change (black dot) as the shorting plane is decreased and the corresponding resonant frequency decreases (as computed with FDTD analysis). The PIFA dimensions H, L_1, and L_2 are the same as Taga's with a

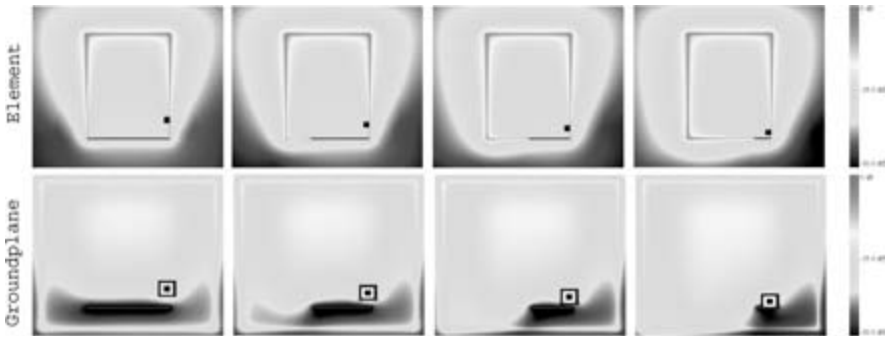

Figure 7-29 The operating frequency of a PIFA is decreased as the width of the shorting plane is decreased. The edge resistance of the patch increases because the electrical width of the antenna narrows. Because of this edge resistance increases and the location of a 50 Ω driving point moves toward the shorting plane. This is illustrated with electric field magnitude plots for a normal PIFA using FDTD analysis.

63 mm × 63 mm groundplane. The impedance bandwidth of a PIFA with a finite-size groundplane is generally smaller than that predicted for an infinite groundplane. This finding is consistent with the results for a centered shorting plane PIFA reported by Huynh and Stutzman.[26]

The movement of the 50 Ω feed point location toward the shorting plane as W is decreased for a centered shorting plane is shown in Figure 7-30. The results are very similar to those for the standard PIFA geometry.

In practice, a PIFA is often realized using a shorting post rather than a shorting plane. FDTD analysis demonstrates that as the radius of the shorting post decreases, so does the resonant frequency. As the resonant frequency decreases, the 50 Ω driving point position moves closer to the shorting post, as seen previously with the shorting planes.

HFSS analysis illustrates that a contour of 50 Ω driving point locations exists for the case of a PIFA realized with a shorting post (Figure 7-31). The PIFA dimensions H, L_1, and L_2 are the same as Taga's with a 63 mm × 63 mm groundplane and 2 mm radius shorting post. As the shorting plane width or shorting post radius is decreased, the location of the 50 Ω driving point can become so close to the short as to be unrealizable.

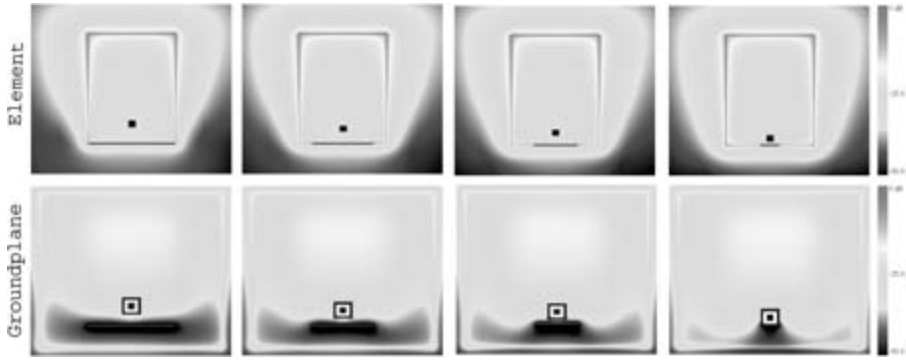

Figure 7-30 The operating frequency of a PIFA is decreased as the width of the centered shorting plane is decreased. The edge resistance of the patch increases because the electrical width of the antenna narrows. Because of this edge resistance increase, the location of a 50 Ω driving point moves toward the shorting plane. This is illustrated with electric field magnitude plots for a normal PIFA using FDTD analysis.

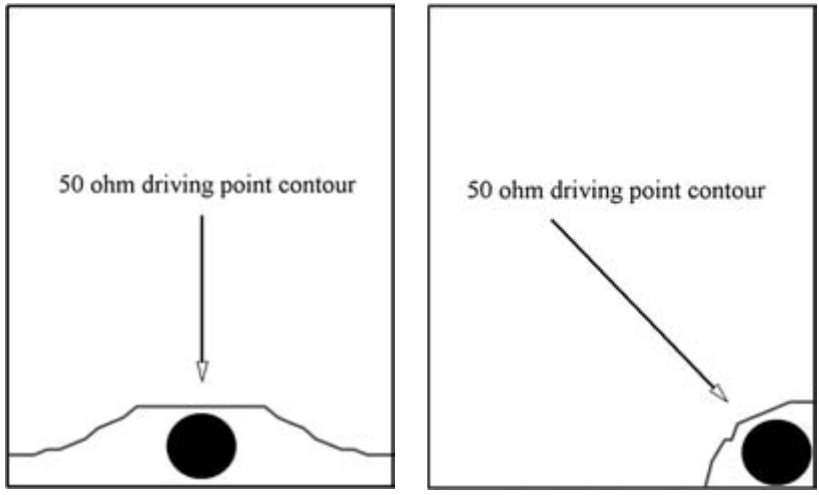

Figure 7-31 The 50 Ω driving point locations for PIFA with centered (2 mm radius) shorting post (left) and offset shorting post (right). The 50 Ω contour is longer for the centered shorting post case, but the resonant frequency is also higher. The resonant frequency for the centered shorting post is 1.267 GHz, whereas the resonant frequency of the offset shorting post is 1.090 GHz.

In many practical applications the groundplane and PIFA dimensions can produce a driving point antiresonance that renders the antenna unrealizable. The currents on the feed center conductor, which have upward and downward currents that tend to cancel, can begin to couple to the PIFA shorting post/plate. When the feed probe is close enough, the coupling increases to the point where the current on the feed and shorting post/plate travel in phase, and in practice produce an antiresonance.

The main advantage of using a PIFA is that it is a very compact ESA. The majority of the radiation is from the vertical current on the shorting plane (post) which is between two thin conductive plates. The impedance bandwidth and gain of a PIFA are consistent with the fundamental limits of an ESA with a vertical current as described by equation (7.5) and equation (7.8). Other comparable printed antenna designs (such as a half slot) must be physically thicker than a PIFA for the same effective height because the radiating length is less than the physical height.

Alternative methods of decreasing the resonant frequency of a patch without the use of a short exist. Slots and rectangular apertures have been cut into rectangular microstrip antenna elements to reduce the resonant frequency. Details of these designs may be found in the literature.[27]

7.4.1 Dual-Band PIFA

The PIFA has proved popular as a dual-band antenna for mobile devices. Often a slot is cut into the planar conductor to create a dual-band element. A radiating and balanced mode analysis of a dual-band PIFA performed by Boyle and Ligthart revealed important insight into this design.[28] The dual-band PIFA design geometry is shown in Figure 7-32. The slot introduces an additional resonance that is proportional to the length of the slot. As the slot length becomes approximately one-half wavelength, the currents on each side of the slot shift from cophase to antiphase. The natural resonant mode of the radiator is between the two modes. The proper choice of dimensions allows for dual-band operation. A long slot is required to create a dual-band PIFA of this geometry. The PIFA is analyzed on a circuit board which represents a mobile device. The half-wave resonances of the circuit board need to be understood and taken into account for a workable design.

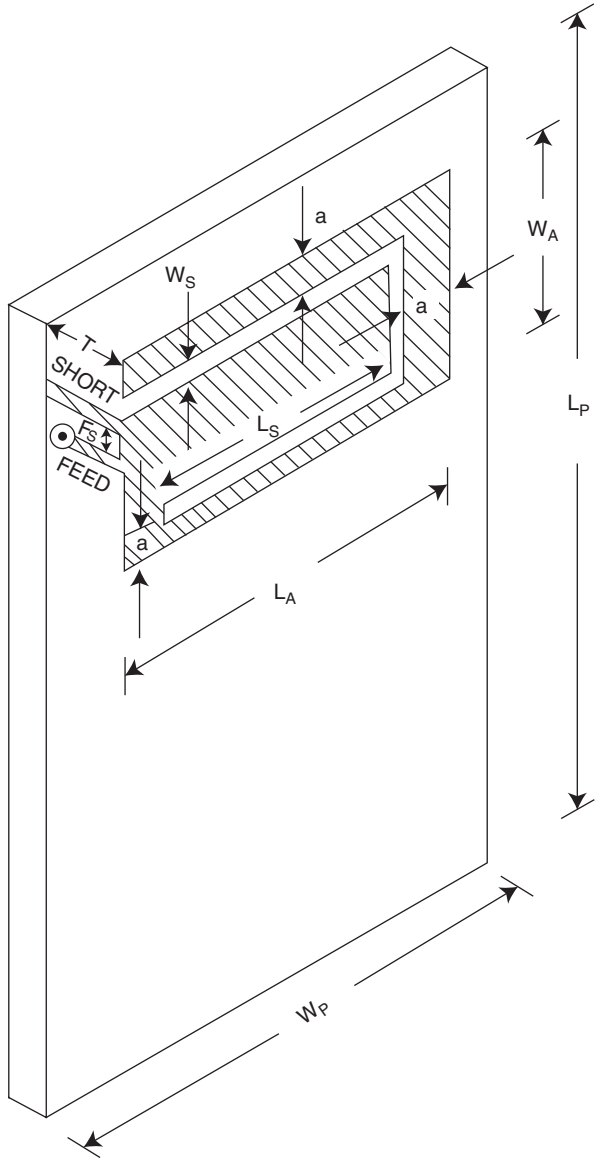

Figure 7-32 Geometry of a dual-band PIFA antenna on a metal plate which represents a mobile device.

The radiating/balanced mode analysis reveals there is an impedance bandwidth trade-off between the two desired frequencies. As the impedance bandwidth of one resonance increases, it is at the expense of the second resonance bandwidth. The dual-band PIFA may be represented by a series (one resonance) or parallel (second resonance) pair of resonance circuits in series. Both bandwidths are maximized when the two circuits resonate at the geometric mean between the two desired design frequencies. If either resonant frequency differs from the geometric mean a bandwidth trade-off occurs.

If a dual-band PIFA design has a short circuit (vertical current) that is so electrically small (i.e., T is very small) that the radiation from the horizontal (planar) current dominates over the vertical current at both frequencies, the radiation efficiency from the cophase mode will be much larger than that of the antiphase mode. For many systems, this large decrease in radiation efficiency renders the antenna unusable at the antiphase frequency.

Boyle and Ligthart designed a dual-band PIFA to operate at 920 MHz (GSM) and 1800 MHz (DCS). The design parameters are $F_s = 2$ mm, $a = 4$ mm, $L_A = 30$ mm, $W_A = 20$ mm, $L_s = 23$ mm, $W_s = 1$ mm, $T = 8$ mm, $L_p = 100$ mm, and $W_p = 40$ mm.

7.5 Rectangular Microstrip Fed Slot Antenna

A slot antenna fed with a microstrip transmission line is shown in Figure 7-33. The radiating slot has a width W_S and length L_S. The slot antenna may be viewed as a slot in the groundplane of a microstrip transmission line that is shorted to the back side of the slot radiator. The microstrip transmission line is offset from the center of the slot by X_S. This is done to match the transmission line to the driving point impedance of the antenna.

A $\lambda/2$ slot antenna is complimentary to a $\lambda/2$ dipole antenna. The relationship between the input resistance of a slot antenna (Z_S) in an infinite groundplane and a dipole antenna (Z_d) is

$$Z_d Z_S = \frac{\eta}{4} \tag{7.11}$$

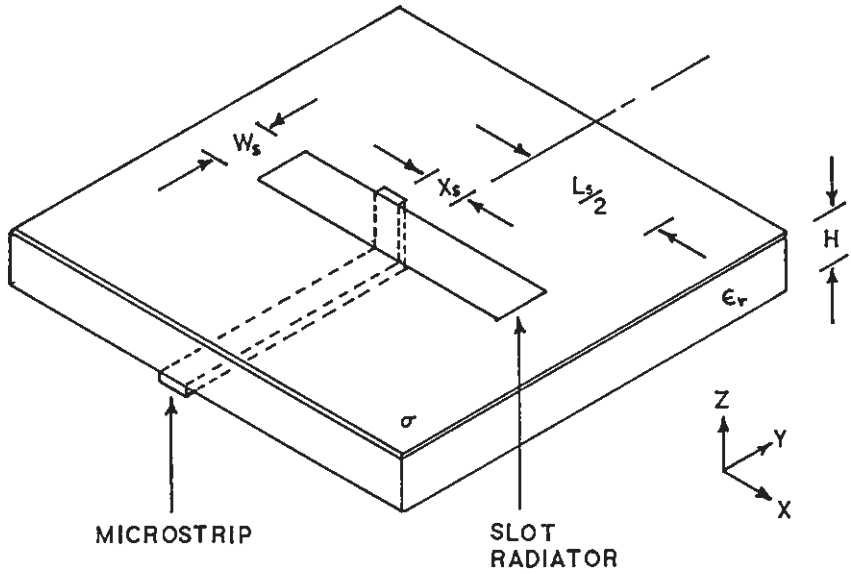

Figure 7-33 A $\lambda/2$ slot antenna of width W_S and length L_S is fed with a microstrip transmission line that is shorted to the backside of the slot. The position of the microstrip feed line is placed at a location X_S between the center and an edge which provides a driving point impedance that matches the microstrip transmission line.

The input impedances of round $\lambda/2$ dipoles have been extensively computed. The equivalent radius of a round wire dipole is about one-half of the strip width of the complimentary (flat) dipole. If we restrict ourselves to a thin flat dipole ($W_S \ll \lambda$), its resonant resistance is approximately 67 Ω. Using equation (7.11), we compute a typical value for the resonant resistance of a slot:

$$R_S = \frac{(376.73)^2}{4 \cdot (67)} \approx 530\,\Omega$$

The driving point resistance is maximum at the center of the slot and decreases to zero as the driving point moves toward the end of the slot. The current increases in a sinusoidal manner as one moves from the center of the slot toward an edge. The voltage decreases in a sinusoidal manner as one

moves from the center of the slot to an edge. This implies the driving point resistance (R_{drv}) will vary as[29]

$$R_{drv} \approx R_S \sin^2 k\left[\frac{L_s}{2} - X_S\right]\Omega \tag{7.12}$$

This allows us to compute the approximate position of a 50 Ω (R_{drv} = 50 Ω) driving point:

$$X_S = \frac{L_s}{2} - \frac{\lambda}{2\pi}\sin^{-1}\sqrt{\frac{R_{drv}}{R_S}} \tag{7.13}$$

For a slot that is at resonance with $L_s = 0.46\lambda$ and $R_S = 530$ Ω, the 50 Ω driving point location X_s is

$$X_S = \frac{0.46\lambda}{2} - \frac{\lambda}{2\pi}\sin^{-1}\sqrt{\frac{50}{530}} = 0.180\lambda$$

which is 0.050λ from the end of the slot.

As an example rectangular slot antenna design, we use a substrate with ε_r = 3.5 and a $\tan\delta$ = 0.0055. The thickness of the substrate is H = 0.5 mm. The slot dimensions are L_s = 22 mm and W_s = 1.0 mm. The feed point is X_s = 8.0 mm. The microstrip line width is 1.0 mm.

The predicted negative return loss plot of the rectangular slot antenna is presented in Figure 7-34. The antenna is seen to have an 18.78% (2:1 VSWR) impedance bandwidth.

The current has a maximum value along the ends of the slot radiator. These currents are directed parallel with the $\hat{y}$ axis. The electric field of the radiator is across the narrow dimension of the slot which produces $\hat{y}$-directed polarization. The maximum driving point impedance at the center of the slot antenna allows one to cut the slot radiator in half to produce a λ/4 version. A single $\hat{y}$-directed current then becomes the radiation source. Further reducing the groundplane surrounding the λ/4 slot produces a printed circuit version of an inverted F antenna (IFA).[30]

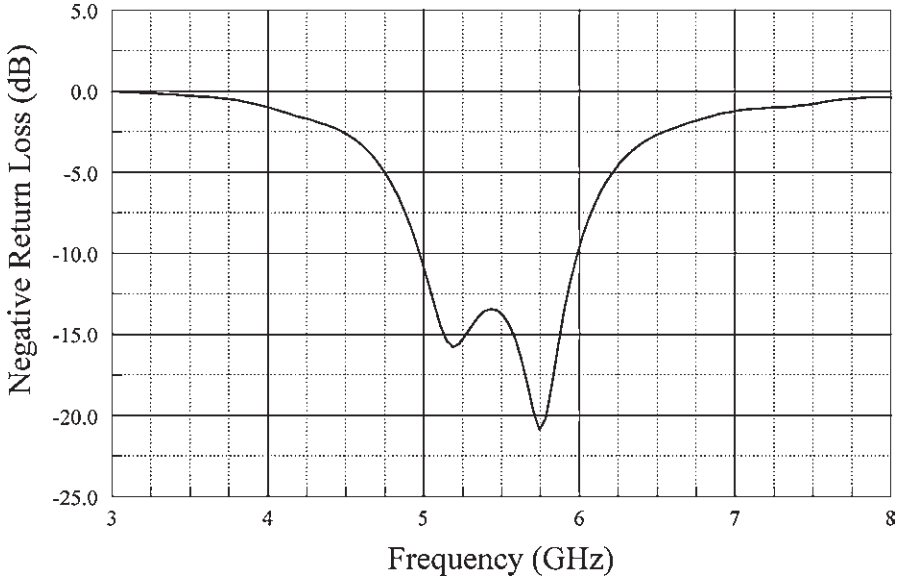

Figure 7-34 Negative return loss (in dB) of the example slot antenna.

Figure 7-35 shows the E- and H-plane radiation patterns of the example microstrip fed slot antenna computed using FDTD analysis. The pattern directivity is 4.66 dB.

7.5.1 Microstrip Slot Antenna "Fictitious Resonance"

One may have noted the considerable bandwidth and pair of negative return loss minimums of the previous microstrip slot antenna design example. It was noted by Behdad and Sarabandi that a slot fed in this manner can contain two resonances.[31,32] The first resonance is the expected normal resonance of the full slot, but a second "fictitious" resonance may also exist in some slot designs. The fictitious resonance occurs when the tangential electric field component of the feed conductor is in a position along the slot which cancels the electric field of the slot excited by the groundplane return current. The width of the feed line, the slot width, and the distance from the edge of the slot to the center of the feed line (L_s) determines the existence and location of the fictitious reso-

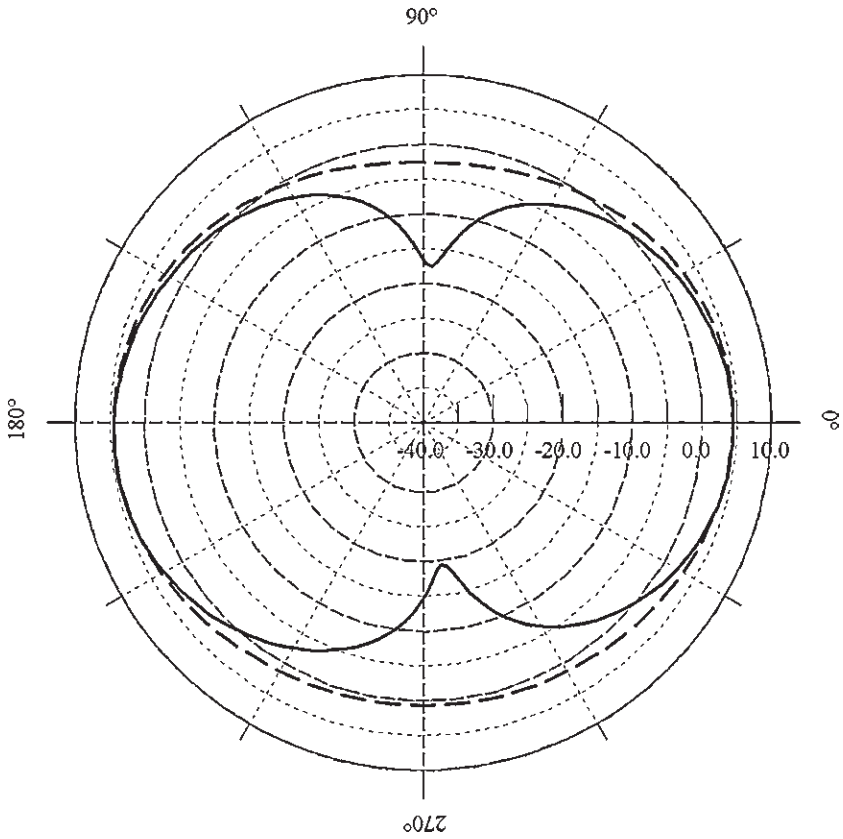

Figure 7-35 Radiation pattern of the example rectangular microstrip fed slot antenna computed with FDTD analysis. The solid line is the E-plane pattern, the dashed line is the H-plane pattern.

nance. The frequency of the fictitious resonance may be increased by increasing L_s, which increases the total impedance bandwidth or produces dual-band operation. The overall length of the slot L determines the frequency of the lower resonance. The length of the microstrip line L_m above the slot feed conductor allows for matching. The magnetic current distribution illustrated in Figure 7-36 is similar at both resonances, producing a relatively stable radiation pattern over the impedance bandwidth. A parametric study of the design of this slot antenna is available in the literature.[33]

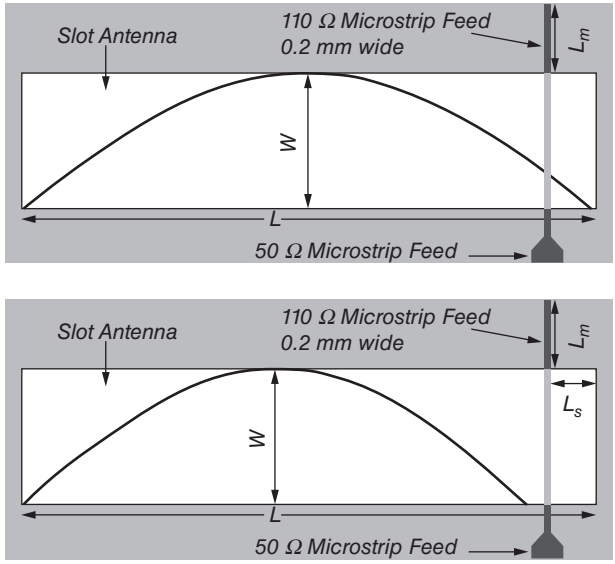

Figure 7-36 Magnetic current distribution of the normal (top) and "fictitious" (bottom) resonance of a slot antenna fed with a narrow line from a microstrip transmission line and impedance matched using an open microstrip line. (From [32], copyright 2004, IEEE. Reprinted with permission.)

In light of the results obtained by Behdad and Sarabandi, FDTD analysis of the design example slot antenna presented above (and in the first edition) was undertaken at the two negative return loss minimums. A sinusoidal source was used at 5.189 GHz and 5.744 GHz. The results are presented in Figure 7-37(a) and Figure 7-37(b). Although the researchers indicated that a fictitious resonance was best driven by using a thin conductive strip across the slot, it appears in this case that the fictitious resonance was at work to produce a wideband slot antenna.

This design method was implemented to create a multiband antenna for laptop use. A half slot is used for 802.11b (2.4 to 2.5 GHz) band and a full dual-band slot (with normal and "fictitious" resonances) covers multiple high-frequency bands (4.9 to 5.875 GHz). The use of a half slot for the low band removes the odd-numbered resonances F_1, F_3, . . . ($F_0 = 2.45$ GHz) by removing the required short-circuit boundary condition for these slot resonances. The

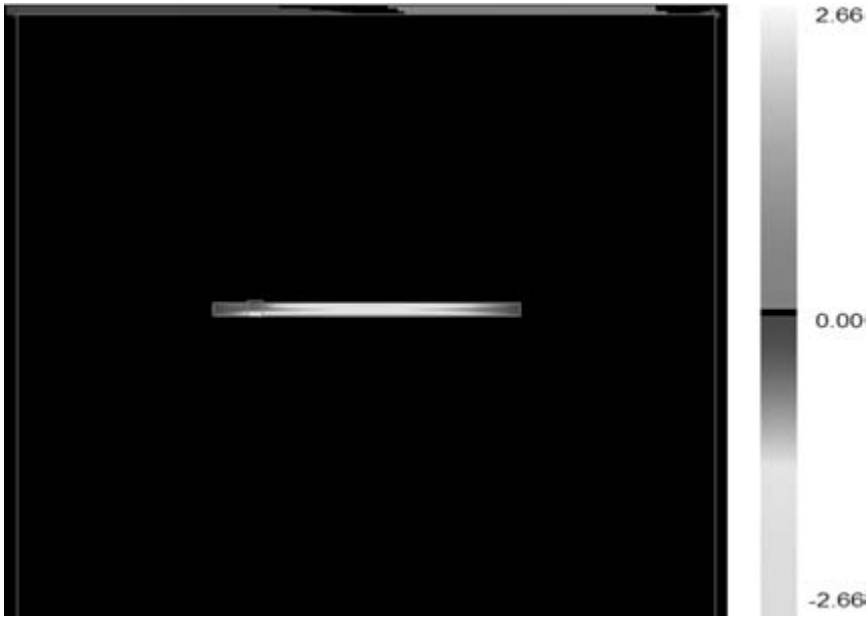

Figure 7-37 (a) Electric field magnitude (linear) for 5.189 GHz resonance of the example design.

removal of the F_1 resonance allows the bottom full dual-band slot antenna to operate from 4.9 to 5.875 GHz without interference from the upper slot's driving point impedance.[34]

7.6 Microstrip Fed Log-Periodic Balun Printed Dipole

A printed dipole antenna fed using microstrip is illustrated in Figure 7-38.[35] Microstrip is an unbalanced transmission line and requires a balun to produce the desired balanced transmission line mode for the printed twin-lead transmission line, which in turn feeds the dipole. The microstrip input is at the bottom of the figure and connects to the input port of a two-section log-periodic microstrip balun described by Al Basraoul and Shastry.[36] The two 50 Ω microstrip transmission lines are of opposite phase and equal magnitude as

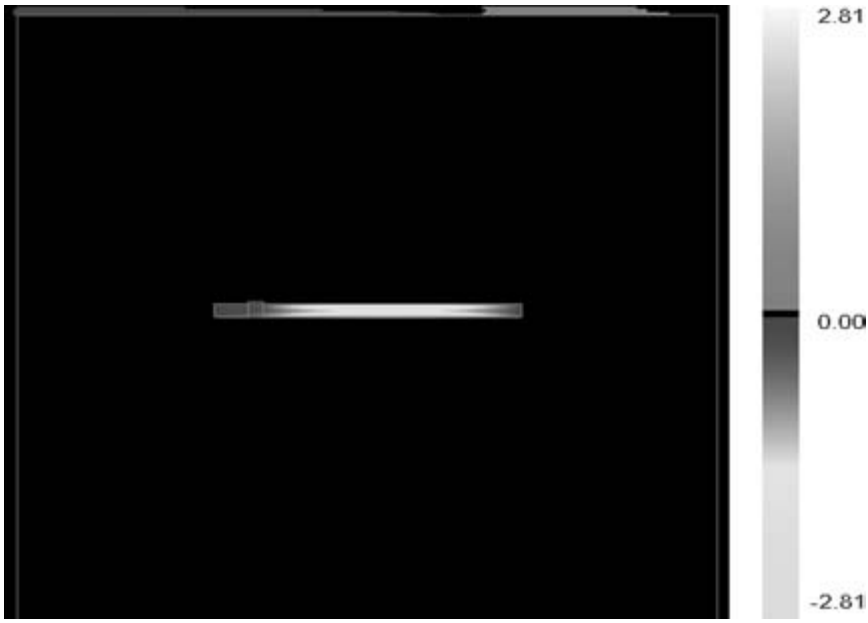

Figure 7-37 (b) Electric field magnitude (linear) for 5.744 GHz resonance of the example design. The fictitious resonance as described by Behdad and Sarabandi is clearly visible.

they emerge from the balun. They connect to flat balanced twin-lead transmission line which feeds the printed dipole.

A planar dipole of this design can have as much as a 25% normalized impedance bandwidth. An example design that operates with a center frequency of 2.22 GHz, has a substrate with $\varepsilon_r = 3.2$, and a thickness of 1.524 mm (0.060 inches) is used for illustration. The 50 Ω microstrip line that forms the balun has a width of $W = 3.64$ mm. The value of $L = 19.09$ mm, which is a $\lambda/4$ guide wavelength at the center frequency. The width of the delay section of the balun is $W_1 = 33.30$ mm, which is an approximately $\lambda/2$ guide wavelength at the center frequency. The delay section produces a 180° phase shift. $L_1 = 30.61$ mm, which is an approximately $\lambda/4$ free space wavelength from the edge of the groundplane. Each dipole element is $L_2 = 30.77$ mm, $W_2 = 2.0$ mm, $W_3 = 1.374$ mm, and $W_4 = 2.0$ mm. The last horizontal section of microstrip has an edge that is 5.0 mm below L_G ($L_G = 55.907$ mm). The width of the groundplane section is

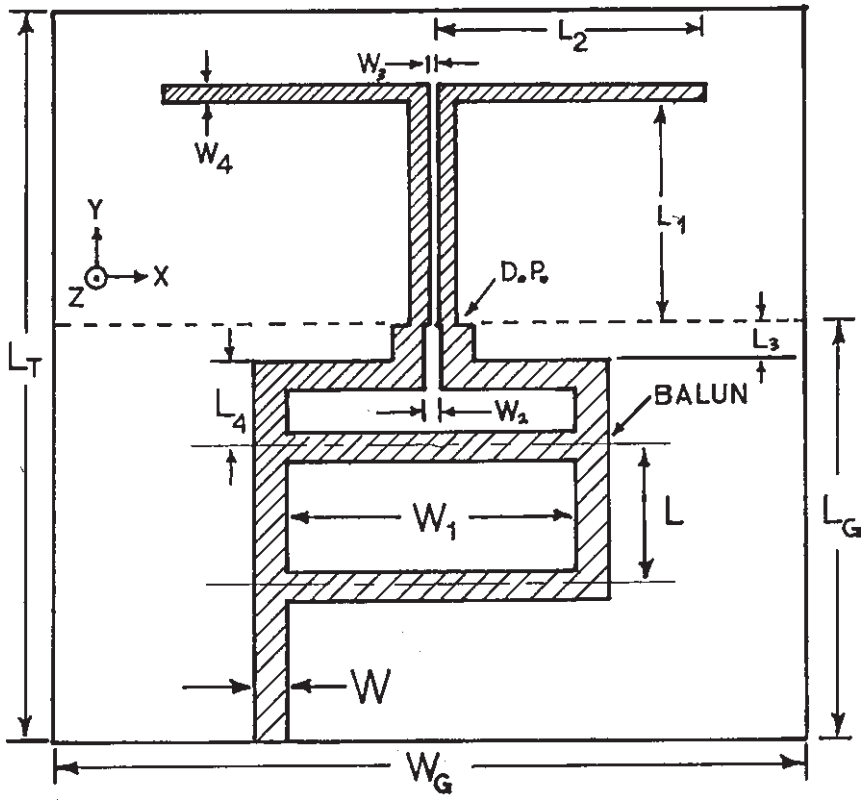

Figure 7-38 Geometry of a printed dipole antenna with microstrip balun.

$W_G = 78.0$ mm. The total length of the antenna board is $L_T = 91.0$ mm, $L_3 = 5$ mm, and $L_4 = 9.545$ mm.

In Figure 7-39, the negative return loss plot of the printed dipole with microstrip balun example is plotted. We can see the dipole example has (approximately) a 25% (2:1 VSWR) impedance bandwidth. The maximum directivity of the example dipole design varies from 5.52 dB to 4.82 dB over the 2:1 VSWR bandwidth. The wave radiated by the dipole in the direction of the groundplane edge is reflected back toward the dipole. The quarter-wave spacing of the dipole from the groundplane edge causes the wave to add in phase with the wave radiating outward away from the groundplane. This produces a direc-

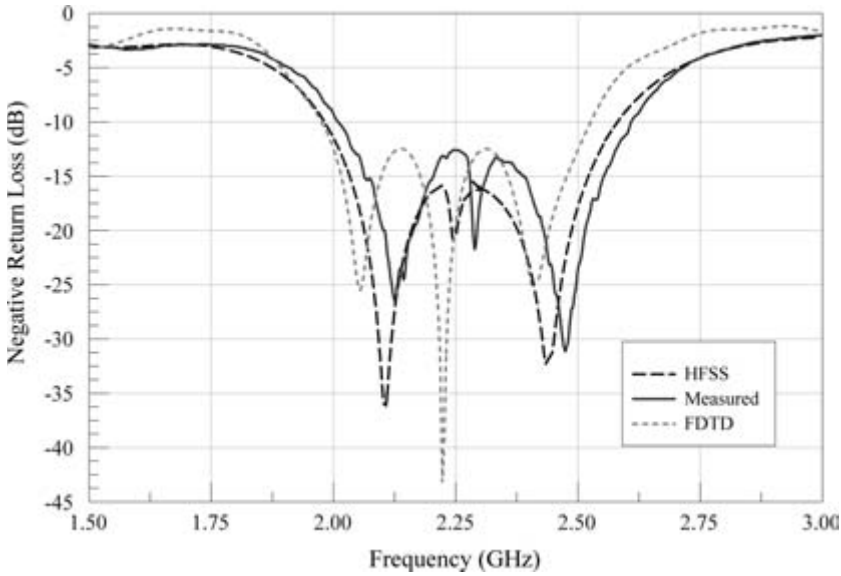

Figure 7-39 Negative return loss of the printed dipole antenna with microstrip balun example predicted by HFSS and FDTD analysis compared with measurement.

tivity that is larger than that of a dipole in free space. Figure 7-40 shows the antenna radiation patterns computed using FDTD, HFSS, and measured at 2.222 GHz.

7.7 Microstrip Fed Tapered Balun Printed Dipole

The printed dipole of Section 7.6 uses the groundplane as a reflector to increase the gain of the antenna. A more traditional printed dipole may be created using a microstrip line with a tapered groundplane which acts as a balun.

The geometry of the microstrip fed tapered balun dipole antenna (MFTBA) is found in Figure 7-41. The taper chosen is generally exponential, as expressed in equation (7.14):

$$\pm x = \pm W_0 e^{-ay} \tag{7.14}$$

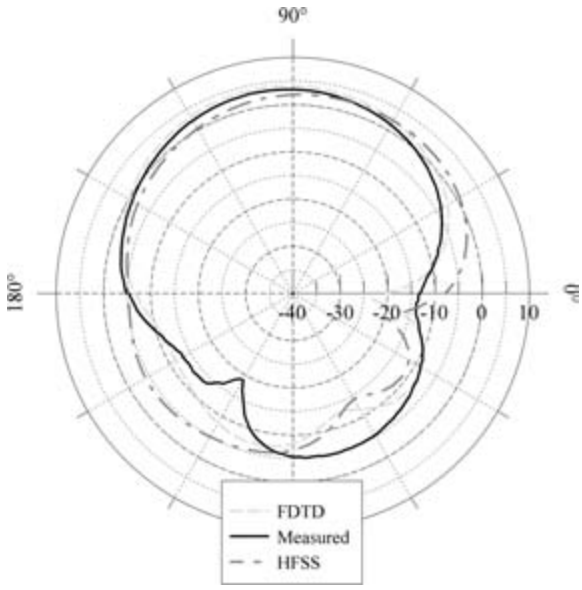

Figure 7-40 (a) E-plane radiation patterns of the printed dipole antenna with microstrip balun example at 2.222 GHz measured and predicted by FDTD analysis and HFSS.

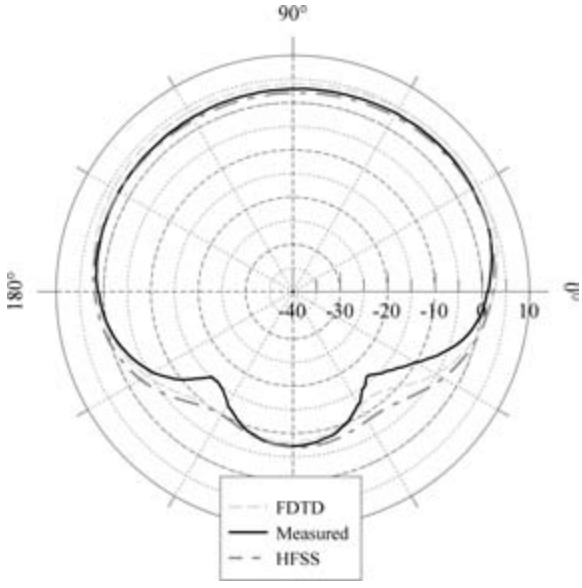

Figure 7-40 (b) H-plane radiation patterns of the printed dipole antenna with microstrip balun example at 2.222 GHz measured and predicted by FDTD analysis and HFSS.

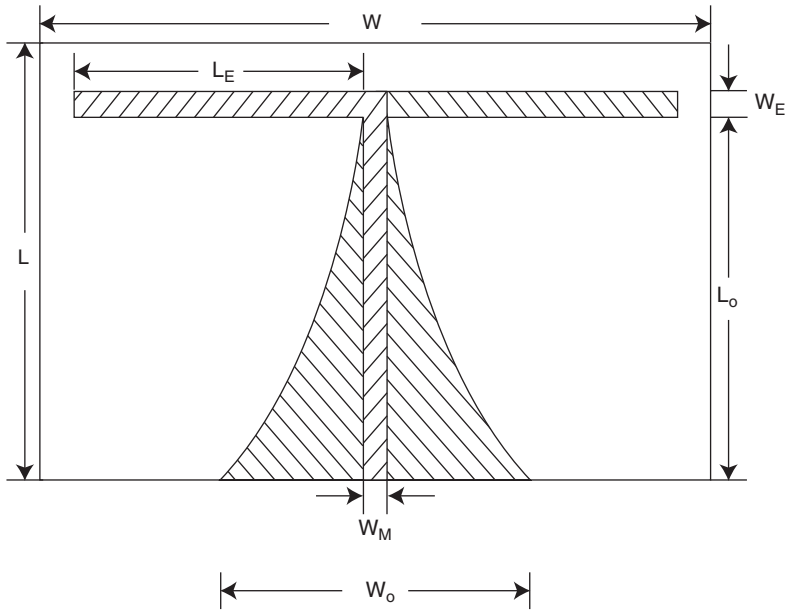

Figure 7-41 The geometry of a microstrip fed tapered balun dipole (MFTBA).

$$a = \frac{-\ln(W_m/W_0)}{(L_0 + We)} \tag{7.15}$$

An example antenna was analyzed with HFSS and FDTD and realized using Taconic TLC-32 substrate. The thickness H is 1.5748 mm (0.062 inches) with ε_r = 3.2 and $\tan\delta$ = 0.003. The antenna dimensions are W = 62.97 mm, L = 40.96 mm, L_e = 27.0 mm, W_e = 1.794 mm, L_0 = 34.68 mm, W_0 = 15.536 mm, and W_m = 1.794 mm (width of microstrip transmission line). The design frequency is 2.20 GHz.

The negative return loss predicted by FDTD, HFSS, and measured is found in Figure 7-42. The best match was measured at 2.207 GHz; FDTD predicted 2.212 GHz and HFSS predicted 2.200 GHz. The measured value essentially splits the predicted ones. The impedance match was found to be better for increased values of W_0 for this design.

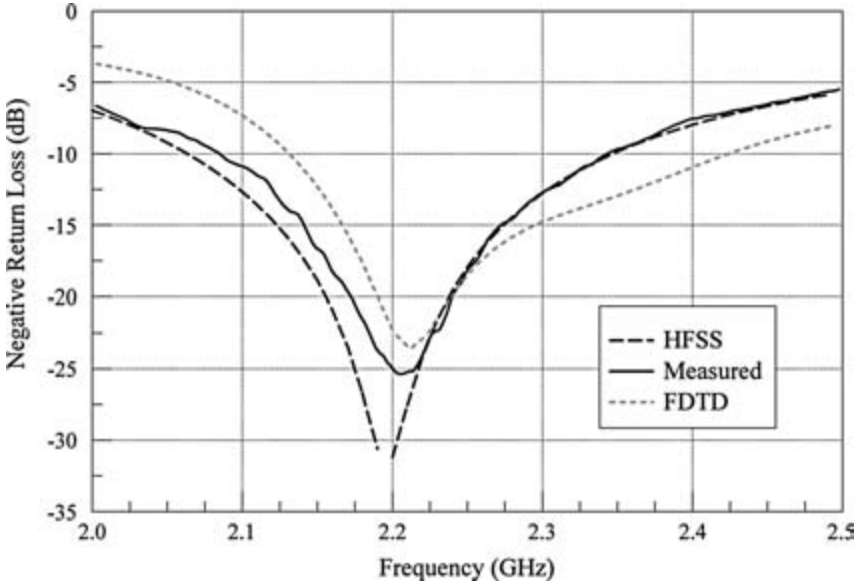

Figure 7-42 Negative return loss of a printed dipole antenna with microstrip tapered balun as predicted by FDTD analysis, HFSS, and measured.

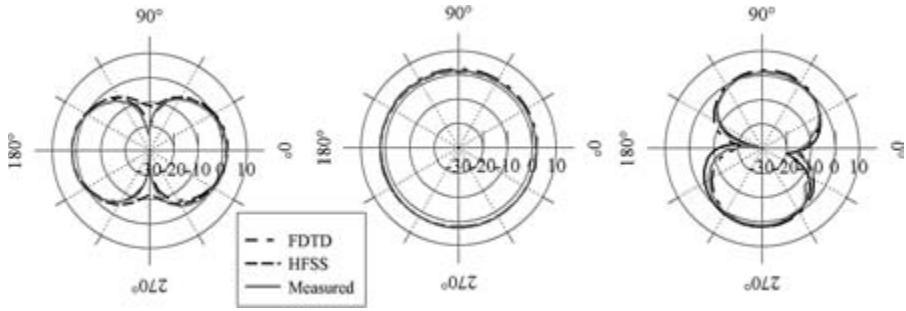

Figure 7-43 Radiation patterns of a printed dipole antenna with microstrip tapered balun as predicted by FDTD analysis, HFSS, and measured.

The radiation patterns of the MFTBA are presented in Figure 7-43. The directivity predicted by FDTD analysis is 2.54 dB; HFSS predicts 2.30 dB directivity and 2.15 dBi gain. The measured gain is 2.53 dBi. The FDTD patterns are closer to measurement than the HFSS predictions.

The tapered balun of the MFTBA produces a pattern with some beam squint, but still reduces the current on a coaxial connection line to small values. This dipole design is useful when a dipole is required that does not have as pure dipole patterns as a Roberts dipole, but is required for a test fixture or other purpose where the ease of fabrication may be of greater importance.[37–39]

References

[1] Nesic, A., and Nesic, D., "Omnidirectional uniplanar electromagnetically coupled antenna array," *Microwave and Optical Technology Letters*, March 20, 2004, Vol. 40, No. 6, pp. 516–518.

[2] Bancroft, R., and Bateman, B. "An omnidirectional microstrip antenna," *IEEE Transactions on Antennas and Propagation*, November 2004, Vol. 52, No. 11, pp. 3151–3153.

[3] Bancroft, R., "Design parameters of an omnidirectional planar microstrip antenna," *Microwave and Optical Technology Letters*, December 5, 2005, Vol. 47, No. 5, pp. 414–418.

[4] Jasik, H., Myslicki, R. L., and Rudish, R. M., "Sheet antenna array structure," U.S. Patent 3,757,342.

[5] Rudish, R. M., "Comments on 'An omnidirectional planar microstrip antenna'," *IEEE Transactions on Antennas and Propagation*, November 2005, Vol. 53, No. 11, p. 3855.

[6] Hill, R., "A twin line omni-directional aerial configuration," *8th European Microwave Conference*, September 1978, pp. 307–311.

[7] Ono, M., Numazaki, T., and Mizusawa, M., "A high-gain omnidirectional antenna made of a printed element," *Transactions of the IECE of Japan*, January 1980, Vol. E63, No. 1, pp. 58–60.

[8] Yee, K. S., "Numerical solution of initial boundary value problems involving Maxwell's equations in isotropic media," *IEEE Transactions on Antennas and Propagation*, May 1966, Vol. 14, No. 3, pp. 302–307.

[9] Bancroft, R., "Radiation properties of an omnidirectional planar microstrip antenna," *Microwave and Optical Technology Letters*, January 2008, Vol. 50, No. 1, pp. 55–58.

[10] Bancroft, R., and Bateman, B., "An omnidirectional microstrip antenna with low sidelobes," *Microwave and Optical Technology Letters*, July 5, 2004, Vol. 42, No. 1, pp. 68–69.

[11] Pozar, D., "Directivity of omnidirectional antennas," *IEEE Transactions on Antennas and Propagation*, October 1993, Vol. 35, No. 5, pp. 50–51.

[12] McDonald, N., "Omnidirectional pattern directivity in the presence of minor lobes: revisited," *IEEE Transactions on Antennas and Propagation*, April 1999, Vol. 41, No. 2, pp. 63–65.

[13] Gibson, P. J., "The Vivaldi aerial," 9th European Microwave Conference, Brighton, UK, 1979, pp. 101–105.

[14] Shin, J., and Schaubert, D. H., "A parameter study of stripline-fed Vivaldi notch-antenna arrays," *IEEE Transactions on Antennas and Propagation*, May 1999, Vol. 47, No. 5, pp. 879–886.

[15] Noronha, J. A. N., Bielawa, T., Anderson, C. R., Sweeney, D. G., Licul, S., and Davis, W. A., "Designing antennas for UWB systems," *Microwaves & RF*, June 2003, pp. 53–61.

[16] Wheeler, H. A., "Fundamental limits of small antennas," *Proceedings IRE*, December 1947, pp. 1479–1484.

[17] McLean, J. S., "A re-examination of the fundamental limits on the radiation Q of electrically small antennas," *IEEE Transactions on Antennas and Propagation*, May 1996, Vol. 44, No. 5, pp. 672–675.

[18] Sten, J. C.-E., Hujanen, A., and Koivisto, P. K., "Quality factor of an electrically small antenna radiating close to a conducting plane," *IEEE Transactions on Antennas and Propagation*, May 2001, Vol. 49, No. 5, pp. 829–837.

[19] Thiele, G. A., Detweiler, P. L., and Penno, R. P., "On the lower bound of the radiation Q for electrically small antennas," *IEEE Transactions on Antennas and Propagation*, June 2003, Vol. 51, No. 6, pp. 1263–1268.

[20] Harrington, R. F., "Effect of antenna size on gain, bandwidth, and efficiency," *Journal of Research of the National Bureau of Standards-D, Radio Propagation*, January–February 1960, Vol. 64D, No. 1, pp. 1–12.

[21] Staub, O., Zurcher, J. F., and Skrivervlk, A., "Some considerations on the correct measurement of the gain and bandwidth of electrically small antennas," *Microwave and Optical Technology Letters*, February 20, 1998, Vol. 17, No. 3, pp. 156–160.

[22] Taga, T., Tsunekawa, K., and Sasaki, A., "Antennas for detachable mobile radio units," *Review of the ECL, NTT, Japan*, January 1987, Vol. 35, No. 1, pp. 59–65.

[23] Taga, T., "Analysis of planar inverted-F antennas and antenna design for portable radio equipment," in *Analysis, Design, and Measurement of Small and Low-Profile Antennas*, Hirasawa, K., and Haneishi, M., eds., London: Artech House, 1992, pp. 160–180.

[24] Taga, T., Tsunekawa, K., and Sasaki, A., "Antennas for detachable mobile radio units," *Review of the Electrical Communications Laboratories, Nippon Telegraph and Telephone Corporation, Japan*, January 1987, Vol. 35, No. 1, pp. 59–65.

[25] Zurcher, J. F., Staub, O., and Skrivervlk, A. K., "SMILA: a compact and efficient antenna for mobile communications," *Microwave and Optical Technology Letters*, November 5, 2000, Vol. 27, No. 3, pp. 155–157.

[26] Huynh, M. C., and Stutzman, W., "Ground plane effects on planar inverted-F antenna (PIFA) performance," *IEE Proceedings on Microwave, Antennas and Propagation*, August 2003, Vol. 150, No. 4, pp. 209–213.

[27] Deshmukh, A. A., and Kumar, G., "Formulation of resonant frequency for compact rectangular microstrip antennas," *Microwave and Optical Technology Letters*, February 2007, Vol. 49, No. 2, pp. 498–501.

[28] Boyle, K. R., and Ligthart, L. P., "Radiating and balanced mode analysis of PIFA antennas," *IEEE Transactions on Antennas and Propagation*, January 2006, Vol. 54, No. 1, pp. 231–237.

[29] Milligan, T. A., *Modern Antenna Design*, New York: McGraw-Hill, 1985, pp. 83–84.

[30] Wong, K.-L., *Planar Antennas for Wireless Communications*, New York: John Wiley & Sons, 2003, p. 10.

[31] Behdad, N., and Sarabandi, K., "A novel approach for bandwidth enhancement of slot antennas," Proceedings of the 2003 Antenna Applications Symposium, Allerton Park, Monticello, IL, September 17–19, 2003, pp. 176–188.

[32] Behdad, N., and Sarabandi, K., "Dual resonator slot antennas for wireless applications," *IEEE AP-S International Symposium Digest*, Monterey, CA, June 20–25, 2004.

[33] Behdad, N., and Sarabandi, K., "A wide-band slot antenna design employing a fictitious short circuit concept," *IEEE Transactions on Antennas and Propagation*, January 2005, Vol. 53, No. 1, pp. 475–482.

[34] Bancroft, R., "A commercial perspective on the development and integration of an 802.11a/b/g HiperLan/WLAN antenna into laptop computers," *IEEE Antennas and Propagation Magazine*, August 2006, Vol. 48, No. 4, pp. 12–18.

[35] Bancroft, R., "Microstrip antenna," U.S. Patent 7,098,863.

[36] Al Basraoui, M., and Shastry, P. N., "Wideband planar log-periodic balun," *International Journal of RF and Microwave Computer-Aided Design*, October 2001, Vol. 11, No. 6, pp. 343–353.

[37] Roberts, W. K., "A new wide-band balun," *Proceedings IRE*, December 1957, pp. 1628–1631.

[38] Fitzgerrell, R. C., "Standard linear antennas, 30 to 1000 MHz," *IEEE Transactions on Antennas and Propagation*, December 1986, Vol. AP-34, No. 12, p. 131.

[39] McLean, J., and Sutton, R., "The minimization of spurious radiation from the baluns and feed regions of Roberts dipole antennas," Antenna Measurement Techniques Association 23rd Annual Meeting & Symposium, Denver, CO, October 21–26, 2001, pp. 217–223.

Appendix A

Microstrip Antenna Substrates

A.1 Microstrip Antenna/Transmission Line Substrates

The selection of a substrate material is a balance between the required electrical, mechanical, and environmental performance required by a design versus economic constraints. Generally, if one has the available design volume to use air as a substrate for a microstrip antenna, this is a good choice. The antenna efficiency is high and the gain is maximized, as is the impedance bandwidth of a conventional microstrip antenna. The surface wave loss when air is used as a substrate is minimal.

When a dielectric substrate is selected, one is often interested in a material with the lowest loss tangent (tan δ) available. The loss tangent is a metric of the quantity of electrical energy that is converted to heat by a dielectric. The lowest possible loss tangent maximizes the antenna efficiency (decreases the losses); this was discussed in Section 2.8 of Chapter 2.

The relative dielectric constant, ε_r, of the substrate determines the physical size of a patch antenna. The larger the dielectric constant, the smaller the element size, but also the smaller the impedance bandwidth and directivity, and the surface wave loss increases. The use of substrates with higher dielectric constants also tightens fabrication tolerances.[1]

The tolerance of the dielectric value is also of significant importance in manufacturing yield. A Monte Carlo-type analysis using the cavity model is a good method for estimating antenna manufacturing yield for a rectangular microstrip antenna when etching tolerance, substrate thickness tolerance, feed point location tolerance, and dielectric tolerances are known. Substrate electrical and physical parameters also vary with temperature. Recent work by Kabacik and Bialkowski indicates that Teflon/fiberglass substrates can have significant variations in dielectric constants for many airborne and space-borne

applications.[2] The dielectric constants and loss tangents of Teflon and fiberglass often differed from what was quoted by manufacturers in their data sheets compared with measurements and were valid over a much narrower temperature range than encountered in many aerospace applications. The performance variations are due to changes in the material dielectric properties—thermal expansion had a minor effect on microstrip antenna performance.

Generally the metal cladding attached to the dielectric substrate material is copper. Two types of copper foil are used as cladding, rolled foil and electrodeposited foil. Rolled foil is passed through a rolling mill a number of times until the desired physical dimensions are obtained and is then bonded to the substrate. Rolled copper has a polished mirror-like appearance. It is generally used for flexible circuitry. Electrodeposited foil is created by electrodeposition of copper onto an inert form which is generally a rolling titanium or steel drum. A thin layer of copper is continuously removed from the form then bonded to the substrate.[3]

Oxidation of copper traces is the primary cause of copper bond failure over time. The copper traces oxidize on both sides (top and bottom) of the trace. The diffusion of oxygen in the substrate material causes the bottom side of the trace to oxidize. Continuous ambient temperatures above 250°F will ultimately degrade the copper bonds on the surface of the board. The most effective way to mitigate this oxidation is to use an effective high-temperature conformal coating. This coating will provide a barrier between the air and the surface of the resin and copper traces.[4]

The computation of characteristic impedance and losses of a microstrip transmission line (see Appendix C) depend on the copper foil thickness. The copper cladding is described in terms of weight per square foot. The thickness of the cladding may then be derived and is listed in Table A-1.[5] Thinner copper traces have smaller etching undercut than thicker traces. This allows for fine (narrow) traces as compared with thicker copper. Thicker copper has higher power-handling capability. This is important where the small cross section of a trace could produce heat buildup and eventual failure.

Generally, the dielectric constant (ε_r) and loss tangent ($\tan \delta$) increase with temperature. In space applications, moisture outgassing produces a lower dielectric constant and loss tangent.

Table A-1 Standard copper foil weights and foil thicknesses.

Foil Weight	Foil Thickness
1/2 oz (14 g)	0.0007 in (0.01778 mm)
1 oz (28 g)	0.0014 in (0.03556 mm)
2 oz (57 g)	0.0028 in (0.07112 mm)
4 oz (142 g)	0.0056 in (0.14224 mm)

Table A-2 Common substrate materials.

Material	ε_r	$\tan\delta$
Teflon (PTFE)	2.1	0.0005
Rexolite 1422	2.55	0.0007
Noryl	2.6	0.0011
FR-4	4.1	0.02
Alumina (99.5%)	9.8	0.0003

Table A-2 lists some common substrate materials used in the design of microstrip antennas and typical dielectric constant and loss tangent values. Teflon [polytetrafluoroethylene (PTFE)] has very desirable electrical qualities, but is not recommended for many space applications. An extensive discussion of PTFE substrates and their fabrication may be found in the literature.[6]

Rexolite 1422 (cross-linked polystyrene) is among the earliest materials used to create planar transmission line.[7] Rexolite 1422 is a very good material for space applications and has many desirable mechanical properties.[8] Rexolite 1422 is easily machined, and its dielectric constant remains stable up to 100 GHz. Rexolite 2200 is a fiberglass-reinforced version that has similar properties to unfilled Rexolite 1422, but it is more rigid and dimensionally stable. Noryl (modified polyphenylene oxide) is suitable for many commercial microwave applications. It has a much lower loss than FR-4 and is relatively cost effective, but it is soft and melts at a relatively low temperature, which can create soldering complications, and sometimes has unsuitable mechanical properties for some applications.

FR-4 is inexpensive and is used in many commercial applications (usually below 1 GHz).[2] FR-4 can be used for some wireless applications, but great care must be taken to budget and minimize the losses when it is used as a substrate above 1 GHz. The dielectric constant of FR-4 formulations varies considerably from 3.9 to 4.6.[9]

Alumina has desirable microwave properties for applications that require a relatively high dielectric constant ($\varepsilon_r \approx 10.0$) and a low loss tangent. Its drawbacks are the difficulty involved in machining it and its brittleness. Alumina has good thermal conductivity, and in some aerospace applications it more readily dissipates heat and remains cooler than other common microwave substrates. In some missile applications where high temperatures may compromise solder joints, alumina is a viable option for the dissipation of heat. Alumina's dielectric constant is very sensitive to the processing used to produce it.

All commercially available substrates and laminates have different requirements for processing. Details of fabrication issues and methods can be found in the literature and directly from manufacturers.[10] Other fabrication options, such as screen printing conductive inks directly on substrates, have also been investigated.[11]

In some commercial applications a planar antenna may be enclosed in an injection-molded radome. The dielectric properties of the resins used are a very important consideration in injection-molded radome design. The resin should have known moisture absorption characteristics. Low moisture absorption is important in maintaining a stable resonance frequency and loss characteristics in environments that have humidity changes.

Plastic materials commonly are of two types: thermoset and thermoplastic. When exposed to heat, thermoset materials undergo a chemical change that is irreversible. When reheated, thermoset materials do not melt, but generally begin charring. FR-4 is an example of a substrate made from a thermoset material. When exposed to heat, thermoplastic materials melt, but do not undergo an irreversible chemical change. They may be remelted after molding. Thermoplastic materials can be reprocessed a number of times, however, the polymer will degrade after a large number of reprocessing cycles. Noryl is an example of a thermoplastic substrate.

[2] FR-4 is a flame retardant version of G-10. FR-4 can generally be used in applications which call for G-10, but G-10 should not be used when FR-4 is specified. G-10 and FR-4 are rated at 285°F. FR-4 does not melt above its rated temperature, but instead begins charring.

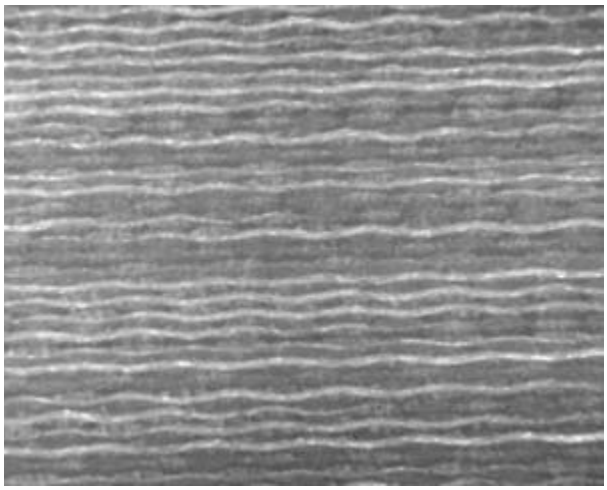

Figure A-1 Cross section of ½ inch thick FR-4 showing the resin (dark) and glass cloth (lighter) layers.

When glass is drawn into thin fibers (which can be 1/100 the width of a human hair) it becomes flexible enough to combine into a yarn.[12] These yarns may then be woven into a fiberglass cloth. A common glass cloth is Type 7628, in which each filament is specified to have a diameter of 9.40 μm (0.37 mil). Each yarn has 408 filaments. When woven into cloth, Type 7628 is 44 yarns/inch (warp) × 32 yarns/inch (weft). Therefore this glass cloth has 17,952 filaments/inch (warp) × 13,056 filaments/inch. The typical thickness of Type 7628 is 0.006 to 0.0078 inches. Ten layers of Type 7628 material can be impregnated with a resin, then stacked and laminated to create a 0.062 inch thick woven fiberglass material.

Type 7628 is created using E-glass, which is an electrical-grade glass.[13] This is considered a general-purpose glass fiber. The relative dielectric constant is $\varepsilon_r = 6.1$ at 10 GHz with a $\tan \delta = 0.0026$.[14] The effective dielectric constant of the material depends on the ratio of the fiberglass to the material impregnated into the glass cloth. In the case where Teflon (PTFE) is filled to produce a dielectric constant of 6.0, the laminate is almost isotropic. This is because E-glass has a dielectric constant of 6.1 and the material consists of mostly glass fibers.[15]

When fiberglass is being drawn, air bubbles may be present in the glass, which end up as capillaries in the glass fibers. These are often referred to as "hollow fibers." These hollow fibers can provide a conductive path which can create a conductive filament and possibly lead to board failure.[16,17]

Microwave Substrate Manufacturers

Arlon
1100 Governor Lea Road
Bear, DE 19701
(302) 834-2100
www.arlonmed.com

CoorsTek
17750 W. 32nd Avenue
Golden, Co 80401
(303) 277-4779
www.coorsceramics.com

Park Electrochemical Corporation (ParkNelco)
5 Dakota Drive
Lake Success, NY 11042
(516) 354-4100
www.parknelco.com

Polyflon Company
One Willard Road
Norwalk, CT 06851
(203) 840-7555
www.polyflon.com

Rogers Corporation
One Technology Drive
P.O. Box 188
Rogers, CT 06263-0188
(860) 779-9605
www.rogerscorporation.com

Sheldahl
1150 Sheldahl Road
Northfield, MN 55057
(507) 663-8000
www.sheldahl.com

Taconic Advanced Dielectric Division
136 Coonbrook Road
Petersburgh, NY 12138
(518) 658-3202
www.taconic-add.com

References

[1] James, J. R., Henderson, A., and Hall, P. S., "Microstrip antenna performance is determined by substrate constraints," *Microwave System News (MSN)*, August 1982, pp. 73–84.

[2] Kabacik, P., and Bialkowski, M. E., "The temperature dependence of substrate parameters and their effect on microstrip antenna performance," *IEEE Transactions on Antennas and Propagation*, June 1999, Vol. 47, No. 6, pp. 1042–1049.

[3] James, J. R., and Hall P. S., eds., *Handbook of Microstrip Antennas*, Vol. 2, Stevenage, UK: Peter Peregrinus, Ltd., 1989, chap. 15.

[4] Guiles, C. L., *Everything You Ever Wanted To Know About Laminates . . . But Were Afraid To Ask*, 8th ed., Version 3.0, Rancho Cucamonga, CA: Arlon Inc., 2000.

[5] Bahl, I. J., and Bhartia, P., *Microstrip Antennas*, London: Artech House, 1980, Appendix C.

[6] James, J. R., and Hall, P. S., eds., *Handbook of Microstrip Antennas*, Vol. 2, Stevenage, UK: Peter Peregrinus, Ltd., 1989, chap. 15.

[7] Howe, Jr., H., "Dielectric material development," *Microwave Journal*, November 1978, pp. 39–40.

[8] Bouquet, F. L., Price, W. E., and Newell, D. M., "Designer's guide to radiation effects on materials for use on Jupiter fly-bys and orbiters," *IEEE Transactions on Nuclear Science*, August 1979, Vol. NS-26, No. 4, pp. 4660–4669.

[9] Wang, C., "Determining dielectric constant and loss tangent in FR-4," UMR EMC Laboratory Technical Report TR00-1-041, University of Missouri, Rolla, MO, March 2000.

[10] Laverghetta, T. S., *Microwave Materials and Fabrication Techniques*, 3rd ed., London: Artech House, 2000.

[11] Bancroft, R., "Conductive ink a match for copper antenna," *Microwaves & RF*, February 1987, Vol. 26, No. 2, pp. 87–90.

[12] Lamm, M., "The fiberglass story," *Invention and Technology*, Spring 2007, pp. 8–16.

[13] Wallenberger, F. T., Watson, J. C., and Li, H., "Glass fibers," in *ASM Handbook*, Vol. 21, *Composites* (#06781G), www.asminternational.org.

[14] Hartman, D., Greenwood, M., and Miller, D., "High strength glass fibers," Technical Paper, AGY Inc., 1996, Table 3.

[15] Olyphant, M., and Nowicki, T. E., "MIC substrates—a review," Paper prepared for presentation at ELECTRO-80, May 13, 1980, Boston, MA, p. 5.

[16] Rogers, K., Van Den Driessche, P., and Pecht, M., "Do you know that your laminates may contain hollow fibers?," *Printed Circuit Fabrication*, April 1999, Vol. 22. No. 4, pp. 34–38.

[17] Rogers, K., Hillman, C., and Pecht, M., "Hollow fibers can accelerate conductive filament formation," *ASM International Practical Failure Analysis*, August 2001, Vol. 1, No. 4, pp. 57–60.

Appendix B

Numerical Methods

B.1 Numerical Integration

The integrations presented in Chapter 2 to compute the directivity of a rectangular microstrip antenna [equation (2.44)], and the integrations in Chapter 3 to compute the radiation conductance and radiation Q of a circular microstrip antenna [equation (3.9)] have no known closed-form solution and are evaluated numerically. When an integrand is sufficiently smooth and contains no singularities, a very efficient method of numerical integration is Gaussian quadrature. Gaussian quadrature integrates a polynomial which curve fits the integrand. The integrations presented in this book all have well-behaved integrands and may be integrated using this method. The integrations of interest are of this form:[1]

$$\int_a^b f(x)\,dx \quad \text{or} \quad \int_a^\infty f(x)\,dx \tag{B-1}$$

$$\int_a^b f(x)\,dx = \frac{b-a}{2}\sum_{i=1}^{N} W_i f\left(\frac{Z_i(b-a)+b+a}{2}\right) \tag{B-2}$$

$$\int_a^\infty f(x)\,dx = 2\sum_{i=1}^{N} \frac{W_i}{(1+Z_i)^2} f\left(\frac{2}{1+Z_i}+a-1\right) \tag{B-3}$$

where N is the number of Gaussian quadrature points, W_i are the weights, $\pm Z_i$ are the abscissas.

For a 16-point Gaussian quadrature, the sums are evaluated as

$$\int_a^b f(x)dx = \frac{b-a}{2}\left(\sum_{i=1}^{8} W_i f\left(\frac{Z_i(b-a)+b+a}{2}\right)+\sum_{i=1}^{8} W_i f\left(\frac{-Z_i(b-a)+b+a}{2}\right)\right) \quad \text{(B-4)}$$

and

$$\int_a^\infty f(x)dx = 2\sum_{i=1}^{8}\frac{W_i}{(1+Z_i)^2} f\left(\frac{2}{1+Z_i}+a-1\right)+2\sum_{i=1}^{8}\frac{W_i}{(1-Z_i)^2} f\left(\frac{2}{1-Z_i}+a-1\right) \quad \text{(B-5)}$$

The Gaussian weights W_i and abscissas $\pm Z_i$ for a 16-point Gaussian quadrature are presented below:

$\pm Z_i$				W_i			
0.09501	25098	37637	440185	0.18945	06104	55068	496285
0.28160	35507	79258	913230	0.18260	34150	44923	588867
0.45801	67776	57227	386342	0.16915	65193	95002	538189
0.61787	62444	02643	748447	0.14959	59888	16576	732081
0.75540	44083	55003	033895	0.12462	89712	55533	872052
0.86563	12023	87831	743880	0.09515	85116	82492	784810
0.94457	50230	73232	576078	0.06225	35239	38647	892863
0.98940	09349	91649	932596	0.02715	24594	11754	094852

The integrations in this text are all calculated using a 96-point Gaussian quadrature.[2]

B.2 Evaluation of Sums

A common metric used to estimate the relative error when summing a series is[3]

$$\frac{|p-p^*|}{|p|} < 5\times 10^{-t} \quad \text{(B-6)}$$

where p is not equal to zero. The value p^* is said to approximate p to t significant digits (or figures) if t is the largest nonnegative integer for which the relationship is satisfied. The assumption is that we know p a priori as the final value we are attempting to evaluate. This relationship is useful as it provides a continuous measure of relative error. Unfortunately many summations in practice converge slowly enough to satisfy this relationship before it is sufficiently converged to an accurate approximation. For example, calculating the driving point impedance of a rectangular microstrip antenna using the cavity model entails computing equation (B-7):

$$Z_{drv} = \sum_{m=0}^{\infty} \sum_{n=0}^{\infty} \frac{j\omega\alpha_{mn}}{\omega_{mn}^2 - (1 - j\delta_{eff})\omega^2} \tag{B-7}$$

One should account for the relative error of the real and imaginary parts of the driving point impedance separately. The contribution of the higher order modes to the driving point impedance can be slow in converging. It is often best to start with a fairly large number of modes, say 100 (0 to 99), then compute nearly double that value, to 199, then calculate a relative error, compute the sum a third time, nearly doubling the number of modes again to 399. The relative error may be checked after each doubling inside a summation loop. Generally this method produces convergent results even for slowly converging green's functions expressed as a summation. Generally testing four to five significant places of relative error is sufficient.

The summations are

$$Z_{drv}^{i} = \sum_{m=100(i-1)}^{(100i)-1} \sum_{n=100(i-1)}^{(100i)-1} \frac{j\omega\alpha_{mn}}{\omega_{mn}^2 - (1 - j\delta_{eff})\omega^2} \tag{B-8}$$

where

$$i = 1, 2, 3, \ldots \frac{\left|Z_{drv}^{i} - Z_{drv}^{(i+1)}\right|}{\left|Z_{drv}^{i}\right|} < 5 \times 10^{-t}$$

where $t = 4$.

B.3 Fixed-Point Iteration

A solution to the equation $x = f(x)$ is said to be a fixed point of the function f. In the case of computing the resonant dimension L (= W) of a square patch, we can use fixed-point iteration on equation (2.74) to find the solution for an equal patch length and width. It is also useful for the computation of the radius of a circular patch antenna from equation (3.6).

The fixed-point algorithm presented in pseudocode is given below:[4]

```
**************************
** FIXED POINT ALGORITHM **
**************************

A solution for x = f(x) may be found given an initial
approximation x0 for the solution of this equation:

The INPUT is an initial approximation of x0, a desired rela-
tive accuracy TOL, and a maximum number of iterations N0.
The OUTPUT is an approximate solution x or failure to locate
a fixed point.

STEP 1. SET i = 1.

STEP 2. WHILE i ≤ N0 DO STEPS 3 TO 6

STEP 3. SET xi = f(x(i-1))

STEP 4. IF |x(i-1) − xi|/|xi| < TOL, THEN
          OUTPUT SOLUTION: xi
          STOP

STEP 5. SET i = i + 1

STEP 6. SET xi − 1 = xi
```

```
STEP 7. OUTPUT 'No fixed point after N0 iterations'
        STOP
```

B.4 Bisection Algorithm

Often it is useful to locate the root of an equation (i.e., the value of x where $f(x) = 0$). The transmission line model of a microstrip antenna can be used to predict the driving point impedance of a rectangular microstrip antenna. If the impedance function is represented by $Z(x)$, and we wish to find the value of x at which the real part of the impedance is R_0, we define $f(x) = RE(Z(x)) - R_0$ and locate the root. $RE(Z)$ is a function that returns the real part of a complex number Z.

A rectangular microstrip antenna in its lowest order mode has a maximum driving point impedance at one radiating edge and decreases to zero at its center. This provides boundaries that may be used with the bisection algorithm to determine the driving point location which provides a desired driving point resistance. Pseudocode for the bisection algorithm is

```
Given a continuous function f on the interval [a,b], where
f(a) and f(b) have opposite signs.
A solution to f(x) = 0 may be found with this procedure:

*****************************
** THE BISECTION ALGORITHM **
*****************************

STEP 1. SET a1 = a and b1 = b

STEP 2. SET i = 1

STEP 3. SET pi = 1/2(ai + bi)

STEP 4. IF pi is an acceptable approximation, GOTO STEP 10
        IF pi is not an acceptable approximation, GOTO STEP 5
```

STEP 5. IF $f(p_i) \cdot f(a_i) > 0$ GOTO STEP 6
IF $f(p_i) \cdot f(a_i) < 0$ GOTO STEP 8

STEP 6. SET $a_{i+1} = p_i$ and $b_{i+1} = b_i$

STEP 7. ADD 1 to i and GOTO STEP 3

STEP 8. SET $a_{i+1} = a_i$ and $b_{i+1} = p_i$

STEP 9. ADD 1 to i and GOTO STEP 3

STEP 10. The procedure is completed

References

[1] Hewlett-Packard, *High Level Math*, HP-41 User's Library Solutions, Palo Alto, CA: Hewlett-Packard, pp. 35–41.

[2] Abramowitz, M., and Stegun, I. A., *Handbook of Mathematical Functions*, Mineola, NY: Dover, 1972, pp. 916–917.

[3] Burden, R. L., and Faires, J. D., *Numerical Analysis*, 4th ed., Boston: PWS-Kent, 1989, pp. 12–14.

[4] Burden, R. L., and Faires, J. D., *Numerical Analysis*, 4th ed., Boston: PWS-Kent, 1989, p. 41.

Appendix C

Microstrip Transmission Line Design and Discontinuities

C.1 Microstrip Transmission Line Design

There are many approaches for developing microstrip transmission line design and analysis equations.[1–7] Relationships presented by Kajfez and Tew have proven to be very flexible for the analysis of microstrip transmission line.[8–9] The characteristic impedance of a microstrip line is given by

$$Z_0 = \frac{42.4}{\sqrt{\varepsilon_r + 1}} \ln\left\{1 + \left(\frac{4h}{\acute{w}}\right)\left[b + \sqrt{b^2 + a\pi^2}\right]\right\} \tag{C-1}$$

where Z_0 is the characteristic impedance of the microstrip transmission line,

$$b = \left(\frac{14 + 8/\varepsilon_r}{11}\right)\left(\frac{4h}{\acute{w}}\right) \tag{C-2}$$

$$\acute{w} = w + a\Delta w \tag{C-3}$$

$\acute{w}$ is the corrected transmission line width, t is the thickness of the transmission line conductor (foil thickness) (see Appendix A),

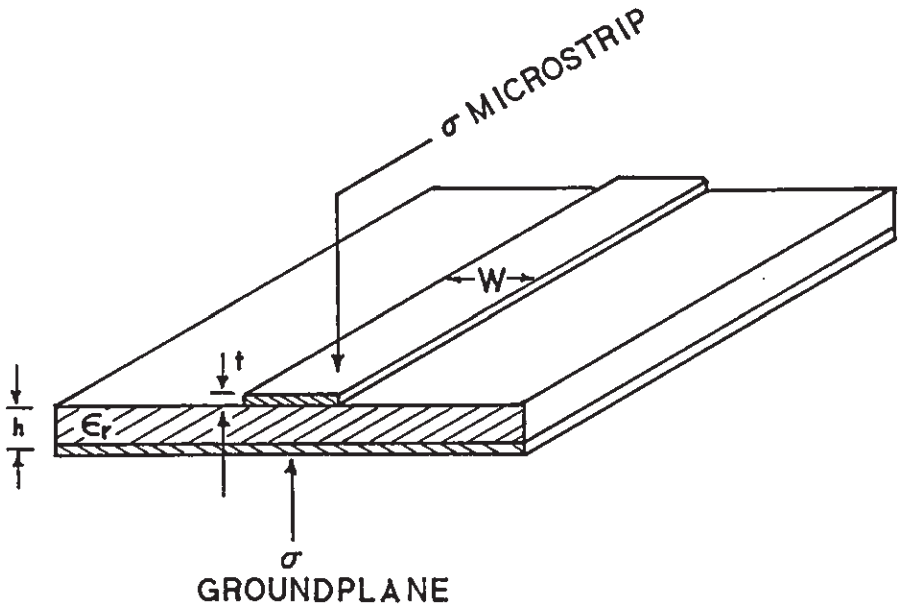

Figure C-1 Microstrip transmission line configuration.

$$\Delta w = \frac{t}{\pi}\left\{1 + \ln\left(\frac{4}{\sqrt{\left(\frac{t}{h}\right)^2 + \left[\frac{1}{\pi\left(\frac{w}{t} + 1.1\right)}\right]^2}}\right)\right\} \tag{C-4}$$

Δw is the width correction factor, and

$$a = \frac{1 + 1/\varepsilon_r}{2} \tag{C-5}$$

The use of a root finding method such as the bisection method (Appendix B) allows one to use this set of equations for synthesis.

Dispersion is a very important property of microstrip lines which must be accounted for in order to expect a successful transmission line design realized using microstrip. The guide wavelength of microstrip transmission line varies with frequency:

$$\lambda_g = \frac{\lambda_0}{\sqrt{\varepsilon_{eff}}} \tag{C-6}$$

where λ_0 is the free space wavelength at a given frequency.

The effective dielectric constant computation is undertaken with

$$\varepsilon_{eff} = \varepsilon_r - \frac{\varepsilon_r - \varepsilon_{eff\,0}}{1 + G(f/f_p)^2} \tag{C-7}$$

$$G = 0.6 + 0.009 Z_0 \tag{C-8}$$

$$f_p(GHz) = \frac{Z_0}{0.8\pi h(mm)} \tag{C-9}$$

$$\varepsilon_{eff\,0} = \left(\frac{Z_0^1}{Z_0}\right)^2 \tag{C-10}$$

where Z_0^1 is Z_0 computed with the dielectric removed and Z_0 is computed with the dielectric present.

The computation of microstrip transmission line loss using the following relationships has the advantage that different microstrip and groundplane conductivities can be used:

$$\alpha(\mathrm{dB/m}) = 90.96\sqrt{\varepsilon_{eff}} \cdot \frac{f(GHz)}{Q} \tag{C-11}$$

$$Q = \frac{1}{1/Q_c + 1/Q_d} \tag{C-12}$$

$$\frac{1}{Q_c} = \frac{Z_0^2 - Z_0^1 + Z_0^3 - Z_0^1}{Z_0^1} \tag{C-13}$$

Table C-1 Computation of Z_0 values ($\varepsilon_r = 1$).

Impedance	Width	Substrate	Metalization
Z_0^1	w	h	t
Z_0^2	w	$h + \delta_p/2$	t
Z_0^3	$w - \delta_s$	$h + \delta_s/2$	$t - \delta_s$

$$\frac{1}{Q_d} = \frac{1 - 1/\varepsilon_{eff}}{1 - 1/\varepsilon_r} \tan\delta \tag{C-14}$$

$$\delta(\text{mm}) = \frac{1}{20\pi\sqrt{f(GHz)\cdot 58\cdot\delta_r}} (\text{copper}) \tag{C-15}$$

The losses are evaluated using three computations of characteristic impedance with the dielectric removed, Z_0^1, Z_0^2, and Z_0^3, as listed in Table C-1. The first calculation, Z_0^1, is the characteristic impedance of the transmission line with perfect electrical conductors (zero skin depth). We use h, w, and t. The second calculation, Z_0^2, is evaluated with a groundplane that has been decreased by half of a skin depth of the material from which it is constructed. The last calculation, Z_0^3, is computed for a microstrip transmission line in which all the sides of the microstrip conductor have been recessed by one-half of the skin depth of the material from which the conductor has been fabricated (Figure C-2). The conductor Q (Q_c) may then be computed. Next, the dielectric Q (Q_d) is obtained. The microstrip losses may then be obtained using the total Q.

C.2 Discontinuity Compensation

When microwave devices such as a branchline hybrid are realized in microstrip transmission line, they deviate from the ideal transmission line model representation because of discontinuities. In order to design these devices as accurately as possible, it is necessary to compensate for discontinuities. In high-frequency devices, it is also imperative to include the effects of dispersion.

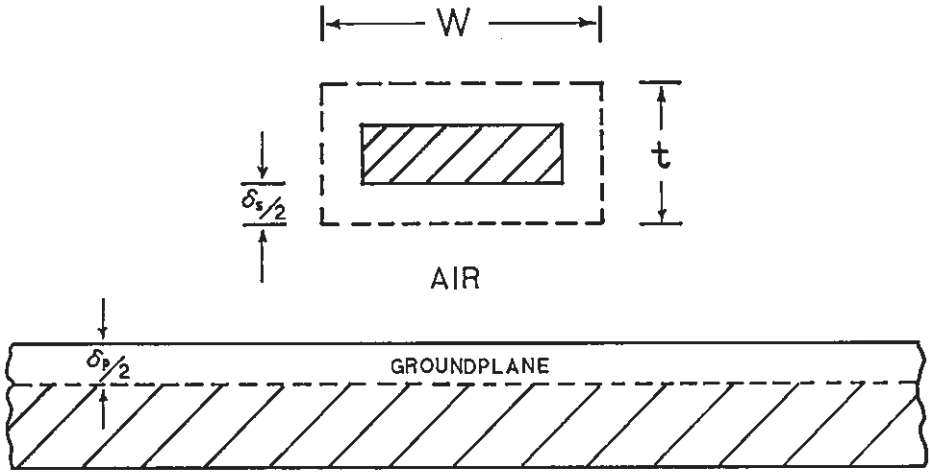

Figure C-2 Microstrip transmission line configuration.

In Figure C-3 we have two common discontinuities encountered when realizing microstrip transmission line designs. The first case is an open-circuited transmission line. This is encountered when using open-circuited matching stubs. The fringing capacitance at the end of the transmission line causes it to be electrically longer than its physical length. We compensate for this affect by reducing the line length by ΔL.[10]

$$\Delta L = 0.412\left(\frac{\varepsilon_{re}+0.3}{\varepsilon_{re}-0.258}\right)\left(\frac{W/h+0.262}{W/h-0.813}\right)h \tag{C-16}$$

where h is the substrate thickness and W is the microstrip line width.

The second case is T-junction compensation. The electrical length of the shunt arm of the T-junction must be reduced by length D_2. The currents take a shortened path close to the corner which requires compensation. The formula for the shunt arm reduction is

$$D_2 = \frac{120\pi}{Z_1\sqrt{\varepsilon_{re}^1}}\left(0.5 - 0.16\frac{Z_1}{Z_2}[1-2\ln(Z_1/Z_2)]\right)h \tag{C-17}$$

where ε_{re}^1 is the effective dielectric constant of the through-arm.

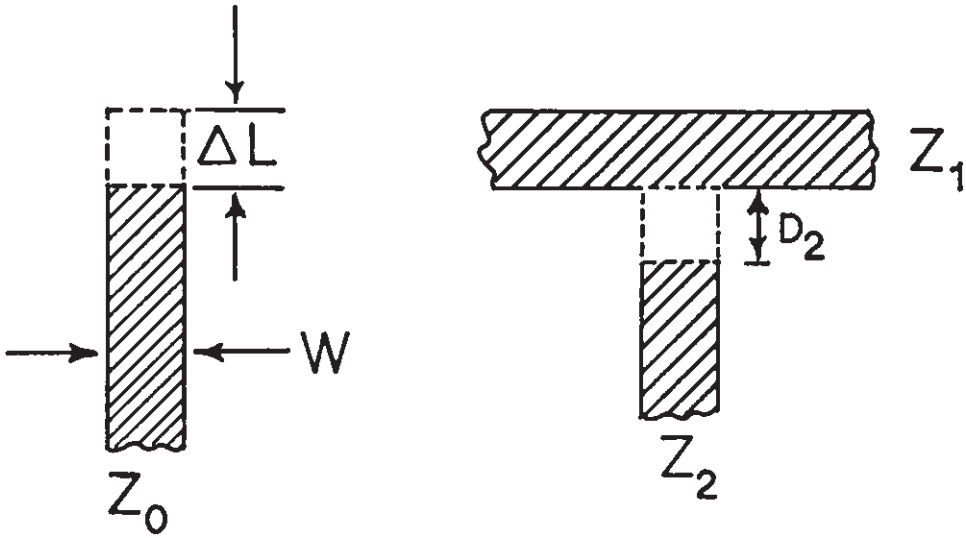

Figure C-3 (a) Open circuit end correction in microstrip. (b) Shortening of the shunt arm of a microstrip T-junction.

When a pair of microstrip lines form a junction of high- and low-impedance lines, the exposed section of the low-impedance (wider) line requires a capacitive end correction. Equation (C-18) can be used to compute an approximate correction. It is assumed the low-impedance (wider) line has a width of W_2 and the narrower high-impedance line has a width of W_1. Δ_s is the step correction:

$$\Delta_s \approx \Delta L\left(1-\frac{W_1}{W_2}\right) \tag{C-18}$$

When a microstrip transmission line forms a sharp right-angle bend, excess capacitance appears at the corner of the line. A reflection will be produced by the corner capacitance. To compensate for this effect, the corner is often mitered. This can be seen in Figure C-5. Figure C-5(a) shows a microstrip transmission line with a right-angle bend and a step in width. Figure C-5(b) illustrates the use of a miter to reduce the corner capacitance and reduce the reflection it causes. The miter fraction m is defined as

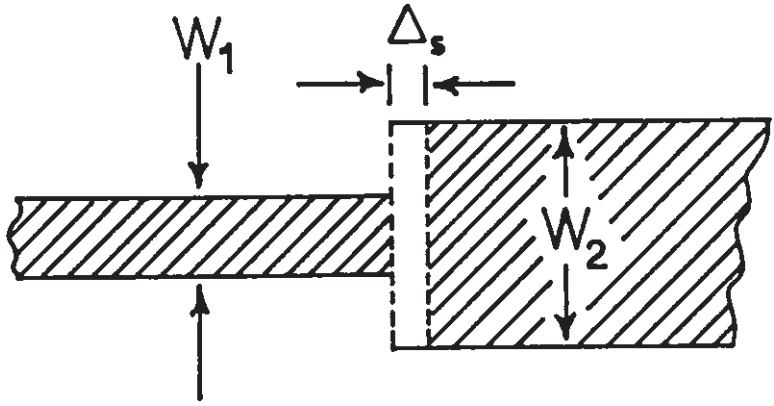

Figure C-4 Microstrip line step discontinuity.

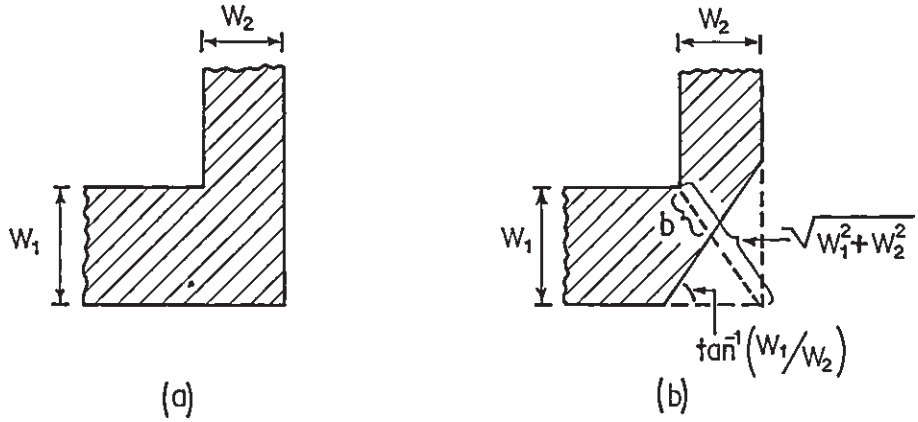

Figure C-5 (a) Microstrip transmission line with a 90° bend and width change. (b) Miter of a microstrip 90° corner to reduce discontinuity from corner capacitance.

$$m = 1 - \frac{b}{\sqrt{W_1^2 + W_2^2}} \tag{C-19}$$

A value of 0.6 is a good choice for m. When $W_1 = W_2$, equation (C-19) reduces to a definition conventionally found in the literature.[11]

References

[1] Wu, T. T., "Theory of the microstrip," *Journal of Applied Physics*, March 1957, Vol. 28, No. 3, pp. 299–302.

[2] Schneider, M. V., "Microstrip lines for microwave integrated circuits," *Bell System Technical Journal*, May–June 1969, pp. 1421–1444.

[3] Lev, J. J., "Synthesize and analyze microstrip lines," *Microwaves & RF*, January 1985, pp. 111–116.

[4] March, S., "Microstrip packaging: watch the last step," *Microwaves*, December 1981, pp. 83–94.

[5] March, S., "Errata: 'Microstrip packaging: watch the last step'," *Microwaves*, February 1982, p. 9.

[6] Pucel, R. A., Massé, D. J., and Hartwig, C. P., "Losses in microstrip," *IEEE Transactions on Microwave Theory and Techniques*, June 1968, Vol. 16, No. 6, pp. 342–350.

[7] Pucel, R. A., Massé, D. J., and Hartwig, C. P., "Errata: 'Losses in microstrip'," *IEEE Transactions on Microwave Theory and Techniques*, December 1968, Vol. 16, No. 12, pp. 1064.

[8] Kajfez, D., and Tew, M. D., "Pocket calculator program for analysis of lossy microstrip," *Microwave Journal*, December 1980, Vol. 23, pp. 39–48.

[9] Wheeler, H. A., "Transmission line properties of a strip on a dielectric sheet on a plane," *IEEE Transactions on Microwave Theory and Techniques*, August 1977, Vol. 25, No. 8, pp. 631–647.

[10] Hammerstad, E. O., and Bekkadal, F., "A microstrip handbook," ELAB Report, STF 44 A74169, N7034, University of Trondheim, Norway, 1975.

[11] Edwards, T. C., *Foundations for Microstrip Engineering*, New York: John Wiley & Sons, 1981.

Appendix D

Antenna Topics

D.1 Friis Transmission Formula

An equation that describes the path loss between two antennas was introduced by Friis.[1] The formula was introduced in terms of the effective area of the transmitting and receiving antenna:

$$P_r = \frac{A_t A_r}{\lambda^2 R^2} P_t \tag{D-1}$$

where

P_r = power available at the output port of the receiving antenna
P_t = power fed into the input port of the transmitting antenna
A_r = effective area of the receiving antenna
A_t = effective area of the transmitting antenna
R = distance between the antennas
λ = wavelength.

The power delivered to the terminals of an antenna is defined as

$$P_r = SA_e \tag{D-2}$$

where

S = power density of a plane wave incident on the antenna (in W/m^2)
A_e = effective area of the antenna (in m^2).

The gain of an antenna in terms of effective area is

$$G = \frac{4\pi}{\lambda^2} A_e \tag{D-3}$$

The Friis equation may now be written in terms of antenna gain:

$$P_r = G_t G_r \left(\frac{\lambda}{4\pi R} \right)^2 P_t \tag{D-4}$$

where

G_t = transmit antenna gain

G_r = receive antenna gain.

The relationship between gain over an isotropic source (G) and that gain in decibels with respect to an isotropic source is

$$G_{dBi} = 10 \log_{10} G \tag{D-5}$$

It is often useful to write the Friis equation using logarithms to determine path loss:

$$\text{Path Loss (dB)} = 20 \log_{10}(FR) - 27.558 - G_r(dB) - G_t(dB) \tag{D-6}$$

where

F = frequency (in MHz)

R = distance between antennas (in m).

The Friis transmission formula assumes the value of R is sufficiently large so a plane wave is incident at the receive antenna. To satisfy this requirement, the separation distance should be at least

$$R > \frac{2d^2}{\lambda} \tag{D-7}$$

where d is the largest linear dimension of either antenna. The formula also assumes free space.

D.2 Wireless Link Range versus Power Input Level

It is often of interest to estimate the effective range of a communications link. If we assume the noise environment remains constant at any given distance,

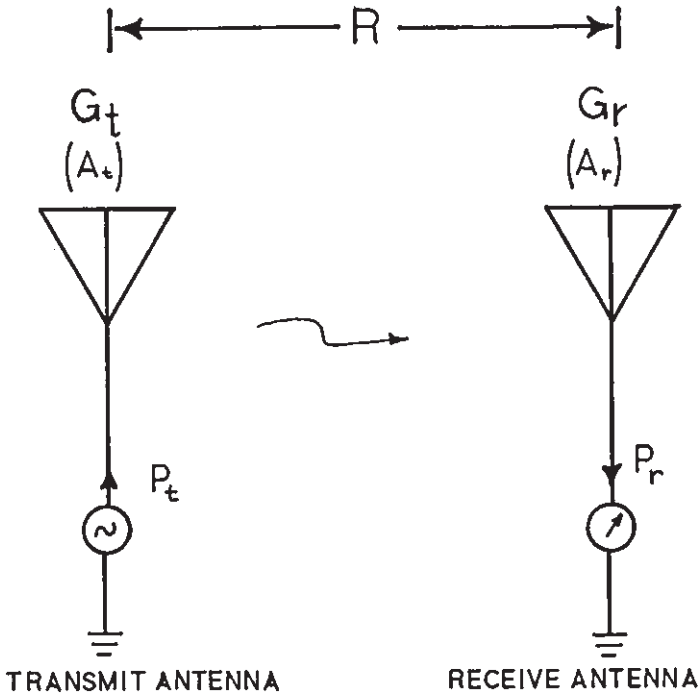

Figure D-1 Friis transmission formula geometry.

this allows us to write an equation for the maximum distance of a communications link, R_0, for a given power input, P_{t_0}, which just meets the systems signal-to-noise ratio requirement.

$$P_r = G_t G_r \left(\frac{\lambda}{4\pi R_0} \right)^2 P_{t_0} \tag{D-8}$$

If we wish to increase the range of the communications link to a distance R_1, which may be defined as a multiple of R_0:

$$R_1 = \Delta R_0 \tag{D-9}$$

We can write a second equation using the Friis transmission formula:

$$P_r = G_t G_r \left(\frac{\lambda}{4\pi \Delta R_0} \right)^2 P_{t_1} \tag{D-10}$$

The two equations are equated so the receive power is identical in both cases, which after canceling common terms becomes

$$\frac{P_{t_1}}{P_{t_0}} = \Delta^2 \tag{D-11}$$

The power increase in decibels required to increase the maximum range of a communications link is

$$\text{Power}_{dB} = 10 \log_{10} \left(\frac{P_{t_1}}{P_{t_0}} \right) = 20 \log_{10} (\Delta) \tag{D-12}$$

To double the distance we use $\Delta = 2$. Equation (D-12) shows the power into the antenna used for transmission must be increased by 6.02 dB to double the range. Table D-1 shows the relationship between antenna gain (or system gain) versus the increase in link distance factor. If the gain of an antenna increases by 6.02 dB, the distance a link will be maintained is twice the original distance. When increased by 9.54 dB, the link distance will be increased by a factor of three. This assumes the signal-to-noise ratio remains constant.

Table D-1 Power increase (in dB) versus increased link distance factor.

dB	Δ
3.01	$\sqrt{2}$
6.02	2
9.54	3
12.04	4

D.3 Decibels

The decibel provides a logarithmic comparison of two power levels. A power level is assigned as a reference value, P_r. This value is used for comparison to a measured or computed power level, P. The decibel (dB) is defined as

$$\mathrm{dB} \equiv 10\log_{10}(P/P_r) \tag{D-13}$$

The decibel is a convenient method of expressing power because of its logarithmic definition, which transforms the mathematical operations of multiplication and division to addition and subtraction, and powers and roots become multiplication and division. Addition and subtraction must be done with the numerical values prior to conversion to decibels, or they must be converted from decibels to numerical values. This may be accomplished with

$$P/P_r = 10^{(dB)/10} \tag{D-14}$$

When a power level reference value is tied to a known absolute reference value such as a milliwatt, the power in decibels is generally referred to as decibels with respect to a milliwatt and written dBm. When 1 W is used as P_r, this is called decibels with respect to a watt and written dBW. The gain value of an antenna is referenced with respect to an isotropic antenna's power level and is known as decibels with respect to an isotropic radiator and written dBi. Acoustic sound pressure levels are also expressed using decibels.

The definition of a decibel in equation (D-13) can be expressed in terms of units which equivalently express power. The power dissipated by a resistor in a given electric circuit is V^2/R. We can choose a reference voltage V_r and resistance R_r. When substituted into equation (D-13) we obtain

$$\begin{aligned} \mathrm{dB} &= 10\log_{10}\left[\frac{V^2/R}{V_r^2/R_r}\right] \\ &= 20\log_{10}(V/V_r) - 10\log_{10}(R/R_r) \end{aligned} \tag{D-15}$$

For the special case of $R = R_r$, this expression reduces to

$$\mathrm{dB} = 20\log_{10}(V/V_r) \tag{D-16}$$

Table D-2 Decibel to power ratio estimates.

dB	P/P_r
3	2
6	4
9	8
10	10
13	20
20	100
26	400
30	1000
39	8000
40	10000

Decibels allow one to express large dynamic ranges in an accessible manner. When power is expressed in decibels, one can readily determine the approximate change in power. A change of 3 dB is close to a factor of two in power (1.995), a 10 dB change is a factor of 10 in power. A 13 dB difference is a factor of 10 in power multiplied by a factor of two, or approximately 20 (19.95).

Table D-2 has estimates of the power ratios for a number of decibel values. These estimates are very useful in engineering work for a quick view of the magnitude of quantities. The exact values are given by equation (D-14). For instance, 39 dB is estimated to be a power ratio of 8000 ($= 10 \cdot 10 \cdot 10 \cdot 2 \cdot 2 \cdot 2 = 10^{39.03/10}$). The actual value is $10^{39/10} = 7{,}943.38$, which is only a 0.71% difference.

D.4 Antenna Gain and Directivity

An antenna with a radiation pattern which is constant (independent of angle) is an isotropic antenna. An isotropic antenna that radiates 100% of the power it accepts at its driving point (P_0) is generally used as a reference antenna to which physically realizable antennas are compared. The radiation from an isotropic antenna may be described mathematically as

$$S = \frac{P_0}{4\pi R^2} \tag{D-17}$$

where S is in power per unit area or power density.

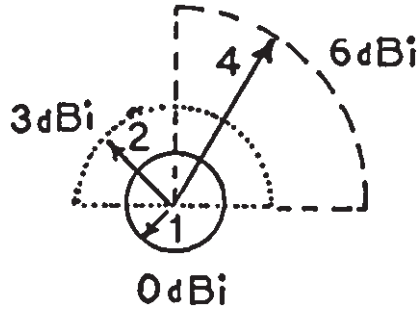

Figure D-2 Isotropic antenna, hemispherical antenna, quarter sphere antenna.

The input power accepted by the driving point of an isotropic antenna is spread equally over a sphere with a surface area of $4\pi R^2$. If the radiation pattern of an isotropic source is altered so it radiates only over an upper hemisphere but is still constant over that hemisphere, but zero otherwise, the same amount of power (P_0) is distributed over half of the area of the isotropic case. This means the power over this radiation hemisphere is twice as large as the isotropic case.

$$S = 2\frac{P_0}{4\pi R^2} \; (0 < \phi < 2\pi, 0 < \theta < \pi) \tag{D-18}$$

If the upper hemisphere is again divided in half so the radiation is allowed to radiate equally over one-fourth of the area of the full (isotropic) sphere, and is zero elsewhere, the amount of power will be four times the power of an isotropic antenna:

$$S = 4\frac{P_0}{4\pi R^2} \; (0 < \phi < \pi, 0 < \theta < \pi) \tag{D-19}$$

In each case we are able to use a factor to describe the increase in radiation level experienced in terms of radiation over a sphere. We can rewrite this with a value of D:

$$S = D\frac{P_0}{4\pi R^2} \; (0 < \phi < \pi/2, 0 < \theta < \pi) \tag{D-20}$$

We have restricted the radiation of the antenna to one-eighth of a sphere ($0 < \phi < \pi/2$, $0 < \theta < \pi$) in the equation above, then $D = 8$. We will refer to this factor as the directivity of an antenna.

The antennas discussed so far to illustrate directivity are not physically realizable. When measuring an antenna you will have a varying function $D(\phi,\theta)$ which describes the radiation pattern:

$$S = D(\theta, \phi)\frac{P_0}{4\pi R^2} \tag{D-21}$$

The maximum value of $D(\theta,\phi)$ is assumed to be the directivity of an antenna.

Physical antennas have losses that decrease the total amount of power radiated with respect to the input power, P_0. The pattern of an antenna is assumed to not be affected by the losses inherent in its construction. The gain of an antenna (G) is related to its directivity by the antenna's efficiency (e):

$$G = eD \tag{D-22}$$

$$S(\theta, \phi) = eD(\theta, \phi)\frac{P_0}{4\pi R^2} = G(\theta, \phi)\frac{P_0}{4\pi R^2} \tag{D-23}$$

As with directivity, the gain of an antenna is assumed to be the maximum value of $G(\theta,\phi)$ over the radiation sphere. Directivity is a property of pattern shape alone. At one time, directivity was called pattern gain, and when losses were included it became antenna gain. Methods to estimate the directivity of antennas have been developed and are very useful for approximating expected gain before measurement. The gain of an antenna is in terms of power and may be written in decibels with respect to an isotropic antenna:

$$G_{dBi} = 10\log_{10}(G) \tag{D-24}$$

Gain is generally assumed to be with respect to an isotropic antenna. In some instances, antennas are compared with a dipole as a reference (dBd). This reduces the gain (in dBi) by 2.14 dB.

Both sides of equation (D-23) can be multiplied by R^2 to obtain the radiation intensity U:

$$U(\theta,\phi) = G(\theta,\phi)\frac{P_0}{4\pi} \tag{D-25}$$

The total power radiated (P_r) by an antenna is the surface integral of the radiation intensity over the entire radiation sphere:

$$P_r = \int_0^{2\pi}\int_0^{\pi} G(\theta,\phi)\frac{P_0}{4\pi}\sin\theta\, d\theta\, d\phi \tag{D-26}$$

The ratio of the total amount of power radiated by an antenna divided by the amount of power accepted by the antenna's driving point is the efficiency (e) of the antenna. Dividing equation (D-26) by P_0, we obtain

$$e = \frac{P_r}{P_0} = \int_0^{2\pi}\int_0^{\pi}\frac{G(\theta,\phi)}{4\pi}\sin\theta\, d\theta\, d\phi \tag{D-27}$$

Losses in the materials out of which an antenna is constructed reduce the total radiated power.

Directivity may be more formally defined in terms of radiation intensity:

$$\text{Directivity} = \frac{\text{maximum radiation intensity}}{\text{average radiation intensity}} = \frac{U_{\text{maximum}}}{U_0} \tag{D-28}$$

The average radiation intensity of an antenna may be obtained by integrating the radiation intensity over the entire radiation sphere and then dividing by the area of a sphere in steradians, which is 4π:

$$U_0 = \frac{1}{4}\int_0^{2\pi}\int_0^{\pi} U(\theta,\phi)\sin\theta\, d\theta\, d\phi \tag{D-29}$$

The average radiation intensity is assumed to have accounted for all the power in an electromagnetic wave (i.e., total power in two orthogonal polarizations).

D.5 Attenuation and VSWR

In some wireless applications, a considerable amount of cable may exist between the driving point of an antenna and the signal source which feeds it. If the attenuation due to a length of cable is known, its affect on VSWR may be approximated as if it were a lumped attenuator.[2] Generally a length of cable produces ripple in the measured VSWR and an attenuator does not. The attenuation of a cable is frequency dependent, whereas, over its operating bandwidth, an attenuator is approximately constant. When the attenuation introduced is known, equation (D-30) may be used to predict the new input VSWR if the original driving point VSWR is known:[3]

$$\mathrm{VSWR}_{\mathrm{input}} = \frac{\sqrt{\left(\frac{\mathrm{VSWR}_{\mathrm{DP}}-1}{\mathrm{VSWR}_{\mathrm{DP}}+1}\right)^2 10^{-(A/5)}}+1}{1-\sqrt{\left(\frac{\mathrm{VSWR}_{\mathrm{DP}}-1}{\mathrm{VSWR}_{\mathrm{DP}}+1}\right)^2 10^{-(A/5)}}} \tag{D-30}$$

where

A = attenuation of an attenuator (in dB, positive)
$\mathrm{VSWR}_{\mathrm{DP}}$ = VSWR at the driving point of an antenna (or load)
$\mathrm{VSWR}_{\mathrm{input}}$ = VSWR following the attenuator.

Example D.5.1: A resistive microwave load of 150 Ω is connected to a 50 Ω system that produces a 3.0 : 1 VSWR. What will the VSWR measured be if a 7 dB attenuator is placed between the load and the 50 Ω system? Using equation (D-30), we obtain:

$$\mathrm{VSWR}_{\mathrm{input}} = \frac{\sqrt{\left(\frac{3-1}{3+1}\right)^2 10^{-(7/5)}}+1}{1-\sqrt{\left(\frac{3-1}{3+1}\right)^2 10^{-(7/5)}}} = 1.22$$

In terms of return loss, equation (D-30) becomes:

$$RL_{\mathrm{input}} = [RL_{\mathrm{DP}} + 2A] \tag{D-31}$$

Example D.5.2: A return loss of 2.922 dB (6.0 : 1 VSWR) is produced by a resistive load. A 7 dB attenuator is used to pad the load. What is the return loss measured at the input of the attenuator?

$$RL_{\text{input}} = 2.922\,\text{dB} + 2 \cdot 7.0\,\text{dB} = 16.92\,\text{dB}$$

References

[1] Friis, H. T., "A note on a simple transmission formula," *Proceedings IRE*, May 1946, pp. 254–256.

[2] *Reference Data for Radio Engineers*, Indianapolis, IN: Howard W. Sams & Co., 1982, chap. 11.

[3] Rizzi, P. A., *Microwave Engineering Passive Circuits*, Upper Saddle River, NJ: Prentice Hall, 1988, p. 267.

Appendix E

Impedance Matching Techniques

E.1 The λ/8 Transmission Line Transformer

In 1967 Donald Steinbrecher at the Massachusetts Institute of Technology (MIT) published a single-page paper on the use of λ/8 transmission line sections.[1] He stated in this work: "Any load impedance can be transformed to a real impedance by a λ/8 transformer whose characteristic impedance is equal to the magnitude of the load impedance."

If one has an impedance of $Z_L = R_L + jX_L$, this can of course be written in polar form as $|Z_L| \angle \theta$. When a λ/8 transmission line section is attached to this load, and its characteristic impedance Z_0 is equal to $|Z_L|$, the input impedance becomes pure real.

The requirement that $Z_0 = |Z_L|$ can often produce Z_0 values which are impractically large for microstrip realization in many cases, but should be considered as an option, especially for lower impedances. A quarter-wave impedance transformer can be used with the eighth-wave transformer to match a complex impedance to a desired resistance value.

Example E-1. Combined λ/8 and λ/4 Transformer Matching

As an example of a complex to real impedance transformation using a λ/8 transmission line section we will use the load impedance presented in Figure E-1. The circuit consists of a 55.76 Ω resistor and a 3.01 nH inductor at 2.715 GHz. The load impedance is $Z_L = 55.76 + j51.36\ \Omega$, which in polar form is $|75.765|\ \Omega \angle 42.678^\circ$.

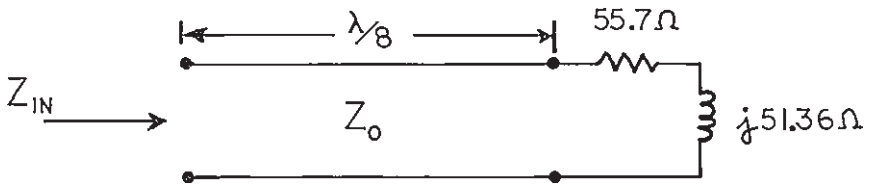

Figure E-1 The example load impedance of $55.76 + j51.36\ \Omega$ is connected to an eight-wave transformer which will produce an input impedance that is pure real when the characteristic impedance of the λ/8 matching transformer is equal to the magnitude of the load impedance.

The lossless transmission line equation is

$$Z_{in} = Z_0 \frac{Z_L + jZ_0 \tan \beta L}{Z_0 + jZ_L \tan \beta L} \tag{E-1}$$

In the case of a λ/8 section of transmission line, this reduces to

$$Z_{in} = Z_0 \frac{Z_L + jZ_0}{Z_0 + jZ_L} \tag{E-2}$$

We use a λ/8 matching transformer with $|Z_0| = Z_{01} = 75.765\ \Omega$. The input impedance becomes

$$Z_{in} = 75.765 \frac{55.7 + j51.36 + j75.765}{75.765 + j(55.7 + j51.36)}$$

$$Z_{in} = 173.0 - j89.6 \cdot 10^{-6}\ \Omega$$

$$Z_{in} \approx 173.0\ \Omega$$

We now need to transform this pure real impedance value to 50 Ω in order to match the system reference impedance. Because the input impedance is now

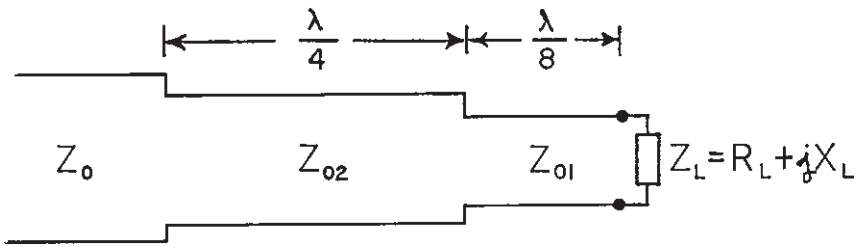

Figure E-2 A quarter-wave impedance transformer can be used with an eighth-wave impedance transformer to match a load to a desired system impedance.[1]

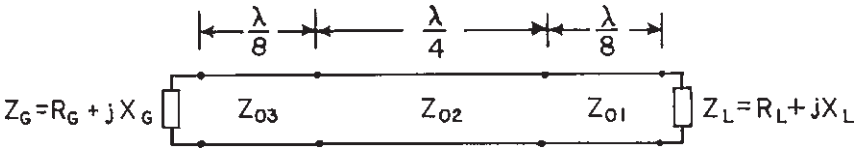

Figure E-3 Two λ/8 and one λ/4 transformers can be used to conjugate match source and load impedances simultaneously.[1]

pure real, this can easily be done using a quarter-wave transformer, as shown in Figure E-2:

$$Z_{02} = \sqrt{50 \cdot R_{in}} = 93.0\,\Omega$$

The transmission line impedances in this example are all very realizable in most microstrip transmission line media using common substrates.

E.2 Dual λ/8 Transmission Line Transformer

Two λ/8 transformers and a single λ/4 transformer can be used to conjugate match a source and load impedance with a total section length of λ/2. This is shown in Figure E-3.

The following relations are used to accomplish this matching:

$$Z_{01} = |Z_L| \tag{E-3}$$

$$Z_{02} = \sqrt{\frac{R_L R_G |Z_L||Z_G|}{(|Z_L| - X_L)(|Z_G| - X_G)}} \tag{E-4}$$

$$Z_{03} = |Z_G| \tag{E-5}$$

E.3 *Q* Matching with a λ/8 Transmission Line Transformer

There may be a design where one would like to minimize the amount of physical area used to match a load. It is possible to use a λ/8 transformer with lumped element *Q* matching in place of the quarter-wave transformer in Figure E-2 to decrease the footprint of the matching network.

Q matching is based on the transformation of a series to a parallel circuit. In our example, we start with a pure real load created by a λ/8 transformer, add parallel reactance to produce the desired real part of 50 Ω in the series equivalent circuit, and then add a second reactance in series to cancel the series reactance, leaving a desired pure real resistance of 50 Ω. The use of *Q* matching is detailed by White.[2]

Example E-2. Combined λ/8 Transformer and *Q* Matching

We will use the load of Example E-1 with the λ/8 transformer. At the design frequency, the input impedance at the input of the λ/8 transformer becomes a real impedance value of 173 Ω. At the design frequency we can view this network as equivalent to a single resistive load of 173 Ω, shown in Figure E-4. We now use *Q* matching to transform the impedance level from 173 Ω (rather than using a quarter-wave transformer) to the system reference impedance (50 Ω).

The equations governing the two situations (series and parallel) are presented in Figure E-5. We can use the parallel relationship which transforms the resistance between parallel and series circuits to compute the circuit *Q*:

$$R_P = R_S\left(1 + Q^2\right) \tag{E-6}$$

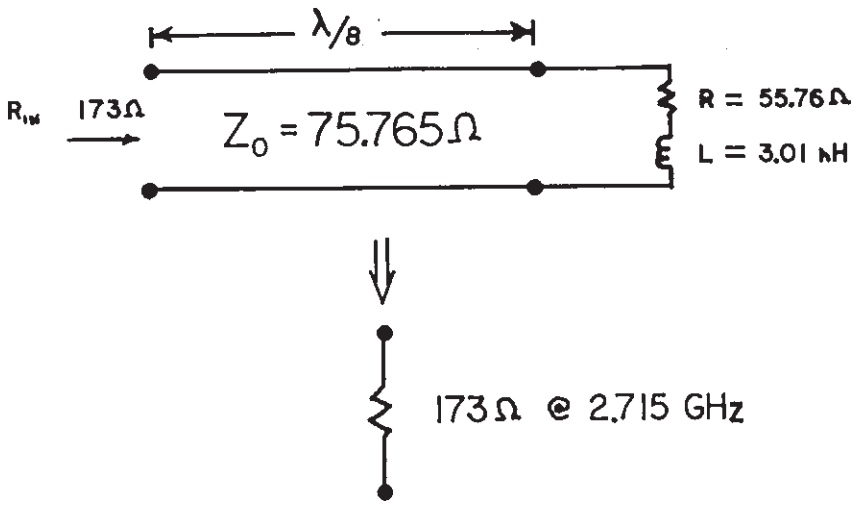

Figure E-4 The λ/8 transformer with impedance transformation to pure real can be viewed as a single resistive element.

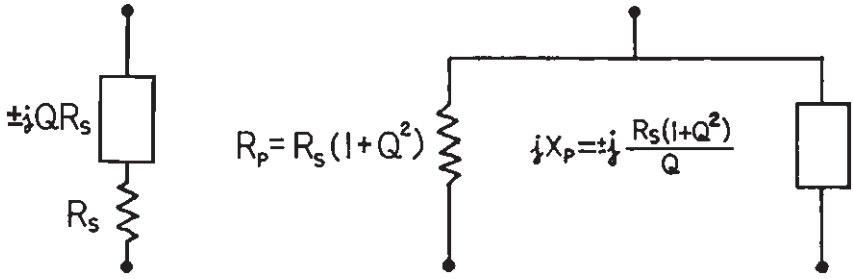

Figure E-5 Series to parallel equivalent circuits used in the Q matching method.

We know $R_P = 173\ \Omega$ and we desire a series resistance of $R_S = 50\ \Omega$. Using equation (E-6), we obtain the circuit Q:

$$Q = \sqrt{\frac{173}{50} - 1} = 1.568$$

We now determine what shunt reactance is required in the parallel circuit to produce a series circuit with a real part of 50 Ω. The reactance is

$$X_p = \frac{R_s\left(1+Q^2\right)}{Q} \tag{E-7}$$

$$X_p = \frac{50\left(1+(1.568)^2\right)}{1.568} = 110.288\,\Omega$$

If we choose a shunt inductor as our parallel circuit reactance, we compute the inductance from the inductive reactance as 6.45 nH:

$$L = \frac{|X_L|}{2\pi f} = \frac{110.288}{2\pi\left(2.715\cdot 10^9\right)} = 6.45\,\text{nH}$$

The reactance of the series circuit is determined from the circuit Q:

$$X_s = QR_s = 1.568\cdot 50 = 78.4\,\Omega$$

We will need a series capacitive reactance $|X_c|$ to cancel the series inductive reactance, which gives us a capacitance value of 0.750 pF. This is a very small capacitance to realize in an actual circuit, but may be used for illustration:

$$C = \frac{1}{2\pi f\,|X_c|} = \frac{1}{2\pi\left(2.715\cdot 10^9\right)78.4} = 0.75\,\text{pF}$$

The final matching circuit is shown in Figure E-6. One can choose to use a shunt capacitor with a series inductor as an alternative Q matching design. In some instances this may produce a more desirable topology or component values.

A circuit simulator was used to analyze these two designs for comparison. The results are in Figure E-7 and Figure E-8. The original impedance is designated with triangles on the Smith chart and the negative return loss plot. The matched impedance with an eighth- and quarter-wave transformer is marked with squares and the eighth-wave transformer with an LC Q matching circuit

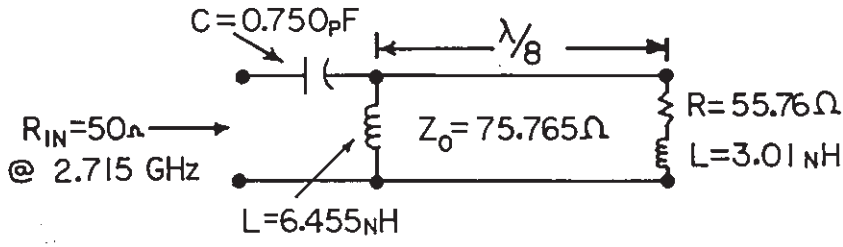

Figure E-6 Impedance matching design using a λ/8 transformer with *Q* matching in place of a λ/4 transformer.

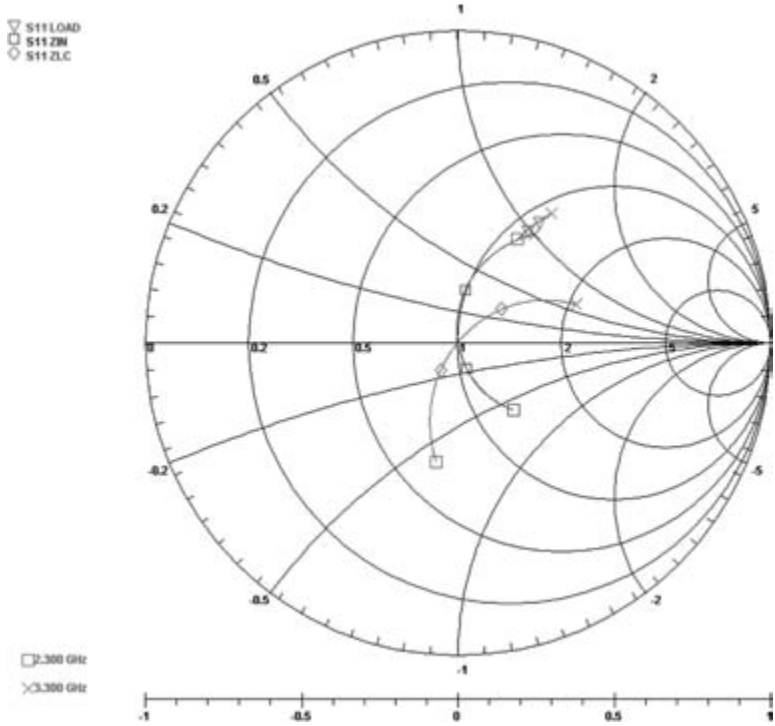

Figure E-7 Smith chart plot of the original impedance (triangle), λ/8 with λ/4 matching (square), and λ/8 with *Q* matching circuit (diamond).

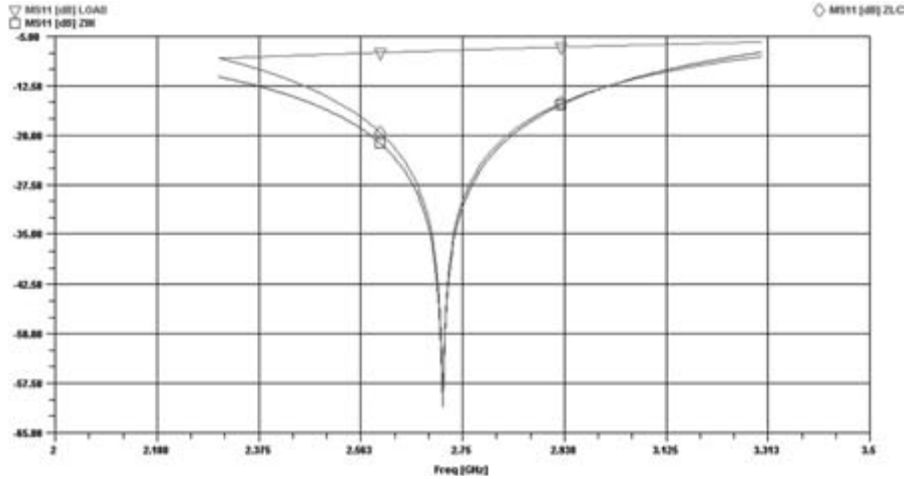

Figure E-8 Negative return loss plot of the original impedance (triangle), λ/8 with λ/4 matching (square), and λ/8 with Q matching circuit (diamond).

is designated with diamonds. The matching results are nearly identical. One should keep in mind that in general the Q of transmission line sections is larger (lower loss) than discreet components. The Q of an inductor may produce larger losses in a circuit than desired. This is of course a trade-off between size and matching efficiency. In some cases, one may be able to use Q matching directly for an even simpler matching circuit design.

E.4 Single-Section Series Transmission Line Impedance Transformer

The single-section transformer in Figure E-9 cannot match all complex loads, but its simplicity makes it attractive as a method for a simple matching network. This network is detailed in an online monograph by Orfanidis.[3] In order to match a complex load, $Z_L = R_L + jX_L$, with a single-section impedance transformer of characteristic impedance Z_0 and normalized length $L_1 = l_1/\lambda_1$ (l_1 is the physical length, λ_1 is the transmission line wavelength) to a transmission line

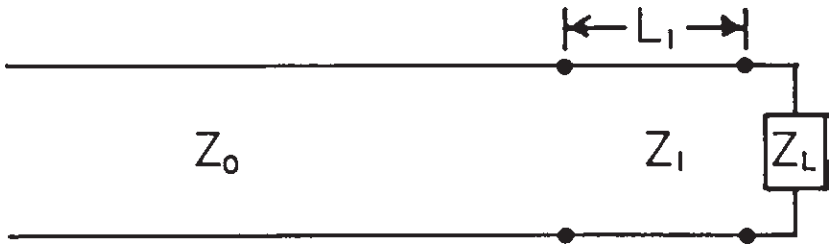

Figure E-9 Single-section series impedance transformer.

system with a reference value of Z_0 (usually 50 Ω) either of these conditions must be satisfied:

$$Z_0 < R_L \quad \text{or} \quad Z_0 > R_L + \frac{X_L^2}{R_L} \tag{E-8}$$

There is always a solution when Z_L is a pure real impedance. This suggests it might be useful to consider using this type of transmission line matching solution with an λ/8 transformer.

When the conditions are met for a single line match, the transformer impedance and length are given by

$$Z_1 = \sqrt{Z_0 R_L - \frac{Z_0 X_L^2}{Z_0 - R_L}} \tag{E-9}$$

$$L_1 = \frac{1}{2\pi} \tan^{-1}\left[\frac{Z_1(Z_0 - R_L)}{Z_0 X_L}\right] \tag{E-10}$$

Example E-3. Single-Section Impedance Match

Once again we use the matching problem introduced in Example E-1 for illustration. The solution is negative and normalized to the wavelength. We obtain a realizable solution by adding one-half wavelength of transmission line to obtain $L = 0.4451\lambda$. Orfanidis has Matlab code available online for the solution of these equations for a single-section series transmission line transformer that uses the mod() function to produce a physically realizable length: L1 = mod(L1,0.5).

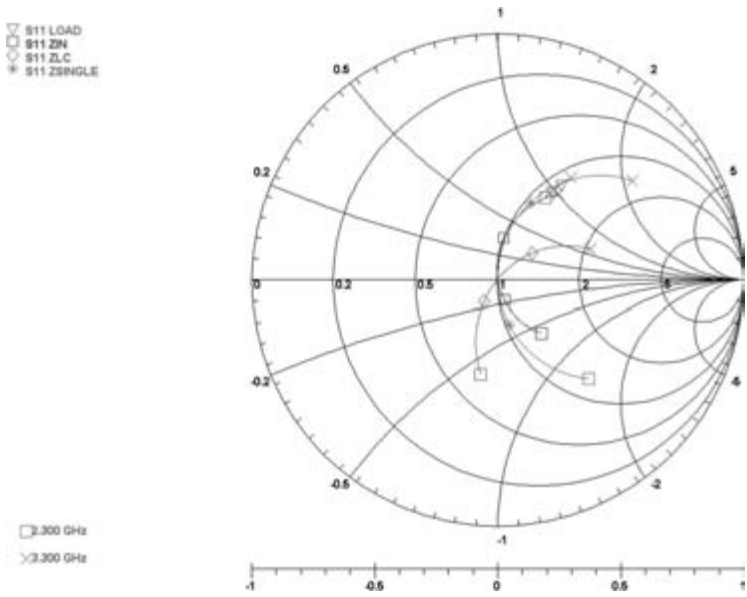

Figure E-10 Smith chart plot of the original impedance (triangle), λ/8 with λ/4 matching (square), λ/8 with *Q* matching circuit (diamond), and with a single line section (star).

Figure E-10 and Figure E-11 present a comparison of the different methods used to match the example antenna impedance of Example E-1 so far. The single line section has a number of disadvantages compared with the other methods. It is longer than the other methods in this case and so it will take up more physical area to realize, and the single line section has a reduced impedance bandwidth compared with the other methods. There may be circumstances where this solution will be shorter than other options and so one should always check to see if it is a realistic possibility.

E.5 Two Section Chebyshev Impedance Transformer

If one has the available physical space to implement a more sophisticated impedance transformer than often exists in many wireless applications, one could combine a λ/8 transformer with two λ/4 section Chebyshev impedance transformers, as shown in Figure E-12.

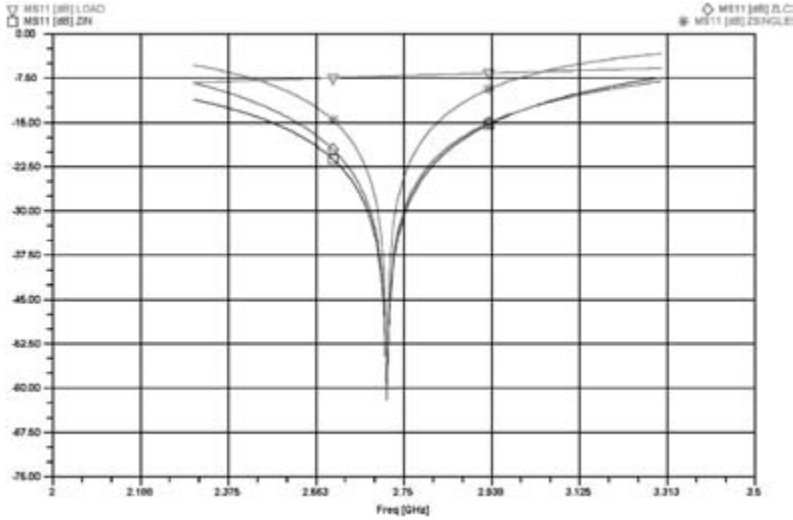

Figure E-11 Negative return loss plot of the original impedance (triangle), λ/8 with λ/4 matching (square), λ/8 with *Q* matching circuit (diamond), and with a single line section (star).

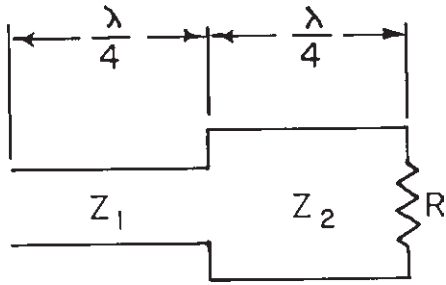

Figure E-12 Two-section Chebyshev quarter-wave transmission line transformer design.

The normalized equations for the design of a two section Chebyshev impedance transformer are[4]

$$Z_1 = (RS)^{1/4} \tag{E-11}$$

where R is the normalized load resistance, S is the maximum allowable standing wave ratio S:1, and Z_1 is the normalized characteristic impedance of the input (first section) of the transformer. After obtaining Z_1, we can then calculate Z_2 using

$$Z_2 = \frac{R}{Z_1} \tag{E-12}$$

where Z_2 is the normalized impedance of the section connected to the normalized load resistance R. The normalizing resistance is the system reference impedance, which is 50 Ω (Z_0 = 50 Ω) in this example.

Example E-4. λ/8 with Two Section Chebyshev Transformer

Using equation (E-11) and equation (E-12), we compute the normalized values to match the impedance. We will once again use the RL circuit from Example E-1 as an example load to match. From previous computations we know the input resistance of the eighth-wave transformer is 173.0 Ω:

$$R = 173.0/50.0 = 3.46$$

We will allow a maximum VSWR of 1.7 : 1 (S = 1.7):

$$Z_1 = (3.46 \cdot 1.7)^{1/4} = 1.5573$$

$$Z_2 = 3.46/1.5573 = 2.221$$

Multiplying the values of Z_1 and Z_2 by 50 Ω we obtain our final design parameters:

$$Z_1 = 78.0\,\Omega$$

$$Z_2 = 111.1\,\Omega$$

The transformer was implemented and analyzed with a circuit simulator, as done previously. The previous matching solutions and the two section

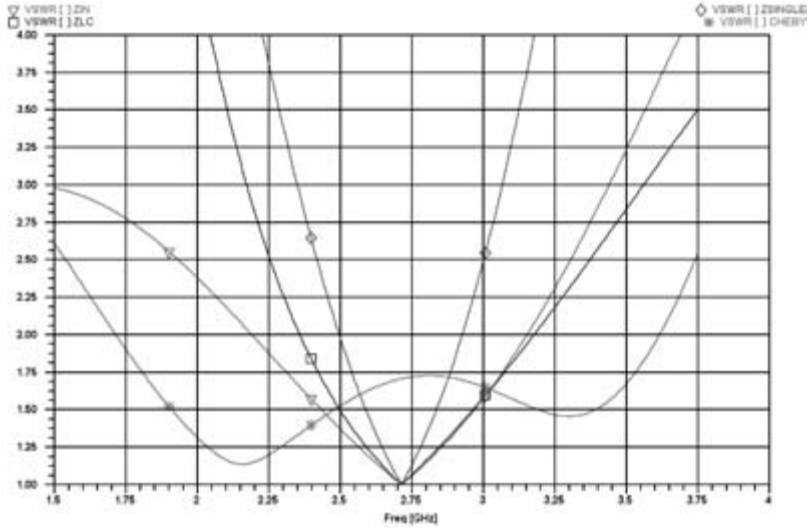

Figure E-13 VSWR plot of the different matching solutions examined previously compared with a Chebyshev transformer and eighth-wave stub: λ/8 transformer with λ/4 transformer matching (triangles); λ/8 transformer with LC *Q* matching (squares); single transmission line impedance matching (diamonds); and λ/8 transformer with two-section Chebyshev λ/4 transformer matching (stars).

Chebyshev transformer with eighth-wave series transformer is presented in Figure E-13. We see a considerable increase in bandwidth when using a two section Chebyshev transformer. Of course, what one gains in bandwidth is traded off with line length and larger mismatch over the band.

E.6 Bode-Fano Limits/Matching Overview

A classic textbook about the subject of impedance matching is *Microwave Filters, Impedance-Matching Networks, and Coupling Structures*.[5] A footnote on page 5 of this text states:

> Simple matching networks can give very great improvements in impedance match, and as the number of matching elements is increased, the improvement per additional element rapidly becomes smaller and smaller. For this reason,

fairly simple matching networks can give performance which comes close to the theoretically optimum performance for an infinite number of impedance-matching elements.

This is good news for realizing minimum footprint matching networks with maximum matching bandwidth. There are fundamental trade-offs one must keep in mind when designing a matching network. These are known as the Bode-Fano criteria. Pozar has a good discussion of impedance matching limitations which are presented as a set of gloss points:[6]

1. A broader band match can only be achieved at the expense of a poorer match over the larger frequency range.
2. The matching bandwidth cannot be perfectly matched except at a single point, which means only a finite number of frequencies can be matched in with a perfect match.
3. High Q circuits are harder to match than low Q circuits.

As the bandwidth of an impedance match is increased, the level of match decreases (i.e., more mismatch is introduced). Some people refer to this as a gain bandwidth product. This is an approximate, but fairly accurate way to look at this restriction. In order to keep a constant gain bandwidth product, one must give up match for bandwidth or bandwidth for match.

A dominant single mode (linearly polarized) rectangular microstrip antenna has a driving point impedance that looks very much like an RLC circuit. It was shown in Chapter 4 that by using an impedance matching network with a 2:1 VSWR matching requirement one is limited to four times the bandwidth of an unmatched antenna.

In Section E.5, the design of a two section Chebyshev impedance transformer was illustrated. This improved the (2:1 VSWR) bandwidth considerably over other methods described. It has been proverbially believed that a Chebyshev impedance transformer is the optimum compromise between mismatch ripple in the matched bandwidth and the maximum bandwidth achievable. In 1981 Carlin and Amstutz challenged this assumption.[7] The researchers provide examples of loads with which they first use a Chebyshev impedance transformer as a matching network, then proceed to use a method they call the real frequency technique to match the load with better results. Clearly a Chebyshev

match is not the optimum possible. The technique is very mathematically intensive and a "simplified real frequency technique" has been proposed. It too is mathematically intensive. This simplified method has been detailed by Gerkis.[8]

Increasingly there is a demand to create dual-band antennas which may require dual-band matching networks. Unfortunately there appears to be very little literature extant on the subject. A recent paper on the design of dual-band Chebyshev impedance transformers by Castaldi et al. has a useful discussion of dual-band matching.[9] The lack of any developed analytical methods for matching two separate frequency bands leaves only computer optimization as a viable solution.

There are many pitfalls one can encounter when designing a matching network. In some cases one can design a matching network that has components with an effective series resistance (ESR) that produces large energy dissipation. There are instances when an antenna may appear to be matched by a circuit, but if the antenna is removed from this matching circuit, the measured return loss does not change drastically, indicating the network is acting more as an attenuator than a matching circuit. A matching circuit is a resonant circuit and has its own Q, which can mask the fact that the circuit is acting more like a resonant attenuator rather than a matching circuit.

The design and implementation of a matching network is only as good as the quality of the physical inductors and capacitors used. The accuracy of any circuit simulation is dependent upon how well these physical devices mirror the elements used in the circuit simulator. One needs to characterize the lumped elements with measurement or nonideal models to obtain good results. Often deviations seen between analysis and measurement are from the use of ideal resistors, inductors, and capacitors in a circuit simulator when the physical elements are nonideal. Kielkowski provides a detailed discussion of the importance of device characterization in successful circuit design.[10]

The attentive reader may have noted the load impedance used for illustration in the previous methods ($Z_{in} = 55.76 + j51.365\ \Omega$) has a real part that is very close to 50 Ω, and that a single series capacitor could be used to match the driving point impedance. In practice, this was done to match the driving point impedance of a tapered omnidirectional microstrip antenna.[11] A surface mount 1 pF capacitor was used as a "via" through the circuit board in series

with the antenna's driving point impedance to cancel the series inductive reactance and produce an acceptable match.

References

[1] Steinbrecher, D. H., "An interesting impedance matching network," *IEEE Transactions on Microwave Theory and Techniques*, June 1967, Vol. 15, No. 6, p. 382.

[2] White, J. F., *High Frequency Techniques*, New York: John Wiley & Sons, 2004, pp. 67–74.

[3] Orfanidis, S. J., *Electromagnetic Waves and Antennas*, Piscataway, NJ: Rutgers University, 2008, http://www.ece.rutgers.edu/~orfanidi/ewa/.

[4] Wheeler, G. J., *Microwave Engineer's Handbook*, London: Artech House, 1971.

[5] Matthaei, G., Young, L., and Jones, E. M. T., *Microwave Filters, Impedance Matching Networks, and Coupling Structures*, London: Artech House, 1980 (reprint).

[6] Pozar, D. M., *Microwave Engineering*, New York: McGraw-Hill, 1990, pp. 325–327.

[7] Carlin, H. J., and Amstutz, P., "On optimum broad-band matching," *IEEE Transactions on Circuits and Systems*, May 1981, Vol. CAS-28, No. 5, pp. 401–405.

[8] Gerkis, A. N., "Broadband impedance matching using the 'real frequency' network synthesis technique," *Applied Microwaves and Wireless*, July–August 1988, pp. 26–36.

[9] Castaldi, G., Fiumara, V., and Pinto, I. M., "A dual-band Chebyshev impedance transformer," *Microwave and Optical Technology Letters*, October 20, 2003, Vol. 30, No. 2, pp. 141–145.

[10] Kielkowski, R., *SPICE: Practical Device Modeling*, New York: McGraw-Hill, 1995, chap. 2.

[11] Bancroft, R., and Bateman, B., "An omnidirectional microstrip antenna with low sidelobes," *Microwave and Optical Technology Letters*, July 5, 2004, Vol. 42, No. 1, pp. 68–69.

Index

A

Active Impedance 166–167

Antenna 1, 3–7, 10–20, 24–49, 51–68, 70, 76–80, 82–95, 97–100, 102–108, 111–114, 116–117, 110–123, 126–129, 131–135, 137–138, 140–141, 142–143, 146, 148–149, 152, 155–157, 160–161, 163, 165, 166–168, 170–172, 176, 178, 180–183, 185–186, 188, 190–192, 194–201, 203–207, 200–225, 227–232, 235–238, 243, 245–247, 257–258, 260–266, 277, 281–283

Axial Ratio 44–47, 49, 52, 54, 65, 87, 89, 121

B

Bandwidth 3, 5, 16, 19, 27–28, 35, 45, 47, 49, 51–54, 60–61, 65, 67–68, 81–83,85,94,102–106,110–113, 116, 118, 120–123, 132, 140, 160–161, 178, 182, 185–186, 191–192, 196–203, 205–207, 209, 212–213, 215, 217, 219, 221–223, 226–227, 235, 266, 277, 280–281

- axial ratio 44–47, 49, 52, 54, 65, 87, 89, 121
- circular polarization 5–6, 39–44, 47–50, 52–53, 63–65, 85–90, 100, 123, 126, 133
- electrically small antenna (ESA) 65, 99
- fundamental limit 105, 122, 199, 205, 209, 217
- Impedance 10–12, 14, 16–17, 19, 21, 24, 26–28, 35, 40–41, 43–54, 57, 59–62, 64–65, 67, 80–83, 92, 94, 102–109, 111–1 17, 119–123, 127, 124, 140, 155–157, 161, 163, 166–167, 170, 178, 181–182, 185–186, 191–192, 197–198, 200–203, 206, 207, 212–213, 215, 217, 219–221, 223–227, 230, 235–236, 245, 247, 249, 252, 254, 268–283
- linear polarization 14, 40–41, 64, 76, 100, 121, 126
- Pattern 5–7, 16–17, 28, 30–24, 65, 68–70, 76, 79–80, 82–84, 87–92, 94–95, 100, 143, 148–149, 151–153, 160, 163–165, 167–168, 180, 182–189, 191, 193, 196, 207, 210–211, 222–223, 228–229, 231–232
- received power 53–54

C

Cavity Model 10, 19–20, 24, 27–28, 40, 43–47, 52–54, 62, 64, 85, 98, 104, 127–129, 134, 167–172, 175, 235, 245

Characteristic Admittance 12–13, 115

Circular Polarization 5–6, 39–14, 47–50, 52–53, 63–65, 85–90, 100, 122, 126, 133

- Circular Patch 78, 81, 83–87, 89, 92, 94–96, 99–100, 246

Rectangular Patch 6, 10, 20, 24–25, 27, 41, 44, 47, 50, 52, 62, 64, 70, 76, 83–84, 100, 126, 129, 134, 137–138, 173
Single Feed Design 49
TM11 76, 79, 83–84, 87–89, 94–95, 99
TM21 6, 76, 79, 88–91, 94–95, 99
cross polarization 63–64, 92, 94–96

D

Dielectric 1, 3–6, 10, 13, 14, 21–22, 28–30, 33, 36, 42, 47, 52–65, 68, 70, 77, 81–84, 89, 94, 98, 100, 102, 106, 142, 157, 160, 163, 183, 186, 194, 200, 211, 235–241, 251–253
Directivity 28, 30–31, 33–34, 54, 62, 86–81, 83–84, 89, 91–92, 145–148, 153, 160, 163, 168, 170, 186–187, 207, 222, 227, 231, 235, 243, 262, 264–265
Driving Point 11–17, 20–21, 23, 26–27, 35, 38, 44–47, 52, 54, 60–65, 76–77, 80, 92, 94, 103–108, 119, 127–129, 161, 163, 166–167, 171, 178–181, 185–186, 191, 197, 200, 203, 207, 214–217, 219–221, 225, 245, 247, 262–262, 265–206, 281–283
Driving Point Impedance 11–12, 14, 16–17, 21, 26–27, 35, 44, 46, 52, 60, 62, 80, 92, 103–104, 106–108, 119, 127, 163, 166, 178, 181, 1.91, 210–221, 225, 245, 247, 281–282

E

edge 3–4, 10–21, 28–29, 33–36, 40, 48–40, 59–60, 64, 67, 77, 79, 83, 87, 92, 98, 111, 116–117, 127, 146, 150, 156–158, 160, 163, 168, 170–171, 173–176, 180, 185, 195, 205, 207, 211–212, 214–216, 220–222, 226–227, 247
conductance 13, 16–17, 158
Non-radiating 11, 14–15, 17–19, 60, 163, 168
radiating 3, 10–17, 28–29, 34, 36, 40, 60, 67, 111, 116, 157, 160, 247
suceptance 13, 59
effective dielectric constant 4, 13, 57, 59, 100, 239, 251, 253
Efficiency 3, 5, 49, 54–56, 59, 61–62, 80, 82–84, 91, 182, 190, 200, 202, 219, 235, 264–265, 275
electrically small antenna (ESA) 65, 99
E-Plane 30, 84, 94–96, 146, 148–140, 160, 196, 223, 220

G

Gain 5, 16, 19, 44, 54, 62, 67–68, 70, 82–84, 91, 94, 105, 138, 142, 146, 148, 150–151, 157, 166, 178, 181–182, 185–186, 190–191, 195, 210–211, 217, 228, 231, 225, 245, 257–258, 260–264, 276, 279–281

H

H-Plane 30–31, 33, 84, 94, 96, 148–149, 152, 160, 168, 196, 222–223, 229

J

J inverter 115, 118, 120

K

K inverter 115, 118

L

liquid crystal field detector 17
Loss Tangent 21–22, 235–238
effective 4, 13, 21–22, 57, 5 l–62, 78, 100, 119, 142, 146, 148, 157, 217, 236–237, 239, 251,253, 257–258, 282

M
Magnetic Current 170–173, 175, 223–224
Microstrip Antennas 1, 3–5, 7, 10, 19, 38, 56, 62, 65, 67, 76, 84, 92, 102, 106–107, 119–120, 126, 131–132, 137, 140, 142–143, 146, 148, 168, 170, 176, 178, 237
annular 6, 97, l00
Circular 2–3, 5–6, 39–44, 47–50, 52–53, 62–65, 76–97, 99–100, 105–106, 123, 126, 133, 188, 190–191, 197, 243, 246
dipole 6, 14, 130–132, 207, 219–220, 225–232, 264
elliptical 14, 87, 188
omnidirectional 7, 178, 180, 182, 186–188, 191–192, 207, 282
Quarter Wave 16, 24–26, 51, 67, 84, 91, 112–113, 115–116, 120–121, 133, 136–137, 155–157, 160, 211–212, 227, 268, 270–271, 273, 278
Quarter by Quarter Wave Patch 34–35, 84, 133
Rectangular 2–6, 10–12, 14–17, 19–20, 24–31, 33–34, 36, 38–42, 44–50, 52–55, 57–67, 70, 76–79, 83–85, 100, 104, 106–107, 113–1 14, 120, 126–129, 131–132, 134, 137–138, 142–144, 146, 157, 168–160, 171–173, 176, 178–179, 181–182,185, 188, 190–191, 203, 217, 219, 221, 223, 235, 243, 245, 247, 281
with dielectric cover (radome) 56
Microstrip 1–7, 10–17, 19–20, 24–43, 46–70, 76–86, 88–94, 97, 100, 102–108, 111–114, 116–122, 126–132, 134, 136–137, 140, 142–143, 146, 148, 154–160, 162–163, 165–166, 168–172, 178–180, 186, 188, 191, 198, 203–205, 211–214, 217, 219, 226–231, 235–237, 243, 245, 247, 249–255, 268, 270, 281–282
modes 2, 17, 19–20, 24–27, 36–42, 47, 49, 52,61, 63, 76, 78–80, 83, 85, 88, 94, 98, 100, 103, 105, 111, 120, 126–128, 134–135, 182, 211, 217, 245
Annular Patch 6, 97, 100
Circular Patch 78, 81, 83–87, 89, 92, 94–96, 99–100, 246
Rectangular Patch 6, 10, 20, 24 25, 27, 41, 44, 47, 50, 52, 62, 64, 70, 76, 82–84, 100, 126, 129, 134, 137–138, 173
TM10 24–26, 36–38, 40–42, 47, 49, 63–64, 83, 95, 107, 120, 126–128, 134

O
Omnidirectional Variation 7, 178, 180, 182, 186–188, 191–192, 207, 282

P
Polarization 5, 6, 14, 39–44, 47–51, 53, 63–65, 76, 85–90, 94, 100, 121, 123, 126, 133, 168, 202–203, 205, 221, 265
Circular 2–3, 5–6, 39–44, -46–50, 52–53, 62–65, 76–97, 99, 105–106, 123, 126, 133, 188, 190–191, 197, 243, 246
Linear 5, 14, 17, 19, 26, 28, 32–33, 37, 40–47, 52–53, 55–56, 60, 62, 64, 76, 87, 90–91, 100, 102, 120–121, 123, 126, 132, 142, 150–155, 162, 165, 168, 170, 185–189, 192, 195–196, 201, 205, 225, 258
Slant Linear 37, 40, 42–47

Q
Q 22–28, 25, 42–43, 45, 47–48, 52, 55, 61, 64, 82, 85–86, 89, 103, 200–203, 205, 207. 243, 271–275, 277–278, 281–282
and Bandwidth 68
conductor 1, 3, 5, 14, 22, 54–56, 81–82, 97, 100, 170, 181, 200, 202–203, 208, 214, 217, 222–223, 249, 252

dielectric 1, 3–6, 10, 13–14, 21–22, 28–30, 33, 36, 42, 47, 52–65, 68, 70, 77, 81–84, 89, 94, 98, 100, 102, 106, 142, 157, 160, 163, 183, 186, 194, 200, 211, 235–239, 251–253
and efficiency
estimate 29, 31, 62, 64, 83, 85, 146–148, 203, 207, 244, 258, 262, 264
minimum and electrically small antenna 65, 199
radiation 2–3, 6, 10–11, 13, 16, 18, 19, 21–23, 28–32, 34, 36–38, 40, 55, 60, 65, 68–70, 76, 80, 82–85, 88–91, 94–95, 100, 126, 143–146, 164–165, 167–168, 180, 182–186, 188–189, 196, 200, 202–203, 205, 207, 209–210, 217, 219, 221–223, 228–220, 231, 243, 262–265
surface wave 22–23, 54–56, 61, 166, 235
Quadrature Hybrid 50, 52
Quarter Wave Patch 34–35, 84, 133

R

Radiation Pattern 6, 16, 28, 30–32, 34, 65, 68–70, 76, 82–84, 88–91, 100, 126, 143, 164, 167–168, 182–184, 186, 188–189, 196, 207, 210, 222–223, 228–229, 231, 262–264
Radiation Resistance 31, 200
Resonant Frequency 24–25, 28, 36, 40, 49, 54, 60, 63–65, 78–79, 83, 85, 94, 100, 103, 163, 171, 203, 207, 21 1–217, 219

S

Stripline 1–2, 50, 192–197
Surface Wave Loss 22–28, 55, 235

T

tolerence
Transmission Line Equation 11, 91, 269
Transmission line model 4, 10–12, 14, 17, 19, 28, 35–36, 57–58, 62, 127, 214, 247, 252

Pulls everything together in one place... an indispensable reference on my desk... brilliantly helpful and practical to my needs.

Howard Friedenberg
Senior RF Engineer, Mosely Associates, Inc.

Microstrip and Printed Antenna Design 2nd Edition

A major update of the popular and practical text-reference covers "basic designs" in more detail than books that skip important electrical properties and implementation aspects. Numerous additions make the concepts even clearer. New cavity model analysis equations of circular polarization bandwidth, axial ratio bandwidth and power fraction bandwidth have been included. A new appendix now contains simple matching approaches, design details (gain, matching, sidelobes) of the little-studied omnidirectional microstrip antenna (OMA), limits and properties of common single and dual band Planar Inverted F Antenna (PIFA) designs.

Key Features

- Provides a complete introduction to useful elegant microstrip antenna designs that are unique
- Provides extensive section on the design of omni-directional microstrip antennas:
  - *De-mystifies basic PIFA designs and expands on their limitations*
  - *Discusses Electrically Small Antenna (ESA) limits, often ignored by other books.*
  - *Appendices include numerical methods for designs, practical aspects of substrate materials, copper thickness, dielectric values, types of plastics, and the manufacturing of Teflon fiberglass boards.*

Related Books

Blake and Long – *Antennas: Fundamentals, Design, Measurement* 3rd Edition (2009)

Elsherbeni and Inman – *Antenna Design and Visualization Using MATLAB* (CD with downloads)

Monzingo and Miller – *Introduction to Adaptive Arrays*, 2nd Edition (2009)

SCITECH PUBLISHING, INC.

SciTech Publishing, Inc., Raleigh, NC www.scitechpub.com

ISBN 9781891121739